Preparation of transition metal oxide thin films used as solar absorbers

Thi Ly Le

Université Fédérale
Toulouse Midi-Pyrénées

THÈSE

En vue de l'obtention du

DOCTORAT DE L'UNIVERSITÉ DE TOULOUSE

Délivré par :

Université Toulouse 3 Paul Sabatier (UT3 Paul Sabatier)

Présentée et soutenue par :

Thi Ly LE

le vendredi 30 septembre 2016

Titre:

PREPARATION OF TRANSITION METAL OXIDE THIN FILMS USED AS SOLAR ABSORBERS

École doctorale et discipline ou spécialité :

ED SDM : Sciences et génie des matériaux – CO034

Unité de recherche:

UMR 5085 CIRIMAT – Centre Inter-Universitaire de Recherche et d'Ingénierie des Matériaux

Directeur/trice(s) de Thèse :

Sophie GUILLEMET-FRITSCH
Christophe TENAILLEAU

Jury:

André AYRAL	Professeur, IEM, Montpellier	Rapporteur
Fabrice ROSSIGNOL	Directeur de Recherche, SPCTS, Limoges	Rapporteur
Catherine AMIENS	Professeur, LCC, Toulouse	Examinateur
Dinh Phong TRAN	Docteur, USTH Hanoï, Vietnam	Examinateur
Sophie GUILLEMET-FRITSCH	Directeur de Recherche, CIRIMAT, Toulouse	Examinateur
Christophe TENAILLEAU	Maître de Conférences, CIRIMAT, Toulouse	Examinateur
Pascal DUFOUR	Maître de Conférences, CIRIMAT, Toulouse	Invité

ACKNOWLEDGEMENTS

In 2nd October 2013, I started as a PhD student in the *Centre Inter-Universitaire de Recherche et d'Ingénierie des Matériaux* (CIRIMAT) laboratory. My three-years journey arrived to its end, with all its fine and became to a part of my life. The journey would not have succeeded without the cooperation and encouragement I received all along.

First of all, I would like to thank Dr. Philippe TAILHADES, the director of CIRIMAT for accepting me in the laboratory. I appreciate the working conditions and the warming reception.

Thanks to the Vietnamese government and University of Sciences and Technology in Hanoi (USTH) program, that opened the door of research for me in Toulouse.

I am very thankful to two reviewers of my manuscript, Professor André AYRAL and Research Director Fabrice ROSSIGNOL, as well as all the jury members, Dr. Dinh Phong TRAN and Professor Catherine AMIENS. Thank you for your time and your expertise.

My deepest and most sincere gratitude goes to my supervisors, Sophie GUILLEMET-FRITSCH, Christophe TENAILLEAU and Pascal DUFOUR, who have guided me through the doctoral research. I would like to thank you for giving me support and encouragement. Special thanks to you for your kindness and enthusiasm, for providing me valuable suggestions in research. Without your help, my thesis would not have been possible.

I would like to thank Professor Juan Claudio Nino from University of Florida, who has guided me to prepare the thin films by Pulsed Laser Deposition method and Dr. Rémis Arras from CEMES (Centre d'élaboration de Matériaux et d'études structurales) who calculated and explained for me about the first-principles electronic structure calculation.

I would like to thank equally to people who provided me logistic, administrative and technical assistance, Marie-Claire, Murielle, Nabila, Maryse, Isabelle, Benjamin, Abdé, Vincent, Yohan, Jean-Jaque… from CIRIMAT. Thank you for your kindness and easy going manner of work.

Thanks to all the colleagues in CIRIMAT. Thank you Mai Anh and Hoa for sharing all the tips and helping me all the papers that I needed for my first days in laboratory. Sébastien, Tawfik, Hyksu, Mong Cam, Soufiane, Nahum, Precious, Elsa, thank you for the friendly atmosphere in the office and all the encouragement during the last few months of my thesis. I had with you in

the office and in the lab will be part of good memories in my life. Thank you Candida, Luciana, Cyril, Inthuga, Pauline…Thank you all for sharing good moments with me.

I want to thank all my friends from Vietnam, Hoa & Nhi, Viet & Thu, Thao, Yen, Tam, Dung, Thuy, Trung…Thank you all for sharing with me the great moments apart from work no matter where, thank you for your support from everywhere, and most importantly thank you for your confidence in me. Thank you Yen and Tam for helping me to prepare the party for my defense.

From bottom of my heart, I would like to express my honest gratitude to my family for love and encouragement. Thank for them, I always be on the right track.

All my thanks,
LE Thi Ly.

TABLE OF CONTENTS

LIST OF ABBREVIATIONS

AALD	Atmospheric Atomic Layer Deposition
ASR	Area Specific Resistance
AZO	Aluminium doped Zinc Oxide
CB	Conduction Band
CCD	Charge Coupled Device
CET	Coefficient of Temperature Expansion
CIGS	Copper Indium Gallium Selenide
CIS	Copper Indium Selenide
CMOS	Complementary Metal Oxide Semiconductor
CNG	Compressed Natural Gas
CSD	Chemical Solution Deposition
CZTS	Copper Zinc Tin Sulfide
DFT	Density Function Theory
DOS	Density Of States
DSSC	Dye Sensitized Solar Cells
EQE	External Quantum Efficiency
FEG-SEM	Field Emission Gun Scanning Electron Microscope
FTO	Fluorine doped Tin Oxide
FWHM	Full Width at Half Maximum
GI-XRD	Grazing Incidence X-Ray Diffraction
HTM	Hold Transport Material
ICP-AES	Induced Coupled Plasma Atomic Emission Spectrometry
IQE	Internal Quantum Efficiencies
ITO	Indium Tin Oxide
MOS	Metal Oxide Semiconductor
P25	Degussa, average size equal to 25 nm of TiO_2
PES	Photoemission Spectroscopy
PLD	Pulsed Laser Deposition
PLZT	$(Pb, La)(Zr, Ti)O_3$
PMMA	Polymethylmethacrylate
PSCs	Perovskite Solar Cells
PV	Photovoltaic

PVD	Physical Vapor Deposition
SPS	Spark Plasma Sintering
TCOs	Transparent Conducting Oxides
TGA	Thermal Gravimetric Analysis
TMA	Thermal Mechanical Analysis
UPS	Ultraviolet Photoelectron Spectroscopy
UV-VIS-NIR	Ultraviolet Visible Near Infrared
VASP	Vienna Ab initio Simulation Package
VB	Valence Band
XPS	X-ray Photoelectron Spectroscopy
XRD	X-Ray Diffraction
XRF	X-Ray Fluorescence

GENERAL INTRODUCTION

General introduction

The development of societies across the world and increase in energy consumption show that we will require more energy in the future. In the context of energy crisis, climate change, long-term supply and security, solar energy is an attractive source. It is plentiful, virtually inexhaustible and can provide more than enough energy to our society. However, the issue with producing electricity and fuels from solar energy is that it is still expensive, primarily from the materials used in building the cells.

Metal oxide semiconductors are an attractive class of materials that are extremely low cost and can be produced at the scale needed to meet widespread demand. The synthesis and studies of nanosized materials have been intensively pursued in the recent years not only because of their characterization interest but also for their interesting properties such as catalytic, thermal, magnetic, electrical and optical properties and the variety of applications related to them. In the recent years, various methods have been developed for the preparation of nanostructured spinel oxides: physical and chemical vapor depositions, soft-chemistry methods, etc… The spinel structure is an important class of materials and metal oxide based spinels exhibit very interesting properties for uses in sensors, fuel cells, catalysis, solar cells, transformers, etc.

We wish to develop further a young thematic at the CIRIMAT based on the search for new inorganic materials, including spinel oxides, that can be integrated in solar cells. Researchers around the globe are racing to develop efficient thin film solar cells. Besides the Si and $CuInSe_2$ main families of inorganic semiconductor materials for solar cell applications, CdTe and GaAs are also important. However, indirect band gap energies (for Si), scarcity and/or toxicity of elements, and expensive ways of production are restricting factors for mass production of such type of solar cells. Thus, simultaneously to the search for solar cell efficiency improvements, it is necessary to find new compounds with suitable semiconducting properties in order to open new horizons for lower cost cells. Metal oxide based solar cells have the potential to counteract all the difficulties encountered in the usual solar cells. The all-oxide photovoltaic approach is very attractive due to the chemical stability, negligible toxicity and abundance of many metal oxides that potentially allow manufacturing of solar cells under ambient conditions. Metal oxides are widely used as components in photovoltaic cells such as

transparent conducting front electrodes or electron-transport layers, while only very few metal oxides have been used as light absorbers, basically *p*-type Cu_2O.

It is proposed here to synthesize by soft-chemistry routes and study nanoparticles and powders of new semiconductor and light absorber spinel oxides, with controlled size and morphology, for processing as thin films that could be easily integrated in an energetic system of conversion. Various doping schemes will drive to suitable physical characteristics such as the energy gap, sunlight absorption and charge transport for different applications, firstly for photovoltaics. The new semiconductors will be processed into thin layers for being used in simple photovoltaic cells with the ambition of preparing a complete solid oxide solar cell and replacing Si-based solar cells thanks to higher performances and lower production costs.

Therefore, the main objective of this thesis is to develop and study new photon-absorbing oxide materials based on the spinel structure with semiconducting properties. Our study focuses on Metal-doped $MnCo_2O_4$ spinel oxides (with Metal = Ni, Zn or Cu), since the reference material $MnCo_2O_4$ exhibits good electrical *p*-type semi-conductivity and sun light absorbance, while trying to improve these properties thanks to doping.

A large description of the world energy resources, the main families of inorganic materials usually found in thin film solar cells, the future and promising alternative of photovoltaics and the main features of spinel metal oxides that can be integrated in solar cells will be done in the first chapter. The second chapter will present all the experimental procedures and systems used during this work to prepare and characterize our materials. Chapter III presents first-principles calculations performed over the whole solid solution range of manganese and cobalt spinel oxides aimed at determining their density of states and electronic band structure, through a collaborative work with the essential contribution of an academic partner. In chapter IV, a full description of the synthesis method used to prepare nanopowders of metal spinel oxides, with controlled size and morphology, is given. Various characterization techniques were used in order to address the (micro-)structural properties of nano materials obtained at low temperature ($T < 120$ °C). Colloidal dispersions were also stabilized in order to prepare oxide thin films at room temperature without complexing agent. Their structural properties were characterized in details at room and high temperatures on various substrates, essentially by means of X-ray diffraction and electron microscopy. Finally, chapter V presents the optical and electrical transport measurements performed at different temperatures on the

Metal-doped $MnCo_2O_4$ spinel oxides prepared to increase the film compactness and density, as well as its electrical conductivity. The energy band gaps were also determined for each compound. Thin films light absorption and electrical conductivity were studied in detail in order to incorporate these materials into existing or especially designed types of solar cells in the near future. A study based on thin film preparation of Cu_2O and pure $MnCo_2O_4$ obtained by using the Pulsed Laser Deposition technique is also discussed in this last chapter.

CHAPTER I

TOWARDS ALL-OXIDE SOLAR CELLS

I.1. Introduction

The world energy demands are based on limited natural resources. These natural resources are harder to reach and can take hundreds of thousand years to replenish while the world demands are increasing with the expected 9.7 billion population growth from now to 2050. Global warming and climate change refer to an increase in average global temperatures. Moreover, the burning of fossil fuels releases greenhouse gases such as CO_2 or CO_x and also NO_x, SO_x …which causes air pollution to the atmosphere.

The main reason for international energy crisis in the 1970s was due to a lack of oil procurement in major industrial nations such as Germany, France, the United States, Canada, and other main developed countries. More recently, fuel protests in the United Kingdom (UK) in 2000 were caused by a rise in the price of crude oil combined with already relatively high taxation on road fuel in the UK. North American natural gas crisis occurred from 2000 to 2008. Central Asia energy crisis in 2008 was caused by abnormally cold temperatures and low water levels in an area dependent on hydroelectric power. At the same time, the South African President was appeasing fears of a prolonged electricity crisis in his country. China experienced severe energy shortages towards the end of 2005 and again in early 2008. During the latter crisis they suffered severe damage to power networks along with diesel and coal shortages. Supplies of electricity in Guangdong province, the manufacturing hub of China, were predicted to fall short by an estimated 10 GW. In 2011, China was forecast to have a second quarter electrical power deficit of 44.85 - 49.85 GW [1].

Alternative resources are thus necessary and renewable energies, including solar cells, which can provide enough energy to the world should now be a priority.

I.1.1. Decreases in fossil fuels reserves

Fossil fuels are created within the earth's crust, over extended periods of time, due to the extreme pressure applied to fossilized plants, animals and other organisms. Fossil fuels include coal, oil, and natural gas. Fossil fuels play a crucial role in the world energy market.

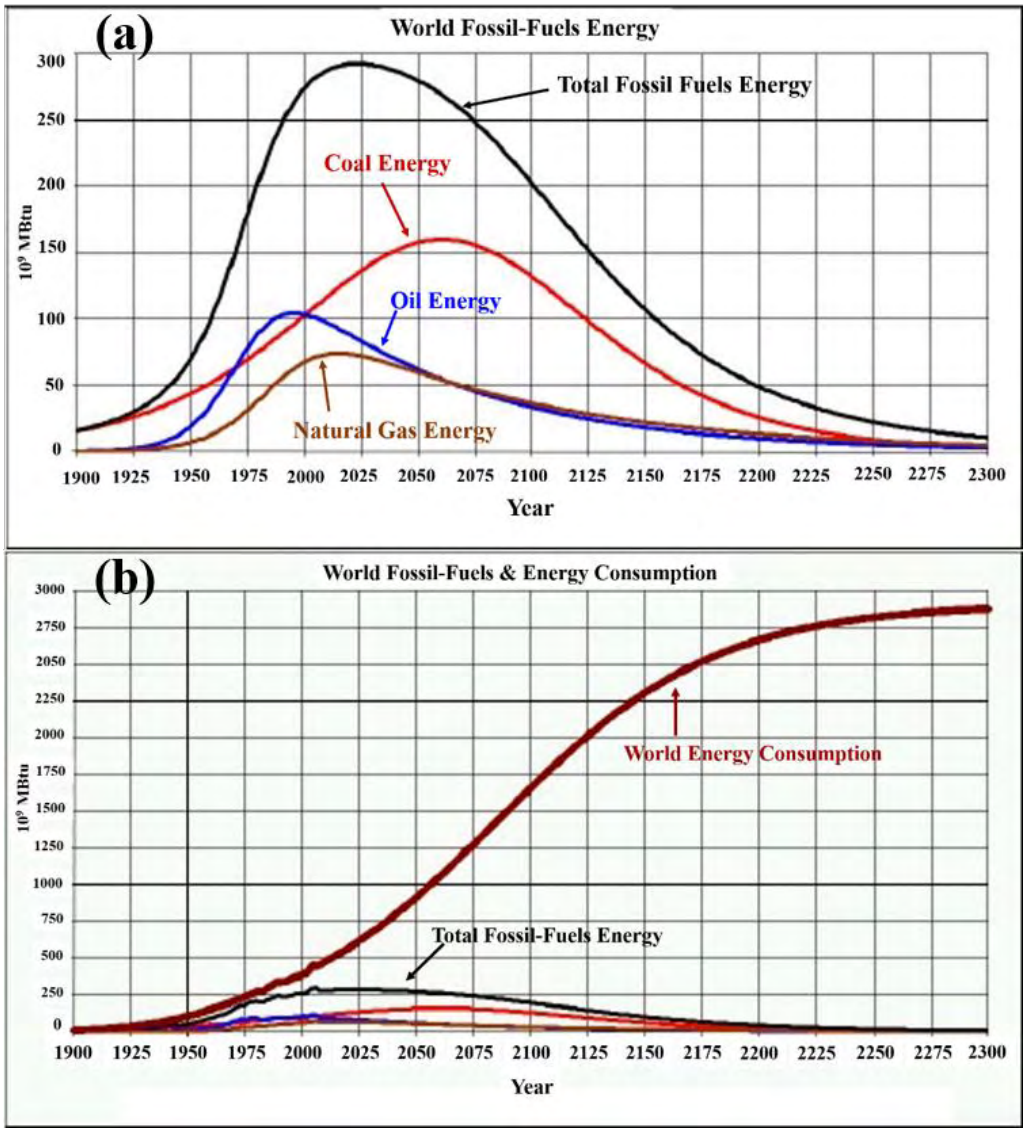

Figure I. 1: Energy obtainable from fossil fuels as a function of time (a) and comparison of the world energy consumption to the total energy supplied by fossil fuels (b) [2].

Figure I. 1 shows the energy obtainable from fossil fuels as a function of time and the world energy consumption compared to the total energy supplied by fossil fuels. Since 1900, the consumption of fossil fuels has nearly doubled every 20 years (Figure I. 1a). It is obvious that current use of fossil fuels continues threatening global stability and sustainability. This problem is even further compounded by increasing world population, rapid technological development, increasing energy requirements. With the rapid increase of world energy demand and energy consumption (Figure I. 1b), the fossil fuels energy cannot be considered as the principal energy sources in the future.

I.1.2. Climate change and global warming

Climate change is a change in the statistical distribution of weather patterns when that change lasts for an extended period of time (i.e., decades to millions of years). Climate change may refer to a change in average weather conditions, or in the time variation of weather around longer-term average condition. The primary cause of climate change is the burning of fossil fuels, such as oil and coal, which emits greenhouse gases into the atmosphere, primarily carbon dioxide.

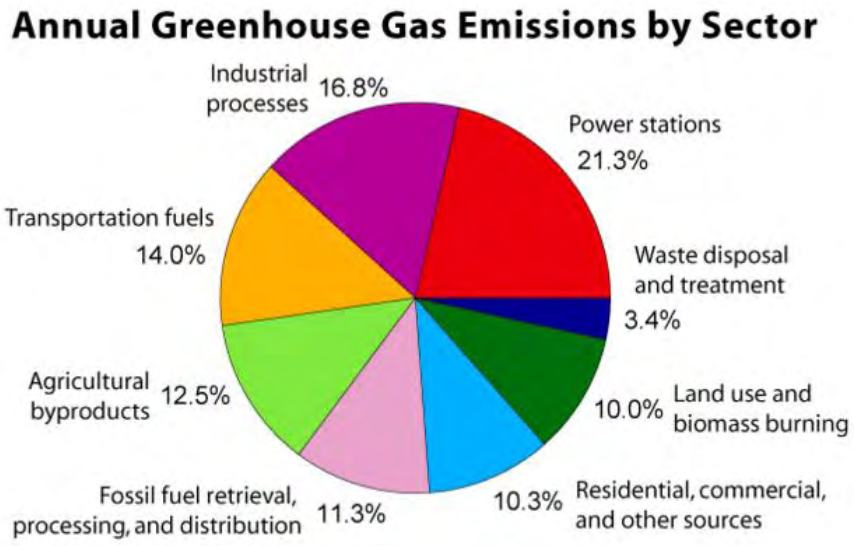

Figure I. 2: The annual greenhouse gas emission by sector [3].

Global warming is caused by greenhouse effect. Greenhouse gases in the atmosphere act like a mirror and reflect back to the Earth a part of the heat radiation, which would otherwise be lost into space. The higher the concentration of greenhouse gases in the atmosphere, the more heat energy is being reflected back to the Earth. As shows in Figure I. 2, the major greenhouse gases emission comes from the fossil fuels.

Evidence for a warming world comes from multiple independent climate indicators, from high up in the atmosphere to the depths of the oceans. They include changes in surface, atmospheric and oceanic temperatures, glaciers, snow cover, sea ice, sea level and atmospheric water vapor. Scientists from all over the world have independently verified this evidence many times [4, 5].

In the context of the present energy crisis and global warming, we need to develop energy generation techniques that support the requirements of sustainability and renewability. The production and use of renewable energy sources needs to be largely improved in order to provide sufficient energy to Humanity and to protect our Environment.

I.2. Renewable energy: Energy of the future

Renewable energy is any energy source that is replaced rapidly by a natural process and virtually inexhaustible, such as sunshine, wind, flowing water, biological processes and geothermal heat flows. Renewable energy sources may be used directly or to create other more convenient forms of energy. Examples of direct use are solar ovens, geothermal heating and windmills. Examples of indirect use, which require energy harvesting, are electricity generation through wind turbines or photovoltaic cells or production of fuels such as ethanol from biomass [6]. Renewable energy sources also are friendly with the environment, economic and are sustainable. However, they have some disadvantages and drawbacks, some of which are intrinsic or due to the status of technology development.

There are many sources of energy that are renewable, considered to be environmentally friendly and harness natural processes. Tidal power, wave power and hot hydrogen fusion are sources that can be used to generate electricity. However, each of these suffers from one or another significant drawback and cannot be relied upon at this time to solve the upcoming energy crunch. Among the most reliable renewable energy sources are wind power, hydroelectric energy, biomass energy, geothermal energy and solar energy.

I.2.1. Wind power

Wind power is the conversion of wind energy by wind turbines into a useful form, such as electricity or mechanical energy. The blades of the windmill are attached to a turbine that turns the kinetic energy (energy of movement) into electricity. Countries that have an abundance of empty land and high wind speeds have been able to utilize this renewable source of energy to fill in the gap between demand and supply from traditional means of energy. For example, France has the third largest wind resources in Europe with a 10358 MW total installed capacity in 2015 from 910 wind farms [7]. Wind power tower can be found singularly, but

usually many together in wind farms. Manufacture and implementation of wind farms can be costly and some local people object to on-shore wind farms, arguing that it spoils the countryside. Figure I. 3 shows the wind farm and wind power schematic.

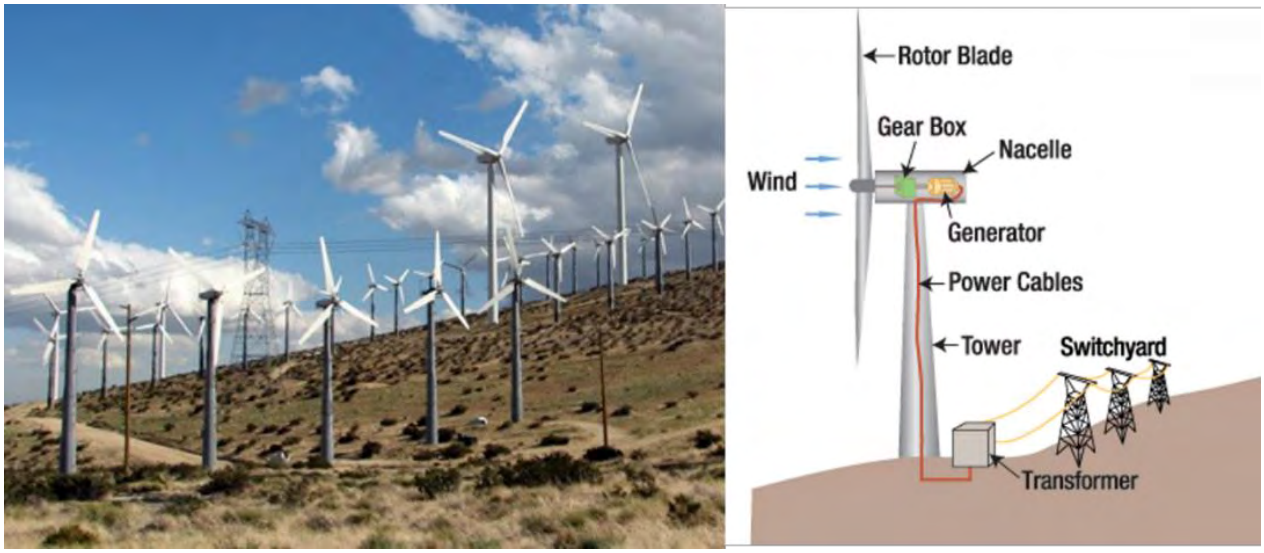

Figure I. 3: Wind farm and wind power schematic.

I.2.2. Hydroelectric energy

Hydroelectricity is electricity produced from the energy of falling water or fast running water. In the late 1800's, hydro-power became a feasible method for generating electricity. Decent-sized bodies of water, such as streams or rivers with high elevation drops and high currents are the best candidates for hydro power. The current provides substantial energy, which is harvested when water pushes through the paddles of an installed turbine, creating mechanical energy. If connected to an electrical generator, the water-powered turbine will spin the generator, converting mechanical energy into electrical energy. The first commercial hydroelectric power plant was built at Niagara Falls in 1879. Hydroelectric power provides about 20 % of the world's electricity. Hydropower has seen a recent jump in popularity with the World Bank naming it as one viable solution to keep up with growing energy demands while simultaneously avoiding carbon and carbon emissions into the atmosphere. Figure I. 4 shows the dam and schematic of hydropower.

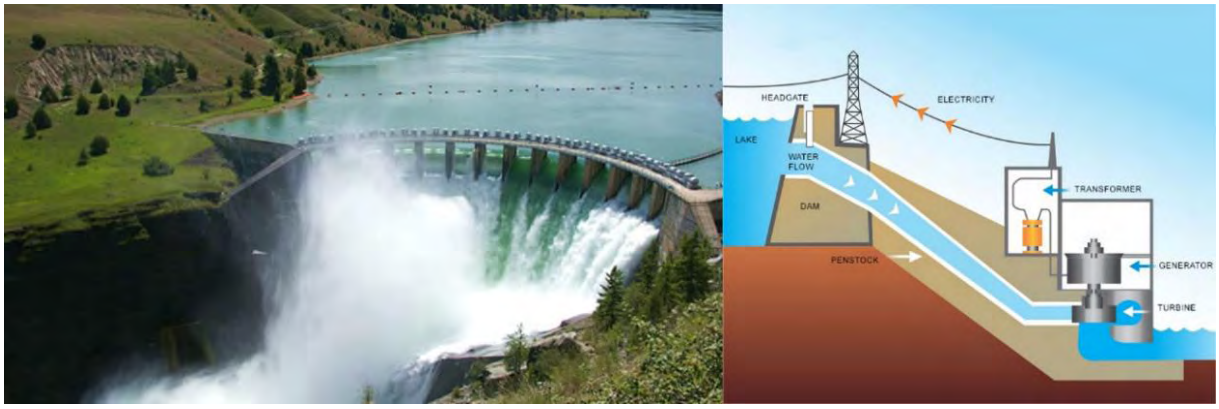

Figure I. 4: Dam hydropower images.

I.2.3. Biomass energy

Biomass energy is obtained from combusting or decomposing organic matter. Types of biomass are obtained from plants, plant waste and crops, landfills, municipal and industrial waste, trees and agricultural waste making them 'biological' in nature. Biogas has been produced in natural circumstances for thousands of years. It is only recently that we have been able to produce it in controlled conditions and compress it to make Compressed Natural Gas (CNG). Biofuels are basically ethanol, which is made when sugar is fermented. Similarly for CNG, this alcohol substance that is normally blended with gasoline as a form of car fuel, is used in the transportation sector. Figure I. 5 presents the converting biomass sources into energy.

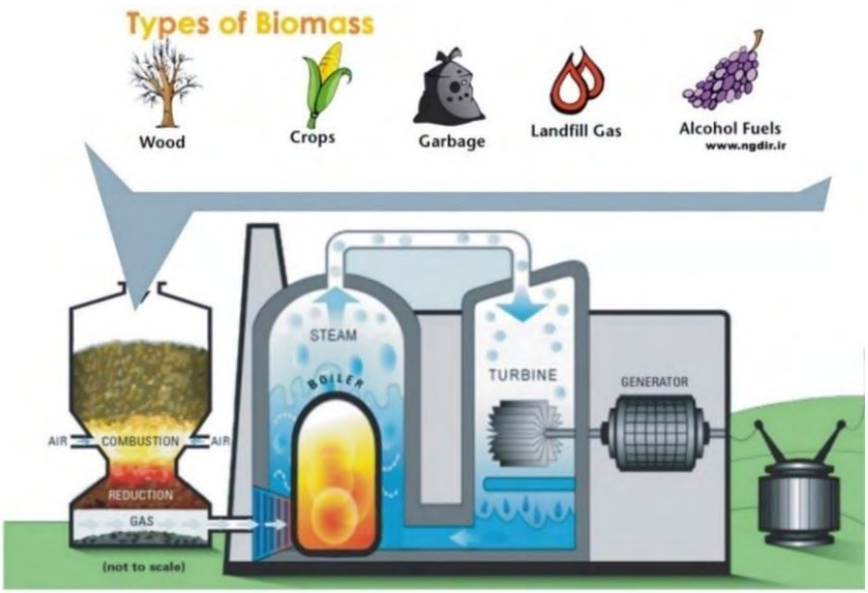

Figure I. 5: Converting biomass sources into energy.

I.2.4. Geothermal energy

Geothermal energy is a very powerful and efficient way to extract a renewable energy from the Earth through natural processes. Within the Earth, there is a great deal of energy trapped inside molten magma. All of this heat moves to the deep stores of water and air that flow through the Earth. In order to release the heat and regulate the temperature of the core, the heated water and air are released through vents, which are seen as holes in the crust of the Earth. The vents of heated air and steam are used to generate power which is yet another renewable source of energy. Geothermal energy is completely renewable, reduces dependence on fossil fuels, provides job benefits and significant cost saving. Figure I. 6 presents a diagram of geothermal power plant.

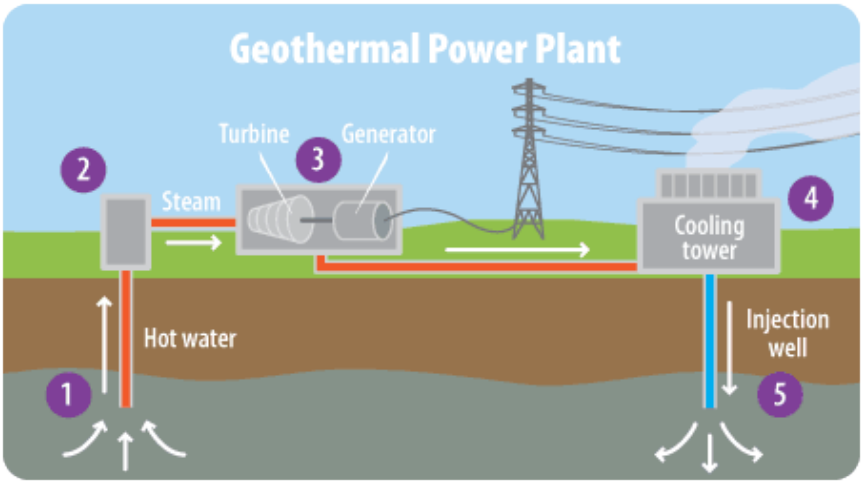

Figure I. 6: Diagram of geothermal power plant.

I.2.5. Solar energy

The primary source of energy is sunlight. Solar energy is used by plants in the process of photosynthesis. It is the reason why life on the planet Earth has flourished. About 70 % of sunlight gets reflected back into the space and only 30 % of sunlight is enough to meet up our energy demands. This source of energy relies on the nuclear fusion power from the core of the Sun. It can be collected and converted in a few different ways. One example is solar heaters. Whether it is industrial grade water heating or simple heating to cook food, solar energy can be utilized quite easily. With the development of solar panels and photovoltaic cells, it can also be used to create and store energy as needed. Solar powered homes, cars and appliances are

becoming common these days, as are solar farms that provide electricity to areas that are not on the grid. Solar cells are becoming more efficient, transportable and even flexible, allowing for easy installation. Two types of solar energy production are presented in Figure I. 7.

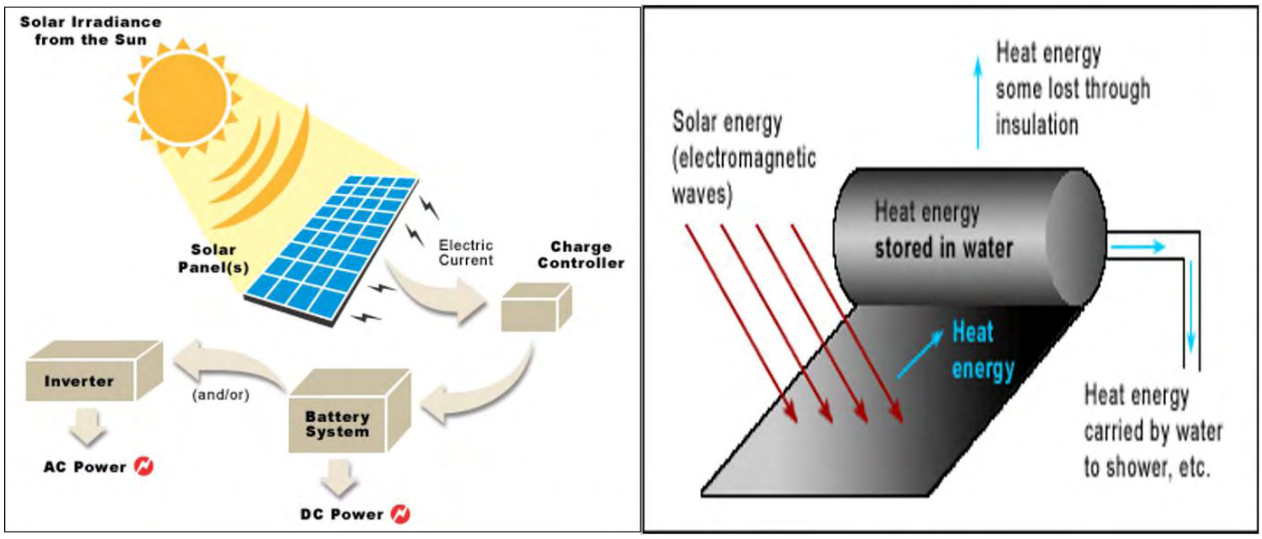

Figure I. 7: Solar energy production.

This thesis is mainly concerned primarily with renewable energy from the sun, which can product electrical energy by using the photovoltaic effect. In the next section, the different generations of photovoltaic cells will be presented.

I.3. Most familiar generations of photovoltaic cells

A solar cell or photovoltaic cell is an electrical device that converts the energy of light (photons) directly into electricity (voltage) by the photovoltaic effect. This effect was first noted by a French physicist, Edmond Becquerel, in 1839. He first observed the photovoltaic effect by using an electrode of platinum covered with a thin layer of light sensitive material such as silver chloride. He was able to demonstrate that the current was not due to a heating effect and obtained a rough spectral response curve by means of color filters placed between the electrode and the light source, which was the sun. In addition, he postulated that the current resulted from a chemical reaction at the electrode and gave the correct reaction [8]. In 1905, Albert Einstein described the nature of light and the photoelectric effect, for which he later won a Nobel Prize in physics. The first photovoltaic module made of silicon was built by Bell Laboratories in 1954. Throughout the 1960s, photovoltaic cells were primarily used to provide electrical power

for earth-orbiting satellites. In the 1970s, improvements in manufacturing, performance and quality of photovoltaic modules helped to reduce the cost. This opened up a number of opportunities for powering remote terrestrial applications, including battery charging for navigational aids, signals, telecommunications equipment and other critical, low-power needs. In the 1980s, photovoltaic cells became a popular power source for consumer electronic devices, including calculators, watches, radios, lanterns and other small battery charging applications. Following the energy crises of the 1970s, significant efforts also began to develop photovoltaic power systems for residential and commercial uses, both for stand alone, remote power and utility connected applications. During the same period, international applications for photovoltaic systems to power rural health clinics, refrigeration, water pumping, telecommunications, and off-grid households increased drastically; it remains a major portion of the present world market for photovoltaic products. Today, the industry's production of photovoltaic modules is growing at approximately 25 percent annually and major programs in the United States, Japan and Europe are rapidly accelerating the implementation of photovoltaic systems on buildings and interconnection to utility networks.

I.3.1. First generation of photovoltaic cells

The first generation includes cells consisting of silicon (or germanium) doped with boron (*p*-type) and phosphorus (*n*-type) in a *pn* junction (see Figure I. 8). This generation is dominating the commercial market. Silicon cells have a quite high efficiency, but very pure silicon is needed. Due to the energy requiring process, the price is too high compared to the power output. Also, silicon possesses an indirect band gap and thicker cells are required in order to compensate for the energy loss (mainly as heat). The first generation solar cells are produced on wafers. Each wafer can supply 2-3 Watts of power. To increase power, solar modules, which consist of many cells, are used. Generally, there are two types of first generation solar cells. They differ by their crystallization levels. If the whole wafer is only one crystal, it is called a single crystal solar cell. If the wafer consists of crystal grains, it is called a polycrystal solar cell as shown in Figure I. 8. Although efficiency of single crystal solar cells is higher than polycrystal solar cells, production of a polycrystal wafer is easier and cheaper. Polycrystal cells do not go through the cutting process used for single crystal cells. Instead, the silicon is melted and poured into a square mold, hence the square shape of polycrystal. Therefore, they are much

more affordable since a negligible amount of silicon is wasted during the manufacturing process and are more competitive than single crystals.

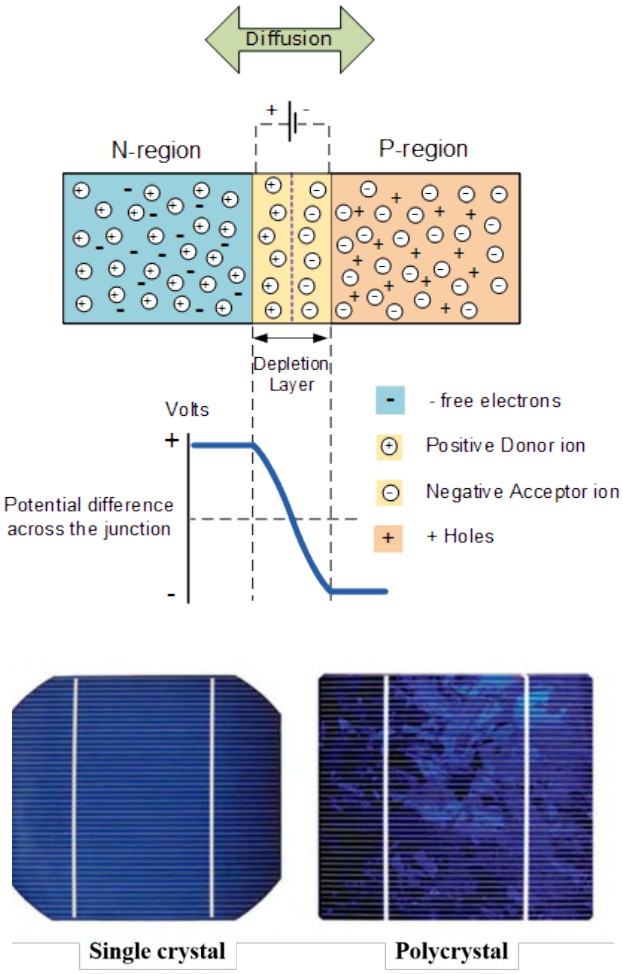

Figure I. 8: pn-junction and two types of first generation solar cells: single crystal and polycrystal.

I.3.2. Second generation of photovoltaic cells

Second generation photovoltaic cells are usually called thin film solar cells. They are made from layers of semiconductor materials only a few micrometers in thickness such as cadmium telluride/cadmium sulfide (CdTe)/CdS, copper indium selenide (CIS) or copper indium gallium selenide (CIGS), copper zinc tin sulfide (CZTS) and gallium arsenide (GaAs). Since the second generation solar cells avoid use of silicon wafers and have a lower material consumption thanks to direct band gaps, it has been possible to reduce production costs. These thin films can also be grown on flexible substrates. So, second generation solar cells are

applicable on textile products or on foldable devices. While many variations of thin film products exist, they typically achieve efficiencies of 7-13 % [9, 10]. However, a lot of research and development is being put into thin film technologies and many scientists suspect efficiencies to climb as high as 23.3 % in coming models (see Figure I. 9).

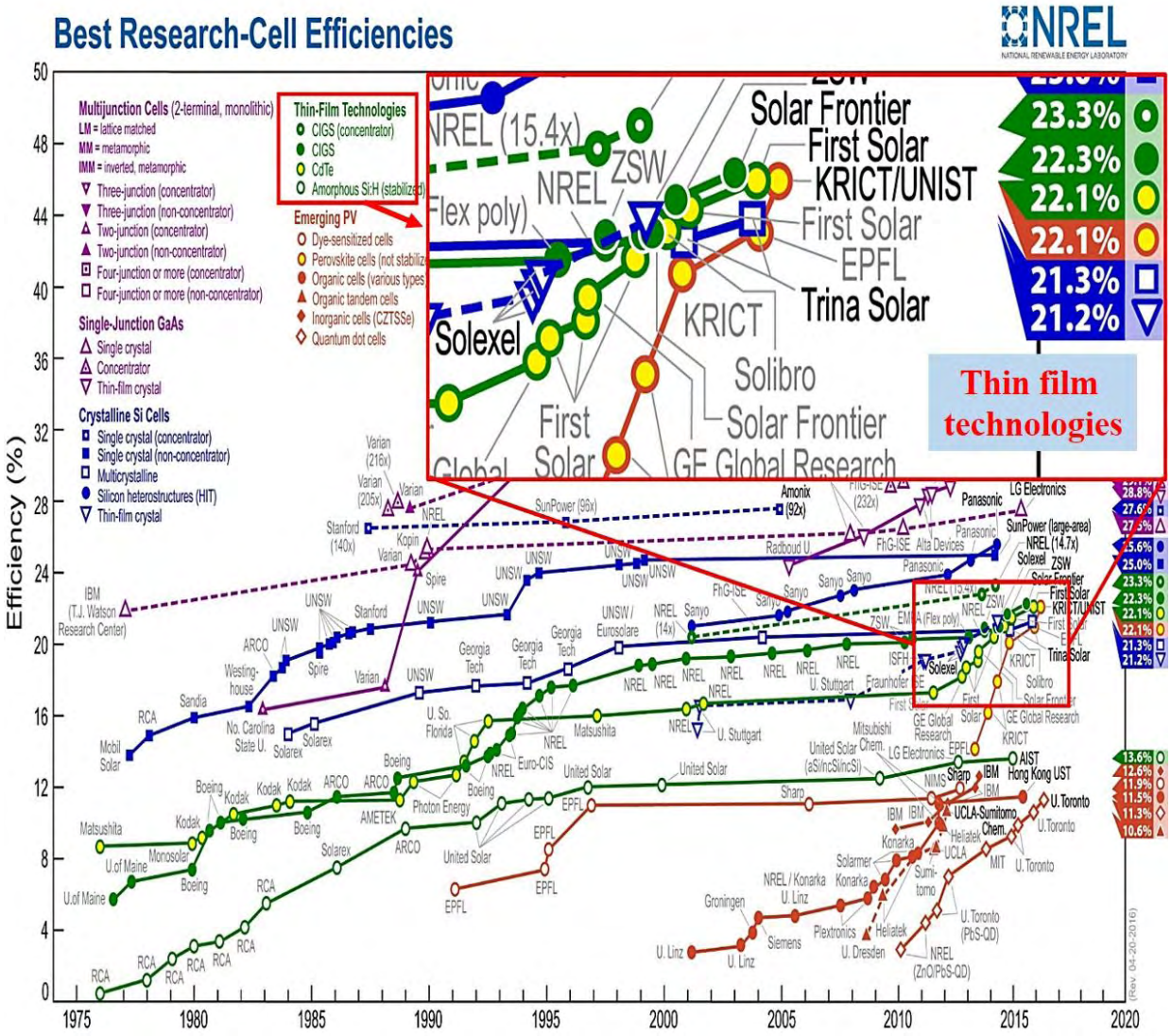

Figure I. 9: Current status of photovoltaic cells and their efficiency [11].

Another perk is that high heat and shading have less of a negative impact on thin film technologies. For these reasons, the thin film market continues to grow. Figure I. 10 shows example of major systems of thin films solar cells.

Thin film solar cells such as CIGS/CdS or CdTe/CdS are particularly studied for improving efficiency. Since CdTe has an optimal band gap of 1.49 eV for single junction

devices, efficiencies above 20 % should be achievable in the commercial CdTe solar cells [12]. Contreras et al. (2005) presented several devices with an energy conversion efficiency of 19.5 % for CIGS (with band gap of 1.14 eV) thin film solar cells [13]. But there are some drawbacks for this type of solar cells as Te is not abundant and Cd is toxic. More recently, copper zinc tin sulfide (CZTS) with a kesterite structure (CZTS/CdS – see Figure I. 10), is considered to be an alternative material to the CIGS which is currently under extensive development. CZTS is assumed to be analogous to CIGS when In (III) is replaced by Zn (II), Ga (III) is replaced by Sn (IV) and Se (VI) by S (VI). For the CZTS, the high absorption coefficient (10^4 cm^{-1}) and optimum band gap (1.0 – 1.5 eV) cover the maximum solar spectrum and open a gateway for economic and ecological thin film devices fabrication. The highest efficiency (12.6 %) was reported using hydrazine based non-vacuum particle solution approach [14-16].

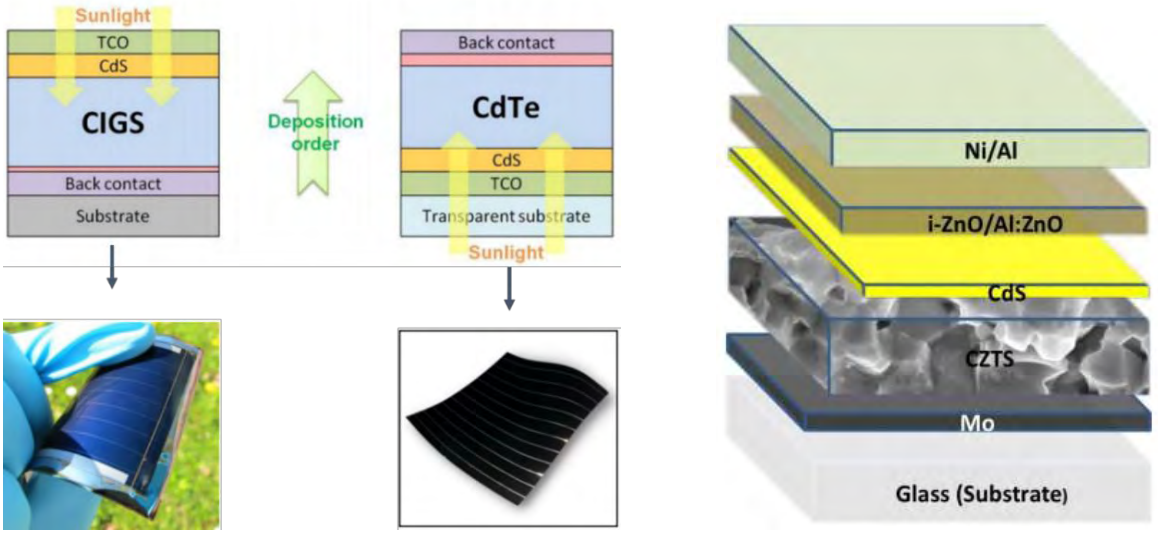

Figure I. 10: Schematic of thin film solar cells systems [14, 17].

I.3.3. Third generation of photovoltaic cells

Third generation photovoltaic cells are novel technologies which are promising but not commercially proven yet. Most developed third generation solar cell types are nanocrystal based solar cells, polymer based solar cells, dye sensitized solar cells (DSSC) and concentrated solar cells. DSSC are based on dye molecules between electrodes that create electron/hole pairs (excitons) after absorbing light and transferring electrons to *n*-type conductive TiO_2

nanoparticles. An electrolyte based on iodine is necessary to refurbish the valence band of the light absorber dye. The structure of a dye-sensitized photovoltaic cell is shown in Figure I. 11.

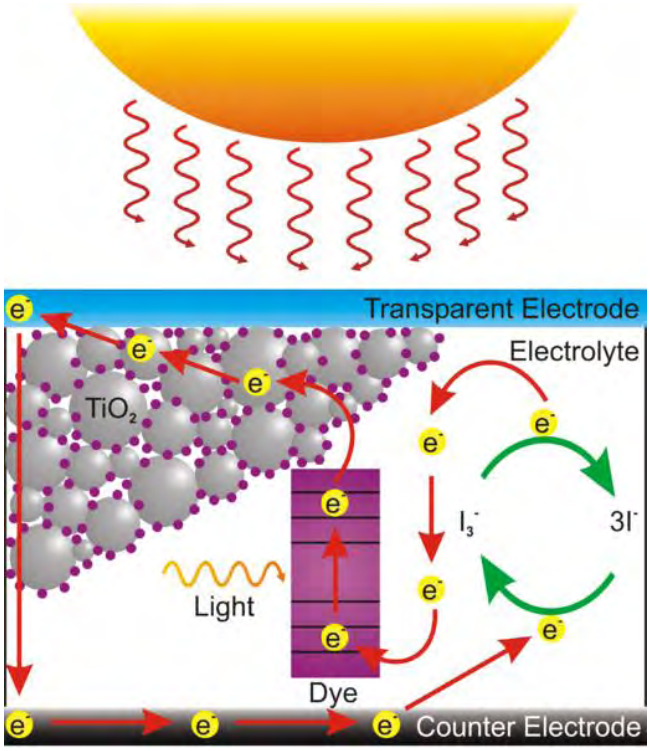

Figure I. 11: Structure of a dye-sensitized solar cell [18].

Their production is easy with respect to other technologies. DSSC can be of various colors and is still efficient under small illumination. Michael Graetzel, the original DSCC designer, recently announced the fabrication of solid state DSSC with 15.0 % power conversion efficiency, by the means of PbI_2 firstly introduced from solution into a nanoporous TiO_2 film and subsequently transformed into the perovskite by exposing it to a solution $CH_3NH_3PbI_3$ [19].

Concentrated photovoltaic cell is another promising technology. The main principle of a concentrated cell is to concentrate large amounts of solar radiations onto a small region where the photovoltaic cell is located. These cells are typically applied in the concentrator modules based on a concept of the small-aperture refractive concentrators. Figure I. 12 shows a schematic of a concentrated photovoltaic cell system. The amount of semiconductor material, which might be very expensive, is reduced in this way. In this system a perfect optical system should be integrated. Concentration levels start from ten suns to thousand suns. Their total cost can be lower than for conventional systems. Concentrated photovoltaic cells are thus promising technologies for the near future.

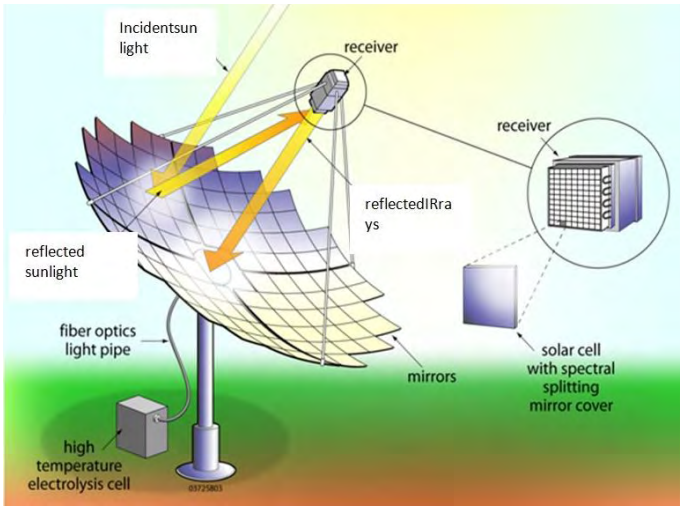

Figure I. 12: Schematic of a concentrated photovoltaic cell.

I.4. Metal Oxide semiconductors for photovoltaic cells

I.4.1. *n*-type wide band gap metal oxides

Wide band gap metal oxides are electrically conductive materials with a comparably low absorption of visible light (from 380 nm to 780 nm of wavelength) and with an optical band gap usually greater than 3.2 eV. *n*-type metal oxide semiconductors are widely used as components in photovoltaic cells and modules, either as transparent conducting front electrodes, as electron (and hole) transport layers that provide the required charge selectivity between absorber and the contacts, or as back electrodes [20, 21]. Among the most popular transparent conducting front electrodes used for electronic devices are the so-called transparent conducting oxides (TCOs) such as fluorine doped tin oxide (FTO), indium tin oxide (ITO) or aluminium doped zinc oxide (AZO) [22]. Wide band gap metal oxides for electron conducting layers such as TiO_2, ZnO, SnO_2 are also *n*-type metal oxides. For instance, ZnO and AZO are used as electron transport layers for the top and front electrodes, respectively, in thin film Cu(In, Ga)Se_2 (CIGS) solar cells [17, 23]. Compact thin films of ZnO and TiO_2 have been used in polymer based thin film solar cells to achieve a selective contact [24, 25]. In organic solar cells, hole transport materials such as V_2O_5, WO_3, MoO_3 and NiO were used for hole-injection, hole-extraction interlayers, charge generation and charge recombination layers [26, 27].

I.4.1.1. Electrical conductivity of *n*-type metal oxide semiconductors

The electrical conductivity of wide band gap metal oxides can be explained by the band theory of semiconductors. When atoms come together to form a compound, their atom orbital energies mix to form molecular orbital energies. As more atoms begin to mix and more molecular orbitals are formed, it is expected that many of these energy levels will start to be very close to, or even completely degenerate, in energy. These energy levels are then said to form bands of energy. Electrons occupy the lowest energy orbitals and electrons in bulk materials fill the bands starting at the lowest energy. The energy gap between the highest energy level of electron-occupation with the next available energy level provide a means for understanding the electrical conductivity of a material. Electrons carry a current by moving through a material, and this motion can be thought of in terms of electrons moving from one orbital to another. But electrons within a filled band cannot move readily to conduct electricity. To have mobile electrons, we will need to have an unfilled band or portion of a band that is close in energy to a filled band or portion of a band. Diagrams of energy bands for solids are shown in Figure I. 13.

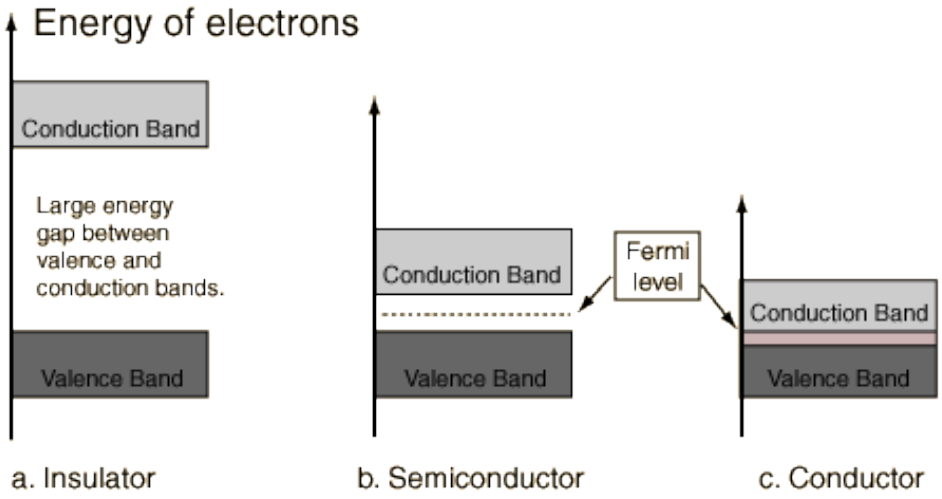

Figure I. 13: Diagrams of energy bands for different solids

For the large energy gap between the valence and conduction bands in an insulator, at ordinary temperatures, no electrons can reach the conduction band. In semiconductors, the band gap is small enough that so thermal energy can bridge the gap for a small fraction of the electrons. The highest filled energy level is at the top of the valence band, but the next band is only modestly higher in energy. In semiconductors, some electrons have enough thermal energy to reach the upper band even at room temperature, and therefore they present limited electrical

conductivity. If the temperature is increased, more electrons should occupy the upper band, and the conductivity of semiconductors increases at higher temperatures. In conductors, there is no band gap since the valence band overlaps the conduction band (or consist of an unfilled valence band). The energy below which an energy level is likely to be filled is called the Fermi level [28].

I.4.1.2. Optical properties of *n*-type metal oxide semiconductors

Optical properties of wide band gap (greater than 3.2 eV) metal oxides thin films usually exhibit transparency in visible and near infrared regions of wavelengths and are reflective to thermal infrared radiation. For long wavelengths, wide band gap metal oxides are reflective due to free electrons in the conduction band and for very low wavelengths, absorption is observed due to the band gap of the material [20, 29, 30].

The most striking feature of band gap absorption in wide band gap metal oxides is a strong blue-shift of the determined band gap for increasing doping. *N*-type semiconductors are materials in which charge carriers are electrons in the conduction band, while *p*-type materials present electrical current carried by holes in the valence band.

I.4.2. *p*-type metal oxide light absorbers

Generally, solar cells are built from different main elements (as shown in section I.3). Besides their electrical properties, it also has to fulfill essential optical requirements. In a typical *n*-transparent/*p*-absorber solar cell, *p*-type and *n*-type are put side by side and a *pn*-junction is formed. Figure I. 14 shows a simplified illustration of a *pn*-junction. When light goes on the *p* layer where most of the absorption takes place, they transfer energy to some valence electrons, promote them to higher energy levels; from the lower energy valence bands to higher energy, i.e. excited states of the conduction bands. When the *pn*-junction is formed, some electrons in the intermediate region are attracted from the *n* side to combine with holes on the nearby *p* side. Charge builds up as electrons and holes combine at the *pn*-junction and excess charges create an electric field. Direct band gaps are a good choice because in a direct band gap semiconductor, the top of the valence band and the bottom of the conduction band occur at the same value of momentum. Therefore, the electron does not need to be given very much momentum to produce

an electron-hole pair. And in the recombination process of electrons and holes to produce photons, the efficiency for a direct band gap is higher. The absorbed photons create electron/hole pairs. Then electric field of the *pn*-junction separates them and directs them in opposite directions to the electric contacts. It is particularly important to ensure a reasonable transport of the photo-generated minority charge carriers because they dominate the electric behavior of the *pn*-junction. In most semiconductors the mobility is higher for electrons than for holes, the latter carried by the absorber of *p*-type conduction [31, 32].

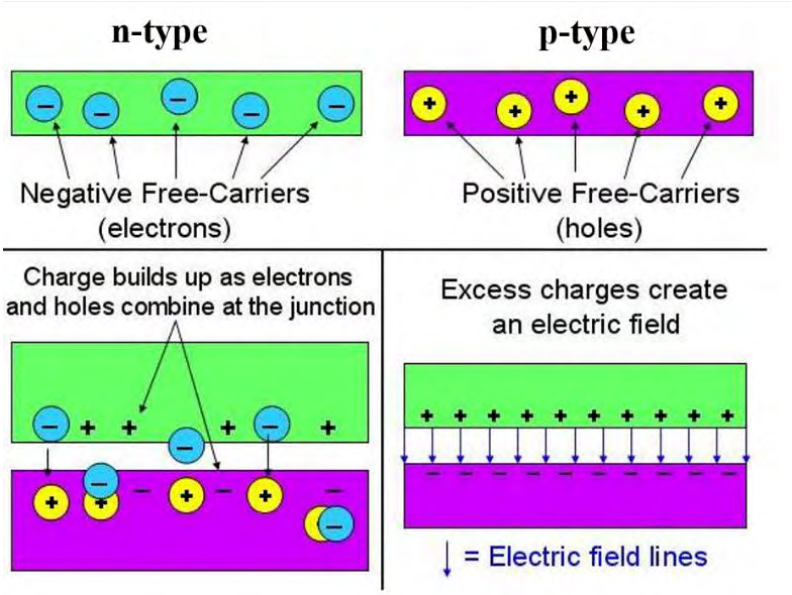

Figure I. 14: pn - junction and electric field inside photovoltaic cells.

For all-oxide photovoltaic cells, the metal oxide absorbing semiconductors should have a direct band gap, high absorption coefficient in the relevant energy range for photovoltaics (10^5 cm^{-1}), with most of sunlight absorbed within a small range beneath the surface, and offer the possibility to fabricate thin films.

Optical characterization is important for *p*-type oxide semiconductors to be applied in photovoltaic cells. When a radiant flux is incident upon a material surface, three processes occur: transmission, absorption, and reflection. Application of conservation of energy leads to the statement that the sum of the transmission, reflection, and absorption of the incident flux is equal to unity (and in the absence of nonlinear effects) [33]. Measurements of the power reflection, transmission or absorption are the simplest and most direct methods of semiconductor materials spectroscopic analyses. The measurements are simple to perform as long as a satisfactory spectroscopic apparatus is available in the wavelength region of interest.

I.5. All-oxide photovoltaics: The next generation of photovoltaic cells?

The market for photovoltaic cells has grown exponentially over the last few years to fulfil the global energy demand. But, one of the primary challenges to the full-scale implementation of solar energy remains the expensive cost associated with the construction of photovoltaic modules and certain toxic elements in some thin film solar cells. To reach grid parity, further price reductions for photovoltaic systems are required; this call for continued up scaling of the production processes or for uses of novel materials for photovoltaic cells based on high efficiency and cheap materials in combination with low cost deposition methods. Metal oxide semiconductors are very attractive to achieve this goal, many of them show great chemical stability, negligible toxicity, abundance, fulfil the requirements for low cost manufacturing methods at ambient conditions, and could show high conversion efficiency for photovoltaic. A schematic of an all-oxide photovoltaic cell is shown in Figure I. 15. The usual design for such cell, like in many previous generations, consists of a glass substrate, a transparent conductive oxide layer (*n*-type semiconductor), a metal oxide light absorber (*p*-type semiconductor) and contact layers (see Figure I. 15).

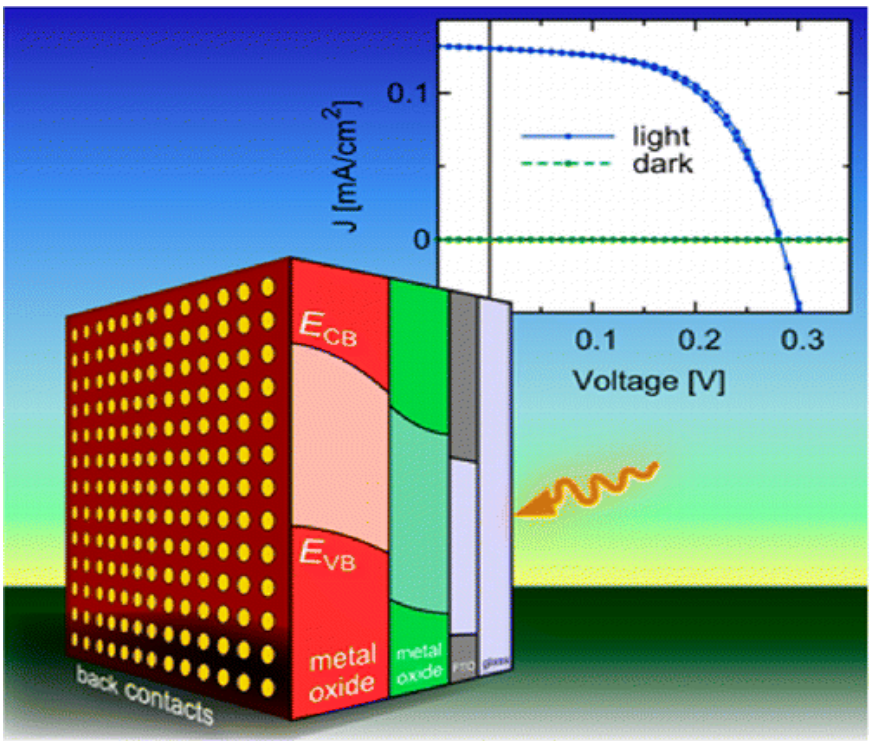

Figure I. 15: Schematic of all-oxide photovoltaic cells [34].

I.5.1. Cu_2O based "all-oxide" photovoltaics

Cu_2O, of cuprite structure, is a semiconductor with a direct energy band gap of about 2.2 eV [35, 36]. It is the most investigated metal oxide used as the light absorber for photovoltaics and it has a theoretical limit of energy conversion efficiency of about 20 % under AM1 (air mass at the surface of Earth at noon) solar illumination [37]. Heterojunction devices were developed, mainly with the wide band gap ZnO as an intrinsic *n*-type semiconductor and cuprous Cu_2O as the *p*-type absorber. Previous attempts to nanostructure Cu_2O/ZnO solar cells required prohibitively long fabrication times or resulted in efficiencies of less than 0.1 % [38, 39]. Hsueh et al. (2007) sputtered Cu_2O onto ZnO nanowires grown by a vapor-liquid-solid technique [39], and Yuhas et al. (2009) drop-cast Cu_2O nanoparticles into a hydrothermally grown ZnO nanowire array with a 10 nm TiO_2 coating [38]. Then, the power conversion efficiency of 1.43 % was improved under air mass 1.5 illumination for photovoltaic device based on a FTO/ZnO/Cu_2O/Au heterojunction structure, which was deposited from a pH-adjusted electrolyte of LiOH by Kazuya el al. (2013) [40]. 1.46 % and 0,49 V are the power conversion efficiency and open-circuit voltage, respectively, which were achieved for ZnO/Cu_2O heterojunctions deposited by atmospheric atomic layer deposition (AALD) technique [41].

In Cu_2O-based heterojunction solar cells, various compounds were used to dope ZnO used as the *n*-type oxide thin-film layer to increase the power conversion efficiency. Heterojunctions of ITO/ $Zn_{0.79}Mg_{0.21}O$/Cu_2O showed a power conversion efficiency of 2.2 %, which were prepared by AALD method [41]. Tadatsugu et al. (2011) reported low cost Al-doped ZnO (AZO)/non-doped ZnO (ZO)/Cu_2O heterojunction solar cells with a high conversion efficiency of 3.83 %, that was fabricated by depositing thin films at a low temperature on thermally oxidized copper sheets using a PLD (Pulsed laser deposition) method [42]. One year later, a high conversion efficiency 4.08 % was obtained with the same AZO/ZnO/Cu_2O heterojunction solar cells fabricated by inserting the buffer layer on low cost, nontoxic Cu_2O sheets prepared by thermally oxidizing Cu sheets [43]. In January 2016, the same group of Tadatsugu published the highest conversion efficiency (over 6 %) for an open circuit voltage of Cu_2O-based heterojunction solar cells so far using multicomponent oxide thin films as the *n*-type semiconductor layer as shown in Table I. 1 [44]. The obtained improvement of photovoltaic properties may be attributable mainly to an increase of the barrier height formed in the *p*-*n* junction, resulting from the inserted buffer layer functioning as an *n*-type ZnO layer

as well as an enhancement of carrier lifetimes near the interface between the non-doped ZnO thin-film buffer layer and the Cu_2O.

Table I. 1: Conversion efficiency and open circuit voltage of Cu_2O-based heterojunction solar cells using multicomponent oxides as the n-type oxide semiconductor thin film layer [44].

Heterojunction solar cell	Conversion efficiency (%)	Circuit voltage (V)
AZO/$ZnGa_2O_4$/Cu_2O	5.38	0.81
AZO/Zn_2SnO_4/Cu_2O	3.64	0.63
AZO/$(Ga_{0.975}Al_{0.025})_2O_3$/$Cu_2O$	5.42	0.84
AZO/$(Zn_{0.91}Mg_{0.09})_2O_3$/$Cu_2O$	4.29	0.80
MgF_2/AZO/AGMZO/Cu_2O:Na	5.40	0.96
MgF_2/AZO/$(Ga_{0.975}Al_{0.025})_2O_3$/$Cu_2O$:Na	6.25	0.84

[*] *AZO: Al doped ZnO; AGMZO: Al-Ga-Mg-Zn-O multicomponent oxides, composed of Al_2O_3, Ga_2O_3, MgO and ZnO.*

Besides ZnO, other metal oxides have been used to form bilayer heterojunction all-oxide photovoltaic cells such as TiO_2 and ITO. Sahrul et al. (2013) prepared a TiO_2/Cu_2O heterojunction solar cell, which was employing polymer electrolyte (containing Li^+ ion) with a power conversion efficiency of 1.05 % [45]. Luo et al. (2012) synthesized TiO_2 by a hydrothermal reaction and Cu_2O thin films are then electrodeposited at the surface of TiO_2 nanorods. The efficiency of the resulting TiO_2/Cu_2O nanorods radial heterojunction solar cells is up to 1.25 % [46]. Mitiga et al. (2006) reported the power conversion efficiency of 1.07 % and 2.01 % obtained for MgF_2/ITO/Cu_2O and MgF_2/ITO/ZnO/Cu_2O heterojunction solar cells, respectively, which were made by deposition of transparent conducting oxide (TCO) films on Cu_2O substrates. The TCO films have been grown by ion beam sputtering on good quality Cu_2O sheets prepared by oxidizing copper at high temperature [47].

I.5.2. Perovskite solar cells (PSCs)

Perovskite are materials with ABX_3 stoichiometry (for example, calcium titanate $CaTiO_3$) that form crystal structures where *B* cations reside in the centers of corner-shared octahedral of *X* anions, with the *A* cation filling the resulting interstices. Perovskite have captivated researchers with properties such as superconductivity, ferroelectricity, piezoelectricity, ferromagnetism and antiferromagnetism. Perovskite solar cells (PSCs) have received considerable attention in recent years as a promising material capable of developing high performance photovoltaic devices at a low cost. Even though most of the known perovskites are metal oxides, metal halide perovskites have recently been taking the field by storm with their record shattering photovoltaic performance combined with low-cost processing methods and earth-abundant elemental compositions.

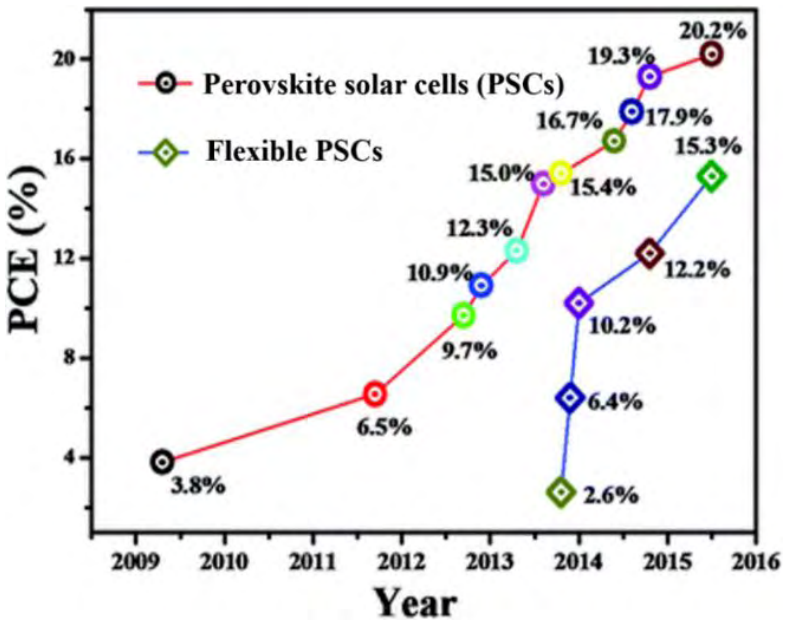

Figure I. 16: Progress of power conversion efficiency of the perovskite solar cells and flexible perovskite solar cells devices in the past 6 years[48].

The best solar cell performance has been obtained from hybrid organic-inorganic metal halide perovskites such as methylammonium lead iodide ($CH_3NH_3PbI_3$) or methylammonium lead bromide ($CH_3NH_3PbBr_3$). Figure I. 16 shows the progress in the perovskite solar cells which have jumped from 3.8 % of methylammonium lead halide $CH_3NH_3PbX_3$ (*X* = Br, I) sensitized liquid solar cells in 2009 [49], to more than 20 % of formamidinium lead iodide ($NH_2CHNH_2PbI_3$) solar cells in 2015 [48]. Qin et al. (2014) presented a device structure

consisting of titanium dioxide as a scaffold as well as electron collector, lead halide perovskite as the light harvester and CuSCN as the hold transport material (HTM) with high power conversion efficiency of 12.4 % under full sun illumination [50].

Recently, ferroelectric perovskite oxides have also drawn much attention due to potential applications in the field of solar energy. When a ferroelectric material is illuminated with light, charge carriers (electron-hole pairs) are generated. These photo-generated carriers are separated and driven to the electrodes by the polarization induced internal electric field, causing a photovoltaic output. The photovoltaic effect in ferroelectrics is a bulk-based effect, which differs from the junction based semiconductor photovoltaic effect. Since the internal electric field is not limited to an interfacial region in a ferroelectric, photovoltaic responses can be generated without forming complex junction structures. Figure I. 17 shows a simplified schematic of photovoltaic mechanism in a ferroelectric material.

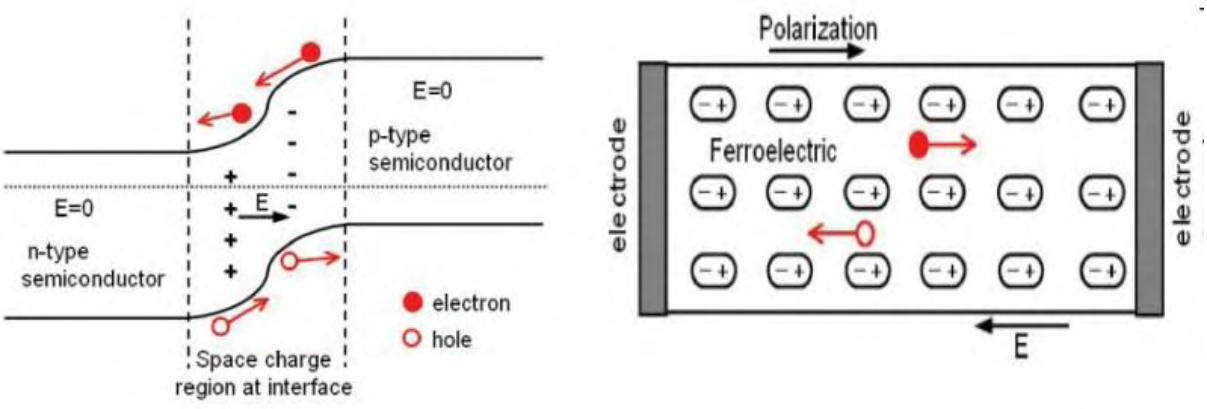

Figure I. 17: Simplified schematics for the interfacial photovoltaic effect in a semiconductor p-n junction (left) and the bulk PV effect in a ferroelectric thin film (right).

Some ferroelectric materials for photovoltaics, such as $BiFeO_3$ (BFO), $Pb(Zr,Ti)O_3$ (PZT) and $(Pb,La)(Zr,Ti)O_3$ (PLZT), are here briefly reviewed:

- ✓ BFO is a promising material with low band gap energy ($2.3 < E_g < 2.8$ eV) [51], and high remnant polarization (50 – 150 $\mu C.cm^{-2}$) [52, 53]. Heterostructures of ITO/BFO/SRO ($SrRuO_3$) are characterized by large V_{OC} ~ 0.8 – 0.9 V and external quantum efficiency (EQE) ~ 10 % [51].
- ✓ PZT has occupied a significant place in the ferroelectric photovoltaic world due to improved photovoltaic efficiency. An efficiency of 1.25 % is reported in PZT

thin films when they are grown on *n*-type Si for heterojunction Ag/*n*-a-Si/PZT/ITO/glass [54].

- ✓ PLZT is another class of ferroelectric material which is being studied for photovoltaic properties. One of the early work investigating the photovoltaic responses was based on ceramic of $Pb_{0.97}La_{0.03}Zr_{0.52}Ti_{0.48}O_3$ (PLZT - 3/52/48) composition [55]. Poosanaas et al. (1999) investigated the maximum photocurrent of PLZT - 4/48/52 composition which is in the tetragonal phase while the maximum photovoltage was found at PLZT - 5/54/46 which is close to the morphotropic phase boundary of the PLZT phase diagram [56]. Unprecedented high photovoltaic power conversion efficiency around 0.28 % was achieved with epitaxial PLZT – 3/52/48 ferroelectric thin films [57].

I.5.3. Spinel oxide solar cells

Recently, many spinel oxides of AB_2O_4 were investigated as a light absorbers for all-oxide thin film photovoltaic cells because of their nearly ideal optical band gap of around 1.5 eV, which could reach 40 % of the theoretical conversion efficiency [37].

There is strong research attention on heterojunctions of spinel oxides for inorganic solar cells such as TiO_2/Co_3O_4 where Co_3O_4 is a *p*-type semiconductor, which has two noticeable direct transitions in the visible range with band gaps energy of 1.45 eV and 2.26 eV [58]. The first *J-V* curve of TiO_2/Co_3O_4 heterojunction (in Figure I. 18) was measured under conditions of dark and light by Rühle and his colleagues in 2012 [34], and was detailed in 2015 by the same group [59]. All-oxide solar cells with a multi-layered geometry of glass/FTO/TiO_2/$(Co_xFe_{1-x})_3O_4$/Au, enhanced photovoltaic performance, with J_{sc} of 53 µA cm^{-2} and V_{oc} of 534 mV for samples with Co/(Co + Fe) composition ratio of approximately 55 % [60].

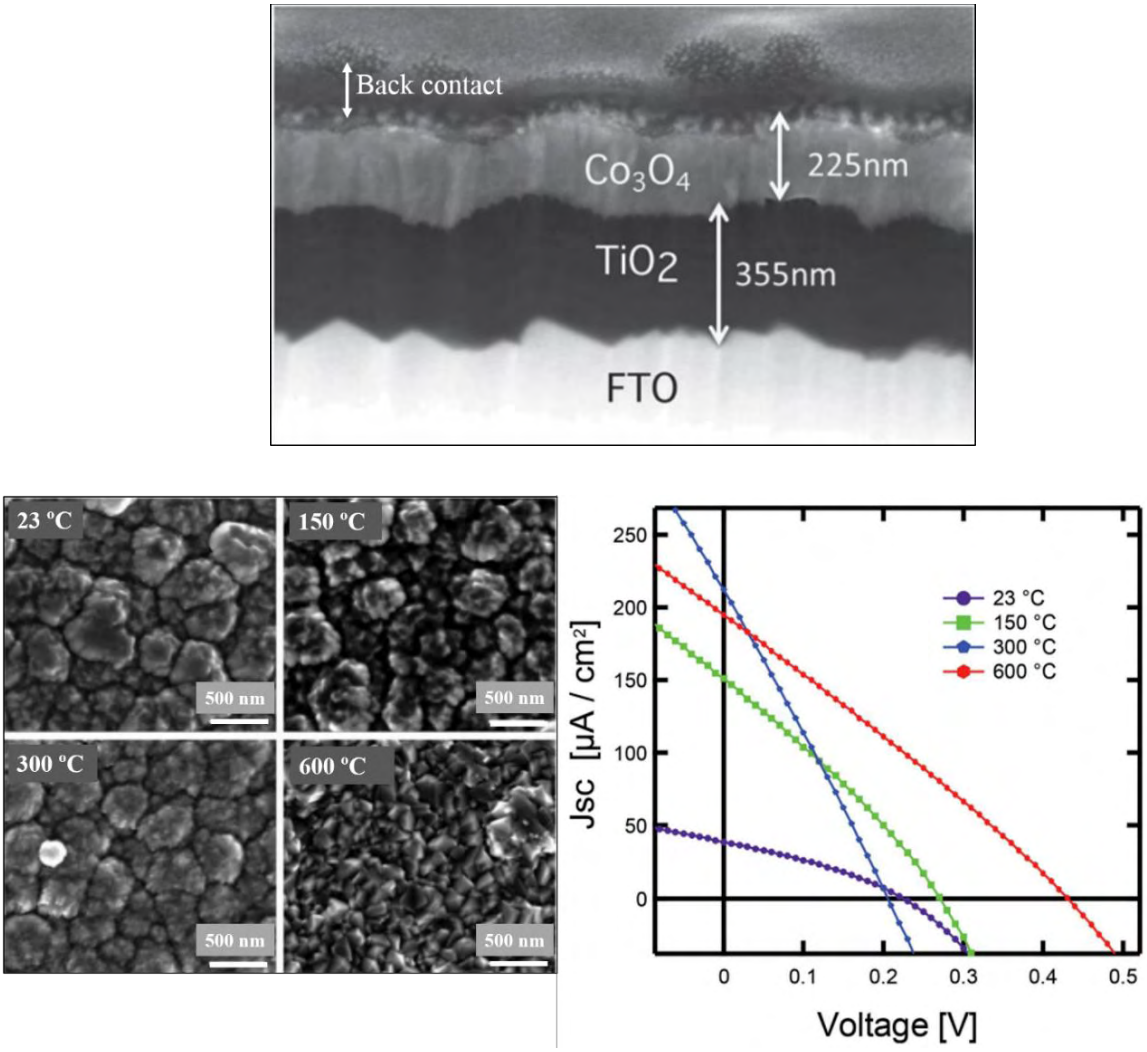

Figure I. 18: Cross section SEM (top) of sprayed TiO_2 and Co_3O_4 thin film deposited at 600 ºC, SEM images of samples at different temperatures and J-V curve of Co_3O_4/TiO_2 heterojunctions when Co_3O_4 was deposited at different temperatures (bottom) [59].

After the pioneer work on dye-sensitized solar cells (DSSC) by O'Regan and Grätzel in 1991 [61], wide variety of oxide-based semiconductors has been studied as alternative electrode materials of DSSC. These researches focus on the simple replacement of TiO_2 for as double-oxide-based phase pure porous electrode. Some spinel oxides have been examined as photo-anodes for DSSC. Tan et al. (2007) examined zinc stannate (Zn_2SnO_4) with band gap of 3.6 eV, and reported the power conversion efficiency of 3.8 %. According to Tan et al., the electron diffusion length for Zn_2SnO_4 is shorter than P25 (Degussa, average size equal to 25 nm of TiO_2) film. However, photo-current density for a Zn_2SnO_4 cell was higher than that for a P25 cell with the same film thickness (~ 6 µm) [62]. Lana-Villarreal et al. (2007) also reported the DSSC performance of Zn_2SnO_4 DSSC [63]. Mercado et al. (2014) presented ternary substituted (zinc

or nickel) cobalt oxide spinels thin films as a dye-sensitized *p*-type hole transport support in a photo-electrochemical cell. The highest photocurrent and quantum efficiencies were measured in zinc-cobalt-oxide devices with an internal quantum efficiencies (IQE) of > 90 % and an open circuit voltage of around 260 mV [64].

I.6. Mixed valence spinel oxides as solar absorbers

I.6.1. Crystal structure

The spinel structure is formulated MM'_2X_4, where M and M' are tetrahedral and octahedral coordinated cations, respectively, and X is an anion (typically O, S or F). The structure is named after the mineral $MgAl_2O_4$, and the compounds from this family have the general formula AB_2O_4. Where A and B are either divalent (+2) and trivalent (+3) or tetravalent (+4) and divalent cations. The crystal structure was determined independently by Bragg [65] and Nishikawa [66]. Figure I. 19 shows Schematic of the spinel structure of $MgAl_2O_4$.

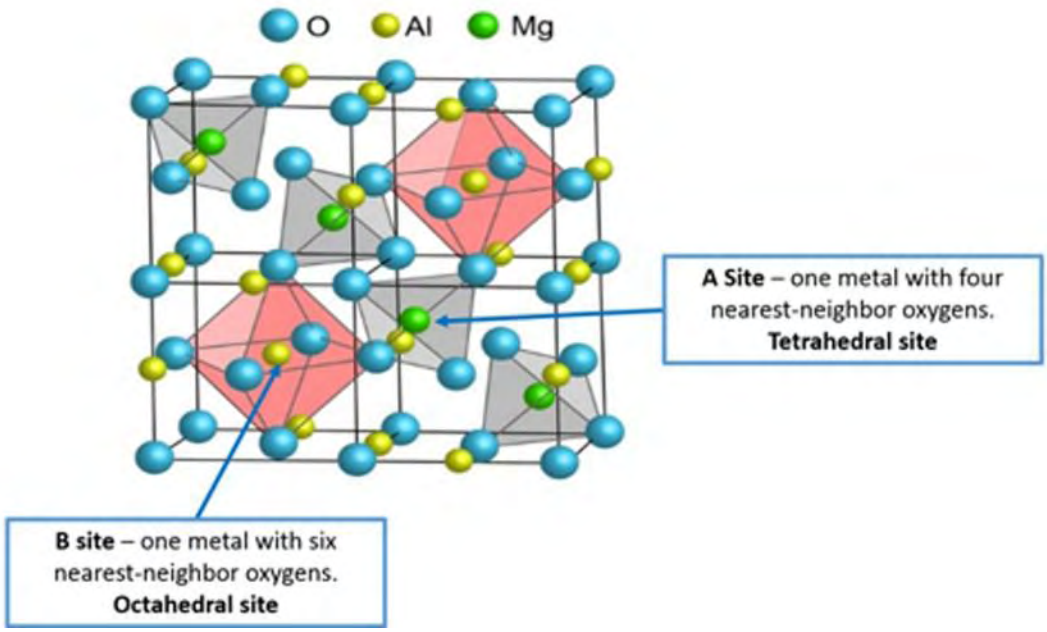

Figure I. 19: Schematic of the spinel structure of $MgAl_2O_4$ [67].

Cubic spinels have been assigned to the space group $Fd\bar{3}m$. The unit cell of a spinel consists of eight formula units with the oxygen ions forming a closed-packed faced centered

cubic (*fcc*) lattice and therefore, may be represented as $8[AB_2O_4]$ so it may be represented as $A_8B_{16}O_{32}$. Within the face-centered cubic lattice formed by 32 oxygen ions two types of interstitial positions exist, which can be occupied by the metallic cations. There are 64 tetrahedral interstitial sites surrounded by 4 oxygen ions (noted as *A* site) and 32 octahedral sites surrounded by 6 oxygen ions (noted as *B* site). In the spinel structure, 8 out of 64 tetrahedral sites and 16 out of 32 octahedral sites are occupied by the cations.

Depending on the occupation and distribution of the cations in the tetrahedral and octahedral sites, spinels can be further classified as normal, inverse and mixed spinels which can be represented by the general formula:

$$(A_{1-2x}B_{2x})[A_{2x}B_{2-2x}]O_4$$

Where ( ) represent the tetrahedral sites and [ ] represent the octahedral sites.

There are three spinel types with general formula:

- ✓ Normal spinel: $x = 0$, the tetrahedral sites are filled with the divalent cations (A^{2+}) and the octahedral site are filled with the trivalent cations [B^{3+}]. It can be represented as:

  $$(A^{2+})[B_2{}^{3+}]O_4$$

  Examples: $MgAl_2O_4$, $ZnFe_2O_4$, $ZnCrFeO_4$, $MnAl_2O_4$, Mn_3O_4, Co_3O_4

- ✓ Inverse spinel: $x = 0.5$, the tetrahedral sites are filled with half of the trivalent cations and the octahedral site are filled with the other half of the trivalent cations and the divalent cations. It can be described as:

  $$(B^{3+})[A^{2+}B^{3+}]O_4$$

  Examples: $MgFe_2O_4$, $NiFe_2O_4$, $CoFe_2O_4$, Fe_3O_4.

- ✓ Mixed spinel (random spinel): $0 < x < 0.5$, the relocation of cations can cause a change in lattice parameter or a deformed crystal structure [68]. The cations *A* and *B* occupied both sites, octahedral and tetrahedral.

  Examples : $NiCo_2O_4$, $Cu_{0.5}Ni_{0.5}Mn_{2.0}O_4$ [69, 70].

Figure I. 20 presents the examples of three spinel types, normal spinel of $MgAl_2O_4$ with all Mg^{2+} cations positioned in tetrahedral sites while the octahedral sites are filled with Al^{3+} cations [67]. In inverse spinel of $NiFe_2O_4$, Fe^{3+} cations are distributed equally across tetrahedral and octahedral sites, while Ni^{+2} cations occupy octahedral sites [71]. In mixed spinel of $NiCo_2O_4$, the cation distribution can be expressed in terms of a general formula as $(Co^{2+}_{x}Co^{3+}_{1-x})$ $[Co^{3+}$ $Ni^{2+}_{1-x}Ni^{3+}_{x}]O^{2-}_{4}$ $(0 < x < 1)$ [72, 73].

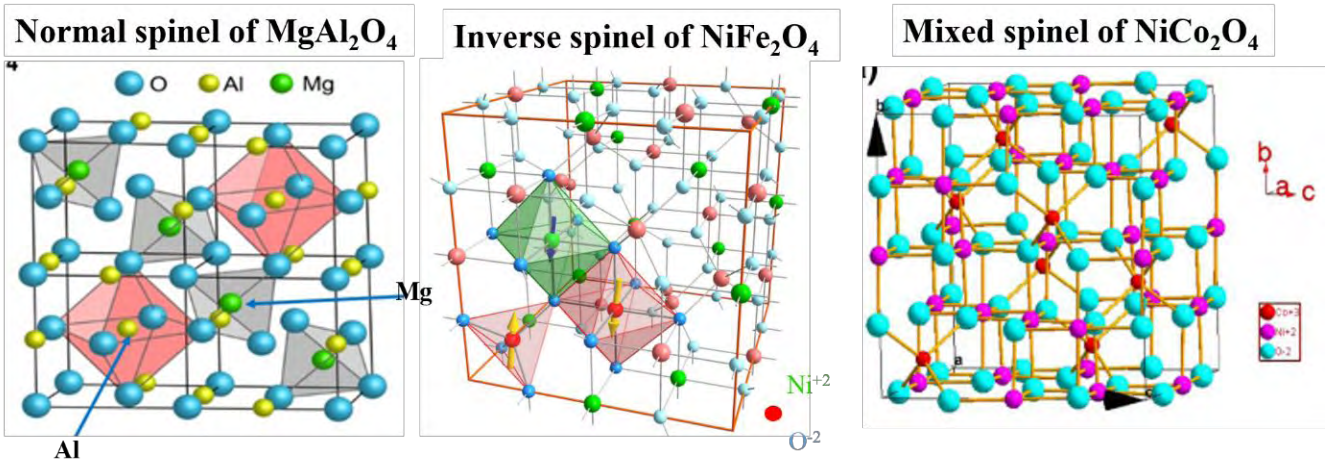

Figure I. 20: Crystallographic structures of normal spinel $MgAl_2O_4$, inverse spinel $NiFe_2O_4$ and mixed spinel $NiCo_2O_4$ [67, 71, 73].

Navrotsky et al. (1967) studied the cations stabilities and distributions in different simple spinels [74]. They show that some cations have a pronounced preference for tetrahedral sites, others for octahedral sites, whereas there is a third type of cations which do not show any preference [74-79].

Figure I. 21 shows the empirical site preference for some divalent and trivalent ions in the spinel structure.

Those with tetrahedral site preference are:

Zn^{2+}, Mn^{2+}, Ga^{2+}, Co^{2+}, Mg^{2+}, Cd^{2+}, Fe^{2+}.

Those with octahedral site preference are:

Cu^{2+}, Ni^{2+}, Al^{3+}, Mn^{3+}, Mn^{4+}, Co^{3+}.

Those with random site preference are:

Fe^{3+}, Cu^{2+}, Ni^{2+}, Li^{+}.

Some authors have shown that Cu^{2+} and Ni^{2+} can occupy both sites [79-81], which depend on the elaboration process.

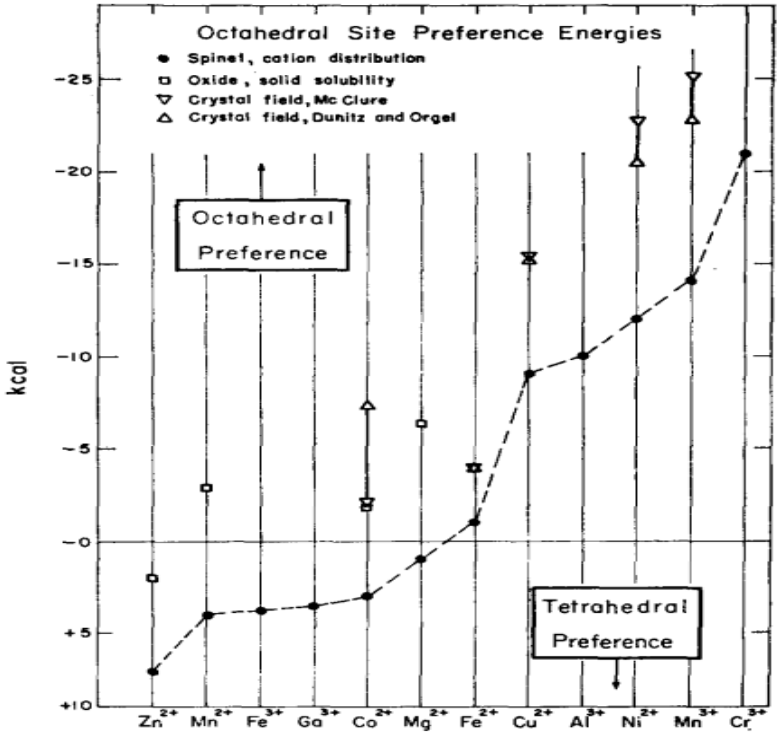

Figure I. 21: Site preference energies for some divalent and trivalent ions in the spinel structure [74].

I.6.2. Electrical conductivity

Spinels can have various electronic properties from highly insulating to highly conductive [76]. For example, studies carried on Co_3O_4 thin films revealed an electrical conductivity $\sigma \sim 10^{-2}$ S.cm^{-1}, while Fe_3O_4 thin films exhibit high electrical conductivity with $\sigma \sim 125$ S.cm^{-1} [82, 83].

Spinels are generally believed to conduct by hopping of charges between octahedral sites. The conduction in spinels occurs when one type of atom is present simultaneously in two different valence states on the same crystallographic site, following Verwey's law [84]. Thus, the presence of different valence states among octahedral cations is beneficial for increasing

conduction. For instance, Fe_3O_4 is an inverse spinel in which tetrahedral sites are occupied by Fe^{3+} and octahedral site are filled with proportions of Fe^{2+} and Fe^{3+}. But this cation distribution would occur only in a perfect crystal at 0 K. At higher temperatures, entropy causes some degree of mixing of cations between the two sites. The conductivity increases with temperature, Fe_3O_4 has the highest conductivity of all spinels at room temperature [85, 86]. In inverse spinels, the conductivity is caused by the orbital extension of the octahedral ions which communicate directly with their neighbors. Hence, the inverse spinels are consistent with conductivity by an electron-hopping mechanism. This direct communication between the orbitals of the metal ions is related to the special electronic properties of many transition metal oxides [87].

I.6.3. Optoelectronic properties

Optoelectronic properties of spinel oxides are directly related to their band structures, as most of transition metal oxides. In general, the valence band (VB) is filled by oxygen orbitals (orbitals $2p^6$ - full), while the conduction band (CB) consists of cations orbitals (orbital *d* - empty). Depending on the value of the band gap, the oxide presents a semiconducting or insulating behavior. The simplified and general band structure diagram of transition metal oxides is shown in Figure I. 22.

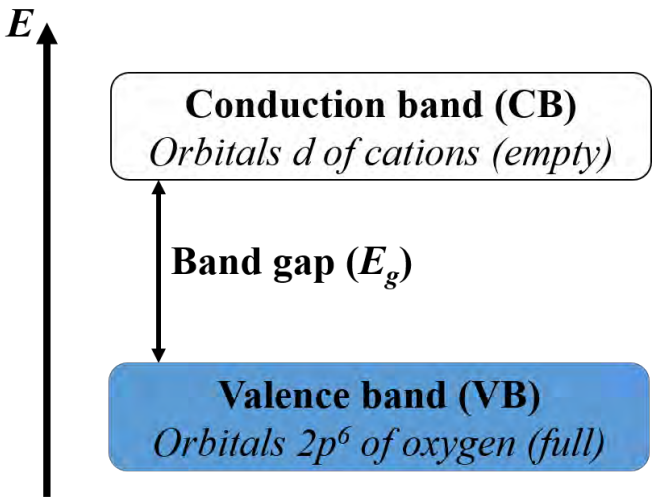

Figure I. 22: Simple band structure diagram of transition metal oxides.

The light absorption properties of spinel oxides are related to the charge (electron) transfer in material. There are two major classes of electronic transitions:

The inter-atomic transitions that generally give rise to broad front absorptions.

Intra-atomic transitions ($d - d$ transition on the same cation) allowed only for some cases with the influence of ligands field.

I.6.3.1. Interatomic (cation - oxygen / cation – cation) charge transfer

In spinel type oxides, the charge transfers of cation – oxygen (band theory) gives the highest absorption intensities. When the energy band gap value of an oxide compound is in the visible range, the absorption phenomenon is explained by a transfer of electrons from orbitals $2p^6$ of oxygen (VB) to the empty orbitals $3d^n$ of metal cation (CB), and the material appears colored. For example, vanadium oxide V_2O_5 is orange with the band gap value equals to 2.65 eV. On the contrary, when the band gap value is not included in the visible range (E_g > 3.2 eV), the charge transfer of electrons is not allowed from orbitals $2p^6$ of oxygen (VB) to the empty orbitals $3d^n$ of metal cation (CB). In fact, some of transition metal oxides (including spinels) with wide band gap appear very clear or transparent. However, some transition metal oxides with wide band gap may appear colored when doped with an electron acceptor element or electron donor element in form of impurities. In this case, type of transition VB → acceptor (h^+, p) or donor (e^-, n) → CB can take place by absorption of a photon within the visible wavelength.

Other absorber properties of transition metal oxides are related to interatomic charge transfer between cations, which is called an "intervalence" charge transfer, representing an internal oxidation – reduction process. Such transfer may be direct (in the case of orbital overlap cations) or indirect (via transfer oxygen). It occurs between two different oxidation states of cations. Zhou et al. (2003) observed this type of transition in spinel oxide thin films of $CoFe_{2-x}M_xO_4$ (M = Mn, Al, Sc), where the charge transfer is associated to a transition between Co^{2+} (t_{2g}) and Fe^{3+} (t_{2g}) via the oxygen site, with an energy of about 2.27 eV [88].

I.6.3.1. Intra-atomic charge transfer ($d - d$)

The absorption properties of transition metal oxides can also be related to another charge transfer type in the same cation, so called intra-atomic charge transfer ($d - d$). In the electron configuration of transition metal oxide, all five degenerate d orbitals of free metal cation have

the same energy. These can be occupied by a maximum of 10 electrons as shown in Figure I. 23.

A crystal field is induced by the interaction between a metal cation and an O^{2-} anion. The *d* orbitals of the metal interact with the electron cloud of the ligand (O^{2-} ion) in such a manner that the *d* orbitals become non-degenerate. When the *d* level is not completely filled, it is possible to promote and electron from a lower energy *d* orbital to a higher energy *d* orbital by absorption of a photon of electromagnetic radiation having an appropriate energy (*d* - *d* transitions).

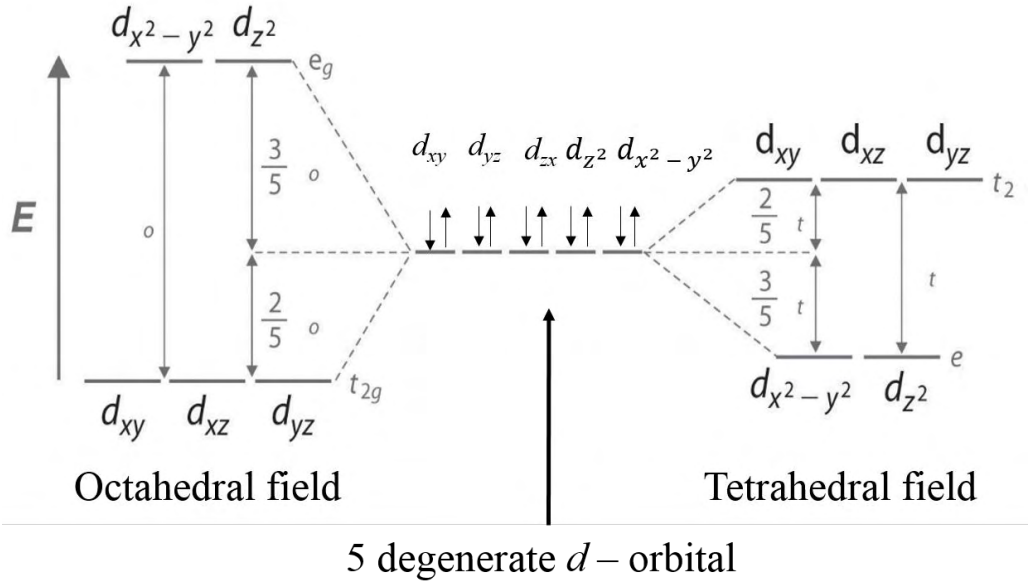

Figure I. 23: Splitting of the degenerate d orbitals due to an octahedral ligand field (left diagram) and the tetrahedral field (right diagram).

For the octahedral complexes group, the $d_{x^2-y^2}$, d_{z^2} orbitals belong to the e_g irreducible representation and they are higher than t_{2g} orbitals which are represented by d_{xy}, d_{yz} and d_{zx} orbitals. The energy difference between the t_{2g} and e_g orbitals is called the octahedral splitting energy Δ_o. Because the overall energy is maintained, the energy of the three t_{2g} orbitals are lowered by $\frac{2}{5}\Delta_o$ and the energy of the two e_g orbitals are raised by $\frac{3}{5}\Delta_o$ relative to the spherical crystal field. The resulting *d* orbital splitting diagram for octahedral coordination is shown on the left of Figure I. 23. In an octahedral complex, when Δ_o is large (strong field ligand), the electrons will first fill the lower energy *d* orbitals before any electrons are placed

on the higher energy *d* orbitals. It is then classified as low spin because there is a minimal amount of unpaired electrons. When Δ_o is small, the pairing energy exceeds the splitting energy, and the electrons will fill the *d* orbitals as if they were degenerate; this is classified as high spin [89].

The splitting of tetrahedral complexes is directly opposite that of the splitting of the octahedral complexes (as shown on the right of Figure I. 23). Note that in octahedral complexes, d_{z^2} and $d_{x^2-y^2}$ (belonging to the *e* representation) orbitals have higher energy than the d_{xy}, d_{yz}, and d_{zx} orbitals (belonging to the t_2 representation). Also, the orbitals are labelled t_2 and *e*, not t_{2g} and e_g; *g* refers to a geometry, such as octahedral, that has a center of symmetry. The tetrahedral geometry has no center of symmetry. In tetrahedral complexes, the opposite occurs because the d_{xy}, d_{yz}, and d_{zx} orbitals have higher energy than d_{z^2} and $d_{x^2-y^2}$ orbitals. This is once again because the contact between the ligands and the orbitals is the opposite of octahedral complexes. Unlike octahedral complexes, the ligands of tetrahedral complexes come in direct contact with the d_{xy}, d_{yz}, and d_{zx} orbitals. Thus, these orbitals have high electron-electron repulsion, due to the direct contact, therefore higher energy. The d_{z^2} and $d_{x^2-y^2}$ orbitals do not have as direct contact as the ligands kind of squeeze past or slide by these orbitals, thus lowering the electron-electron repulsion and the energy of the orbital. In a tetrahedral complex, Δ_t is relatively small even with strong-field ligands as there are fewer ligands to bond with. It is rare for the Δ_t of tetrahedral complexes to exceed the pairing energy. Usually, electrons will move up to the higher energy orbitals rather than pair. Because of this, most tetrahedral complexes are of high spin [89].

I.6.4. Transition metal (Ni or Cu or Zn)-doped cobalt-based spinel systems

We choose the binary spinel Co_2MnO_4 to be doped with other transition metals because in a previous study, we showed that Co_2MnO_4 presents admirable physical and chemical properties with the highest electrical conductivity among the whole range of solid solutions included in the $Mn_3O_4 – Co_3O_4$ spinel family [90]. Wickham et al. (1958) studied the magnetic properties of Co_2MnO_4 and revealed its ordered ferromagnetic behavior and phase transition from paramagnetic to ferromagnetic below 191 K [91]. Furthermore, Co_2MnO_4 binary spinel system is a fully inverted cubic spinel containing, manganese cations located at 8*a* Wyckoff positions (tetrahedral coordination with the oxygen), cobalt cations located at 16*d* positions

(octahedral coordination with oxygen), whereas oxygen is located at the 32*e* positions [76]. An interesting feature is the existence of metal valence fluctuations since the Co and Mn atoms can move between the tetrahedral and octahedral sites, exhibiting several oxidation states coexisting in the material [90]. From the substitution point of view, various trivalent cations can replace a fraction of Co^{3+} ions like Ni, Cu, Zn, Mn, Ti etc. In the reported literature a number of studies have been devoted to manganese rich phases and a few studies have been directed towards the cobalt rich phases. Toh et al. (2015) investigated different substitutions of Ni and Zn for cobalt and manganese in the structure of spinel oxides. $NiCo_2O_4$ and $ZnCo_2O_4$ then exhibit a smaller resistivity than that of $NiMn_2O_4$ and $ZnMn_2O_4$ [92]. In addition, optical properties of Co_2MnO_4 were studied with two optical band gaps (1.48 and 2.13 eV), which are appropriate values for solar absorbers [93-95].

The ternary metal Ni-Co-Mn-O spinel oxides attract important research attentions for many applications such as high performance thermistors, bolometers and uncooled infrared detectors [96-98]. Dannenberg et al. (1999) showed that ternary spinel oxides containing manganese, cobalt and nickel exhibit *p*-type hopping electrical conduction and an optically transparent window from 6 to 14 µm in wavelength [99]. Their electrical conductivity and hopping activation energy strongly depend on the chemical composition. It was suggested that ternary spinel alloys could provide even higher conductivity and lower temperature dependence, while retaining adequate transmissibility at long wavelengths [100]. Yokoyama et al. (2007) showed that the electrical conductivity (σ) of composition $Mn_{1.5}Co_{0.25+x}Ni_{1.25-x}O_4$ ($0 \leq x \leq 0.75$) increased exponentially with increasing temperature, indicating that these oxides have intrinsic negative temperature coefficient thermistor characteristics and the electrical conductivity increases with the Co concentration for a constant Mn quantity [101]. $Mn_{1.56}Co_{0.96}Ni_{0.48}O_4$ spinel oxide thin film thermistors on organic flexible substrates were prepared at room temperature by photoreaction of nanoparticles with KrF laser irradiation, which showed a negative temperature coefficient thermistor behavior with a very high *B* constant of 4429 K and a rapid temperature response, meaning that they are suitable as sensors for flexible devices [97]. Very few studies were directed towards the optical properties of Ni-Co-Mn-O thin films. Zhou et al. (2014) investigated the UV-VIS-NIR and infrared optical constants by spectroscopic ellipsometry for the as-grown and post-annealed $Mn_{1.4}Co_{1.0}Ni_{0.6}O_4$ films. It can be used for the development of optoelectronic devices based on $Mn_{1.4}Co_{1.0}Ni_{0.6}O_4$ films [102]. Gao et al. (2013) prepared thin films of $Mn_{1.56}Co_{0.96}Ni_{0.48}O_4$ on Al_2O_3 substrate by

the chemical solution deposition (CSD) method. The band gap of such thin film was calculated to be about 0.64 eV [103].

A few research studies were carried out on ternary metal Cu-Co-Mn-O and Zn-Co-Mn-O spinel oxides. Xu et al. (2011) reported $Cu_xMn_{1.5-0.5x}Co_{1.5-0.5x}O_4$ (x = 0.1, 0.3, 0.5) powders by citric acid-nitrate method, and it was applied onto the surfaces of ferritic stainless steel via a slurry dip-coating and subsequent sintering process. The $Cu_{0.3}Mn_{1.35}Co_{1.35}$ layer was dense after sintering and the area specific resistance (ASR) value of the coated sample was 16 $m\Omega.cm^2$ [104]. Also, $Cu_{0.2}Mn_{1.4}Co_{1.4}O_4$ were coated on ferritic stainless steel, which showed ASR values as low as 13.9 $m\Omega.cm^2$ at 800 ºC. The electrochemical experiments indicate that the doped spinel coating effectively inhibits the evaporation and migration of Cr containing vapor from interconnect to the cathode. The composition exhibited high electrical conductivity and excellent thermal expansion compatibility with different substrates [105]. The coating layer $Cu_{0.5}MnCo_{1.5}O_4$ was deposited on ferritic stainless steel and SUS430 alloy substrate by the sol-gel method as the cathode of solid oxide fuel cells. The conductivity of the spinel layer is 105.5 $S.cm^{-1}$ at 750 ºC and the average coefficient of temperature expansion (CET) values is 12.27 x 10^{-6} K^{-1} from room temperature up to 1000 ºC. The ASR of the oxide is 0.3 $m\Omega.cm^2$ for a sample oxidized in air and 172.4 $m\Omega.cm^2$ in reducing atmosphere at 750 ºC for 1000 h [106]. Applications of $CuCoMnO_x$ for solar absorbers was studied by He et al. (2015). Thin films were prepared by a citric acid based sol-gel dip coating method. The XRD pattern was indexed by a spinel structure in the *Pnma* space group. Solar absorptance (α_s) was calculated for the AM 1.5 solar spectrum by using the hemispherical reflectance spectrum from 250 to 2500 nm. Strong solar absorptance (α_s ~ 93 %) revealed for the single film synthesized using a molar ratio of citric acid with metal cation equal to 1.2 with high thermal stability. Such spinel films with high spectral selectivity are making them promising candidates for solar absorber coatings, solar collectors and solar facades for buildings [107].

I.7. References

[1] E. D. Coyle and R. A. Simmons, Eds., "*Understanding the global energy crisis"*. Purdue University Press, **2014**.

[2] OECD/IEA, "*Key world energy statistics*," China's National Bureau of Statistics, **2015**.

[3] M. Venkataramanan and Smitha, "*Cause and effects of global warming*," **Indian Jouranl of Science and Technology,** Vol. **4**, 226-229, **2011**.

[4] Hartmann Dennis L, Klein Tank Albert M.G, and M. Rusticucc, "*Observations: Atmosphere and Surface*," Cambridge, United Kingdom and New York, NY, USA., **2013**.

[5] M. Scheffer, V. Brovkin, and P. M. Cox, "*Positive feedback between global warming and atmospheric CO2 concentration inferred from past climate change*," **Geophysical Research Letters,** Vol. **33**, L107021-107024, **2006**.

[6] Wim Turkenburg and Turkenburg Wim, "*Renewable Energy Global Energy Assessment (GEA)"*, **Cambridge University Press**, **2012**.

[7] U.S Departement-of-Energy, "*Wind Power Today and Tomorrow*," Washinton DC, **2004**.

[8] R. Williams, "*Becquerel Photovoltaic Effect in Binary Compounds*," **The Journal of Chemical Physics,** Vol. **32**, 1505-1514, **1960**.

[9] Q. S. Lei, Z. M. Wu, J. P. Xi, X. H. Geng, Y. Zhao, and J. Sun, "*Development of highly stable hydrogenated amorphous silicon films for application in solar cells.*," **International Journal of Modern Physics B,** Vol. **20**, 2035-2047, **2006**.

[10] S. Hitoshi, M. Keigo, M. Takuya, K. Takashi, K. Michio, N. Sachiko, *et al.*, "*High-efficiency microcrystalline silicon solar cells on honeycomb textured substrates grown with high-rate VHF plasma-enhanced chemical vapor deposition*," **Japanese Journal of Applied Physics,** Vol. **54**, 08KB05, **2015**.

[11] NREL. *Research Cell Efficiency Records* [Online]. Available: http://www.nrel.gov/ncpv/images/efficiency_chart.jpg, **2016**.

[12] M. Gloeckler, I. Sankin, and Z. Zhao, "*CdTe Solar Cells at the Threshold to 20 % Efficiency*," **IEEE Journal of Photovoltaics,** Vol. **3**, 1389-1393, **2013**.

[13] M. A. Contreras, K. Ramanathan, J. AbuShama, F. Hasoon, D. L. Young, B. Egaas, *et al.*, "*Short communication: Accelerated publication: Diode characteristics in state-of-*

the-art ZnO/CdS/Cu(In1−xGax)Se2 solar cells," **Progress in Photovoltaics: Research and Applications,** Vol. **13**, 209-216, **2005**.

[14] M. Kumar, A. Dubey, N. Adhikari, S. Venkatesan, and Q. Qiao, "*Strategic review of secondary phases, defects and defect-complexes in kesterite CZTS-Se solar cells*," **Energy & Environmental Science,** Vol. **8**, 3134-3159, **2015**.

[15] S. M. Bhosale, M. P. Suryawanshi, M. A. Gaikwad, P. N. Bhosale, J. H. Kim, and A. V. Moholkar, "*Influence of growth temperatures on the properties of photoactive CZTS thin films using a spray pyrolysis technique*," **Materials Letters,** Vol. **129**, 153-155, **2014**.

[16] W. Wang, M. T. Winkler, O. Gunawan, T. Gokmen, T. K. Todorov, Y. Zhu, *et al.*, "*Device Characteristics of CZTSSe Thin-Film Solar Cells with 12.6% Efficiency*," **Advanced Energy Materials,** Vol. **4**, 13014651-13014655, **2014**.

[17] S. Buecheler, A. Chirilˇa, J. Perrenoud, L. Kranz, C. Gretener, P. Blösch, *et al.*, "*Flexible and lightweight solar modules for new concepts in building integrated photovoltaics*," in ***In Proceedings of the CISBAT***, Lausanne, Switzerland, **2011**.

[18] D. Vatansever, "*Alternative Resources for Renewable Energy: Piezoelectric and Photovoltaic Smart Structures"*, **InTech**, **2012**.

[19] J. Burschka, N. Pellet, S.-J. Moon, R. Humphry-Baker, P. Gao, M. K. Nazeeruddin, *et al.*, "*Sequential deposition as a route to high-performance perovskite-sensitized solar cells*," **Nature,** Vol. **499**, 316-319, **2013**.

[20] C. G. Granqvist, "*Transparent conductors as solar energy materials: A panoramic review*," **Solar Energy Materials and Solar Cells,** Vol. **91**, 1529-1598, **2007**.

[21] K. L. Chopra, S. Major, and D. K. Pandya, "*Transparent conductors—A status review*," **Thin Solid Films,** Vol. **102**, 1-46, **1983**.

[22] E. Fortunato, D. Ginley, H. Hosono, and D. C. Paine, "*Transparent Conducting Oxides for Photovoltaics*," **MRS Bulletin,** Vol. **32**, 242-247, **2007**.

[23] E. Wallin, U. Malm, T. Jarmar, O. L. M. Edoff, and L. Stolt, "*World-record Cu(In,Ga)Se2-based thin-film sub-module with 17.4% efficiency*," **Progress in Photovoltaics: Research and Applications,** Vol. **20**, 851-854, **2012**.

[24] J. Boucle, P. Ravirajan, and J. Nelson, "*Hybrid polymer-metal oxide thin films for photovoltaic applications*," **Journal of Materials Chemistry,** Vol. **17**, 3141-3153, **2007**.

[25] P. Ravirajan, A. M. Peiró, M. K. Nazeeruddin, M. Graetzel, D. D. C. Bradley, J. R. Durrant, *et al.*, "*Hybrid Polymer/Zinc Oxide Photovoltaic Devices with Vertically*

Oriented ZnO Nanorods and an Amphiphilic Molecular Interface Layer," **The Journal of Physical Chemistry B,** Vol. **110**, 7635-7639, **2006**.

[26] J. Meyer, S. Hamwi, M. Kröger, W. Kowalsky, T. Riedl, and A. Kahn, "*Transition Metal Oxides for Organic Electronics: Energetics, Device Physics and Applications*," **Advanced Materials,** Vol. **24**, 5408-5427, **2012**.

[27] E. L. Ratcliff, B. Zacher, and N. R. Armstrong, "*Selective Interlayers and Contacts in Organic Photovoltaic Cells*," **The Journal of Physical Chemistry Letters,** Vol. **2**, 1337-1350, **2011**.

[28] R. J. Singh, "*Solid state physics"*. **New Delhi**, **Dorling Kindersley**, **2012**.

[29] A. R. Hutson, "*Hall Effect Studies of Doped Zinc Oxide Single Crystals*," **Physical Review,** Vol. **108**, 222-230, **1957**.

[30] J. W. Orton and M. J. Powell, "*The Hall effect in polycrystalline and powdered semiconductors*," **Reports on Progress in Physics,** Vol. **43**, 1263, **1980**.

[31] F. Wooten, "*Optical properties of solids. / Frederick Wooten"*. **New York**, **Academic Press**, **1972**.

[32] S. Ruhle and A. Zaban, "*CHAPTER 8 All-oxide Photovoltaics*," in *Advanced Concepts in Photovoltaics*, ed: The Royal Society of Chemistry, p. 258-286, **2014**.

[33] A. Optical Society Of, "*Handbook of Optics, Vol. 2: Devices, Measurements, and Properties, Second Edition"*, **McGraw-Hill Professional**, **1994**.

[34] S. Rühle, A. Y. Anderson, H.-N. Barad, B. Kupfer, Y. Bouhadana, E. Rosh-Hodesh, *et al.*, "*All-Oxide Photovoltaics*," **The Journal of Physical Chemistry Letters,** Vol. **3**, 3755-3764, **2012**.

[35] I. Grozdanov, "*Electroless chemical deposition technique for Cu2O thin films*," **Materials Letters,** Vol. **19**, 281-285, **1994**.

[36] L. Zhang, L. McMillon, and J. McNatt, "*Gas-dependent bandgap and electrical conductivity of Cu2O thin films*," **Solar Energy Materials and Solar Cells,** Vol. **108**, 230-234, **2013**.

[37] W. Shockley and H. J. Queisser, "*Detailed Balance Limit of Efficiency of p-n Junction Solar Cells*," **Journal of Applied Physics,** Vol. **32**, 510-519, **1961**.

[38] B. D. Yuhas and P. Yang, "*Nanowire-Based All-Oxide Solar Cells*," **Journal of the American Chemical Society,** Vol. **131**, 3756-3761, **2009**.

[39] T.-J. Hsueh, C.-L. Hsu, S.-J. Chang, P.-W. Guo, J.-H. Hsieh, and I. C. Chen, "*Cu2O/n-ZnO nanowire solar cells on ZnO:Ga/glass templates*," **Scripta Materialia,** Vol. **57**, 53-56, **2007**.

[40] F. Kazuya, O. Takeo, and A. Tsuyoshi, "*Fabrication and Characterization of ZnO/Cu 2 O Solar Cells Prepared by Electrodeposition*," **Applied Physics Express,** Vol. **6**, 086503, **2013**.

[41] Y. Ievskaya, R. L. Z. Hoye, A. Sadhanala, K. P. Musselman, and J. L. MacManus-Driscoll, "*Fabrication of ZnO/Cu2O heterojunctions in atmospheric conditions: Improved interface quality and solar cell performance*," **Solar Energy Materials and Solar Cells,** Vol. **135**, 43-48, **2015**.

[42] M. Tadatsugu, N. Yuki, M. Toshihiro, and N. Jun-ichi, "*High-Efficiency Oxide Solar Cells with ZnO/Cu2O Heterojunction Fabricated on Thermally Oxidized Cu2O Sheets*," **Applied Physics Express,** Vol. **4**, 062301, **2011**.

[43] Y. Nishi, T. Miyata, and T. Minami, "*Effect of inserting a thin buffer layer on the efficiency in n-ZnO/p-Cu2O heterojunction solar cells*," **Journal of Vacuum Science & Technology A,** Vol. **30**, 04D103, **2012**.

[44] M. Tadatsugu, N. Yuki, and M. Toshihiro, "*Cu2O-based solar cells using oxide semiconductors*," **Journal of Semiconductors,** Vol. **37**, 014002, **2016**.

[45] Sahrul Saehana and Muslimin, "*Performance improvement of Cu_2O/TiO_2 heterojunction solar cell by employing polymer electrolytes*," **International journal of engineering & technology,** Vol. **13**, 83-86, **2013**.

[46] Y. Luo, L. Wang, Y. Zou, X. Sheng, L. Chang, and D. Yang, "*Electrochemically Deposited Cu2O on TiO2 Nanorod Arrays for Photovoltaic Application*," **Electrochemical and Solid-State Letters,** Vol. **15**, H34-H36, **2011**.

[47] A. Mittiga, E. Salza, F. Sarto, M. Tucci, and R. Vasanthi, "*Heterojunction solar cell with 2% efficiency based on a Cu2O substrate*," **Applied Physics Letters,** Vol. **88**, 163502, **2006**.

[48] W. S. Yang, J. H. Noh, N. J. Jeon, Y. C. Kim, S. Ryu, J. Seo, *et al.*, "*High-performance photovoltaic perovskite layers fabricated through intramolecular exchange*," **Science,** Vol. **348**, 1234-1237, **2015**.

[49] A. Kojima, K. Teshima, Y. Shirai, and T. Miyasaka, "*Organometal Halide Perovskites as Visible-Light Sensitizers for Photovoltaic Cells*," **Journal of the American Chemical Society,** Vol. **131**, 6050-6051, **2009**.

[50] P. Qin, S. Tanaka, S. Ito, N. Tetreault, K. Manabe, H. Nishino, *et al.*, "*Inorganic hole conductor-based lead halide perovskite solar cells with 12.4% conversion efficiency*," **Nat Commun,** Vol. **5**, **2014**.

[51] M. A. Jalaja and S. Dutta, "*Ferroelectrics and multiferroics for next generation photovoltaics*," **Advanced Materials Letters,** Vol. **6**, 568-584, **2015**.

[52] K. X. Jin, Y. F. Li, Z. L. Wang, H. Y. Peng, W. N. Lin, A. K. K. Kyaw, *et al.*, "*Tunable photovoltaic effect and solar cell performance of self-doped perovskite SrTiO3*," **AIP Advances,** Vol. **2**, 042131, **2012**.

[53] S. Y. Yang, L. W. Martin, S. J. Byrnes, T. E. Conry, S. R. Basu, D. Paran, *et al.*, "*Photovoltaic effects in BiFeO3*," **Applied Physics Letters,** Vol. **95**, 062909, **2009**.

[54] F. Zheng, Y. Xin, W. Huang, J. Zhang, X. Wang, M. Shen, *et al.*, "*Above 1% efficiency of a ferroelectric solar cell based on the Pb(Zr,Ti)O3 film*," **Journal of Materials Chemistry A,** Vol. **2**, 1363-1368, **2014**.

[55] U. Kenji and A. Motoya, "*Photostrictive Actuator Using PLZT Ceramics*," **Japanese Journal of Applied Physics,** Vol. **24**, 139, **1985**.

[56] P. Poosanaas, K. Tonooka, I. R. Abothu, S. Komarneni, and K. Uchino, "*Influence of composition and dopant on photostriction in lanthanum-modified lead zirconate titanate ceramics*," **Journal of Intelligent Material Systems and Structures,** 72, **1999**.

[57] M. Qin, K. Yao, and Y. C. Liang, "*High efficient photovoltaics in nanoscaled ferroelectric thin films*," **Applied Physics Letters,** Vol. **93**, 122904, **2008**.

[58] P. Y. Keng, B. Y. Kim, I.-B. Shim, R. Sahoo, P. E. Veneman, N. R. Armstrong, *et al.*, "*Colloidal Polymerization of Polymer-Coated Ferromagnetic Nanoparticles into Cobalt Oxide Nanowires*," **ACS Nano,** Vol. **3**, 3143-3157, **2009**.

[59] B. Kupfer, K. Majhi, D. A. Keller, Y. Bouhadana, S. Rühle, H. N. Barad, *et al.*, "*Thin Film Co3O4/TiO2 Heterojunction Solar Cells*," **Advanced Energy Materials,** Vol. **5**, 14010071-14010075, **2015**.

[60] Z. Yan, D. A. Keller, K. J. Rietwyk, H.-N. Barad, K. Majhi, A. Ginsburg, *et al.*, "*Effect of Spinel Inversion on (CoxFe1−x)3O4 All-Oxide Solar Cell Performance*," **Energy Technology,** 1-8, **2016**.

[61] B. O'Regan and M. Gratzel, "*A low-cost, high-efficiency solar cell based on dye-sensitized colloidal TiO2 films*," **Nature,** Vol. **353**, 737-740, **1991**.

[62] B. Tan, E. Toman, Y. Li, and Y. Wu, "*Zinc Stannate (Zn2SnO4) Dye-Sensitized Solar Cells*," **Journal of the American Chemical Society,** Vol. **129**, 4162-4163, **2007**.

[63] T. Lana-Villarreal, G. Boschloo, and A. Hagfeldt, "*Nanostructured Zinc Stannate as Semiconductor Working Electrodes for Dye-Sensitized Solar Cells*," **The Journal of Physical Chemistry C,** Vol. **111**, 5549-5556, **2007**.

[64] C. C. Mercado, A. Zakutayev, K. Zhu, C. J. Flynn, J. F. Cahoon, and A. J. Nozik, "*Sensitized Zinc–Cobalt–Oxide Spinel p-Type Photoelectrode*," **The Journal of Physical Chemistry C,** Vol. **118**, 25340-25349, **2014**.

[65] W. H. Bragg, "*The structure of the spinel group of crystals*," **Philosophical Magazine Series 6,** Vol. **30**, 305-315, **1915**.

[66] S. Nishikawa, "*Structure of some crystals of spinel group*," **Proceedings of the Tokyo Mathematico-Physical Society** Vol. **8**, 199-209, **1915**.

[67] Clean-Diesel-Technologies. *Spinel Technology* [Online]. Available: http://www.cdti.com/spinel/, **2015**.

[68] H. Bordeneuve, S. Guillemet-Fritsch, A. Rousset, S. Schuurman, and V. Poulain, "*Structure and electrical properties of single-phase cobalt manganese oxide spinels Mn3−xCoxO4 sintered classically and by spark plasma sintering (SPS)*," **Journal of Solid State Chemistry,** Vol. **182**, 396-401, **2009**.

[69] G. T. Bhandage and H. V. Keer, "*A correlation of the physical properties of the NixCu1-xMn2O4 system*," **Journal of Physics C: Solid State Physics,** Vol. **9**, 1325, **1976**.

[70] E. Trollund, P. Chartier, and J. L. Gautier, "*Repartition cationique et comportement electrochimique des oxydes mixtes CuxNi0,6−0,2xMn2,4−0,8xO4*," **Electrochimica Acta,** Vol. **35**, 1303-1310, **1990**.

[71] M. Hoppe, S. Döring, M. Gorgoi, S. Cramm, and M. Müller, "*Enhanced ferrimagnetism in auxetic NiFe2O4 in the crossover to the ultrathin-film limit*," **Physical Review B,** Vol. **91**, 054418, **2015**.

[72] Y. Bitla, Y. Y. Chin, J. C. Lin, C. N. Van, R. Liu, Y. Zhu, *et al.*, "*Origin of metallic behavior in NiCo2O4 ferrimagnet*," **Scientific Reports,** Vol. **5**, 15201, **2015**.

[73] D. Zhang, H. Yan, Y. Lu, K. Qiu, C. Wang, C. Tang, *et al.*, "*Hierarchical mesoporous nickel cobaltite nanoneedle/carbon cloth arrays as superior flexible electrodes for supercapacitors*," **Nanoscale Research Letters,** Vol. **9**, 139-139, **2014**.

[74] A. Navrotsky and O. J. Kleppa, "*The thermodynamics of cation distributions in simple spinels*," **Journal of Inorganic and Nuclear Chemistry,** Vol. **29**, 2701-2714, **1967**.

[75] F. A. Kröger, "*The chemistry of imperfect crystals*". **Amsterdam; New York**, **North-Holland Pub. Co.; Interscience Publishers**, **1964**.

[76] E. J. W. Verwey and E. L. Heilmann, "*Physical Properties and Cation Arrangement of Oxides with Spinel Structures I. Cation Arrangement in Spinels*," **The Journal of Chemical Physics,** Vol. **15**, 174-180, **1947**.

[77] D. S. McClure, "*The distribution of transition metal cations in spinels*," **Journal of Physics and Chemistry of Solids,** Vol. **3**, 311-317, **1957**.

[78] J. D. Dunitz and L. E. Orgel, "*Electronic properties of transition-metal oxides-II Cation distribution amongst octahedral and tetrahedral sites*," **Journal of Physics and Chemistry of Solids,** Vol. **3**, 318-323, **1957**.

[79] C. Drouet, C. Laberty, J. L. G. Fierro, P. Alphonse, and A. Rousset, "*X-ray photoelectron spectroscopic study of non-stoichiometric nickel and nickel–copper spinel manganites*," **International Journal of Inorganic Materials,** Vol. **2**, 419-426, **2000**.

[80] A. Meenakshisundaram, N. Gunasekaran, and V. Srinivasan, "*Distribution of Metal Ions in Transition Metal Manganites AMn2O4 (A: Co, Ni, Cu, or Zn)*," **physica status solidi (a),** Vol. **69**, K15-K19, **1982**.

[81] N. Chasserio, B. Durand, S. Guillemet-Fritsch, and A. Rousset, "*Mixed manganese spinel oxides: optical properties in the infrared range*," **Journal of Materials Science,** Vol. **vol. 42**, 794-800, **2007**.

[82] O. Gençyılmaz, T. Taşköprü, F. Atay, and İ. Akyüz, "*Synthesis, characterization and ellipsometric study of ultrasonically sprayed Co3O4 films*," **Applied Physics A,** Vol. **121**, 245-254, **2015**.

[83] S.-S. Kim, "*Hybrid absorbers composed of Fe3O4 thin film and magnetic composite sheet and enhancement of conduction noise absorption on a microstrip line*," **Journal of Applied Physics,** Vol. **117**, 17B703, **2015**.

[84] E.J.V Verwey, P.W Haaijman, F.C Fomeijn, and G. W. v. Oosterhout, "*Controlled-valency semiconductors*," **Philips research reports** Vol. **5**, 173-187, **1950**.

[85] A. Petric and H. Ling, "*Electrical Conductivity and Thermal Expansion of Spinels at Elevated Temperatures*," **Journal of the American Ceramic Society,** Vol. **90**, 1515-1520, **2007**.

[86] C. L. Muhich, V. J. Aston, R. M. Trottier, A. W. Weimer, and C. B. Musgrave, "*First-Principles Analysis of Cation Diffusion in Mixed Metal Ferrite Spinels*," **Chemistry of Materials,** Vol. **28**, 214-226, **2016**.

[87] D. K. Schroder, "*Semiconductor Material and Device Characterization*", **Wiley-Interscience**, **2006**.

[88] B. Zhou, Z. Ya-Wen, Y. Yue-Jun, L. Chun-Sheng, Y. Chun-Hua, C. Liang-Yao, *et al.*, "*Correlation between structure and intervalence charge-transfer transitions in nanocrystalline CoFe2-xMxO4 (M=Mn, Al, Sc) thin films*," **Physical Review B,** Vol. **68**, 0244261-0244268, **2003**.

[89] B. A. Averill, "*Chapter 23: The d-Block Elements*," in *Principles of General Chemistry*, ed: Andy Schmitz, p. 2736-2865, **2012**.

[90] H. Bordeneuve, A. Rousset, C. Tenailleau, and S. Guillemet-Fritsch, "*Cation distribution in manganese cobaltite spinels Co3−x Mn x O4 (0 ≤ x ≤ 1) determined by thermal analysis*," **Journal of Thermal Analysis and Calorimetry,** Vol. **101**, 137-142, **2010**.

[91] D. G. Wickham and W. J. Croft, "*Crystallographic and magnetic properties of several spinels containing trivalent ja-1044 manganese*," **Journal of Physics and Chemistry of Solids,** Vol. **7**, 351-360, **1958**.

[92] R. J. Toh, A. Y. S. Eng, Z. Sofer, D. Sedmidubsky, and M. Pumera, "*Ternary Transition Metal Oxide Nanoparticles with Spinel Structure for the Oxygen Reduction Reaction*," **ChemElectroChem,** Vol. **2**, 982-987, **2015**.

[93] G. Salek, P. Dufour, S. Guillemet-Fritsch, and C. Tenailleau, "*Sustainable low temperature preparation of Mn3−xCoxO4 (0 ≤ x ≤ 3) spinel oxide colloidal dispersions used for solar absorber thin films*," **Materials Chemistry and Physics,** Vol. **162**, 252-262, **2015**.

[94] F. Zasada, J. Gryboś, P. Indyka, W. Piskorz, J. Kaczmarczyk, and Z. Sojka, "*Surface Structure and Morphology of M[CoM']O4 (M = Mg, Zn, Fe, Co and M' = Ni, Al, Mn, Co) Spinel Nanocrystals—DFT+U and TEM Screening Investigations*," **The Journal of Physical Chemistry C,** Vol. **118**, 19085-19097, **2014**.

[95] S. M. A. Shibli, P. S. Arun, and A. V. Raj, "*Exploration of octahedrally shaped MnCo2O4 catalyst particles for visible light driven photocatalytic water splitting reaction*," **RSC Advances,** Vol. **5**, 19393-19399, **2015**.

[96] Z. Huang, W. Zhou, C. Ouyang, J. Wu, F. Zhang, J. Huang, *et al.*, "*High performance of Mn-Co-Ni-O spinel nanofilms sputtered from acetate precursors*," **Scientific Reports,** Vol. **5**, 10899, **2015**.

[97] T. Nakajima and T. Tsuchiya, "*Flexible thermistors: pulsed laser-induced liquid-phase sintering of spinel Mn-Co-Ni oxide films on polyethylene terephthalate sheets*," **Journal of Materials Chemistry C,** Vol. **3**, 3809-3816, **2015**.

[98] Y. Hou, Z. Huang, Y. Gao, Y. Ge, J. Wu, and J. Chu, "*Characterization of Mn1.56Co0.96Ni0.48O4 films for infrared detection*," **Applied Physics Letters,** Vol. **92**, 202115, **2008**.

[99] R. Dannenberg, S. Baliga, R. J. Gambino, A. H. King, and A. P. Doctor, "*Infrared optical properties of Mn1.56Co0.96Ni0.48O4 spinel films sputter deposited in an oxygen partial pressure series*," **Journal of Applied Physics,** Vol. **86**, 2590-2601, **1999**.

[100] R. Dannenberg, S. Baliga, R. J. Gambino, A. H. King, and A. P. Doctor, "*Resistivity, thermopower and the correlation to infrared active vibrations of Mn1.56Co0.96Ni0.48O4 spinel films sputtered in an oxygen partial pressure series*," **Journal of Applied Physics,** Vol. **86**, 514-523, **1999**.

[101] T. Yokoyama, T. Meguro, Y. Shimada, J. Tatami, K. Komeya, and Y. Abe, "*Preparation and electrical properties of sintered oxides composed of Mn1.5Co(0.25+x)Ni(1.25-x)O4 ($0 \leq x \leq 0.75$) with a cubic spinel structure*," **Journal of Materials Science,** Vol. **42**, 5860-5866, **2007**.

[102] W. Zhou, J. Wu, C. Ouyang, Y. Q. Gao, X. F. Xu, and Z. M. Huang, "*Optical properties of Mn-Co-Ni-O thin films prepared by radio frequency sputtering deposition*," **Journal of Applied Physics,** Vol. **115**, 0935121-0935127, **2014**.

[103] Y. Q. Gao, Z. M. Huang, Y. Hou, J. Wu, and J. H. Chu, "*Optical and electrical properties of Mn1.56Co0.96Ni0.48O4 thin films*," in ***Eighth International Conference on Thin Film Physics and Applications***, 90680J90681-90680J90685, **2013**.

[104] Y. Xu, Z. Wen, S. Wang, and T. Wen, "*Cu doped Mn–Co spinel protective coating on ferritic stainless steels for SOFC interconnect applications*," **Solid State Ionics,** Vol. **192**, 561-564, **2011**.

[105] B.-K. Park, J.-W. Lee, S.-B. Lee, T.-H. Lim, S.-J. Park, C.-O. Park, *et al.*, "*Cu-and Ni-doped Mn1.5Co1.5O4 spinel coatings on metallic interconnects for solid oxide fuel cells*," **International Journal of Hydrogen Energy,** Vol. **38**, 12043-12050, **2013**.

[106] J. Xiao, W. Zhang, C. Xiong, B. Chi, J. Pu, and L. Jian, "*Oxidation of MnCu0.5Co1.5O4 spinel coated SUS430 alloy interconnect in anode and cathode atmospheres for intermediate temperature solid oxide fuel cell*," **International Journal of Hydrogen Energy,** Vol. **40**, 1868-1876, **2015**.

[107] M. He and R. Chen, "*Structural and optical properties of CuMnCoOx spinel thin films prepared by a citric acid-based sol–gel dip coating route for solar absorber applications*," **Journal of Sol-Gel Science and Technology,** Vol. **74**, 528-536, **2015**.

CHAPTER II

EXPERIMENTAL TECHNIQUES

II.1. Introduction

This chapter presents all the experimental techniques that were needed to synthesis the spinel oxide powders and deposit thin films. The inorganic polycondensation based method used for the preparation of the powders and dip-coating technique used for obtaining thin films of spinel oxides $M_xCo_{2-x}MnO_4$ (M = Ni, Cu, Zn; x = 0, 0.15, 0.30, 0.60) will be described. The analyses techniques used during this work will then be presented. The analyses techniques regularly used were X-Ray Fluorescence (XRF), X-Ray diffraction (XRD), Field Emission Gun - Scanning Electron Microscope (FEG-SEM), Thermo-Gravimetric Analysis (TGA), Thermo-Mechanical Analysis (TMA), topographic and roughness measurement techniques. Optical and electrical properties were also determined precisely.

II.2. Preparation methods

II.2.1. Powder synthesis

Spinel oxides were synthesized by inorganic polycondensation, a simple method of powder precipitation at room temperature [1]. Table II. 1 shows the chemicals used for the materials synthesis.

Table II. 1: Transition metal salts and alkaline hydroxide LiOH used for synthesis.

Reactant	Purity (%)	Provenance	Impurity	Content (ppm)
$CoSO_4.7H_2O$ Cobalt (II) sulfate	≥ 98	Alfa Aesar	N, Cl, Ca, F, K, Mg, Na, Ni, Pb, Zn, Mn	≤ 50
$MnSO_4.H_2O$ Manganese (II) sulfate	≥ 99	Alfa Aesar	Ca, Co, F, Ni Cu, Fe, K, Mg, Na, Pb, Zr	≤ 50
$NiSO_4.6H_2O$ Nikel (II) sulfate	≥ 99	Sigma-Aldrich	Ca, Co, Cu, Fe, K, Mg, Mn, Na, Pb, Zr	≤ 50
$ZnSO_4.7H_2O$ Zinc sulfate	≥ 99	Sigma-Aldrich	Ca, Co, Cu, Fe, K, Mg, Mn, Na, Pb, Zr	≤ 50
$CuSO_4.5H_2O$ Copper (II) sulfate	100	VWR	N, Cl, Ca, F, K, Mg, Na, Ni, Pb, Zn	≤ 50
$LiOH.H_2O$ Lithium hydroxide	≥ 99	Sigma-Aldrich	Cl^-, SO_4^{2-}, Al, As, Ba, Bi, Cd, Co, Cr, Cu, Fe, K, Mg, Mn, Mo, Na, Ni, Pb, Sr, Zn	≤ 10

The conditions of powder synthesis were optimized by Guillaume SALEK during his PhD work [2]. The inorganic polycondensation method, which consists of mixing an aqueous solution of metal salts with an alkaline solution, is a simple, robust and low cost method. The schematic of our inorganic polycondensation method is shown in Figure II. 1. A volume of 100 mL of metal sulfate salt precursors with a concentration of 0.3 mol/L was quickly introduced in a dilute alkaline solution excess of lithium hydroxide dissolved in 1400 mL of water to obtain complete precipitation and to ensure a strong alkaline solution. A constant stirring (300 rpm) was maintained during the synthesis. Then three successive steps of centrifugation at 4000 rpm and washing with water were used to remove residual ions. An extra step, consisting of a reflux at 120 ºC, was required in order to provide oxygen to the alkali hydroxide intermediate phase and form pure metal oxide nanoparticles.

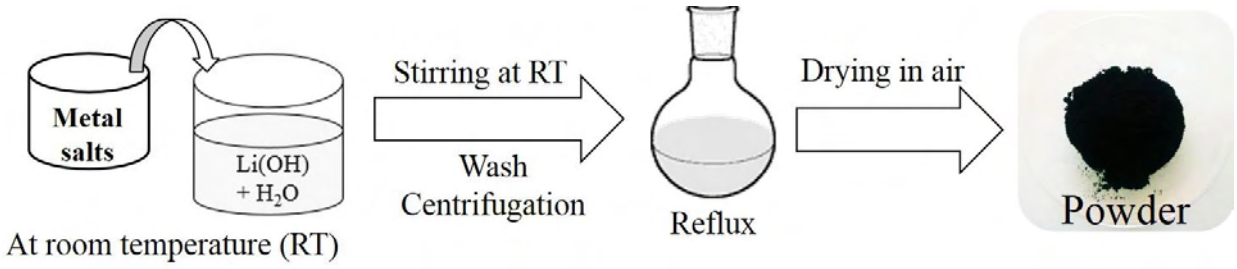

Figure II. 1: Schematic of the inorganic polycondensation method.

II.2.2. Thin film deposition

Thin films were prepared on various substrates by two techniques. The principal technique used during this work was based on:

Dip-coating in colloidal dispersions (at the CIRIMAT laboratory).

Pulsed Laser Deposition (PLD) performed at the department of Materials Science and Engineering, University of Florida, U.S.A. using powder pellets (30 mm of diameter and 5 mm of thickness) of pure oxide powder prepared and sintered in our laboratory.

II.2.2.1. The dip-coating technique

The dip-coating technique is as simple technique based on the dipping and withdrawing of a substrate into a colloidal solution at a constant speed. The colloidal solution was prepared at room temperature using the peptization technique. Details will be shown in chapter IV. A NIMA dip coater system was used, with an automatic control made by the Nima 524 program. The set up values were upper and lower substrate positions, immersion speed, submersion period, withdrawal speed, drying period and number of dip cycles to obtain thin films with smooth surfaces and homogeneous thickness on large areas. Figure II. 2 presents the NIMA dip coater and the schematic of the dip-coating technique.

The dip-coating method enables the coating of various substrates at room temperature. It can also be used for large surfaces. Low temperature coating has little impact on the final properties of the deposited surface and thus enables obtaining specific functional properties that cannot be obtained by other methods.

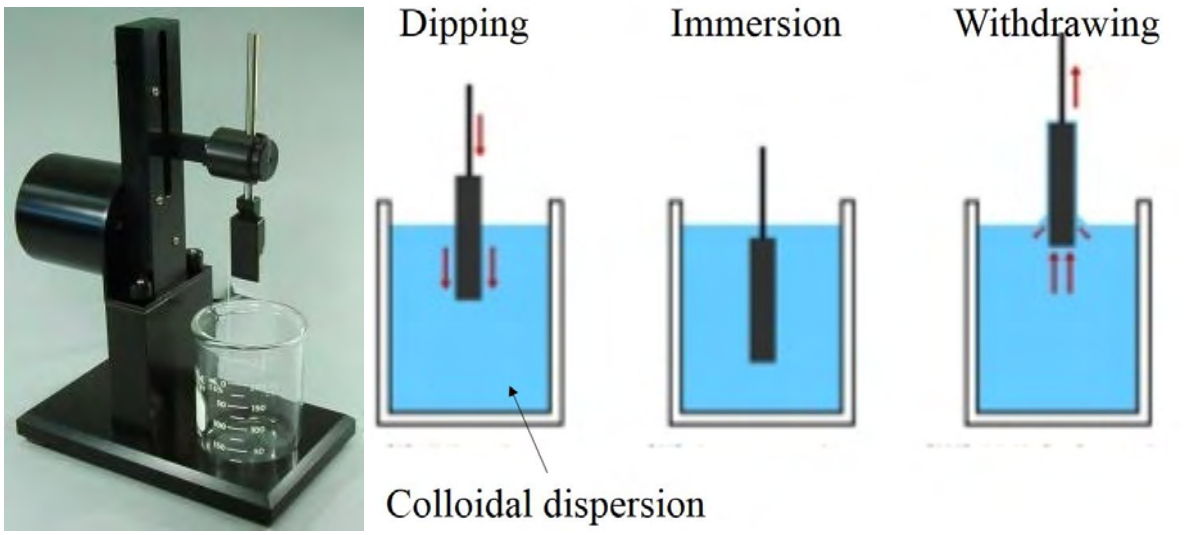

Figure II. 2: NIMA dip coating method – experimental unit (left) and schematic diagram of the dip-coating mechanism (right).

The processing of dip-coating can be separated in three main steps:

- Immersion: The substrate is immersed in the colloidal solution of the coating material at a constant speed.
- Deposition: The thin layer deposits on the substrate while it is pulled up. The withdrawing is carried out at a constant speed.

- Evaporation: The solvent evaporates from the liquid, forming the thin layer.

In the continuous process, the steps are repeated to obtain the desired thickness of thin film. The dip-coating is a simple technique that can be useful to product large areas uniform thin films for application in industry.

Dilute, non-interacting, thin film that make up the coating bath are concentrated on the substrate surface by gravitational draining accompanied by vigorous evaporation and further condensation reactions.

The coating thickness is mainly defined by the withdrawal speed, the solid content and the viscosity of the liquid. If the withdrawal speed is chosen such as the shear rate keeps the system in the Newtonian regime, the coating thickness can be calculated by the Landau-Levich equation [3]:

$$h = 0.94 \frac{(\eta U)^{\frac{2}{3}}}{\gamma^{\frac{1}{6}}(\rho g)^{\frac{1}{2}}} \qquad \text{(II.1)}$$

Where:

h : Film thickness (m)
U : Substrate withdrawal speed ($m.s^{-1}$)
η : Viscosity of the sol-gel ($cP = g.m^{-1}.s^{-1}$)
ρ : Density of the sol-gel ($g.cm^{-3}$)
γ : Liquid-vapor surface tension ($N.m^{-1}$)
g : Gravity ($m.s^{-2}$)

II.2.2.2. Pulsed Laser Deposition (PLD) technique

Thin films were also obtained with pulsed laser deposition technique. The pulsed laser deposition technique requires high power laser pulses to melt the target and evaporate the material from the surface of a target. Then the ionized material is deposited on the substrate. It produces a transient and highly luminous plasma plume that expands rapidly away from the target surface, which is then collected on an appropriately placed substrate across the target upon which it condenses and the thin film grows [4]. The targets were performed at CIRIMAT

laboratory by Spark Plasma Sintering (SPS) technique. Figure II. 3 illustrates the schematic of PLD technique.

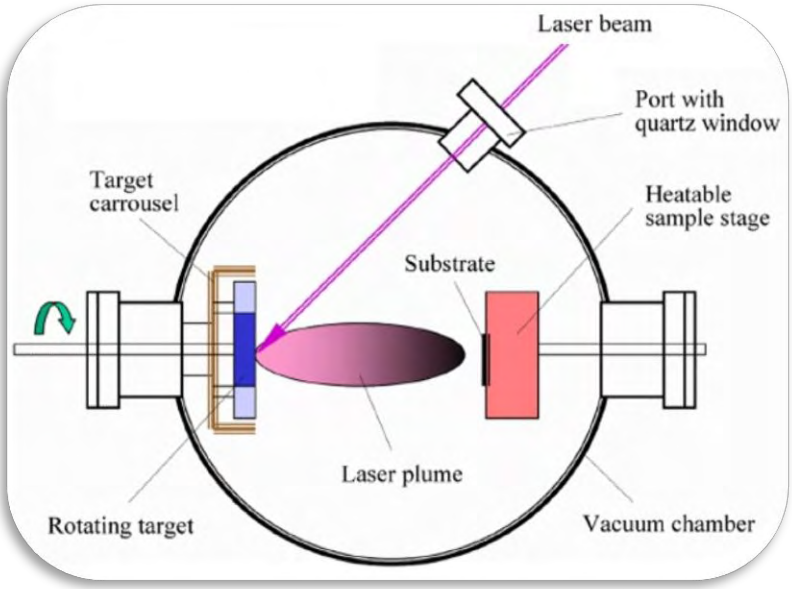

Figure II. 3: Schematic of pulsed laser deposition mechanism.

The PLD process can be described by three steps:

- Laser − target interaction
- Plume expansion
- Film deposition

These features limit the usefulness of PLD in producing large area uniform thin films, and PLD has not been fully developed in industry. In this work, the thin films of Co_2MnO_4 were produced by PLD method to compare with the films prepared by dip-coating technique and conventional sintering.

II.2.3. Elaboration of dense ceramics

The pellets were prepared for dilatometric analysis and for the target of PLD method. The small pellets with 6 mm of diameter (used for dilatometry) were performed by uniaxial pressure technique while bigger pellets with 30 mm of diameter (used for PLD) were performed by Spark Plasma Sintering (SPS) technique.

II.2.3.1. Uniaxial pressure

Uniaxial pressure technique is a mechanical compaction of a powder filled in a metallic mold and pressure is applied from the top and bottom (uniaxial press) to achieve high density materials [5]. In this work, uniaxial pressing technique was used to prepare the pellets with a 6 mm of diameter for dilatometric test. Figure II. 4 shows the schematic of uniaxial pressing cycle.

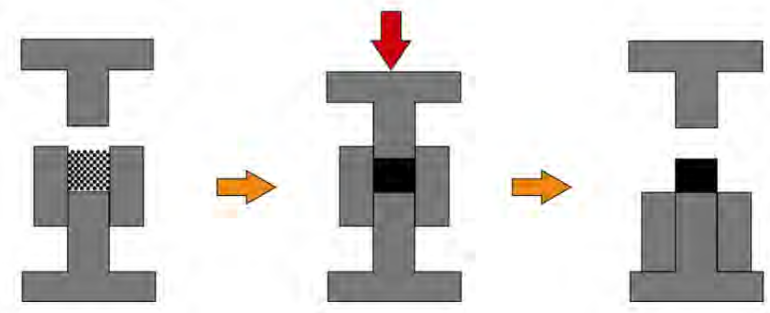

Figure II. 4: Schematic of uniaxial pressing cycle.

The operation of uniaxial pressing is undeniably simple, economical, and suitable for mass production of ceramic parts. However, the applications are usually limited for compaction of small and simple shapes, such as bushings, spacers, tiles, bricks, and crucibles.

The powder was milled and sieved before being mixed with an organic binder for compact cohesion. The binder used is an aqueous solution containing 10 wt. % of polyvinyl alcohol. Pellets (6 mm of diameter and ~ 1 mm of thickness) were obtained by using ~ 90 mg of the powder and applying an uniaxial pressure of 20 bars (~ 15 kN) for one minute.

II.2.3.2. Spark Plasma Sintering (SPS)

Spark Plasma Sintering (SPS) is a recent sintering technique which takes only a few minutes to complete a sintering process compared to conventional sintering which may take hours or even days. In SPS apparatus, the powder is directly fed into the graphite die which is enclosed with suitable punches [6]. The SPS technique was used to prepare pellets of 30 mm in diameter, which were then used for PLD method. Figure II. 5 presents the schematic of the Spark Plasma Sintering Sumitomo 2080 apparatus.

Before SPS treatment, the powder was introduced in a 30 mm internal diameter graphite die which was previously lined with 0.75 mm thick graphitized paper and arranged between two pistons. In this case, it is not necessary to add an organic binder since the samples are sintered directly in the graphite die, consisting of the mold and of the pistons and an uniaxial manual pressure is applied prior to sintering.

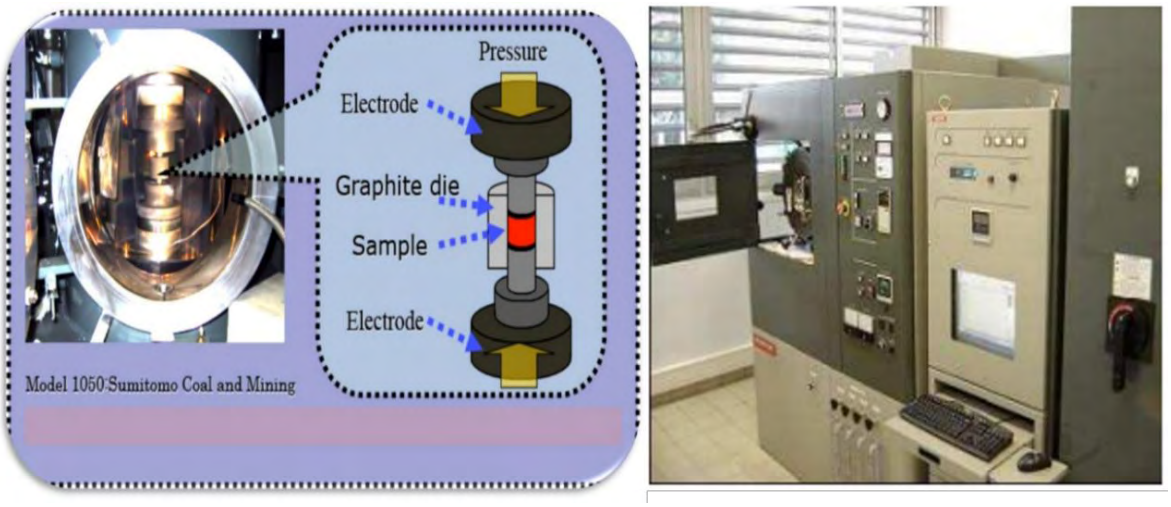

Figure II. 5: Schematic of Spark Plasma Sintering (SPS) and equipment Sumitomo 2080.

The pressure and electric current were applied directly on the sample. The thermal and pressing cycles of SPS to product the Co_2MnO_4 pellet are given in the Figure II. 6. In SPS devices, the temperature was measured using a thermocouple in contact with the graphite matrix. In our case, the powder of Co_2MnO_4 was sintered under vacuum at 700 ºC with an applied load of 35.3 kN.

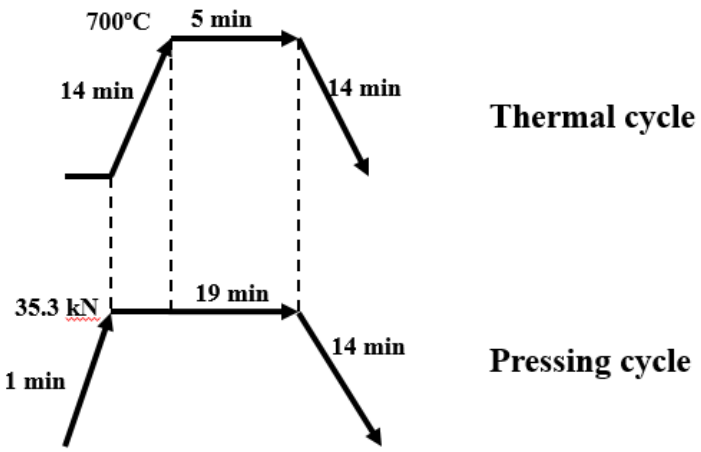

Figure II. 6: The thermal pressing cycle used for SPS.

II.2.4. Conventional sintering

Some thin films prepared by dip-coating were sintered at high temperature by conventional method in order to obtain a compact layer of oxide material on the substrate. The thin films were deposited on quartz, alumina and platinum then sintered in air while thin films prepared on TiN substrate were sintered in nitrogen and argon. The thermal cycle carried out with heating rate is 80 ºC/h from room temperature (T_r) to sintering temperature (T_s), hold for five hours (t_s) before cooling with the same speed.

II.3. Analyses techniques

II.3.1. Analysis of chemical compositions by X-ray fluorescence (XRF)

X-Ray Fluorescence (XRF) is defined as the emission of characteristic "secondary" (or fluorescent) X-rays from a material that has been excited by bombarding with high-energy X-rays or gamma rays. The phenomenon is widely used for elemental analysis. Characteristic X-rays are emitted from elements when their electrons make transitions between the atomic energy levels. If an electron transfers from a level with energy E_i to one with energy E_j, the emitted X-ray has energy $E_x = E_i - E_j$. Because each element has a unique set of atomic energy levels, it emits a unique set of X-rays which are characteristic of this element [7]. Figure II. 7 shows a picture of the S2 Ranger Bruker machine used for analysis and a schematic of the XRF excitation/de-excitation analysis. Samples powders are filled into a cup on a polyethylene of 40 mm in diameter for analysis.

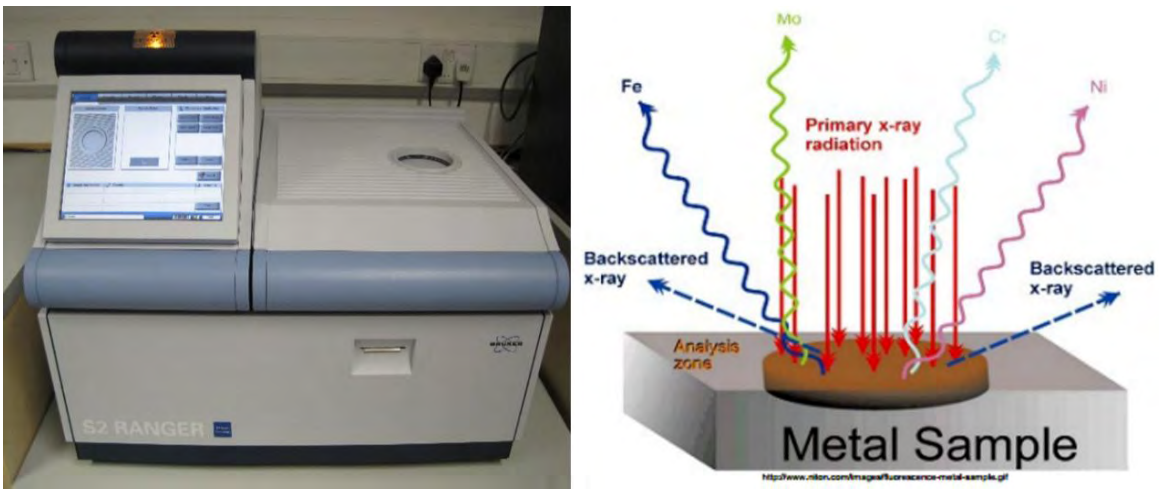

Figure II. 7: XRF machine and schematic of element analysis.

The XRF technique has many advantages; it is fast (about 7 minutes for each powder sample), accurate, non-expensive, non-destructive and has a limit of an acceptable detection range compared with ICP-AES (Induced Coupled Plasma Atomic Emission Spectrometry) method.

II.3.2. Analysis of crystalline structure by X-ray diffraction (XRD)

II.3.2.1. Principle

X-ray diffraction (XRD) is a basic method for determining the crystalline structure of samples. XRD analysis is usually based on constructive and destructive interferences of monochromatic X-rays and a crystalline sample. The X-rays are generated by a cathode ray tube, filtered to produce monochromatic radiation, collimated to concentrate, and directed toward the sample. The interaction of the incident rays with the sample produces constructive interference (and a diffracted ray) when conditions satisfy Bragg's Law [8]:

$$n\lambda = 2d\ \sin\theta \qquad \text{(II.2)}$$

This law relates the wavelength of an electromagnetic radiation to the diffraction angle and the lattice spacing in a crystalline sample. The characteristic X-ray diffraction pattern generated in a typical XRD analysis provides a unique "signal" of the crystalline phase(s) present in the sample. When properly interpreted, by comparison with standard reference patterns and measurements, this signal allows identification of the crystalline form.

The analyses by X-ray diffraction on powders and thin films were conducted to allow phase identification for the different synthesized oxides. The crystallite size was obtained by the resolution of Scherrer's equation [9]:

$$D_{(hkl)} = \frac{K\lambda}{\beta\ \cos\theta} \qquad \text{(II.3)}$$

Where:

$D_{(hkl)}$: The average crystallite size in a direction of plane (hkl) (nm)

λ : The X-ray wavelength (nm)

K : A dimensionless shape factor (K = 0.94)

β : Full Width at Half Maximum (FWHM) of the diffraction peak (rad)

θ : Bragg diffraction angle (deg)

This equation supposes that crystallites are spherical and their average diameter lower than ~ 100 nm. The average diameter of the crystallite was determined by measuring the width of the diffraction peak with the highest intensity for the cubic spinel oxide. The powder samples were analyzed at room temperature by a Bruker D4 Endeavor instrument and at high temperatures by a Bruker D8 Discover apparatus. Thin films XRD patterns were obtained by using a 1° grazing angle with a Siemens D5000 instrument at room temperature. All these, in the Bragg – Brentano geometry.

II.3.2.2. X-ray diffraction at room temperature

The crystalline structures of the powders were studied using a Bruker D4 Endeavor diffractometer shown in Figure II. 8. Powders were deposited on a circular sample holder in poly-(methyl methacrylate) (PMMA).

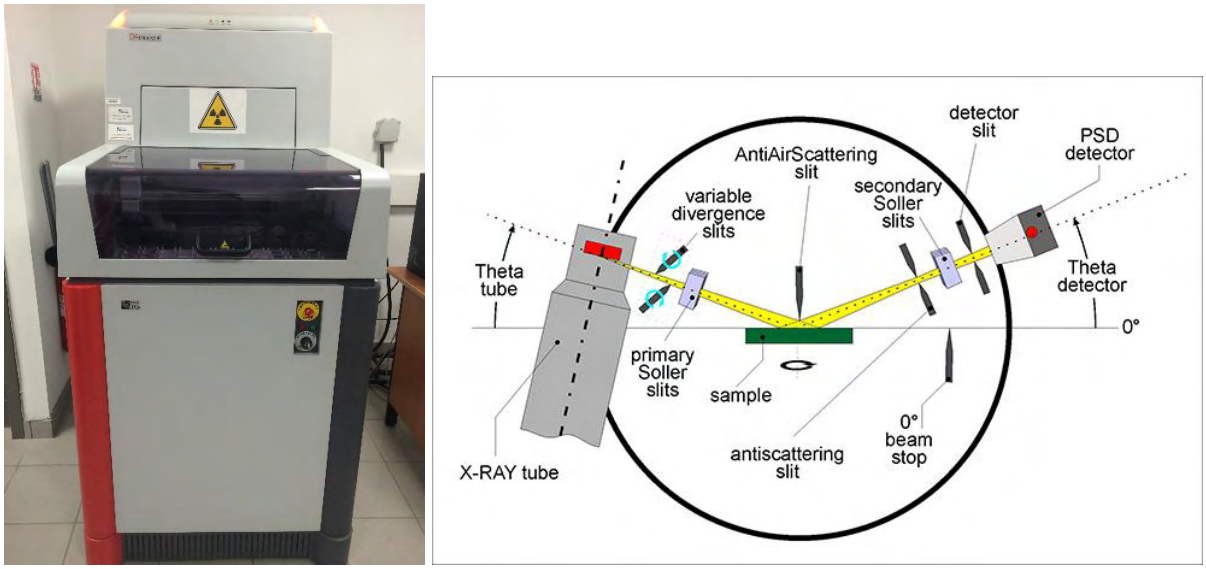

Figure II. 8: Bruker D4 Endeavor diffractometer and the Bragg Brentano configuration.

The diffraction patterns were recorded in 2θ mode from 10 to 100° with a 0.02° (2θ) step scan, the acquisition time of 21.7 s in steps and an opening angle fixed slot equal to 1°. Copper anode was used as an X-ray source emitter by using a generator (40 kV, 40 mA) with the corresponding K_α radiations ($\lambda_{K\alpha 1}$ = 0.15406 nm and $\lambda_{K\alpha 2}$ = 0.15444 nm). The diffraction

patterns were analyzed using the EVA software, and the JCPDS crystallographic database to identify the phases present in the sample.

II.3.2.3. X-ray diffraction at high temperature

High temperature X- ray diffraction was analyzed using a Bruker D8 diffractometer equipped with a high temperature chamber Anton Paar HTK1200N. The copper anode wavelengths were $\lambda_{K\alpha 1}$ = 0.15406 nm and $\lambda_{K\alpha 2}$ = 0.15444 nm. XRD patterns were recorded in the angular range varying from 15º to 70º in 2θ with 0.016º (2θ) counting step, 22.9 s acquisition time per step and an opening angle fixed slot of 1º. Figure II. 9 shows the diffractometer Bruker D8 and the schematic of the Bragg – Brentano high temperature.

Figure II. 9: Bruker D8 diffractometer.

The diffraction patterns of the oxide powders were recorded every 80 ºC from room temperature to 1000 ºC with heating and cooling rates of 80 ºC/h. The powder was put on a circular alumina (alpha-Al_2O_3) sample holder of 20 mm diameter.

II.3.2.4. Grazing Incidence X-ray diffraction (GI-XRD)

Grazing Incidence X-ray diffraction (GI-XRD) was used for thin film characterization at room temperature. In this geometry, the incoming beam is fixed in order to generate a very

small angle (1º) on the thin film surface. Therefore, the beam covers a wider film surface and the analysis is limited to a small thickness (a few tenth of nanometers). Figure II. 10 shows the schematic view of Siemens D5000 diffractometer. Diffraction patterns were recorded from 15º to 70º in 2-Theta angle, with a step size of 0.03º and a counting time of 7 s for each step. Overnight scans with longer step scans (14s/step) and wider angles were also recorded for higher quality data (increased intensity / background ratio).

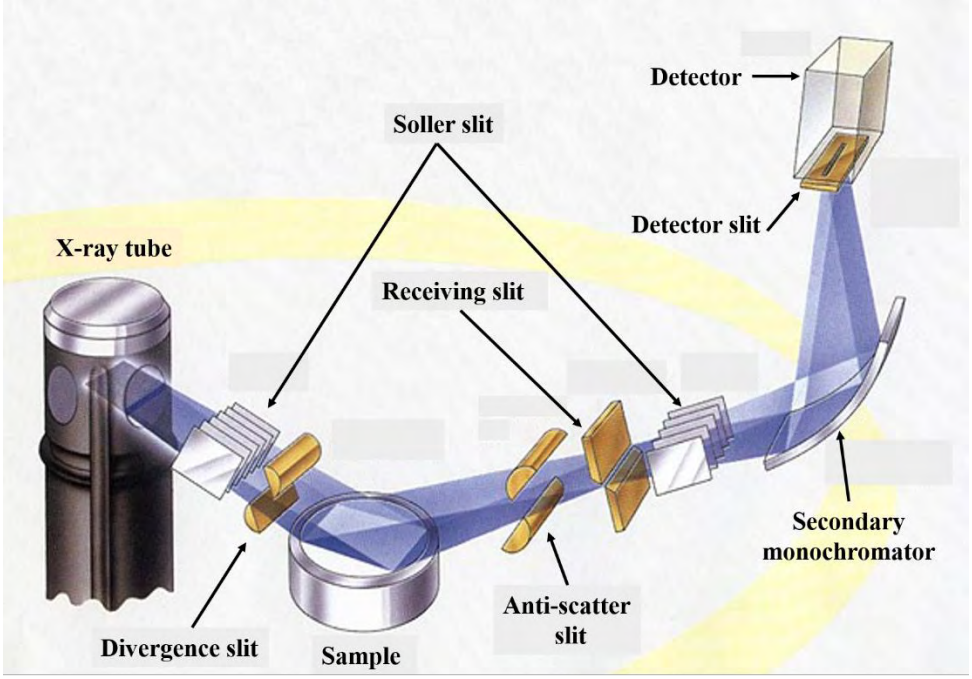

Figure II. 10: The schematic view of Siemens D5000 diffractometer.

The radiation emanating from the line focus of the X-ray tube is diffracted at the sample and recorded by a scintillation detector. Copper anode was used as an X-ray source with the corresponding $K\alpha$ radiation ($\lambda_{K\alpha 1}$ = 0.15406 nm and $\lambda_{K\alpha 2}$ = 0.15444 nm). X-ray diffraction patterns were refined using the EVA software.

II.3.3. Microstructural analysis by Field Emission Gun Scanning Electron Microscope (FEG-SEM)

FEG-SEM is an apparatus that can take surface and cross-sectional images of the powders and thin films by a scanning focused electron beam over a surface to create an image. The signals that derive from electron-sample interactions reveal information about the sample including morphology (texture), chemical composition (using the Energy Dispersive

Spectrophotometry analyzer), crystalline structure and orientation. In this work, a JEOL JEM 6700F Field Emission Gun Scanning Electron Microscope was used. Figure II. 11 shows a picture of the JEOL JEM 6700F machine and a schematic of a scanning electron microscope.

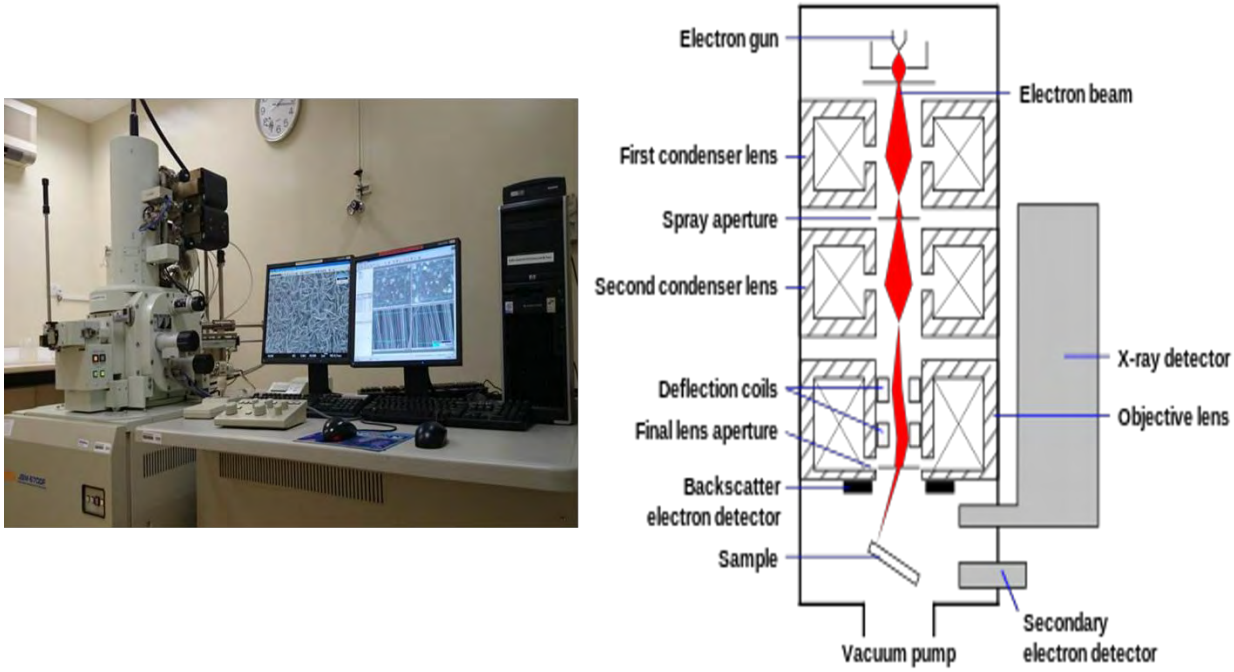

Figure II. 11: JEOL JEM 6700F system.

In the scanning electron microscope an electron beam, which is highly focused (spot size ~ 0.4 to 0.5 nm), is moving over each point of the object. This electron beam, with an energy ranging from 0.2 keV to 40 keV, is focused by one or two condenser lenses to a spot of about 0.4 nm to 5 nm in diameter. The beam passes through pairs of scanning coils or pairs of deflector plates in the electron column, typically in the final lens, which deflect the beam in the x and y axes so that it scans in a rectangular area of the sample surface.

The powders, surface and cross-sectional views of the thin films can be observed by SEM. Prior to observation, the sample was fixed to a sample holder with the surface to be analyzed facing up. The border of the sample was covered by a silver paste to facilitate the electron flow. On the observing surface, gold was deposited by cathodic sputtering to increase the conductivity of the surface. With this analysis, the surface and grain morphologies can be observed.

II.3.4. Thermo-gravimetric analysis (TGA)

Thermo-gravimetric analysis is a technique in which the mass of a substance is measured as a function of temperature or time as the sample specimen undergoes a controlled temperature variation in a specified atmosphere. TGA can provide information about physical phenomena, such as second-order phase transitions, including vaporization, sublimation, absorption, adsorption, and desorption [10].

Thermo-gravimetric analysis (TGA) relies on a high degree of precision in three measurements: mass change, temperature, and temperature change. Therefore, the basic instrumental requirements for TGA are a precision balance with a pan loaded with the sample and a programmable furnace. The furnace can be programmed either for a constant heating rate or for heating to acquire a constant mass loss with time. Figure II. 12 illustrates a thermal gravimetric analyzer SETARAM - TAG 16

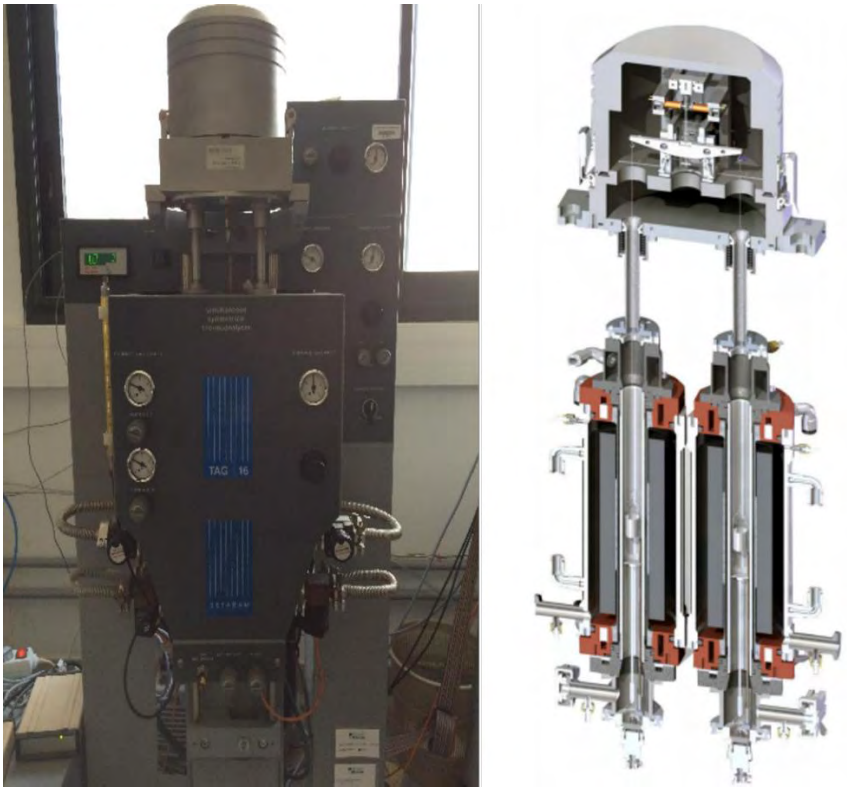

Figure II. 12: The machine and schematic of SETARAM TAG -16 system.

The pan sits in a furnace and is heated up or cooled down during the experiment. The sample mass is precisely determined (down to a few tenth of a micron) during the experiment.

A sample purge gas controls the sample environment. This gas may be inert or a reactive gas that flows over the sample and exits through an exhaust.

In this work, the thermal analyzer Setaram TAG 16 was used to study the powder samples in controlled air atmosphere. All the sample analyses were carried out in air between 25 ºC and 1000 ºC. The temperature scanning rate 1.3 ºC/min for both heating and cooling cycles.

II.3.5. Thermo-mechanical analysis (TMA) or dilatometry

Thermo-mechanical analysis is a technique that measures the deformation of a sample under non-oscillating stress when subjected to a temperature program in a controlled atmosphere. The stresses applied can be compression, traction and flexion. Figure II. 13 shows a SETSYS Evolution TMA and its schematic.

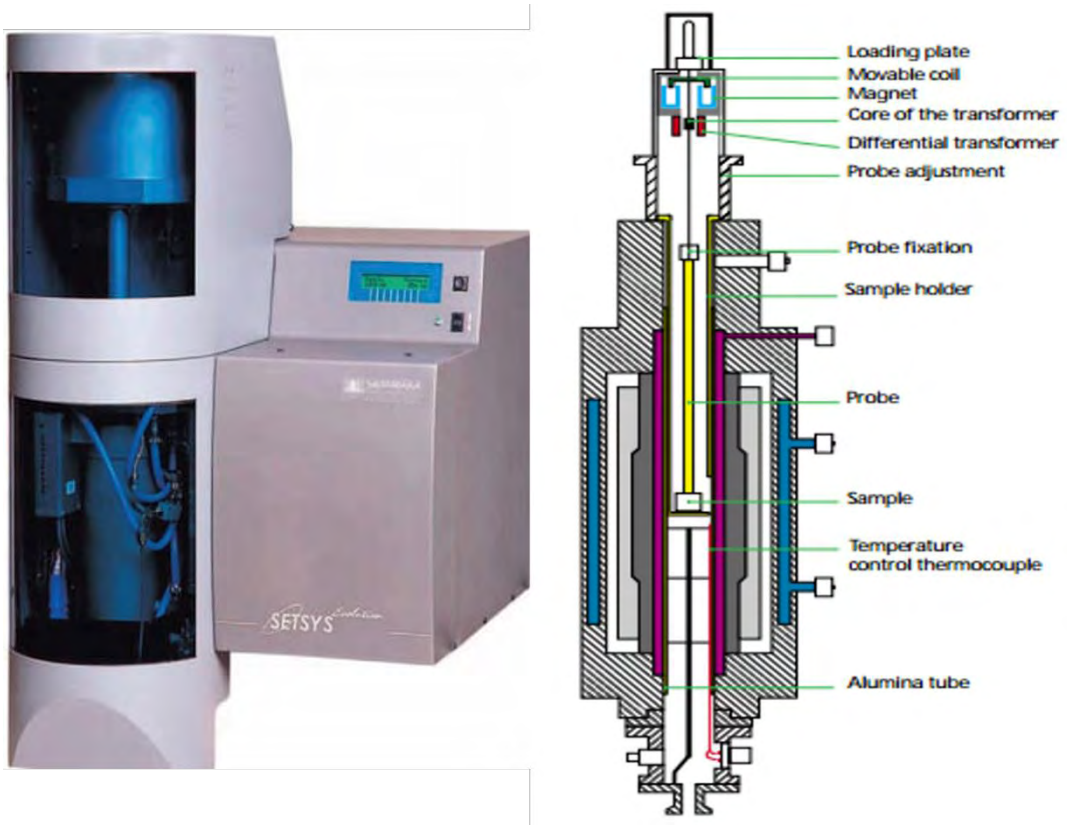

Figure II. 13: The machine and schematic of SETSYS Evolution TMA system.

The displacement transducer on the SETSYS Evolution TMA model is especially distinguished by its robustness and its great accuracy variations in movement as small as

0.01 µm that can be detected with such a transducer which uses an electromagnetic fitting allowing automatic piloting of the force on the sample up to 1.5 N. The software of the SETSYS Evolution TMA can be used as a dilatometer and also for measuring controlled rate sintering. The pellets with 6 mm of diameter for dilatometric analysis were prepared at room temperature by uniaxial pressing technique at 15 kN for 1 minute.

II.3.6. Topographic and roughness surfaces of thin films

Topographical analysis and roughness of surfaces were carried out by optical interferometry using a ZYGO system [11]. The measuring system uses a Mirau interferometer with the optics of a microscope. The schematic layout of an interference microscope with a Mirau objective is shown in Figure II. 14.

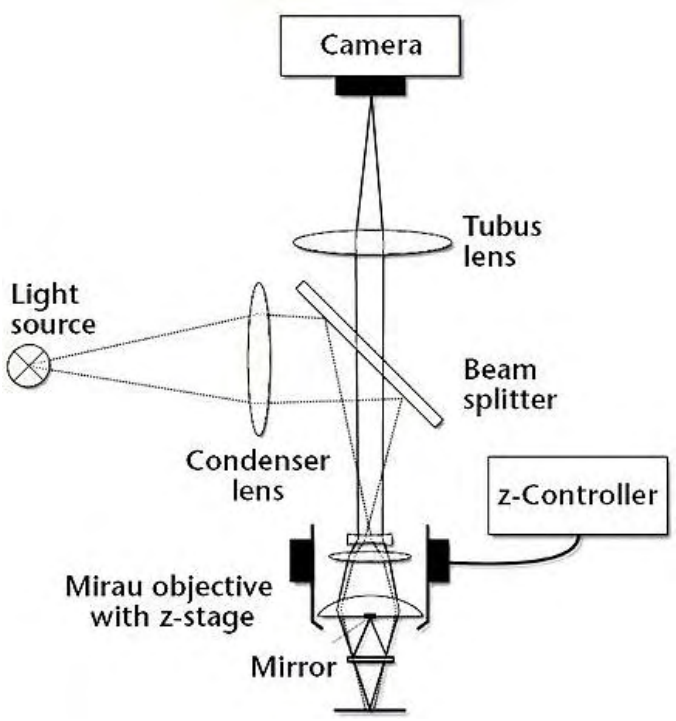

Figure II. 14: Schematic layout of an interference microscope with Mirau objective.

The optical magnification of the image on the charge-coupled device (CCD) does not depend on the distance between the tube lens and objective lens if the microscope images the object at infinity. With a Mirau objective, the reference beam is reflected back in the direction of the objective front lens by a beam splitter. On the front lens there is a miniaturized mirror the same size as the illuminated surface on the object. Therefore, for high magnifications, the

mirror is so small that its shadowing effect can be ignored. Moving the interference objective modifies the length of the measurement arm. The interference signal of a pixel has maximum modulation when the optical path length of light impinging on the pixel is exactly the same for the reference and the object beams [12].

From the interference signal, the topography of the surface was analyzed by Metropro software. This software allows to determine the arithmetic roughness (R_a) of the surface and total roughness (R_t) by measuring the distance from the highest point to the lowest point.

II.3.7. Optical measurements

The optical properties of the thin films can be defined by the interaction between an electromagnetic radiation (light) and the material, including absorption, diffraction, polarization, reflection, refraction and scattering effects. In this work, the optical performances of the thin films, which essentially consist of the transmittance and reflectance, were analyzed by a Bentham PVE 300 PV characterization system shown in Figure II. 15.

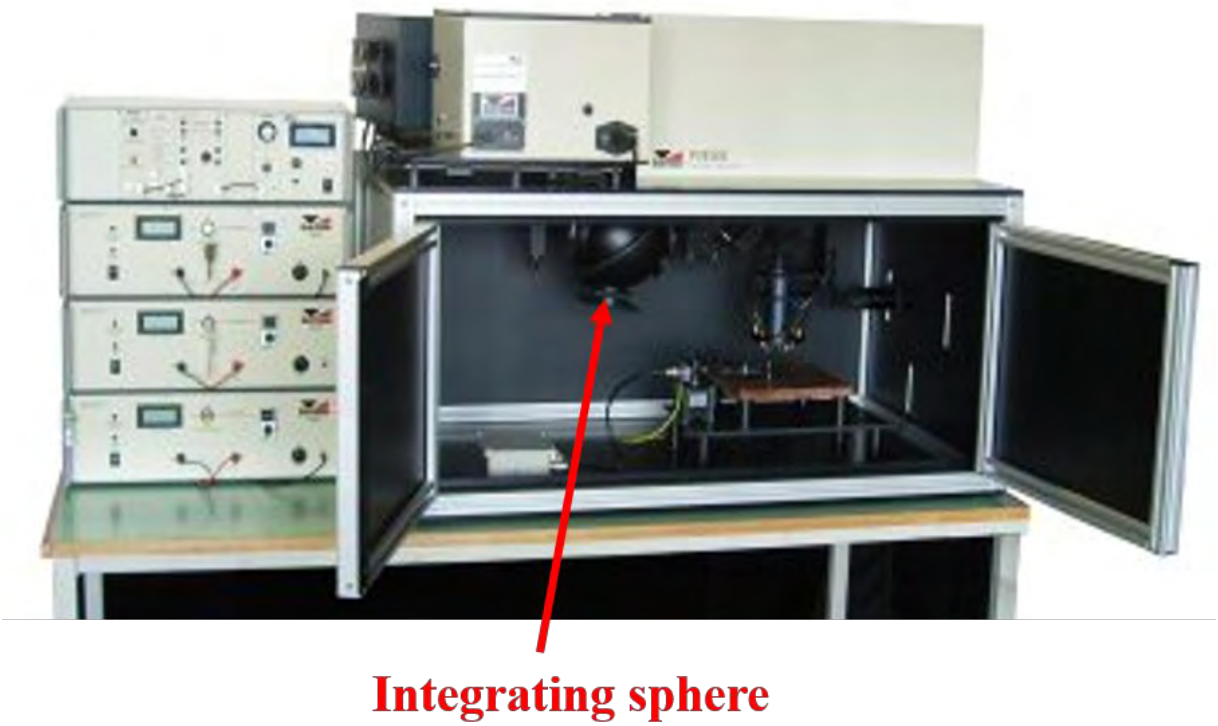

Figure II. 15: Bentham PVE 300 PV characterization system.

The integrating sphere is mounted on an optical rail to the upper part of the PVE300 chamber (in Figure II. 15) to allow the measurement of total reflectance and total transmittance. It is composed of two probe light sources, 75 W Xenon and 100 W Quartz to provide illumination from Ultraviolet (UV) to near Infrared (NIR) with the standard range of 300 – 1100 nm. The Xenon source provides a higher output throughout the visible range but with unstable line emission, whereas the Quartz halogen lamp provides lower output but a very stable source.

The thin film sample is placed on the left or right side of the integrating sphere depending on transmittance or reflectance measurements. The transmitted or reflected light will is collected in the integrating sphere and measured by a silicon detector. After electronic calibration of the silicon detector, the transmittance and reflectance data is extracted by the Benthem Benwin+ spectroradiometer software. The easy user interface allows quick and simple system calibration, measurements of spectral response, reflectance and transmittance. Data may be analyzed directly or exported to another platform as required.

Thin films optical properties (transmittance and reflectance) deposited on glass and quartz were analyzed by steps described as follow:

- Calibration of the Bentham PVE 300 PV system
- Measurement of the first spectrum without sample to determine the baseline corresponding to "blank" optics.
- Measurement of the sample spectrum.

From the total transmittance $T(\lambda)$ and reflectance $R(\lambda)$ measurements of thin films, the optical band gap can be estimated. The absorption coefficient α was computed from $T(\lambda)$ and $R(\lambda)$ by using formulae [13, 14]:

$$T = \frac{(1-R)^2 e^{-\alpha d}}{1-R^2 e^{-2\alpha d}} \quad \text{(II.4)}$$

$$\alpha = -\frac{1}{d} ln\left[\frac{\sqrt{(1-R)^4 + 4T^2R^2} - (1-R)^2}{2TR^2}\right] \quad \text{(II.5)}$$

And the absorbance can be estimated using the simplified formulae:

$$A = 1 - T - R \tag{II.6}$$

Where:

A	: Total absorbance
T	: Total transmittance measurement
R	: Total reflectance measurement
d	: Thin film thickness (cm)
α	: Absorption coefficient (cm^{-1})

The optical band gap E_g was determined by following Tauc's power-law behavior [15]:

$$\alpha h\nu = C\left(h\nu - E_g\right)^m \tag{II-7}$$

$$\Leftrightarrow \quad \ln(\alpha h\nu) = m\ln\left(h\nu - E_g\right) \tag{II-8}$$

$$\Leftrightarrow \quad \frac{d\left(\ln(\alpha h\nu)\right)}{d\left(h\nu\right)} = \frac{m}{h\nu - E_g} \tag{II-9}$$

Here, m is the slope of the curve ln ($\alpha h\nu$) versus ln ($h\nu$ - E_g) (equation (II-8)), m equal to ½ or 2 for direct or indirect allowed transitions, respectively. After determining the m value, by plotting d (ln ($\alpha h\nu$)) / d ($h\nu$) as a function of ($h\nu$), the optical band gap E_g can be estimated. Figure II. 16 shows a direct optical band gap estimation.

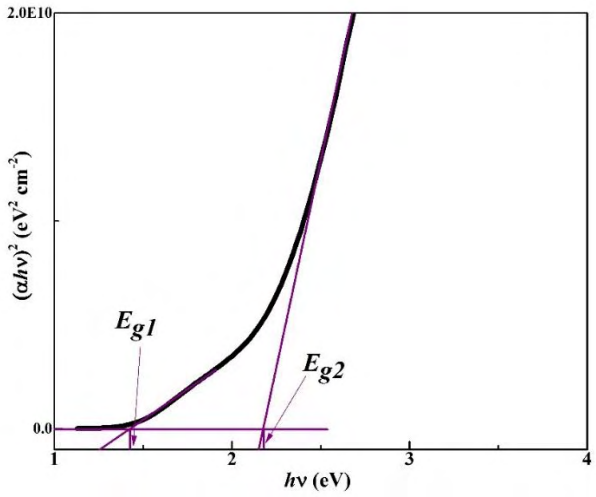

Figure II. 16: Direct optical band gap estimation.

II.3.8. Electrical properties of the thin films

The resistivity ρ of a semiconductor is an essential feature that characterizes the charge transport of a material used mainly for electronic devices. The resistivity contributes to the device series resistance, capacitance, threshold voltage, hot carrier degradation of metal oxide semiconductor (MOS) devices, latch up of complementary metal oxide semiconductor (CMOS) circuits, and other parameters. In this work, the resistivity of the thin film was measured using a classical four-point probe system by passing a current through two outer probes and measuring the voltage through the inner probes [14]. The schematic of an electrical measurement four-point probe system is shown in Figure II. 17.

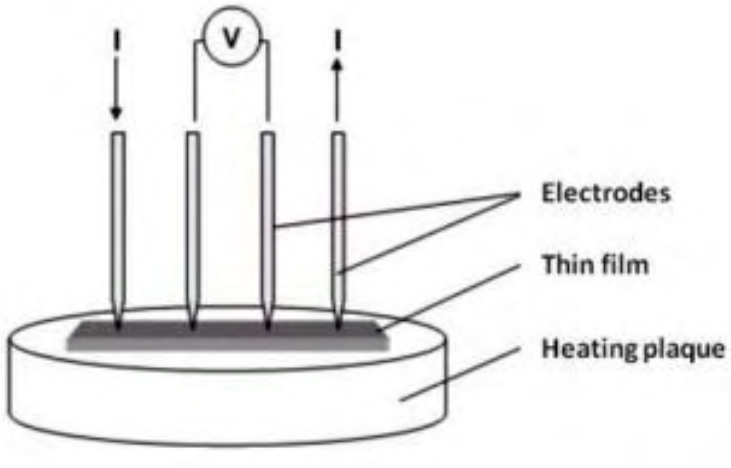

Figure II. 17: Schematic of an electrical measurement.

This system includes a Keithley 237 generator, a four points contact, a heating plate as the sample holder (Quad Pro Resistivity System) and a temperature controller (Signatone, model S-1060R). The maximum resistance that can be measured by this system is 10^{14} Ω with an error range of 3 %, which essentially comes from the error of thickness measurements.

The sample is positioned onto the heating plate. The temperature for the measurement is controlled and maintained by the controller. Upon the application of the generated current through the two outside probes, the potential can be measured by the two interior probes. The sheet resistivity can be calculated with the following formulae [14, 16]:

$$\rho = \frac{\pi}{\ln 2}\, d\, \frac{U}{I} \qquad \text{(II-10)}$$

Where:

ρ	: Resisitivity of sample (Ω.cm)
d	: Thin film thickness (cm)
U	: Measured potential (V)
I	: Applied current (A)

II.4. References

[1] G. Salek, S. Guillemet-Fritsch, P. Dufour, and C. Tenailleau, "*A Simple Preparation Process of Pure Mn3-xCoxO4 (x = 1, 1.5 and 2) Desert Rose-Like Nanoparticles and Their Optical Properties*," **International Journal of Chemistry,** Vol. **4**, 44-53, **2012**.

[2] G. Salek, "*Elaboration et caractérisation de films minces absorbants de lumière à partir de dispersions colloïdales de nanoparticules d'oxydes Mn3-xCoxO4 (0≤x≤3) et Cu2O*," Doctor, Science et Génie des Matériaux, **Université de Toulouse III - Paul Sabatier**, **2013**.

[3] L. D. Landau and V. G. Levich, "*Dragging of a liquid by a moving plate.*," **Acta physicochimica U.R.S.S,** Vol. **17**, 42-54, **1942**.

[4] Hans-Ulrich Krebs, Martin Weisheit, Jorg Faupel, Erik Suske, Thorsten Scharf, Christian Fuhse, *et al.*, "*Pulsed Laser Deposition (PLD) - a Versatile Thin Film Technique*."

[5] S. Leo, C. Tallon, N. Stone, and G. V. Franks, "*Near-Net-Shaping Methods for Ceramic Elements of (Body) Armor Systems*," **Journal of the American Ceramic Society,** Vol. **97**, 3013-3033, **2014**.

[6] O. Guillon, J. Gonzalez-Julian, B. Dargatz, T. Kessel, G. Schierning, J. Räthel, *et al.*, "*Field-Assisted Sintering Technology/Spark Plasma Sintering: Mechanisms, Materials, and Technology Developments*," **Advanced Engineering Materials,** Vol. **16**, 830-849, **2014**.

[7] K. Janssens, "*X-ray fluorescence analysis"*, **Wiley - VCH Verlag GmbH & Co. KGaA, Weinheim**, p. 56, **2003**

[8] W. H. Bragg and W. L. Bragg, "*The Reflection of X-rays by Crystals*," **Proceedings of the Royal Society of London A: Mathematical, Physical and Engineering Sciences,** Vol. **88**, 428-438, **1913**.

[9] P. Sherrer, "*Determination of the size and internal structure of colloidal particles using X rays"*. **Nachr Ges Wiss Goettingen**, p. 394, **1918**.

[10] A. W. Coats and J. P. Redfern, "*Thermogravimetric analysis. A review*," **Analyst,** Vol. **88**, 906-924, **1963**.

[11] P. J. d. Groot, "*Interference microscopy for surface structure analysis"*. **Boca Raton London New York**: **CRC Press Taylor & Francis Group**, **2015**.

[12] O. V. Lyulko, G. Randers-Pehrson, and D. J. Brenner, "*Immersion Mirau interferometry for label-free live cell imaging in an epi-illumination geometry*," 756825-756825-756829, **2010**.

[13] P. J. Dean and D. G. Thomas, "*Intrinsic Absorption-Edge Spectrum of Gallium Phosphide*," **Physical Review,** Vol. **150**, 690-703, **1966**.

[14] D. K. Schroder, "*Semiconductor Material and Device Characterization"*, **Wiley-Interscience**, **2006**.

[15] J. Tauc, "*Amorphous and liquid semiconductors"*, **London and New York**, p. 175, **1974**.

[16] F. M. Smits, "*Measurement of Sheet Resistivities with the Four-Point Probe*," **Bell System Technical Journal,** Vol. **37**, 711-718, **1958**.

CHAPTER III

FIRST-PRINCIPLES ELECTRONIC STRUCTURE CALCULATIONS FOR THE WHOLE SPINEL OXIDE SOLID SOLUTION RANGE $Mn_xCo_{3-x}O_4$ ($0 \leq x \leq 3$)

III.1. Introduction

Few first-principles studies have already been reported for the pure bulk end member compounds Mn_3O_4 [1-4] and Co_3O_4 [5-11]. In these works, the authors aimed at describing accurately the electronic structures with different approximations for the exchange-correlation potential. Other recent first-principles studies showed the correlation between the spinel oxide electronic structure and the surface and catalytic properties of Co_3O_4 [12-15] as well as $MnCo_2O_4$ [16-18].

We propose a fundamental and complete study of the structural, magnetic and electronic properties of $Mn_xCo_{3-x}O_4$, based on first-principles calculations and comparison with our previous and current experimental results.

The calculations were performed by R. Arras at the CEMES laboratory in Toulouse using the density functional theory (DFT) and the projector augmented-wave (PAW) method 31 with a cut-off energy of 650 eV, as implemented in the Vienna Ab initio Simulation Package (VASP) [19, 20]. The first Brillouin zone was sampled by a 10×10×10 Monkhorst Pack grid [21]. A full optimization of the atomic structure (atomic coordinates and volume) was performed for each case using the conjugate-gradient algorithm method and calculating the stress tensor. This step was only done with the exchange correlation energy approximated by the generalized-gradient approximation (GGA-PBE) [22].

The electronic structure was then calculated according to the Tran-Blaha modified Becke-Johnson local spin density approximation (mBJ) [23, 24], or by adding the so-called "+*U*" correction [25], applied to the *d*-electrons of the Mn and Co atoms. We used the rotationally invariant version of this method, as introduced by Dudarev et al. (1998) [26] and the U_{eff} (= $U - J$) parameter was chosen to 5.0 eV and 3.8 eV, for the Co and Mn atoms respectively. Since the mBJ potential is not obtained as a derivative of the exchange functional, it is advised not to use it for energy comparison (structural optimization or stability of magnetic states), but only for electronic structure calculation, where this method has been found to improve the description (with a relatively low computational cost) and, in particular, the band gap values for a large range of materials, including transition metal oxides [24, 27].

III.2. Atomic, magnetic and electronic structures of Mn and Co spinel oxides

III.2.1. Co_3O_4

Co_3O_4 displays a spinel structure, which corresponds to a distorted face-centred cubic lattice of oxygen atoms in which Co atoms occupy 1/8 of the tetrahedral (*A*) and 1/2 of the octahedral (*B*) atomic sites. Co_A, Co_B and O atoms occupy, respectively, the atomic sites 8*a*, 16*d* and 32*e* in the Wyckoff notation. Our calculated value of 8.087 Å is in very good agreement with our experimental lattice parameter (a = 8.081 Å) previously obtained for Co_3O_4 dense ceramics after spark plasma sintering (SPS) [28].

Co_3O_4 is a mixed valence oxide with two oxidation states that provides interesting electronic and magnetic properties. The electronic charge distribution in this material corresponds to the so-called normal spinel structure, which can be described according to the formula $(Co_A^{2+})[Co_B^{III}]_2O_4^{2-}$. We use the Co_B^{III} notation because cobalt in octahedral sites adopts a low spin state with a nil spin magnetic moment. Co_A^{2+} ions are in a high spin state (with a theoretical spin magnetic moment of M_S = ± 3 μ_B) and are antiferromagnetically coupled together, with a low Néel temperature of 40 K. In his experimental study, Roth highlighted the strength of the *A*-*A* antiferromagnetic indirect coupling that is for example higher than in aluminate spinel compounds [29]. The total spin magnetic moment for Co_3O_4 is of 0 μ_B / formula unit (f.u.), which is correctly described as being the fundamental magnetic state by our calculations, with a total energy 27 meV/f.u. lower than that calculated for a ferromagnetic ordering, according to the GGA calculations. A spin magnetic moment of 3.26 μ_B was measured by Roth [30]. This value is higher than the theoretical value of 3 μ_B given before, considering a purely ionic character of the Co^{2+} and the spin only contribution. It is also higher than our calculated value, which is at the most 2.77 μ_B with the mBJ calculations. Roth explained that its high measured value was due to a small contribution from the spin-orbit coupling [30].

Regarding the band structure, a debate is still open with the band gap width of Co_3O_4 at the Fermi level. Most of the results reported in the literature, based on optical measurements mainly, usually described two band gaps of ≈ 1.6 eV and ≈ 2 - 2.5 eV [31-34], while some references also reported a band gap with a lower value, of ≈ 0.8 eV [5-7], and thus claim that

Co_3O_4 would not be a highly-correlated electron material on the contrary to the Mott insulator CoO. This last hypothesis would be described within the GGA+*U* formalism by using a lower value of U_{eff} for the *d* electrons, especially for the Co_B^{III} ions. The electronic structure variation for Co_3O_4 as a function of U_{eff} has been described by Qiao et al. (2013) showing that the spinel cobalt oxide electronic structure was better calculated by standard DFT calculations than by using DFT+*U*, when compared to X-ray photoelectron spectroscopy (XPS) data [6]. Kormondy et al. (2014) also mapped a large combinations of [$U_{eff}(Co_A^{2+})$,$U_{eff}(Co_B^{3+})$], which were compared to magnetization measurements and XPS spectra, that finally conducted to tandem values [4.0,0.0] eV [7]. These values are much lower than those of [4.4,6.7] eV calculated by Chen et al. (2011) from first principles, by using a linear response method [8]. As discussed there, the set of parameters still gives a band gap lower by a factor 1.75 than for PBE0 hybrid functional calculations. For comparison, calculated U_{eff} values for CoO are of the order of 5 eV [35]. Finally, a study performed by Singh et al. (2015) aims at comparing different approximations (GGA-PBE, GGA+*U*, and HSE06 levels as well as a many-body Green function GW) to calculate the electronic, magnetic and optical properties of Co_3O_4. They highlighted that the results obtained with the GGA+*U* and HSE06 hybrid functional are very sensitive to the chosen value of U_{eff} or to the percentage of exact exchange introduced in the exchange correlation DFT functional. After comparison with photoemission spectroscopy (PES) and ultraviolet photoelectron spectroscopy (UPS), they concluded that the pure GGA functional, the hybrid HSE06 (α = 5 %) functional, and the Sc-GW0 method (GW with only full self-consistency over G) are the most reliable methods to calculate the electronic and optical properties of Co_3O_4 [9].

The reason for the low measured band gap is uncertain and was not always discussed. We preferred to keep a high constant value of U_{eff} for every Co atoms, in order to be consistent with the mBJ calculations. GGA results will still be given for each system for comparison.

Our calculated band gap widths are then 0.27 eV, 2.33 eV, and 2.91 eV respectively with the GGA, GGA+*U* (U_{eff} = 5 eV), and mBJ methods, respectively. These values are in good agreement with the results reported elsewhere [11]. Densities of states (DOS) are plotted in Figure III. 1.

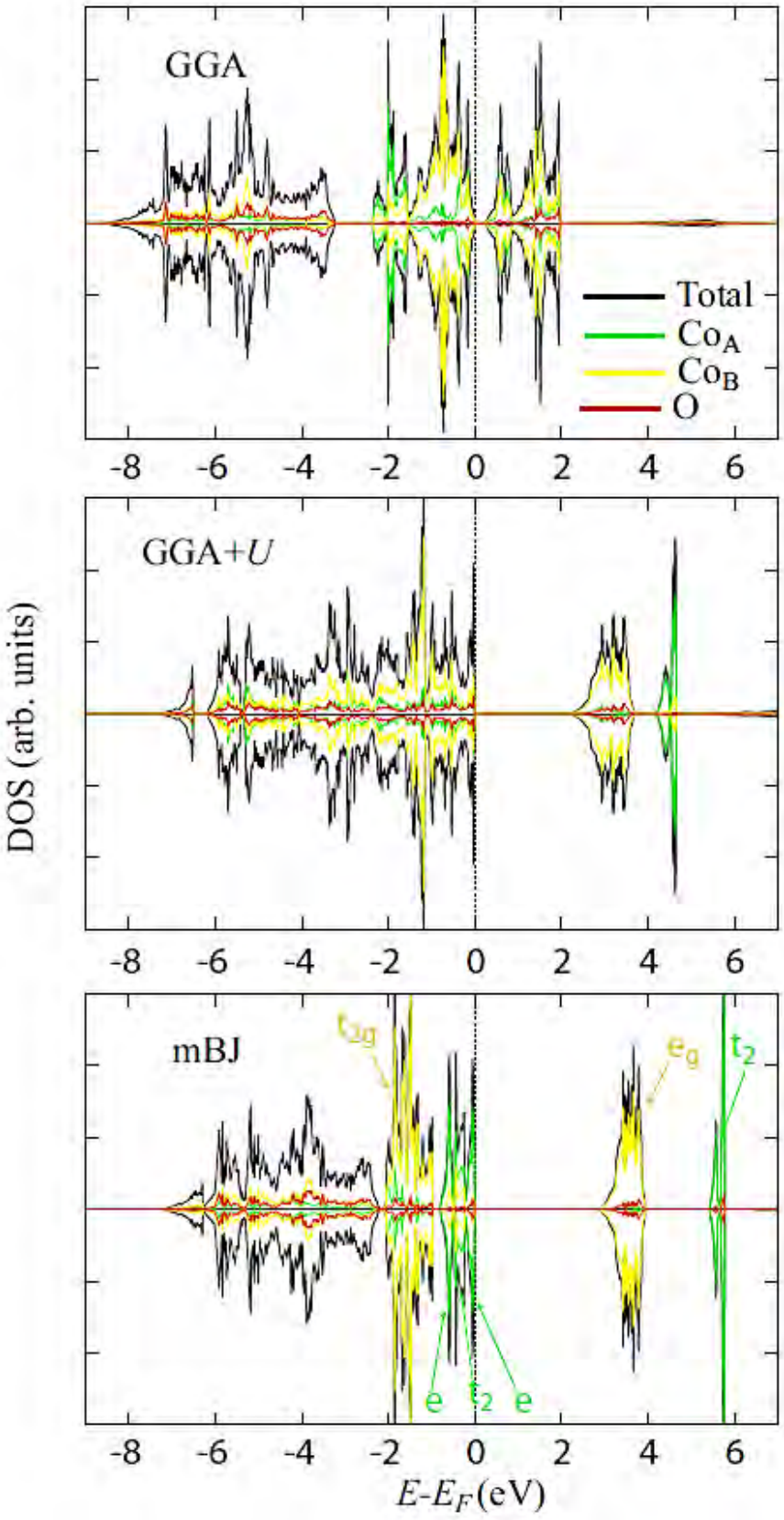

Figure III. 1: Spin-resolved DOS for Co_3O_4 ($x = 0$) calculated with the 3 approximations.

The DOS calculated with the GGA+*U* method displays a strong hybridization between the *d* orbitals of Co atoms in *A* and *B* sites and the *p* orbitals of oxygen atoms over the whole range of occupied valence bands, i.e. from -7.25 eV to E_F. On the contrary, GGA and mBJ calculations show a large separation between bands with a strong *d*-orbital contribution (respectively from -2.38 eV or -2.12 eV to E_F) and *p* bands of the O^{2-} anions. This is characteristic of low hybridization and clearly delimitates the respective localization of the electrons near the cations or the oxygen atoms. According to the mBJ calculations, the band gap observed in Co_3O_4 corresponds to the difference of energy between occupied *e* bands of Co_A and e_g unoccupied bands of Co_B. The difference of energy between the occupied *e* and unoccupied t_2 bands of Co_A ($\Delta E^A(e \rightarrow t_2)$), and the occupied t_{2g} and unoccupied e_g bands of Co_B ($\Delta E^B(t_{2g} \rightarrow e_g)$) is respectively 5.45 and 3.88 eV (Figure III. 2).

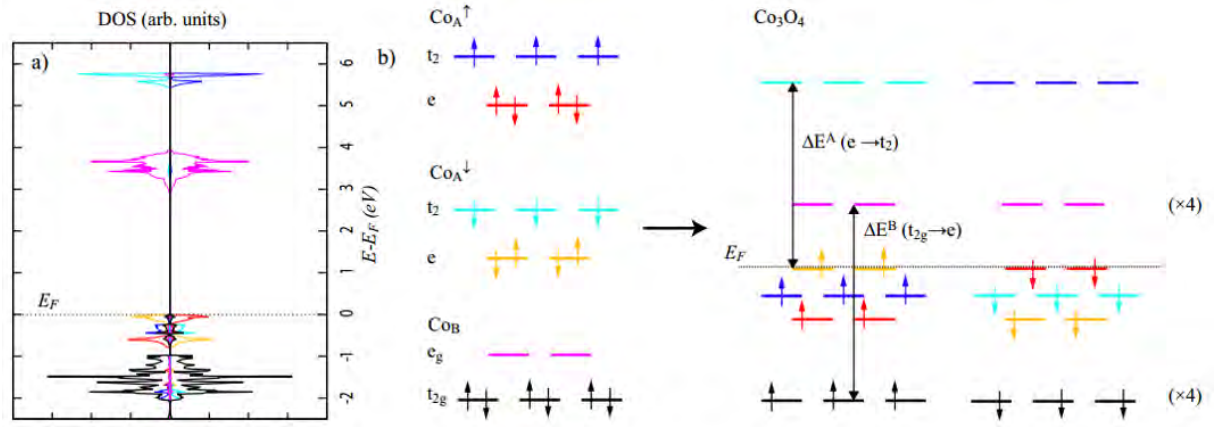

Figure III. 2: a) Spin-resolved Co-d contribution to the DOS of Co_3O_4, b) schematic representation of the electron distribution in the d orbitals.

III.2.2. Mn_3O_4

Hausmannite Mn_3O_4 crystallizes also with the spinel structural type [36], but exhibits a tetragonal distortion with our experimental lattice parameters a = 8.149 Å and c = 9.465 Å (i.e. a c/a ratio equal to 1.162) as previously described for a single phase and dense ceramic [28]. Our calculations here give cell parameter values of a = 8.132 Å and c = 9.493 Å (c/a = 1.167) considering antiferromagnetic ordering, which are again in agreement with the experimental data.

The charge distribution in Mn_3O_4 also corresponds to the normal spinel structure formula $(Mn_A^{2+})[Mn_B^{3+}]_2O_4^{2-}$ but in this case, with both Mn_A^{2+} (M_S = 5 μ_B) and Mn_B^{3+} (M_S = 4 μ_B) cations in the high-spin state.

Mn_3O_4 exhibits a complex ferrimagnetic ordering below the Curie temperature T_C of approximately 42 K [37], below which it undergoes three magnetic phases [38-44]. Between 39 K and T_C, Mn_3O_4 is reported to be commensurate and collinear, coinciding with the atomic unit cell. From 33 K to 39 K, the magnetic ordering changes into an incommensurate spin structure, generally described as a spiral with a [010] propagation vector. Below 33 K, the spin spiral becomes commensurate and the magnetic unit cell is doubled, with the resulting spin magnetic moments of the Mn_B atoms antiparallel in the [010] direction to those of Mn_A. This magnetic phase below 33 K is closely linked to the atomic structure which can undergo a tetragonal-to-orthorhombic phase transition (from the space group $I41=amd$ to $Fddd$) [43, 44]. Kemei et al. (2014) have shown that both structural phases can coexist at low temperature [44]. Strain effects can be envisaged to tune the magnetic properties [44] and the critical temperature [43, 45].

An optical band gap of ≈ 2.4 eV was measured on thin films [46, 47], while a higher value of 3.3 eV was reported on nanoparticles [48]. This shift of band gap was explained by a confinement effect. Hirai et al. (2015) reported absorption spectra from which they did not conclude about a band gap value [4]. However, they found an absorption peak at ≈ 1 eV which can be consistent with the calculations of Franchini et al. (2007) who gave a band gap of 0.3-0.5 eV [2]. They also found two optical band gaps of 1.9 eV and 4.0 eV [4].

We performed calculations with different magnetic orderings (antiferromagnetic, ferromagnetic and ferrimagnetic) and found that the antiferromagnetic configuration with a zero magnetic moment is the most stable. This result is consistent with the literature [1, 4], and highlights a clear difference with a common ferrimagnetic ordering obtained due to a strong antiferromagnetic coupling between cations in *B* and *A* sites. On the contrary, the spin magnetic moments per atoms are in agreement with reported experimental measurements (see Table III. 1) [28].

Table III. 1: Spin-resolved band gap energies ΔE and atomic spin magnetic moments M for different magnetic orderings. DOS from which the band gap energies were extracted are given in Figure III. 3.

	$\Delta E(\uparrow)$ (eV)	$\Delta E(\downarrow)$ (eV)	M (Mn_A) (μ_B/atom)	M (Mn_B) (μ_B/atom)
Antiferromagnetic ($A^{\downarrow\uparrow}[B^{\uparrow\downarrow},B^{\downarrow\uparrow}]$): M_{tot} = 0 μ_B , a = 8.132 Å, c = 9.493 Å				
GGA	0.78	0.78	+/- 4.19	+/- 3.52
GGA + U	1.37	1.37	+/- 4.53	+/- 3.84
mBJ	1.92	1.92	+/- 4.48	+/- 3.64
Ferrimagnetic ($A^{\downarrow}[B^{\uparrow},B^{\uparrow}]$): M_{tot} = 3 μ_B , a = 8.107 Å, c = 9.610 Å				
GGA	0.78	0.52	- 4.13	3.48
GGA + U	1.37	2.42	- 4.51	3.79
mBJ	2.40	1.42	- 4.44	3.56
Ferrimagnetic ($A^{\uparrow}[B^{\downarrow},B^{\uparrow}]$): M_{tot} = 5 μ_B , a = 8.134 Å, c = 9.518 Å				
GGA	0.63	0.93	4.22	+/- 3.67
GGA + U	1.17	1.79	4.53	+/- 3.84
mBJ	1.62	2.45	4.49	+/- 3.65
Ferromagnetic ($A^{\uparrow}[B^{\uparrow},B^{\uparrow}]$): M_{tot} = 13 μ_B , a = 8.234 Å, c = 9.586 Å				
GGA	0.32	2.82	4.32	3.76
GGA + U	0.78	4.00		
mBJ	1.46	3.93	4.55	3.75
Experimental: M_{tot} = 1.85 – 1.89 μ_B [38, 39, 41] , a = 8.149 Å, c = 9.465 Å [28]				
	2.4 [46, 47]		4.64 [39]	3.55 [39]

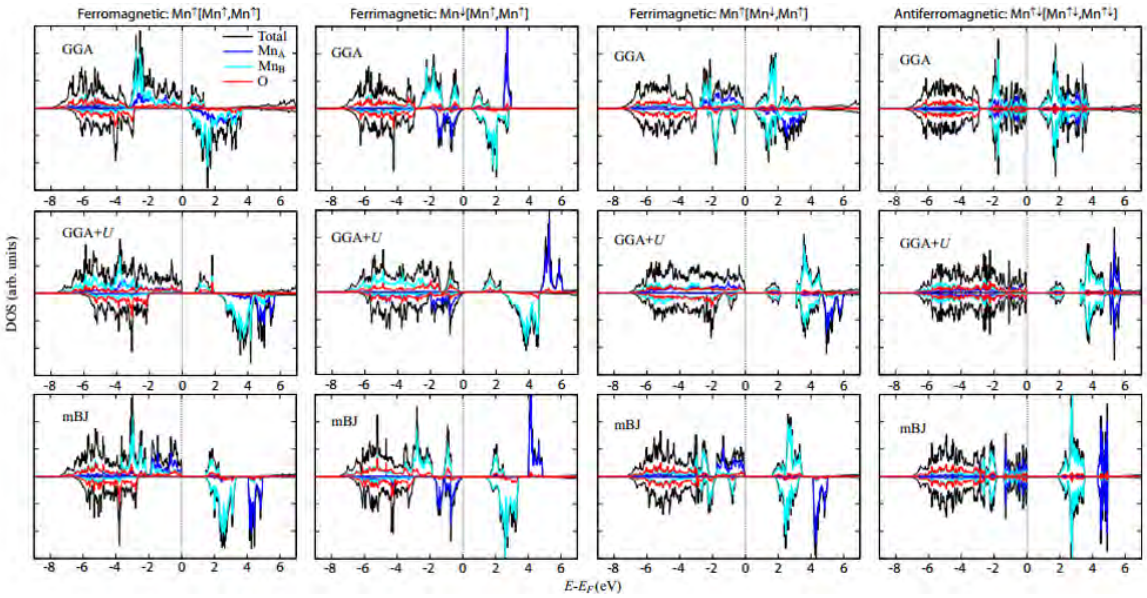

Figure III. 3: Spin-resolved DOS for Mn_3O_4 calculated with the 3 approximations and for 3 different magnetic ordering.

The calculated DOS are displayed in Figure III. 4. According to the mBJ calculations, the bands just below the Fermi level are built from the hybridization of $d(t_2)$ orbitals of Mn_A and $d(z^2)$ of Mn_B cations, and *p* orbitals of oxygen atoms, with, however, a noticeably higher contribution coming from the Mn_A ions, while the DOS present mainly a *d* character from the Mn_B atoms for the GGA. The conduction bands with the lowest energy have a clear $Mn_B(d)$ symmetry no matter what the approximation is.

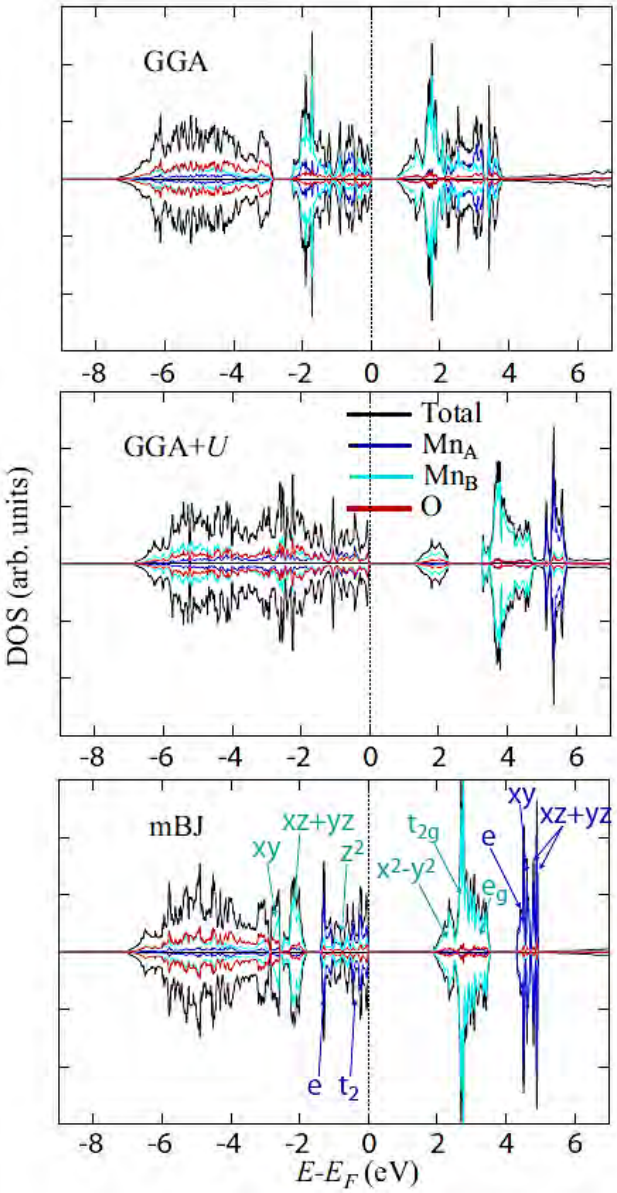

Figure III. 4: Spin-resolved DOS for Mn_3O_4 ($x = 3.0$) calculated with the 3 approximations and for an antiferromagnetic ordering.

According to the mBJ calculations, the top of the valence bands displays a main contribution coming from the Mn_A-t_2 orbitals, mixed with Mn_B-d_{z^2} orbitals (the energy range of which extends from E_F – 1.38 eV to E_F), while the bottom of the conduction band has a clear Mn_B-$d_{x^2-y^2}$ character. We thus found a first band gap of 1.92 eV between the top of the valence band and the bottom of the conduction band, and the energy difference to the bottom of the unoccupied bands of the Mn_A atoms is of 4.31 eV (Figure III. 5). These values are similar to that given by Hirai et al. (2015) of ≈ 1.43 eV and ≈ 3.41 eV using DFT+*U*, and 2.61 eV and 4.17 eV using HSE06 hybrid functional [4].

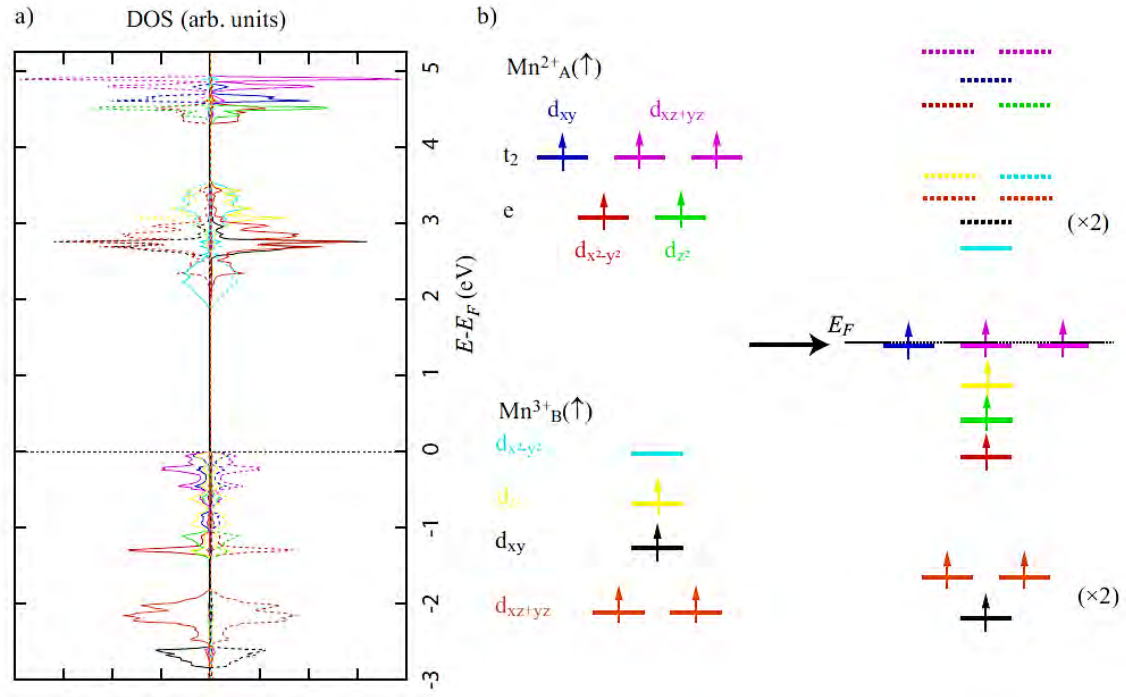

Figure III. 5: a) Spin-resolved Mn-d contribution to the DOS of Mn_3O_4, b) schematic representation of the electron distribution in the d orbitals for one spin direction.

Band gaps, magnetic moments and calculated lattice parameters are given in Table III. 1 for various magnetic configurations. The antiferromagnetic ordering brings to the closest lattice parameters and band gaps (although lower by 20 %), if compared to experimental measurements from the literature [46, 47]. However, the best fit for the total spin magnetic moment is obtained for the ferrimagnetic ordering with the $A^{\downarrow}[B^{\uparrow},B^{\uparrow}]$ configuration.

Although it does not correspond to the fundamental band gap, the band gap energy calculated for the majority spin electrons is still in agreement with values reported in the literature. For an easier understanding, this last case will be used as a reference in the next section.

III.2.3. $Mn_xCo_{3-x}O_4$

For our calculations, we considered 13 different supercells with a varying number x of Mn atoms substituted for Co in Co_3O_4. We first considered the substitution as occurring in the *B* sites, and then, once every Co_B was replaced by Mn atoms (for $x = 2.0$), every added Mn was set into the *A* sites, in accordance with our previous neutron diffraction measurements, Rietveld refinements and Bond Valence Sum calculations [28]. Apart from Co_3O_4, for which we considered an initial antiferromagnetic ordering, all the other calculations were performed using a ferrimagnetic arrangement with antiparallel alignment of spin magnetic moments of cations in *A* sites compared with those in B sites (i.e. $A^{\downarrow}[B^{\uparrow},B^{\uparrow}]$). This last choice will be justified in section **III.2.3.2**.

III.2.3.1. Atomic structures

The complete set of lattice parameters was calculated for all $Mn_xCo_{3-x}O_4$ compounds with the GGA approximation. The results are displayed in Figure III. 6 and compared with experimental data obtained by X-ray diffraction measurements on single phase sintered ceramics [28]. For the cell volume, calculated and experimental data are in agreement for the extremum compositions (i.e. $x = 0 – 0.25$ and $x = 3$). The volume increases almost linearly as a function of x (the average increase of the volume is 34 $Å^3$ per added Mn atoms per f.u.) and the calculated values only underestimate the experimental ones by at most 2.4 % for intermediate compositions.

Considering the lattice parameters, some discrepancies appear more clearly. For $x < 2.0$, the three calculated lattice parameters are very close, while the chosen cationic distribution can artificially break apart the symmetries, the lattice can be considered as cubic in this range of x values. The calculations predict a cubic ($a = b = c$) to tetragonal ($c > a = b$) transition from

$x > 2.0$, i.e. when all the occupied *B* sites are filled by Mn atoms and all the added atoms are thus placed into the *A* sites. If the transition was demonstrated to be correct, the critical composition at which it occurs is not consistent with the experiment: this transition has indeed been measured to happen from $x > 1.25$, and has been attributed to the presence of a sufficient amount (≥ 55 % of the occupied *B* sites, i.e. for $x > 1.25$ [28, 49]) of Mn_B^{3+}, with a d^4s^0 electronic structure, inducing a Jahn-Teller distortion. It is thus surprising that Mn_2CoO_4 (for which 100 % of the *B* sites are occupied by Mn atoms) is still found to be cubic by the calculations.

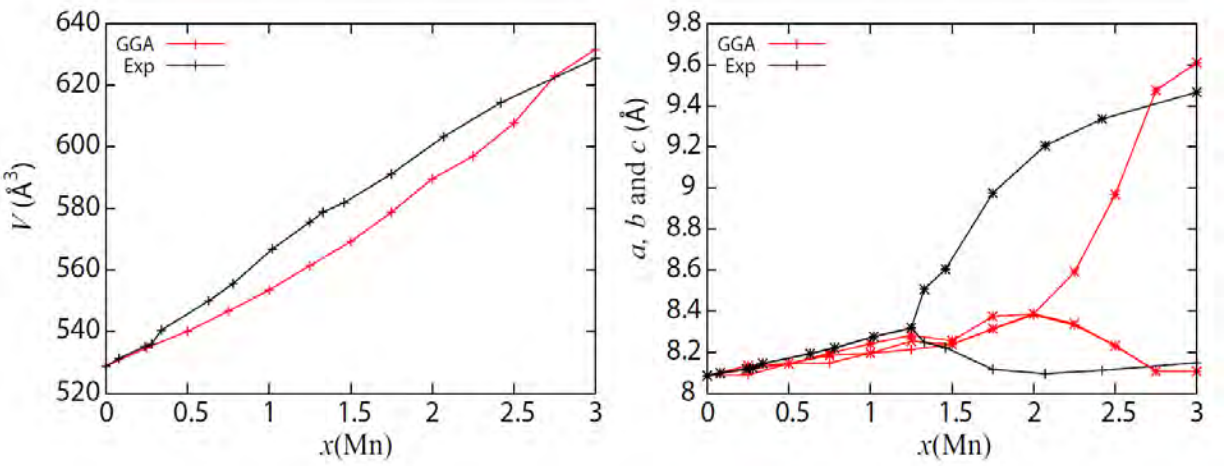

Figure III. 6: Calculated volume V and lattice parameters a (+), b (×) and c (∗) compared to the experimental values [28]. The results are given for a conventional cubic or tetragonal cell of 8 $Mn_xCo_{3-x}O_4$ formula units.

Because the transition only begins when additional Mn atoms are replacing Co atoms in *A* site, we verified that, besides the Jahn-Teller effect, the presence of Mn atoms in these *A* sites could not provide a complementary explanation. A calculation was then performed for $x = 1.0$, and with 1/4 of the Mn atoms swapped with the cobalt in the *A* sites. Again, a cubic structure was found, with a volume only slightly reduced by 1 % in comparison with the ideal case in which all the Mn atoms were in the *B* sites. According to these results, we can thus conclude that the presence of Mn_A sites is not the reason for the tetragonal distortion.

The total energy calculated for the structure with the swap defect was found to be 0.45 eV higher than for the ideal structure, which confirms the experimental cation distribution with a preferential location of Mn atoms in *B* sites.

The inability for GGA calculations to correctly reproduce the tetragonal shape of the lattice between $1.25 < x \leq 2$ can originate from the wrong description of the magnetism to which it is known to be intimately related, as discussed before in the case of Mn_3O_4 [43, 44].

The calculations only predict the cubic-to-tetragonal transition to happen when a critical value of the volume is reached due to a cell increase produced by the addition of Mn atoms in either *A* or *B* sites. This could explain the limit value of *x* calculated for the transition.

The GGA+*U* method has also been tried for the calculations of the lattice parameters, but we did not retain the results as they worsen the comparison with our experimental measurements. In that case, the shape of the structures was completely different and the volume tends to be overestimated (Figure III. 7). Other studies have already underlined the possibility of stabilising tetragonal or orthorhombic manganite spinel lattices by using different approximations [50]. Finally, the influence of the temperature should also be taken into account, as the current experimental data have been obtained at room temperature, whereas magnetic phases under consideration, as well as our calculations, are only considered at low temperatures.

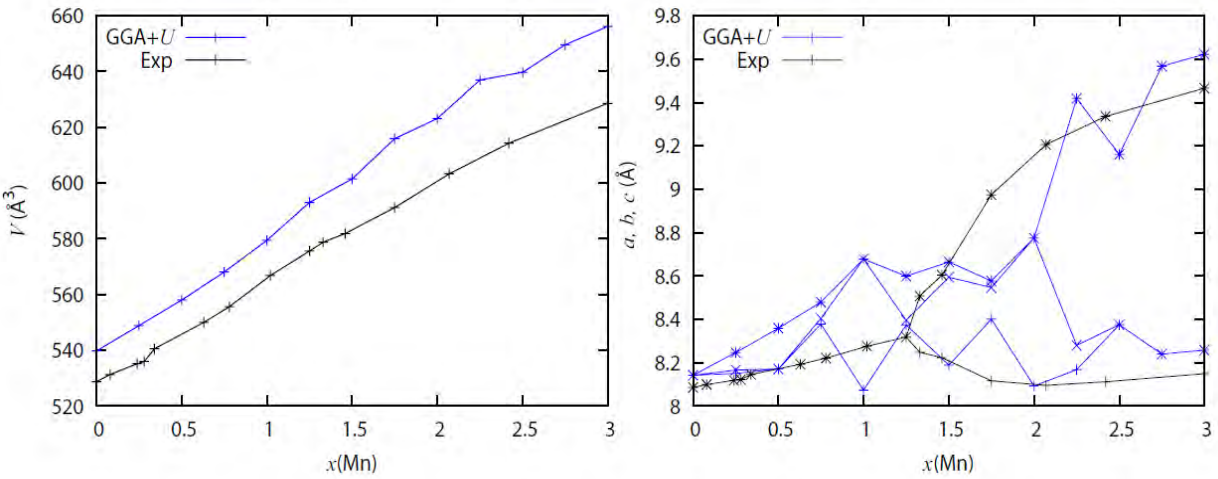

Figure III. 7: Comparison of the volume and lattice parameters of $Mn_xCo_{3-x}O_4$ calculated with the GGA+U method with the experimental measurements.

III.2.3.2. Magnetic properties

For the lowest non-zero concentration of Mn atoms (x = 0.25), the antiferromagnetic coupling between Co_A and Mn_B is sufficient to set up the ferrimagnetic ordering. We indeed mapped different magnetic ordering and found that this composition displays the lowest total energy. Moreover, we have checked that this ferrimagnetic ordering stays robust for high x values, i.e. x = 2.0 and 2.5, by comparing the total energy for the different magnetic states, similarly to the calculations done for Mn_3O_4. The obtained ferrimagnetic state is in agreement with experimental measurements [37, 51, 52], and also with recently published theoretical results obtained on similar compounds $Ni_xCo_{3-x}O_4$ [53].

As shown in Figure III. 8 and following the GGA calculations, the Co_B atoms merely present a low-spin state. From $x > 0.5$, these atoms begin however to be spin-polarized and adopt an intermediate spin state due to the presence of surrounding Mn_B atoms. The increase of the magnetic moments of Co_B is consistent also with an increase of the content and the spin moment of the Mn_B atoms. Such change in the magnetic moments can result from a charge reorganization at the orbital level inside each atom separately, due to their mutual influence, but can also be due to a charge transfer from Mn^{3+} to Co^{III} cations, with an increase and a decrease of the *d*-orbital occupancy, respectively, in agreement with experimental hypothesis given in several references [51, 54, 55]. For the mBJ calculations, performed using the GGA most stable initial magnetic configuration, the Co_B atoms present strictly a low spin state, with no spin-polarization, in the $0 \leq x < 2$ range. The magnetic moments of the different atoms stay approximately constant. On the contrary, with the GGA+*U* method, the spin polarization of the Co_B is more pronounced than with the GGA and the Co_B directly switch from the low-spin to the high-spin configuration for $x > 0.5$. This result certainly strongly depends on the relative strength of the electronic correlations, i.e. on the chosen value of the U_{eff} parameter, with the crystal field splitting. On the other hand, it is also important to keep in mind that the crystal field effect is directly related to the structure and can be enhanced by the tetragonal distortion of the lattice, which is not correctly taken into account in our calculations, for $1.25 \leq x \leq 2.0$.

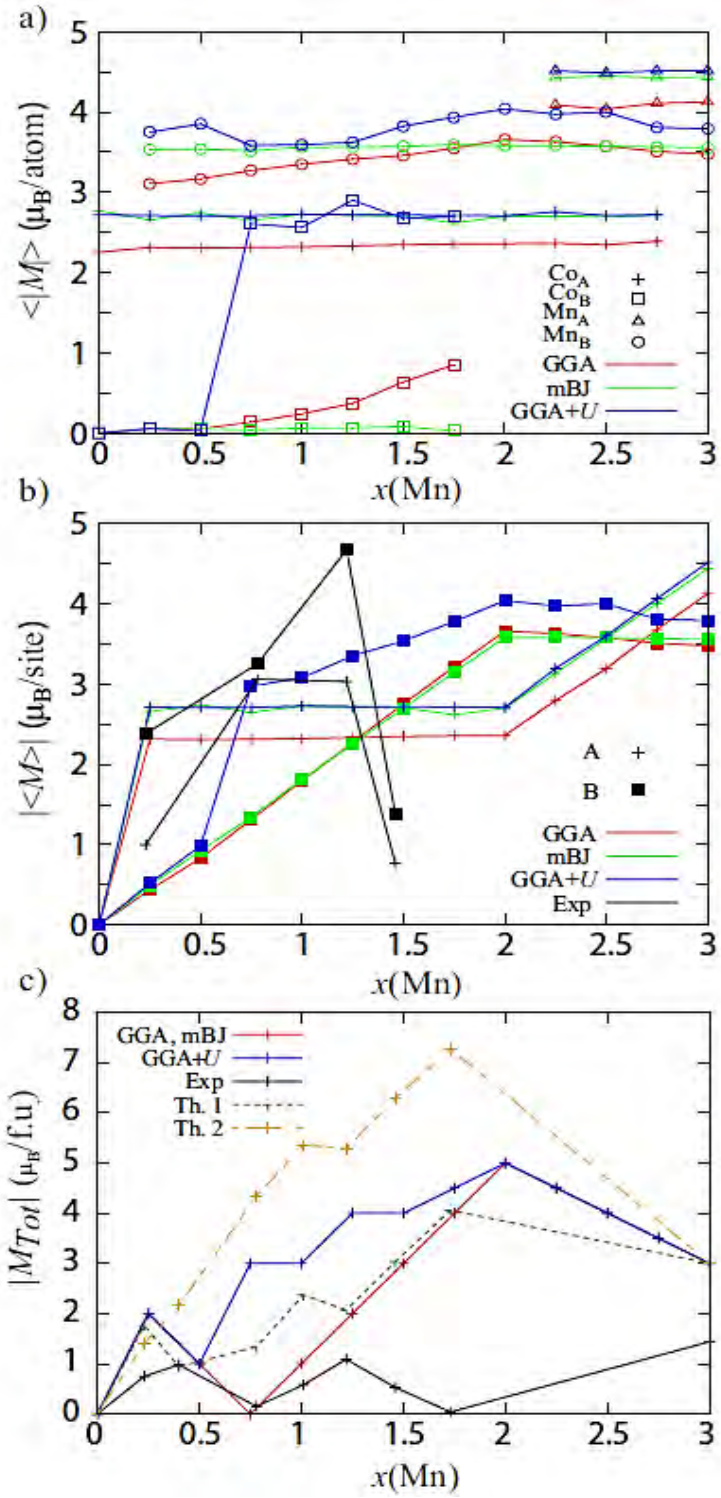

Figure III. 8: Variation of the spin magnetic moments as a function of the Mn concentration x in $Mn_xCo_{3-x}O_4$: a) average of the absolute value per atom and per atomic sites, b) absolute value of the average (Co + Mn atoms) per atomic sites, c) absolute value of the total magnetic moment per f.u., compared to the experimental values [52].

The experimental averaged magnetic moments per atomic site reported in Figure III. 8b were determined at 10 K by the neutron diffraction technique [52]. A complex behaviour is emphasized, being not correctly reproduced by our calculations, in particular for the GGA and mBJ calculations. The low magnetic moment at $x = 0.25$ tends to suggest that the Co_B atoms are still in a low- or intermediate-spin state, and that the Co_A moments are still arranged in a configuration close to the antiferromagnetic ordering. The ferrimagnetism (ferromagnetic alignment of the Co_A magnetic moments) is then set from $x = 0.75$, that is at a higher value of x than found by the calculations, and the Co_B atoms seem to switch to a high-spin state, in agreement with the GGA+*U* results. Then, the lowering of the magnetic moments for both type of cations at $x = 1.25$ is certainly due to the sufficiently high number of Mn atoms which induce a non-collinear ordering involving the *B* sub-lattice.

The calculated variation of the total magnetic moment is shown in Figure III. 8c. According to the GGA calculations, from $x = 0.25$ to 0.75, the direction of the total spin magnetic moment is governed by the magnetic moments of the Co_A and its value increases by 1 μ_B when x increases by 0.25. For $x = 0.75$, the sum of the magnetic moments of the Co_A is exactly equal to the sum of those for the Mn_B atoms (with an opposite sign), which corresponds to a total magnetic moment of 0 μ_B and to an inversion of its direction. For $x > 0.75$, the orientation of the total magnetic moment is then the same than the magnetic moments of the Mn_B cations. A progressive magnetic moment increase is observed until $x = 2.0$, when added Mn^{2+} cations replace Co_A^{2+}, which have a lower magnetic moment, thus inducing a decrease of the total magnetic moment of 0.5 μ_B per $x = 0.25$. The total magnetic moment calculated with the GGA+*U* adopts a higher value than with the GGA calculations for x varying from 0.5 to 1.75 due to the low-spin to high-spin transition.

The magnetization measurements described in Figure III. 8c (black curve) were performed at 5 K [52], well under the ordering temperature, in agreement with very early studies [37, 56]. The curve displays a similar behaviour than for the GGA and mBJ calculations for $x < 1.25$, even if the total magnetic moment value is significantly lower. Then we observed a decrease of the absolute value of the magnetization that takes place simultaneously with the experimentally observed tetragonal distortion of the lattice, for $x = 1.25$.

We also plotted two curves in Figure III. 8c that correspond to the theoretical magnetic moment variations (called Th.1 and Th.2) assuming a collinear magnetic model, that all the Co_B are in a low-spin state (Th.1) or in an averaged state between the low and the high spins (Th.2), and taking into account the oxidation degrees measured from Refs. [28] and [57]. GGA+*U* calculations display a similar tendency as the curves Th.1 and Th.2, but with an absolute value of the total magnetic moment intermediate between that of the two curves. The GGA calculations and the experimental measurements are however clearly different around $x = 0.75$. We can suggest from these observations that the presence of Co_B ions with a magnetic moment different from 0, due to a different oxidation degree or due to the transition toward an intermediate or a high-spin state is not so obvious.

The overall lower measured magnetization, in comparison with theoretical values, can be either attributed to structural defects which can't be avoided in such materials (antiphase boundaries, vacancies, interstitials, Frenkel pairs...), to size effects, and/or to deviations to the collinear magnetic ordering. Indeed, the moment decrease observed at $x = 1.25$ (and not reproduced by any of the theoretical models or calculations) can be due to a transition because of the large number of Mn_B cations, that can induce a new and more complex magnetic ordering, similarly for pure Mn_3O_4. Moreover, such magnetic transition is concomitant with the experimental tetragonal distortion, which is not correctly reproduced by our calculations.

III.2.3.3. Electronic structures

To illustrate the electronic structure calculated for the $Mn_xCo_{3-x}O_4$ materials, two sets of DOS calculated with the three approximations described earlier are shown in Figure III. 9, for $x = 1$ and 2.5, i.e. for the *B* and *A* sites filled by an equal amount of Co and Mn atoms respectively (see, for instance also, the complete set of DOS generated with the mBJ calculations in Figure III. 10). As for pure Co_3O_4 and Mn_3O_4, the GGA+*U* approximation increases the band gap around the Fermi energy, compared to the GGA calculations, by shifting the *d* band energies of the cations, which inevitably induces more overlapping between the cation and oxygen orbitals (originally lying at lower energy) and increases the cation-anion and cation-cation hybridizations. On the contrary, the mBJ calculations result in a net separation of the cations *d* bands and oxygen *p* bands. This is consistent with the fact that the Co_B do not spin

polarize under the magnetic influence of the Mn atoms and that every magnetic moment remains constant as a function of *x*. This result is also in agreement with a constant oxidation degree for each cation, i.e. Co_A^{2+} (d^7s^0), Mn_A^{2+} (d^5s^0), Co_B^{III} (d^6s^0) and Mn_B^{3+} (d^4s^0).

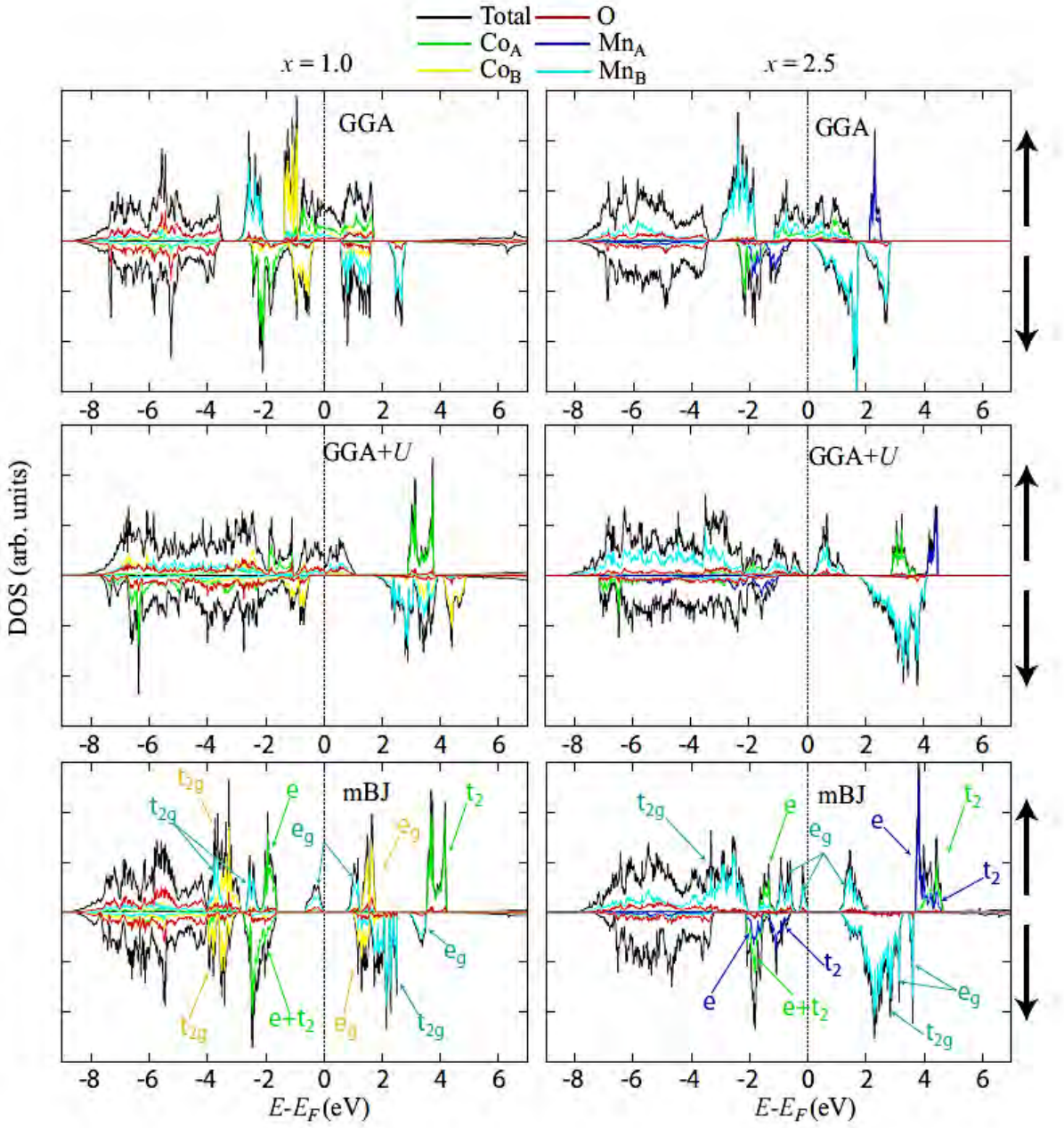

Figure III. 9: Spin-resolved DOS for the $MnCo_2O_4$ (left) and $Mn_{2.5}Co_{0.5}O_4$ (right) determined by GGA, GGA+U and mBJ calculations.

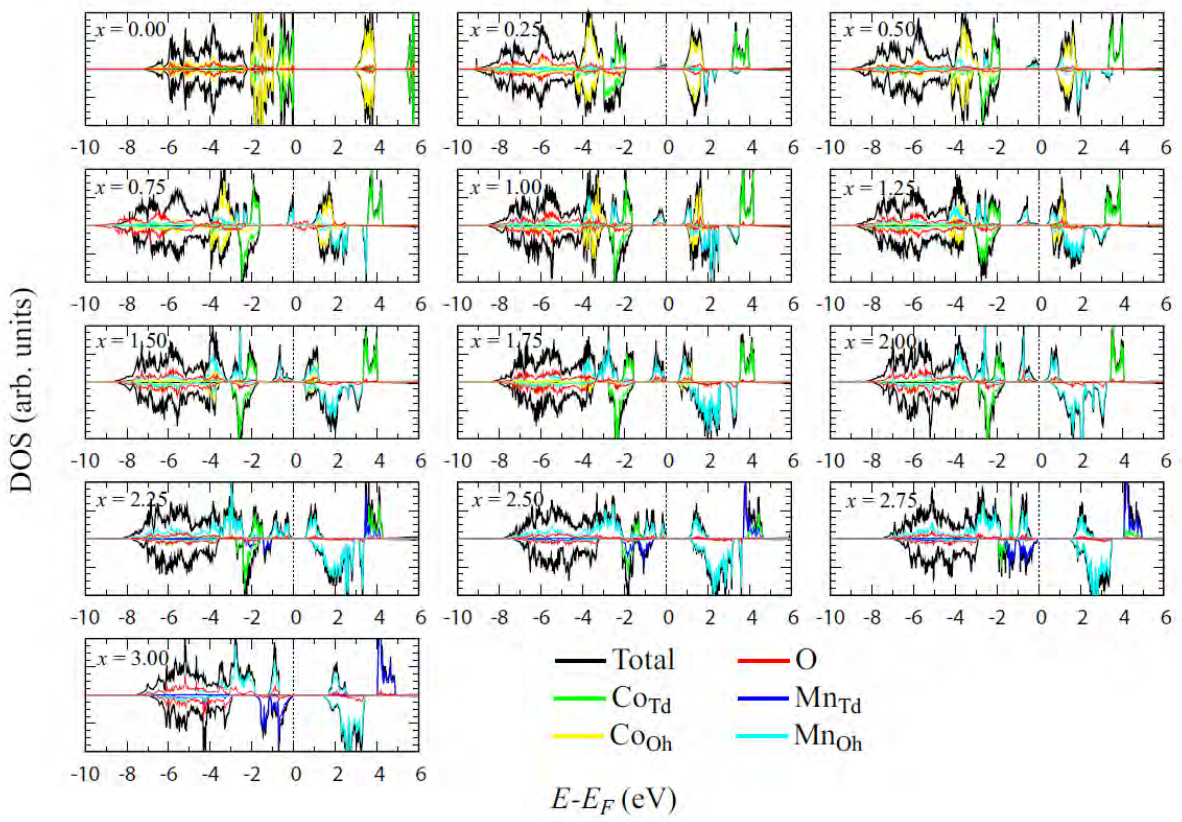

Figure III. 10: Spin-resolved DOS for $Mn_xCo_{3-x}O_4$ ($0 \leq x \leq 3$) calculated by the mBJ method.

The variation of the electronic structure calculated in mBJ as a function of the composition is given in Figure III. 11. A schematic representation of the main atomic contributions to the electronic structure (Figure III. 11a) and the energy differences ΔE between the top of the occupied bands (composed of O-*p*, (Mn, Co)$_A$-*d* or [Mn, Co]$_B$-*d*) and the bottom of the unoccupied bands (constituted of (Mn, Co)$_A$-*d* or [Mn, Co]$_B$-*d*) are also detailed (Figure III. 11b). All of this data has been directly extracted from the DOS [48]. The up and down directions for the spin of the electrons are defined by the up and down arrows (↑,↓) respectively, which can either correspond to minority or majority spin directions, depending on the *x* concentration of Mn ions. For an easier comparison of the electronic structure evolution, the magnetic moments of the *B*-site atoms are always chosen parallel to ↑, while the magnetic moments of *A* atoms are parallel to ↓, therefore the total magnetic moment will then be parallel to the ↓ direction for $0 < x < 0.75$ and to the ↑ direction for $0.75 < x < 3.0$.

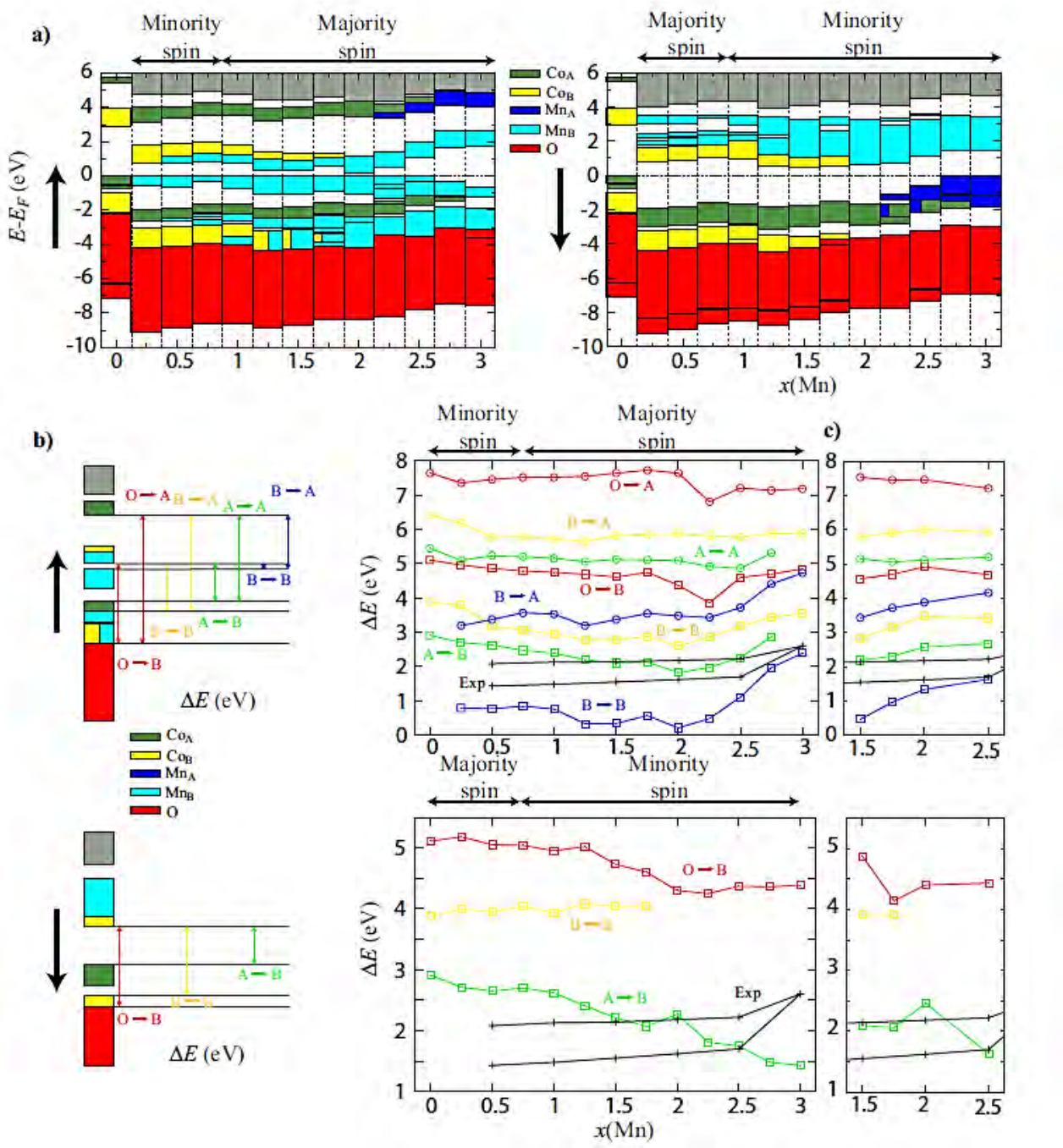

Figure III. 11: a) Schematic representation of the band distributions as calculated with the mBJ approximation and for a ferrimagnetic ordering (except for antiferromagnetic Co_3O_4). b) Calculated energy differences ΔE, which may correspond to optical transition, as a function of x and obtained using calculated lattice parameters (experimental data are taken from Ref. [58] and [59]), and c) using the experimental tetragonal lattice parameters.

Also, all calculations show a strong decrease of the fundamental band gap compared to the two end members Co_3O_4 and Mn_3O_4, with a more pronounced effect for the GGA and GGA+*U* approximations that tends to describe a half-metallic character for any $Mn_xCo_{3-x}O_4$ compounds with $x \neq 0$ and 3 (Figure III. 12). Similar results have been reported on $Ni_xCo_{3-x}O_4$ by Shi et al. (2016) [53].

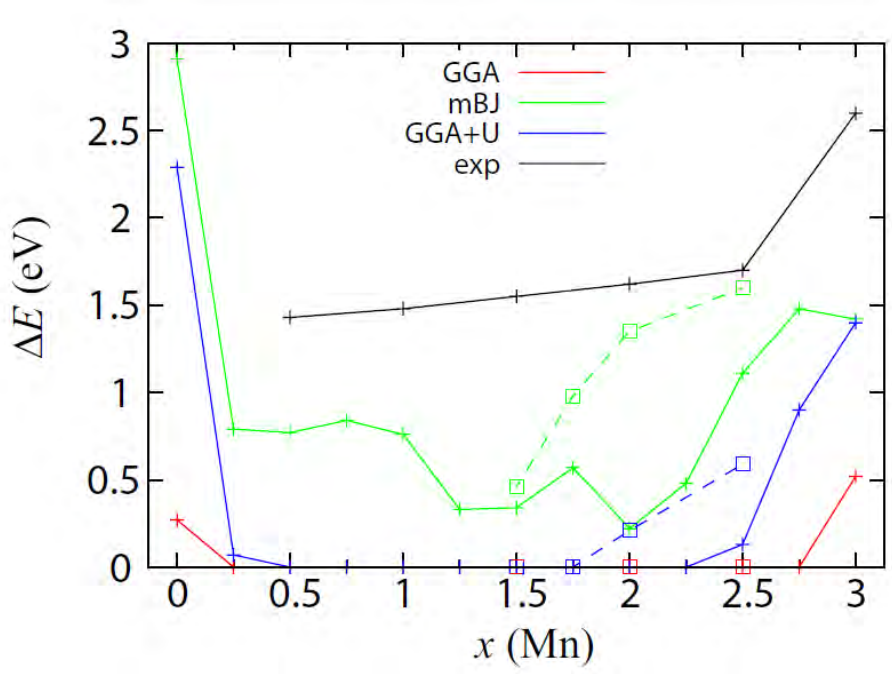

Figure III. 12: Band gap energy as a function of x. Solid lines with + symbols correspond to values obtained with the calculated lattice parameters, while dashed lines with □ symbols are the values calculated with the experimental lattice parameters.

The mBJ calculated fundamental band gap corresponds to the energy separation between the occupied and unoccupied e_g bands (d_{z^2} and $d_{x^2-y^2}$, respectively) of Mn_B atoms, for $0.25 \leq x \leq 3$. Therefore, introducing a small fraction of Mn in Co_3O_4 will directly induce a large decrease of the band gap value (of 73 % from $x = 0$ to $x = 0.25$ according to the mBJ calculations), by strongly lowering the occupied d-bands energies of the Co atoms for the ↑-spin configuration. Between $x = 0.25$ and $x = 2$, the band gap, calculated with the mBJ method, varies from ≈ 0.2 to 0.8 eV, while $Mn_xCo_{3-x}O_4$ becomes half-metallic with the GGA and GGA+*U* methods. The band gap then increases almost linearly from $x = 2$ to 3, when the tetragonal distortion is set. The non-zero DOS at the Fermi level could be indicative of the

simultaneous presence of Mn^{3+} and Mn^{4+} in the *B* sites and of the conductivity setting by a double-exchange mechanism. According to the mBJ calculated band gap, only a small excitation energy would be necessary to activate such process.

Occupied *d*-bands of the Co_A atoms for the ↑-spin configuration are located between the e_g bands of the Mn_B atoms and the t_{2g} bands of the Co_B or Mn_B. This can be associated with the presence of intermediate bands as suggested in the literature [5, 58]. However, we find that only the e_g bands of the Mn_B strongly contribute to the band gap width.

The two sets of experimental optical band gaps determined at the CIRIMAT [58], reported in Figure III. 11b for comparison with our calculated values, should then correspond to transitions between *d* bands of cations in *A* sites toward cations in *B* sites ($A \rightarrow B$ with green curve) for the lowest experimental values, and from *B* sites to *B* sites ($B \rightarrow B$ with the yellow curve) for the highest values, all with the ↑-spin, although the highest band gap corresponding to the absorption peak in the UV-VIS region is usually admitted to be related to $O \rightarrow B$ transitions. Transition from *A* to *B* sites for the minority spin between $x = 1.5$ and $x = 2.5$ are also in the good range of energies. It is also important to note that the fundamental band gap (corresponding, for each compound, to the lowest value between the $B \rightarrow B$ transition with the blue curve in the top panel of Figure III. 11b, and the $A \rightarrow B$ green curve of the bottom panel) is still much lower than the energy gap values determined experimentally, which can be explained by the fact that such energy range is not usually explored experimentally. Qiao et al. (2015) have recently evidenced a fundamental band gap of ≈ 0.74 eV for Co_3O_4 [6], far smaller than that the generally accepted values, originating from a direct dipole-forbidden *d-d* transition between Co^{2+} ions in tetrahedral sites. For a very low value of *x*, we can also expect that the electronic states of the Mn_B atoms are too localized to be mapped experimentally.

Finally, ΔE corresponding to possible electronic transitions in the $1.5 \leq x \leq 2.5$ range, obtained from electronic structure calculations performed by using the experimental lattice parameters [28], i.e. with a higher tetragonal distortion, are shown in Figure III. 11c. This data clearly shows that the tetragonal distortion of the lattice, related to the Jahn-Teller effect, induces a significant increase of the band gap values, while they still remain lower than the measured experimental values. Such increase is similar to the one determined with the calculated lattice parameters, for $2 \leq x \leq 3$, and goes along with a small shift toward higher

energies of the bands, which are the closest from the Fermi level, for the majority spin electrons. But further theoretical and experimental works need to be done in order to have a better understanding of the structural, electric and magnetic properties of such complex oxide materials.

III.3. Conclusion

The electronic band structure, cell parameters and magnetic characteristics of $Mn_xCo_{3-x}O_4$ ($0 \leq x \leq 3$) were determined for the first time over the whole solid solution range thanks to ab-initio DFT-based calculations and compared with experimental data.

Our results are in accordance with those reported in the literature for the pure end member compounds Co_3O_4 ($x = 0$) and Mn_3O_4 ($x = 3$). The main properties of the antiferromagnetic Co_3O_4 are quite well reproduced even if an uncertainty can remain regarding the band gap value which could be lower (≈ 0.8 eV) than that we calculated using the mBJ calculations (≈ 2.91 eV). The case of Mn_3O_4 is more complicated as this compound displays a complex ferrimagnetic ordering at low temperature, which can be described with collinear magnetism calculations by different magnetic states with a close total energy. We found that the most stable solution corresponds to a full antiferromagnetic ordering, with a band gap of 1.92 eV.

The interpretation of the calculated results, which strongly depends on the used methods and parameters, can be harder for the intermediate compounds ($0 < x < 3$), due to the complexity of the cation distribution and oxidation states possible for the cubic and tetragonal phases. However, our calculations give a cubic-to-tetragonal distortion of the lattice when increasing x. This transition is however predicted at $x > 2.0$, instead of $x > 1.25$ from the experimental data, which is not consistent with the usual Jahn-Teller effect description. Several inter-correlated contributions can be suggested to explain such difference, as a lower calculated volume and a wrong description of the electron correlation effects or a complex non-collinear magnetic ordering.

All intermediate compositional materials are ferrimagnetic, with cations in *A* sites having spin magnetic moments antiparallel to those in *B* sites, in agreement with experimental

studies. However, this ferrimagnetic ordering is certainly non-collinear, and might become more complicated to describe as the Mn content increases in *B* sites. In addition, the potential presence of structural defects could partly explain the lower experimental magnetization and its decrease measured for $x \geq 1.25$. Co_B^{III} cations are always found in a low-spin state for $0 \leq x < 2$ with the mBJ calculations, while the GGA+*U* method predicts a transition toward a high-spin state for $x > 0.5$. Monte-Carlo calculations could be envisaged in order to take into account the highly complex magnetic ordering, as well as the temperature effect, and shall conduct to the ordering temperature determination.

The electronic and band structures of the cobalt and manganese spinel oxide materials were also determined. The band gap is strongly decreased upon doping of the pure end members of the Mn_3O_4-Co_3O_4 spinel family, which can be explained by the lowest band gap always found between the split e_g bands (d_{z^2} for the occupied band, and $d_{x^2-y^2}$ for the unoccupied bands). Such band gap is barely mentioned in the literature based on experimental studies, but mainly because of the restricted measurement range areas. It is supposed to have a value of ~ 0.5 eV for the cubic phase, and a higher value, up to ≈ 1.5 eV, for the tetragonal phase. This transition would be related to cation-cation transitions with an up-spin direction in octahedral sites.

III.4. References

[1] A. Chartier, P. D'Arco, R. Dovesi, and V. R. Saunders, "*Ab initio Hartree-Fock investigation of the structural, electronic, and magnetic properties of Mn3O4*," **Physical Review B,** Vol. **60**, 14042-14048, **1999**.

[2] C. Franchini, R. Podloucky, J. Paier, M. Marsman, and G. Kresse, "*Ground-state properties of multivalent manganese oxides: Density functional and hybrid density functional calculations*," **Physical Review B,** Vol. **75**, 195128, **2007**.

[3] R. Kaur, T. Maitra, and T. Nautiyal, "*Study of structural and electronic properties of Mn3O4*," **AIP Conference Proceedings,** Vol. **1591**, 1137-1139, **2014**.

[4] S. Hirai, Y. Goto, Y. Sakai, A. Wakatsuki, Y. Kamihara, and M. Matoba, "*The Electronic Structure of Structurally Strained Mn3O4 Postspinel and the Relationship with Mn3O4 Spinel*," **Journal of the Physical Society of Japan,** Vol. **84**, 114702, **2015**.

[5] S. Thota, A. Kumar, and J. Kumar, "*Optical, electrical and magnetic properties of Co3O4 nanocrystallites obtained by thermal decomposition of sol–gel derived oxalates*," **Materials Science and Engineering B,** Vol. **164**, 30-37, **2009**.

[6] L. Qiao, H. Y. Xiao, H. M. Meyer, J. N. Sun, C. M. Rouleau, A. A. Puretzky, *et al.*, "*Nature of the band gap and origin of the electro-/photo-activity of Co3O4*," **Journal of Materials Chemistry C,** Vol. **1**, 4628-4633, **2013**.

[7] K. J. Kormondy, A. B. Posadas, A. Slepko, A. Dhamdhere, D. J. Smith, K. N. Mitchell, *et al.*, "*Epitaxy of polar semiconductor Co3O4 (110): Growth, structure, and characterization*," **Journal of Applied Physics,** Vol. **115**, 243708, **2014**.

[8] J. Chen, X. Wu, and A. Selloni, "*Electronic structure and bonding properties of cobalt oxide in the spinel structure*," **Physical Review B,** Vol. **83**, 245204, **2011**.

[9] V. Singh, M. Kosa, K. Majhi, and D. T. Major, "*Putting DFT to the Test: A First-Principles Study of Electronic, Magnetic, and Optical Properties of Co3O4*," **Journal of Chemical Theory and Computation,** Vol. **11**, 64-72, **2015**.

[10] V. Singh and D. T. Major, "*Electronic Structure and Bonding in Co-Based Single and Mixed Valence Oxides: A Quantum Chemical Perspective*," **Inorganic Chemistry,** Vol. **55**, 3307-3315, **2016**.

[11] A. F. Lima, "*Interpretation of the optical absorption spectrum of Co3O4 with normal spinel structure from first principles calculations*," **Journal of Physics and Chemistry of Solids,** Vol. **75**, 148-152, **2014**.

[12] X.-L. Xu, Z.-H. Chen, Y. Li, W.-K. Chen, and J.-Q. Li, "*Bulk and surface properties of spinel Co3O4 by density functional calculations*," **Surface Science,** Vol. **603**, 653-658, **2009**.

[13] X.-Y. Pang, C. Liu, D.-C. Li, C.-Q. Lv, and G.-C. Wang "*Structure Sensitivity of CO Oxidation on Co3O4: A DFT Study*," **ChemPhysChem,** Vol. **14**, 204-212, **2013**.

[14] J. Chen and A. Selloni, "*Electronic states and magnetic structure at the Co3O4(110) surface: A first-principles study*," **Physical Review B,** Vol. **85**, 085306, **2012**.

[15] L. Cun-Qin, L. Chang, and W. Gui-Chang, "*A DFT study of methanol oxidation on Co3O4*," **Catalysis Communications,** Vol. **45**, 83-90, **2014**.

[16] P. S. Arun, B. P. Ranjith, and S. M. A. Shibli, "*Control of Carbon Monoxide (CO) from Automobile Exhaust by a Dealuminated Zeolite Supported Regenerative MnCo2O4 Catalyst*," **Environmental Science & Technology,** Vol. **47**, 2746-2753, **2013**.

[17] F. Zasada, J. Gryboś, P. Indyka, W. Piskorz, J. Kaczmarczyk, and Z. Sojka, "*Surface Structure and Morphology of M[CoM']O4 (M = Mg, Zn, Fe, Co and M' = Ni, Al, Mn, Co) Spinel Nanocrystals—DFT+U and TEM Screening Investigations*," **The Journal of Physical Chemistry C,** Vol. **118**, 19085-19097, **2014**.

[18] Y. Li, M. S. Wu, and C. Y. Ouyang, "*The structural and electronic properties of spinel MnCo2O4 bulk and low-index surfaces: From first principles studies*," **Applied Surface Science,** Vol. **349**, 510-515, **2015**.

[19] G. Kresse and J. Hafner, "*Ab initio molecular-dynamics simulation of the liquid-metal–amorphous-semiconductor transition in germanium*," **Physical Review B,** Vol. **49**, 14251-14269, **1994**.

[20] G. Kresse and J. Furthmüller, "*Efficient iterative schemes for ab initio total-energy calculations using a plane-wave basis set*," **Physical Review B,** Vol. **54**, 11169-11186, **1996**.

[21] H. J. Monkhorst and J. D. Pack, "*Special points for Brillouin-zone integrations*," **Physical Review B,** Vol. **13**, 5188-5192, **1976**.

[22] J. P. Perdew, K. Burke, and M. Ernzerhof, "*Generalized Gradient Approximation Made Simple*," **Physical Review Letters,** Vol. **77**, 3865-3868, **1996**.

[23] A. D. Becke and E. R. Johnson, "*A simple effective potential for exchange*," **The Journal of Chemical Physics,** Vol. **124**, 221101, **2006**.

[24] F. Tran and P. Blaha, "*Accurate Band Gaps of Semiconductors and Insulators with a Semilocal Exchange-Correlation Potential*," **Physical Review Letters,** Vol. **102**, 226401, **2009**.

[25] V. I. Anisimov, I. V. Solovyev, M. A. Korotin, M. T. Czyżyk, and G. A. Sawatzky, "*Density-functional theory and NiO photoemission spectra*," **Physical Review B,** Vol. **48**, 16929-16934, **1993**.

[26] S. L. Dudarev, G. A. Botton, S. Y. Savrasov, C. J. Humphreys, and A. P. Sutton, "*Electron-energy-loss spectra and the structural stability of nickel oxide: An LSDA+U study*," **Physical Review B,** Vol. **57**, 1505-1509, **1998**.

[27] D. Koller, F. Tran, and P. Blaha, "*Merits and limits of the modified Becke-Johnson exchange potential*," **Physical Review B,** Vol. **83**, 195134, **2011**.

[28] H. Bordeneuve, C. Tenailleau, S. Guillemet-Fritsch, R. Smith, E. Suard, and A. Rousset, "*Structural variations and cation distributions in Mn3−xCoxO4 (0≤ x ≤3) dense ceramics using neutron diffraction data*," **Solid State Sciences,** Vol. **12**, 379-386, **2010**.

[29] W. L. Roth, "*Magnetic properties of normal spinels with only a-a interactions*," **Journal de Physique,** Vol. **25**, 507-515, **1964**.

[30] W. L. Roth, "*The magnetic structure of Co3O4*," **Journal of Physics and Chemistry of Solids,** Vol. **25**, 1-10, **1964**.

[31] P. H. T. Ngamou and N. Bahlawane, "*Influence of the Arrangement of the Octahedrally Coordinated Trivalent Cobalt Cations on the Electrical Charge Transport and Surface Reactivity*," **Chemistry of Materials,** Vol. **22**, 4158-4165, **2010**.

[32] K. J. Kim and Y. R. Park, "*Optical investigation of charge-transfer transitions in spinel Co3O4*," **Solid State Communications,** Vol. **127**, 25-28, **2003**.

[33] X. Wang, X. Chen, L. Gao, H. Zheng, Z. Zhang, and Y. Qian, "*One-Dimensional Arrays of Co3O4 Nanoparticles: Synthesis, Characterization, and Optical and Electrochemical Properties*," **The Journal of Physical Chemistry B,** Vol. **108**, 16401-16404, **2004**.

[34] A. Gasparotto, D. Barreca, D. Bekermann, A. Devi, R. A. Fischer, P. Fornasiero, *et al.*, "*F-Doped Co3O4 Photocatalysts for Sustainable H2 Generation from Water/Ethanol*," **Journal of the American Chemical Society,** Vol. **133**, 19362-19365, **2011**.

[35] W. E. Pickett, S. C. Erwin, and E. C. Ethridge, "*Reformulation of the LDA+U method for a local-orbital basis*," **Physical Review B,** Vol. **58**, 1201-1209, **1998**.

[36] V. Baron, J. Gutzmer, H. Rundlof, and T. R., "*The influence of iron substitution in the magnetic properties of hausmannite, Mn (super 2+) (Fe, Mn) (super 3+)2O4*," **American Mineralogist,** Vol. **83**, 786-793, **1998**.

[37] B. Boucher, R. Buhl, R. D. Bella, and M. Perrin, "*Etude par des mesures de diffraction de neutrons et de magnétisme des propriétés cristallines et magnétiques de composés cubiques spinelles Co3-xMnxO4 (0,6 ~ x ~ 1,2)*," **Le Journal De Physique,** Vol. **31**, 113-119, **1970**.

[38] K. Dwight and N. Menyuk, "*Magnetic Properties of Mn3O4 and the Canted Spin Problem*," **Physical Review,** Vol. **119**, 1470-1479, **1960**.

[39] B. Boucher, R. Buhl, and M. Perrin, "*Proprietes et structure magnetique de Mn3O4*," **Journal of Physics and Chemistry of Solids,** Vol. **32**, 2429-2437, **1971**.

[40] G. B. Jensen and O. V. Nielsen, "*The magnetic structure of Mn 3 O 4 Hausmannite between 4.7K and Neel point, 41K*," **Journal of Physics C: Solid State Physics,** Vol. **7**, 409, **1974**.

[41] G. Srinivasan and M. S. Seehra, "*Magnetic properties of Mn3O4 and a solution of the canted-spin problem*," **Physical Review B,** Vol. **28**, 1-7, **1983**.

[42] B. Chardon and F. Vigneron, "*Mn3O4 commensurate and incommensurate magnetic structures*," **Journal of Magnetism and Magnetic Materials,** Vol. **58**, 128-134, **1986**.

[43] M. Kim, X. M. Chen, X. Wang, C. S. Nelson, R. Budakian, P. Abbamonte, *et al.*, "*Pressure and field tuning the magnetostructural phases of Mn3O4: Raman scattering and x-ray diffraction studies*," **Physical Review B,** Vol. **84**, 174424, **2011**.

[44] M. C. Kemei, J. K. Harada, R. Seshadri, and M. R. Suchomel, "*Structural change and phase coexistence upon magnetic ordering in the magnetodielectric spinel Mn3O4*," **Physical Review B,** Vol. **90**, 064418, **2014**.

[45] L. Ren, S. Wu, M. Yang, W. Zhou, and S. Li, "*Magnetic properties of Mn3O4 film under compressive stress grown on MgAl2O4 (001) by molecular beam epitaxy*," **Journal of Applied Physics,** Vol. **114**, 053907, **2013**.

[46] H. Y. Xu, S. L. Xu, X. D. Li, H. Wang, and H. Yan, "*Chemical bath deposition of hausmannite Mn3O4 thin films*," **Applied Surface Science,** Vol. **252**, 4091-4096, **2006**.

[47] D. P. Dubal, D. S. Dhawale, R. R. Salunkhe, S. M. Pawar, and C. D. Lokhande, "*A novel chemical synthesis and characterization of Mn3O4 thin films for supercapacitor application*," **Applied Surface Science,** Vol. **256**, 4411-4416, **2010**.

[48] N. M. Hosny and A. Dahshan, "*Facile synthesis and optical band gap calculation of Mn3O4 nanoparticles*," **Materials Chemistry and Physics,** Vol. **137**, 637-643, **2012**.

[49] N. Baffier and M. Huber, "*Etude par diffraction des rayons X et des neutrons, des relations entre distribution cationique et distorsion cristalline dans les ferro-manganites spinelles: xMn3O4 + (1 − x) Cu(Fe,Cr)2O4*," **Journal of Physics and Chemistry of Solids,** Vol. **33**, 737-747, **1972**.

[50] G. Singh, S. L. Gupta, R. Prasad, S. Auluck, R. Gupta, and A. Sil, "*Suppression of Jahn–Teller distortion by chromium and magnesium doping in spinel LiMn2O4: A first-principles study using GGA and GGA+U*," **Journal of Physics and Chemistry of Solids,** Vol. **70**, 1200-1206, **2009**.

[51] H. T. Zhang and X. H. Chen, "*Size-dependent x-ray photoelectron spectroscopy and complex magnetic properties of CoMn 2 O 4 spinel nanocrystals*," **Nanotechnology,** Vol. **17**, 1384, **2006**.

[52] S. Guillemet-Fritsch, C. Tenailleau, H. Bordeneuve, and A. Rousset, "*Magnetic properties of cobalt and manganese oxide spinel ceramics*," **Advances in Science and Technology,** Vol. **67**, 143-148, **2010**.

[53] X. Shi, S. L. Bernasek, and A. Selloni, "*Formation, Electronic Structure, and Defects of Ni Substituted Spinel Cobalt Oxide: a DFT+U Study*," **The Journal of Physical Chemistry C,** Vol. **120**, 14892-14898, **2016**.

[54] H. Liu, X. Zhu, M. Li, Q. Tang, G. Sun, and W. Yang, "*Single Crystal (Mn,Co)3O4 Octahedra for Highly Efficient Oxygen Reduction Reactions*," **Electrochimica Acta,** Vol. **144**, 31-41, **2014**.

[55] A. Rousset, C. Tenailleau, P. Dufour, H. Bordeneuve, I. Pasquet, S. Guillemet-Fritsch, *et al.*, "*Electrical Properties of Mn3−xCoxO4 ($0 \leq x \leq 3$) Ceramics: An Interesting System for Negative Temperature Coefficient Thermistors*," **International Journal of Applied Ceramic Technology,** Vol. **10**, 175-185, **2013**.

[56] D. G. Wickham and W. J. Croft, "*Crystallographic and magnetic properties of several spinels containing trivalent ja-1044 manganese*," **Journal of Physics and Chemistry of Solids,** Vol. **7**, 351-360, **1958**.

[57] H. Bordeneuve, "*Etude du système $Mn_{3-x}Co_xO_4$ ($0 \leq x \leq 3$) sous forme de poudres et de céramiques. Structure, microstructure, propriétés magnétiques et électriques. Applications aux thermistances à coefficient de température négatif*," Science et Génie des Matériaux, **Université de Toulouse III - Paul Sabatier**, **2010**.

[58] G. Salek, P. Dufour, S. Guillemet-Fritsch, and C. Tenailleau, "*Sustainable low temperature preparation of Mn3−xCoxO4 ($0 \leq x \leq 3$) spinel oxide colloidal dispersions used for solar absorber thin films*," **Materials Chemistry and Physics,** Vol. **162**, 252-262, **2015**.

[59] G. Salek, "*Elaboration et caractérisation de films minces absorbants de lumière à partir de dispersions colloïdales de nanoparticules d'oxydes Mn3-xCoxO4 ($0 \leq x \leq 3$) et Cu2O*," Doctor, Science et Génie des Matériaux, **Université de Toulouse III - Paul Sabatier**, **2013**.

CHAPTER IV

SYNTHESIS AND CHARACTERIZATION OF POWDERS AND THIN FILMS OF SPINEL OXIDES $M_xCo_{2-x}MnO_4$ (M = Ni, Cu, Zn; x = 0, 0.15, 0.30, 0.60)

IV.1. Introduction

The preparation and characterization of the powders and thin films of spinel oxides based Co_2MnO_4 doped with Ni, Cu or Zn are presented in this chapter. In a previous study on dense ceramics, the single cubic phase Co_2MnO_4 indeed showed the highest electrical conductivity among the whole range of the Mn_3O_4 – Co_3O_4 solid solutions [1]. In addition, the preparation of stoichiometric samples of $M_xCo_{2-x}MnO_4$ were aimed for, in order to primarily check that substitution can occur on both crystallographic sites and determine their influence over the physical (optical and electrical) properties of thin layers. Toh et al. (2015) investigated different substitutions of Ni and Zn for cobalt and manganese in the spinel oxide structure. $NiCo_2O_4$ and $ZnCo_2O_4$ exhibit a lower resistivity than that of $NiMn_2O_4$ and $ZnMn_2O_4$ [2]. Transition metals such as Ni, Cu and Zn are already used as dopants in cobalt-based spinel oxides for many applications including gas sensors, anode material for lithium ion batteries and capacitors. Different methods have been used to prepare spinel oxides powders of various compositions. Zhang et al. (2006) prepared nanotubes of MCo_2O_4 (M = Ni, Cu, Zn) spinel oxides using a porous alumina-template method for gas sensors application with excellent selectivity and high sensitivity to various gases [3]. Spinel type $ZnCo_2O_4$ was obtained by decomposition of the oxalate precursor [4]. $NiCo_2O_4$ was elaborated by solvothermal method followed by pyrolysis of the $Ni_{0.33}Co_{0.76}CO_3$ precursor [5]. $CuCo_2O_4$ was synthesized via a nanocasting strategy using mesoporous silica KIT-6 as the hard template [6]. All of these spinel oxide can be used as an anode material for lithium ion batteries with a high specific discharge capacity, superior rate capability and excellent cycling stability. Zhang et al. (2013) used a low temperature solution method combined with a simple post annealing process for controllable synthesis of 1D hierarchical hybrid nanostructures composed of $NiCo_2O_4$ nanorods or ultrathin nanosheets grown on carbon nanofibers. These materials exhibit excellent electrochemical performance and the cost-effective synthesis can be advantageous to prepare advanced electrode materials for high performance supercapacitors [7].

Spinel oxide powders were synthesized following our previous developed method based on the inorganic polycondensation [8]. The method was optimized for these new compositions and will be detailed in this chapter. Inorganic polycondensation is a soft-chemistry method which drives to the precipitation of oxide nanoparticles in particular

conditions, by the reaction of the appropriate metallic salts with a precipitating agent such as a hydroxide solution. The dip-coating technique was used to produce homogenous thin films on various substrates from a stabilized dispersion sol precursor. This simple process developed at ambient or low temperatures (120 ºC) is cheap, sustainable, environmentally friendly and easy to transfer at a larger scale.

This chapter is split into three parts:

- ✓ Synthesis and structure, microstructure, thermal stability characterization of the spinel oxide powders by soft chemistry at low temperature (T < 120 ºC).
- ✓ Preparation and structure, microstructure, surface morphological characterizations of the spinel oxide thin films prepared by dip-coating from a stabilized colloidal dispersion at room temperature.
- ✓ Structure and microstructure characterization of the spinel oxide thin films after heating at high temperatures (900 ºC ≤ T ≤ 1000 ºC).

IV.2. Synthesis and characterization of the powders

IV.2.1. Synthesis

The inorganic polycondensation method was used to prepare the spinel oxide $M_xCo_{2-x}O_4$ (*M* = Ni, Zn, Cu and x = 0, 0.15, 0.30, 0.60) powders and particularly the compositions Co_2MnO_4, $Ni_xCo_{2-x}MnO_4$ (NCM), $Zn_xCo_{2-x}MnO_4$ (ZCM), $Cu_xCo_{2-x}MnO_4$ (CCM). The compositions optimized in this work are shown in Table IV. 1.

The synthesized process can be described by these following steps:

- ➢ Dissolution of the metal salts in 100 ml of distilled water with a fixed concentration of solution, 0.3 mol/L.
- ➢ Dissolution of 4.19 g of Lithium hydroxide monohydrate ($LiOH.1H_2O$) in a large volume (1400 ml) of distilled water.
- ➢ Fast pouring of the metal salts solution(s) into the alkaline hydroxide solution using a funnel.

- Stirring for 90 minutes at room temperature with a speed of 300 rpm to complete the precipitation.
- Washing several times with distilled water by using centrifugation to remove any interfering ions (Li^+, SO_4^{2-}).
- Reflux with distilled water at 120 °C for two hours in order to provide oxygen to the intermediate alkali oxo-hydroxide and form metal oxide nanoparticles.

The concentration of metal salts was fixed at 0.3 mol/L to ensure the complete dissolution of solid phase. This concentration is considerably higher than the solubility of metal salts in distilled water at room temperature. So, the concentration of the hydroxide solution was used to obtain complete precipitation and to ensure a strong alkaline solution. Free enthalpy can be decreased by the formation of individual nuclei within a suspension of a homogenous phase, which characterizes the germination stage. The system will then evolve until reaching an equilibrium by a growing step that will generate primary particles. The final particle size strongly depends on the germination process. The particle growth can be limited by a strong dilution. Increasing the alkaline solution concentration can increase supersaturation, drive to high nucleation and decrease the particle size.

Table IV. 1: Samples formulae and their abbreviations.

M	*x*	Sample formula	Abbreviation
---	0	$Co_{2.00}Mn_{1.00}O_4$	---
Ni	0.15	$Ni_{0.15}Co_{1.85}Mn_{1.00}O_4$	NCM15
	0.30	$Ni_{0.30}Co_{1.70}Mn_{1.00}O_4$	NCM30
	0.60	$Ni_{0.60}Co_{1.40}Mn_{1.00}O_4$	NCM60
Zn	0.15	$Zn_{0.15}Co_{1.85}Mn_{1.00}O_4$	ZCM15
	0.30	$Zn_{0.30}Co_{1.70}Mn_{1.00}O_4$	ZCM30
	0.60	$Zn_{0.60}Co_{1.40}Mn_{1.00}O_4$	ZCM60
Cu	0.15	$Cu_{0.15}Co_{1.85}Mn_{1.00}O_4$	CCM15
	0.30	$Cu_{0.30}Co_{1.70}Mn_{1.00}O_4$	CCM30
	0.60	$Cu_{0.60}Co_{1.40}Mn_{1.00}O_4$	CCM60

IV.2.2. Characterization of the powders

IV.2.2.1. Structural and compositional determination by X-ray diffraction (XRD) and X-ray fluorescence (XRF)

The structure and the crystalline state of the powders were analyzed by X-ray diffraction (XRD) and are shown in Figure IV. 1. The overall background is fairly high due to the transition metal fluorescence with the Cu wavelength used for X-ray diffraction. Each pattern can be indexed with a single spinel oxide phase structure of cubic symmetry ($Fd\bar{3}m$ space group). All series of planes, written as (111), (220), (311), (222), (400), (422), (511), and (440) corresponding the (hkl) Miller indices, are in good agreement with the diffraction database (JCPDS: 23-1237) for a cubic spinel crystal structure. The wide width of the peaks shapes is characteristic of nanometer scale size crystallites. No significant change is observed in the peak intensities with metal substitution as can be seen for instance when comparing the (311) plane of each sample.

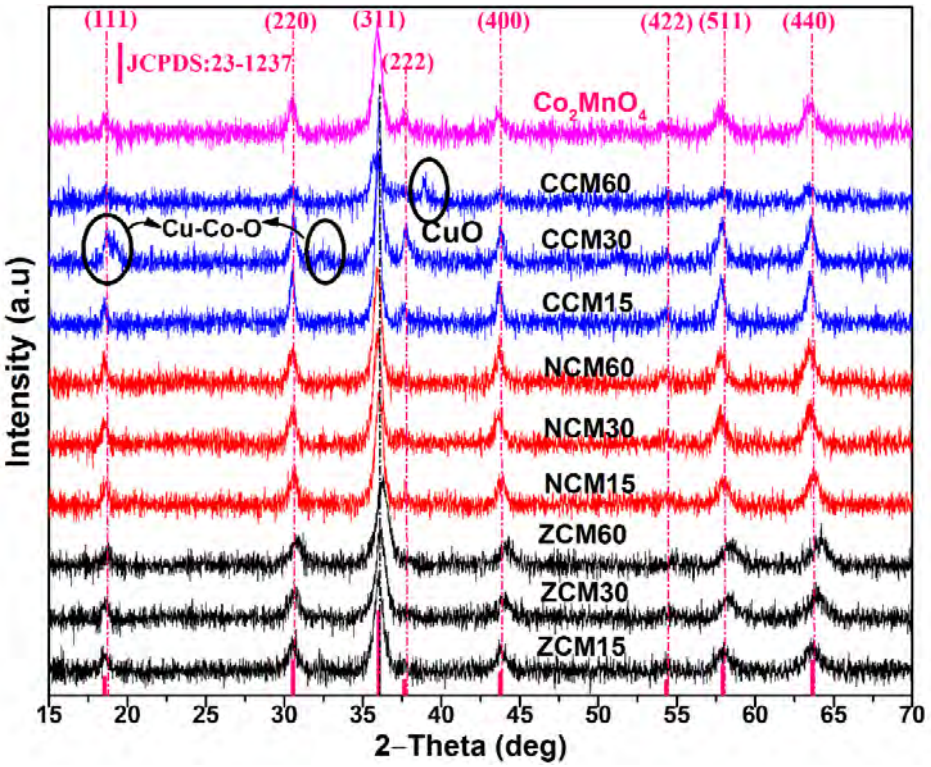

Figure IV. 1: XRD patterns of the spinel oxide powders and the database corresponding pattern JCPDS: 23-1237.

For copper containing spinel oxides (CCM), while CCM15 powder is pure and crystallizes in a cubic structure, the other compositions, richer in copper, show extra peaks which were attributed to a Cu-Co-O structure phase and additional CuO phase for further doping, i.e. CCM60. These latter two materials (CCM30 and CCM60), not pure, were not further studied. The lattice constants extracted from the XRD data are reported in Table IV. 2. We can determine the lattice constants by using Bragg's law for the strongest line (311) of a cubic system [9]:

$$2\,d\,\sin\theta\, = n\,\lambda \qquad \text{(IV-2)}$$

$$d = \frac{a}{\sqrt{h^2 + k^2 + l^2}} \qquad \text{(IV-3)}$$

Where:

d	: Spacing between diffraction planes
θ	: Incident angle (deg)
n	: Positive integer
λ	: X-ray wavelength (nm)
a	: Lattice constant (nm)
h, k, l	: Miller indices

The cell parameter increases with the addition of nickel, because the radius of the Ni^{2+} ion is larger than that of Mn^{2+} and Co^{2+} [10]. Besides, Ni^{2+} shows an octahedral site preference with Mn^{3+}, Mn^{4+} and Co^{3+} while Mn^{2+} and Co^{2+} show a tetrahedral site preference [11]. On the contrary, the lattice constant of ZCM compositions decreases with increasing Zn content because the radius of the Zn^{2+} ion is smaller than that of Mn^{2+} and Co^{2+} and Zn^{2+} shows tetrahedral site preference [11].

The average crystallite size was calculated for each composition from the X-ray diffraction of the (311) peak and is listed in Table IV. 2. The full width at half maximum (FWHM) of the (311) peak for each cubic phase, determined by using the Fityk software is about 0.01 rad. While making the assumption of perfectly spherical particles, the average crystallite size *D* can be estimated by Scherrer's equation [12]:

$$D = \frac{K\lambda}{\beta \cos\theta} \qquad \text{(IV-4)}$$

Where:

λ : X-ray wavelength (nm)

K : Dimensionless shape factor (K = 0.94)

β : FWHM of the (311) diffraction peaks (rad)

θ : Bragg diffraction angle (deg)

The crystallite size is similar for all NCM compositions while it decreases with increasing Zn concentration for ZCM phases. This latter observation is certainly due to the replacement of Mn^{2+} ions on the tetrahedral site by smaller Zn^{2+} ions [13].

The precise chemical compositions of the powders were investigated by X-ray fluorescence (XRF) measurements and result are summarized in Table IV. 2 for Co_2MnO_4, NCM, ZCM and CCM15 materials. Sample formulae determined by XRF are perfectly matching the expected stoichiometries.

Table IV. 2: Chemical compositions, lattice parameters and crystallite average diameters for each spinel oxide powder.

M	Abbreviation of sample	Sample formula determined by XRF	Lattice constant *a* (nm)	Crystallite size (nm)
---	---	$Co_{2.01}Mn_{0.99}O_4$	0.8268(1)	28
Zn	ZCM15	$Zn_{0.16}Co_{1.84}Mn_{1.00}O_4$	0.8274(10)	14
	ZCM30	$Zn_{0.32}Co_{1.68}Mn_{1.00}O_4$	0.8250(5)	12
	ZCM60	$Zn_{0.63}Co_{1.37}Mn_{1.00}O_4$	0.8209(1)	11
Ni	NCM15	$Ni_{0.16}Co_{1.85}Mn_{0.99}O_4$	0.8243(7)	15
	NCM30	$Ni_{0.32}Co_{1.68}Mn_{1.00}O_4$	0.8271(3)	15
	NCM60	$Ni_{0.62}Co_{1.39}Mn_{0.99}O_4$	0.8295(9)	14
Cu	CCM15	$Cu_{0.15}Co_{1.84}Mn_{1.01}O_4$	0.8271(3)	25

IV.2.2.2. Microstructural determination by Field Emission Gun Scanning Electron Microscope (FEG-SEM)

The morphology of particles was examined by direct observations using a Field Emission Gun Scanning Electron Microscope (FEG-SEM). FEG-SEM images of NCM, ZCM, CCM15 and Co_2MnO_4 samples are shown in Figure IV. 2, Figure IV. 3, Figure IV. 4, respectively. All samples particles are spherical in shape. These particles are built up of many smaller crystallites, which size was determined with X-ray diffraction. The ImageJ software was used to determine the average diameter size of particles for twenty particles on each FEG-SEM micrograph.

The average particle size is equivalent for all studied NCM samples, as can be seen in Table IV. 3.

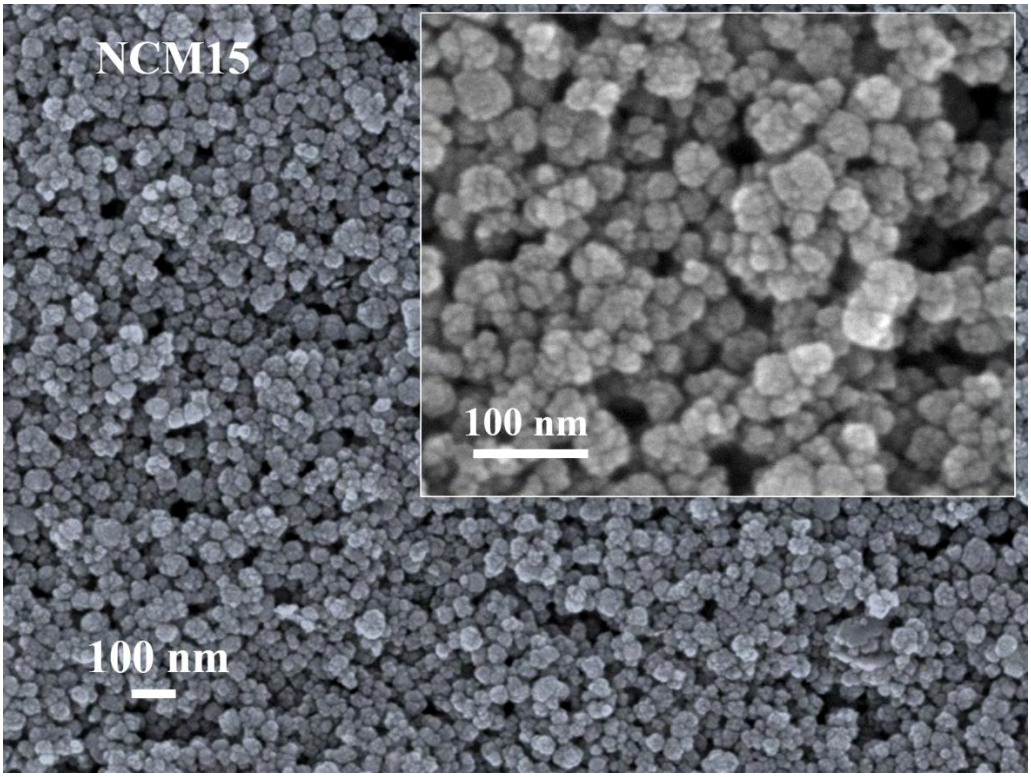

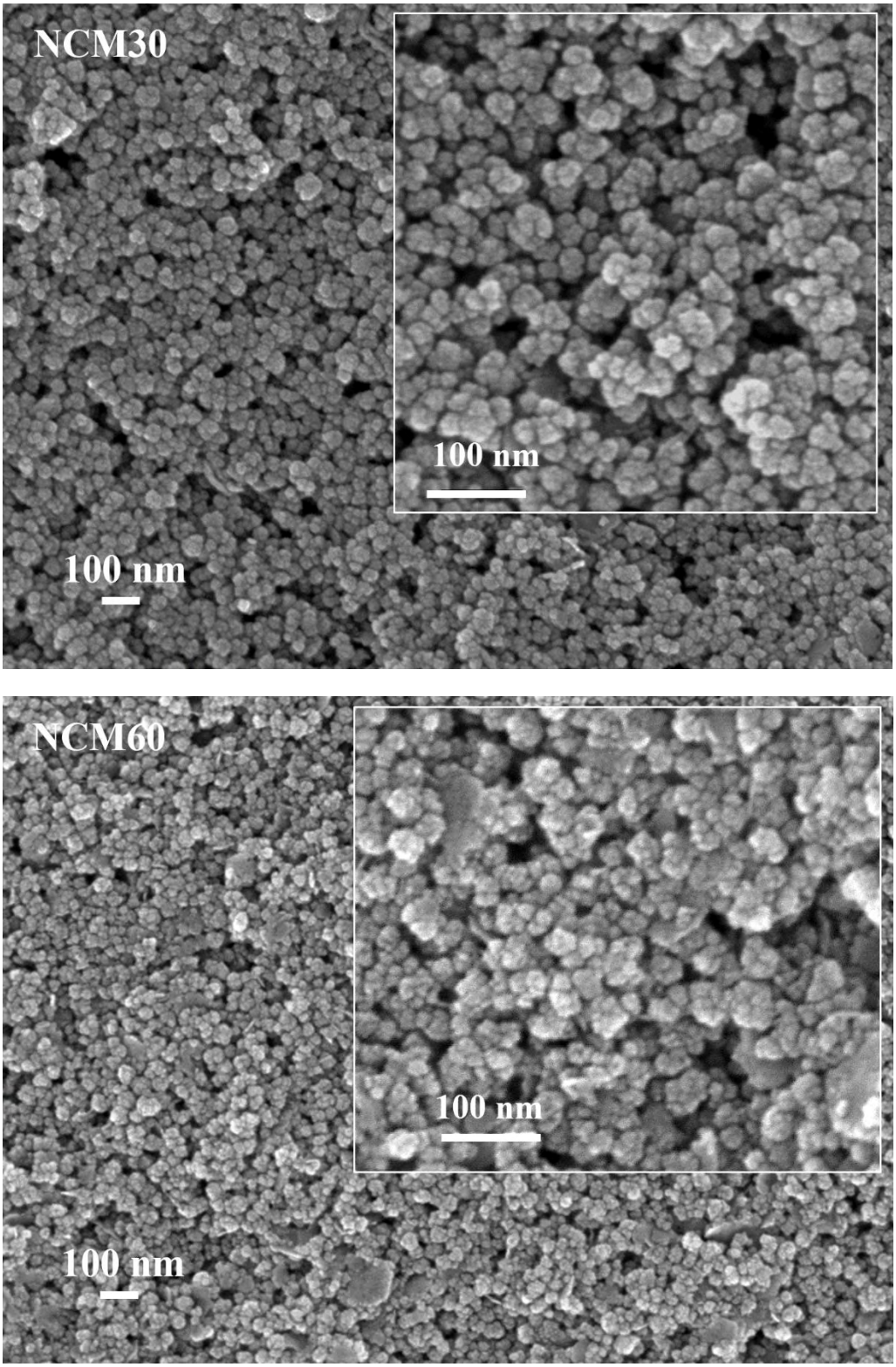

Figure IV. 2: FEG-SEM images of NCM15, NCM30 and NCM60 powders.

Table IV. 3 Average particle size for NCM15, NCM30 and NCM60 samples.

Sample	Mean diameter size (nm)
NCM15	44 ± 2
NCM30	44 ± 4
NCM60	43 ± 5

A mean diameter of 44 (1) nm is obtained with no variation observed with the Ni concentration.

Scanning electron micrographs of ZCM sample powders are given in Figure IV. 3. The average diameter of nanoparticles decreases with increasing Zn content, in accordance with the X-ray diffraction pattern analysis. These values are indicated in Table IV. 4.

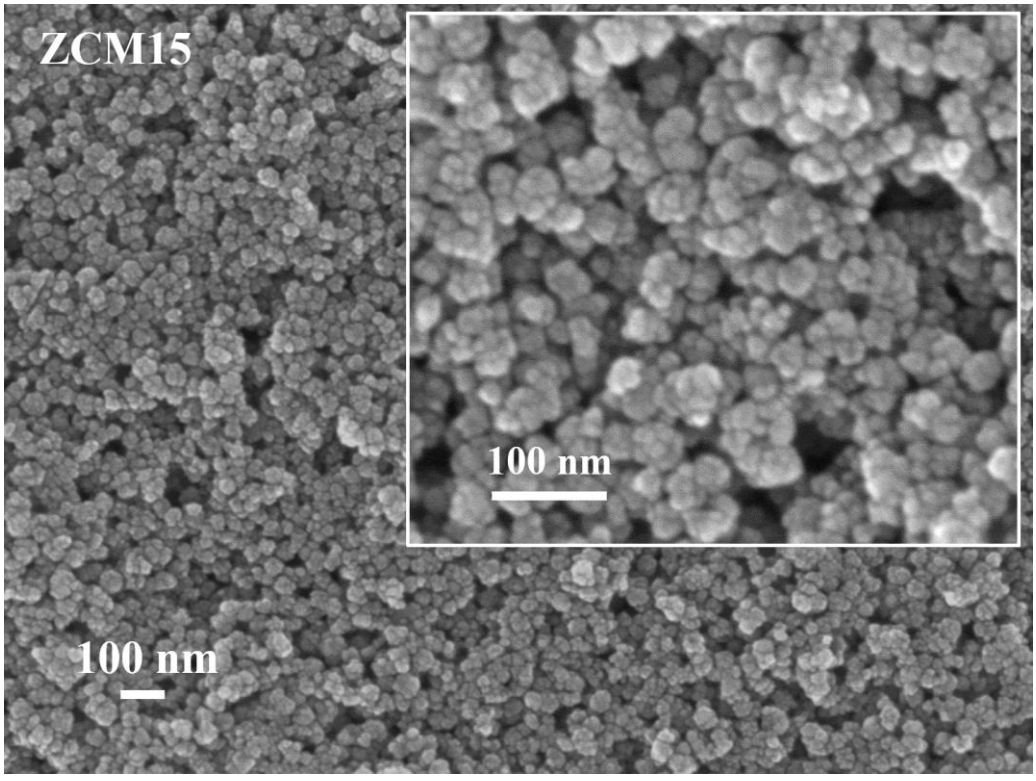

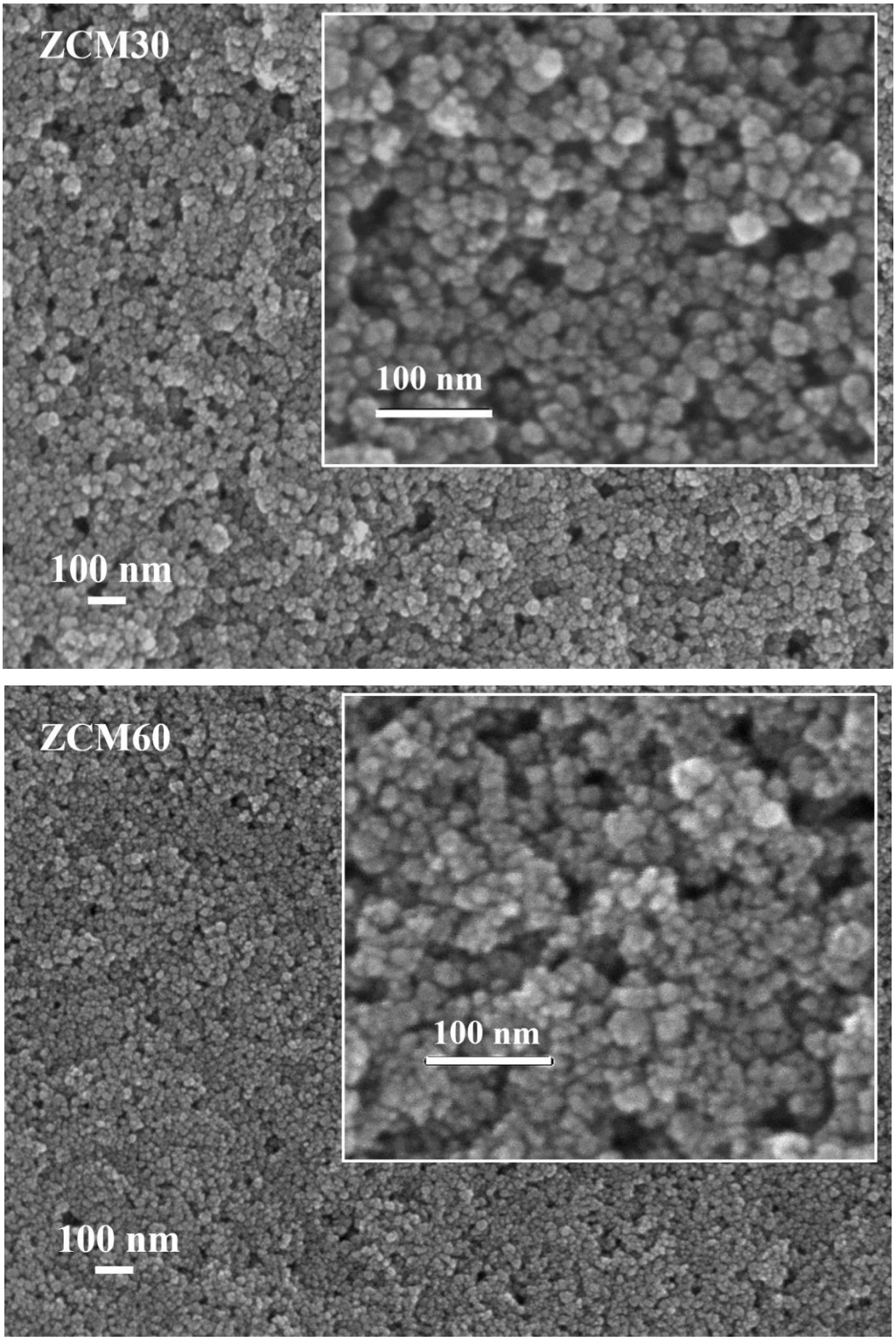

Figure IV. 3: FEG-SEM images of ZCM15, ZCM30 and ZCM60 powders.

Table IV. 4: Average particle size for ZCM15, ZCM30 and ZCM60 samples.

Sample	Mean diameter size (nm)
ZCM15	32 ± 2
ZCM30	28 ± 2
ZCM60	21 ± 1

The average diameter gradually decreases from 32 to 21 nm with increasing the Zn concentration from 15 at. % to 60 at. %.

Scanning electron micrographs for the CCM15 and Co_2MnO_4 samples powders are shown in Figure IV. 4. The average diameter of CCM15 nanoparticles is equivalent to the average diameter of Co_2MnO_4 (~ 50 nm) and is bigger than that of NCM15 and ZCM15, due mostly to steric conditions. These values are shown in Table IV. 5.

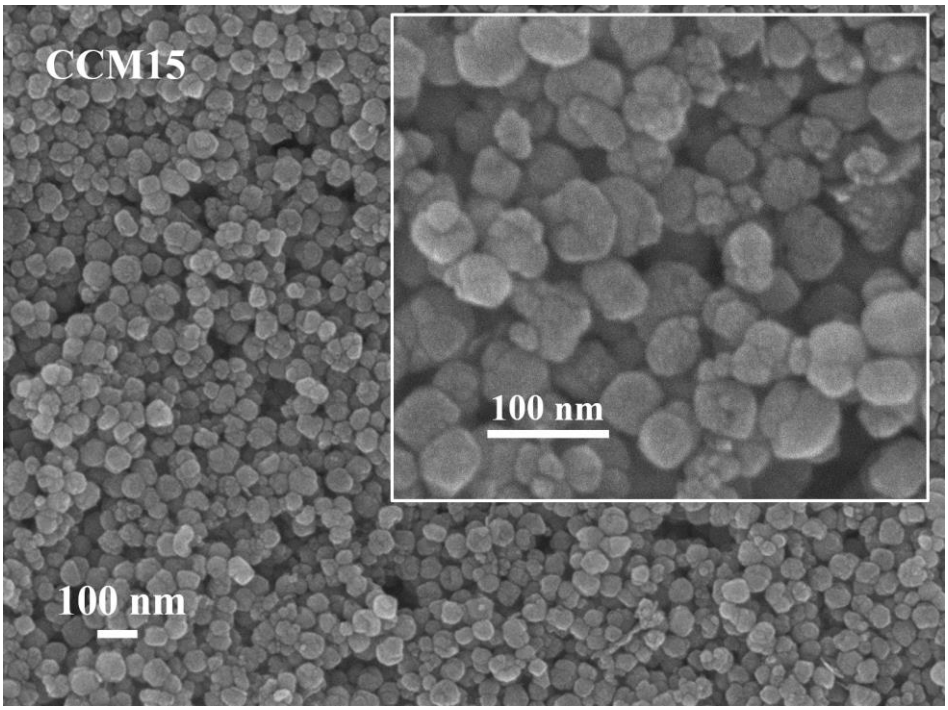

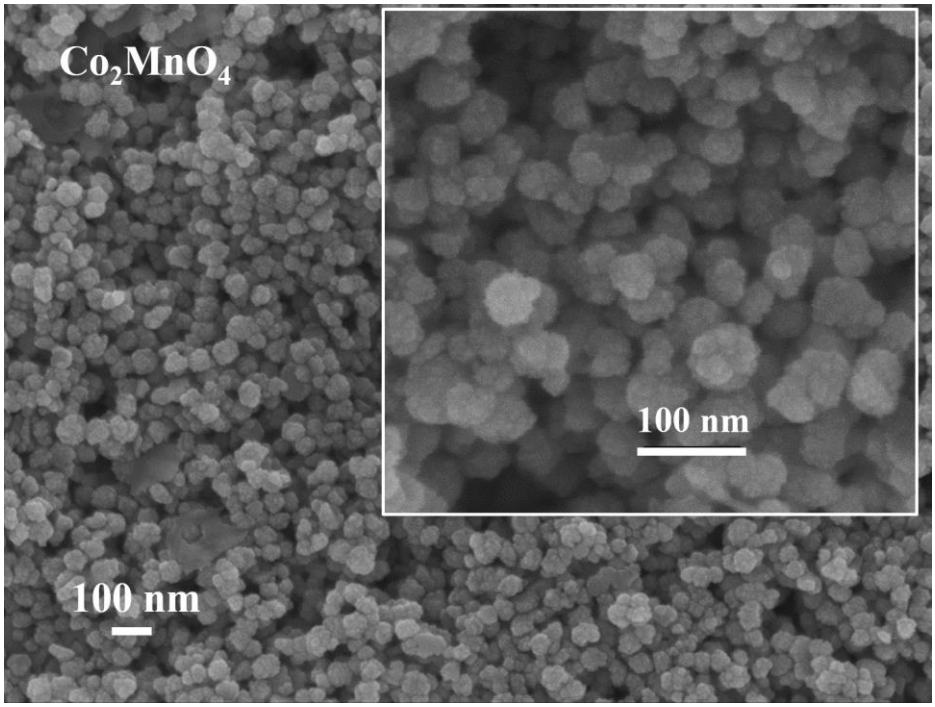

Figure IV. 4: FEG-SEM images of CCM15 and Co_2MnO_4.

Table IV. 5: Average particle size for CCM15, Co_2MnO_4, in comparison with NCM15 and ZCM15 samples.

Sample	Mean diameter size (nm)
CCM15	50 ± 3
Co_2MnO_4	51 ± 2
NCM15	44 ± 2
ZCM15	32 ± 2

IV.2.2.3. Thermal stability analyzed by thermo-gravimetric analysis (TGA)

The thermal stability of the powders was studied by thermo-gravimetric analysis (TGA) from 20 ºC to 1000 ºC at a heating rate of 80 ºC/hour under air atmosphere. The TGA curves of Co_2MnO_4 and NCM compositions are shown in the Figure IV. 5.

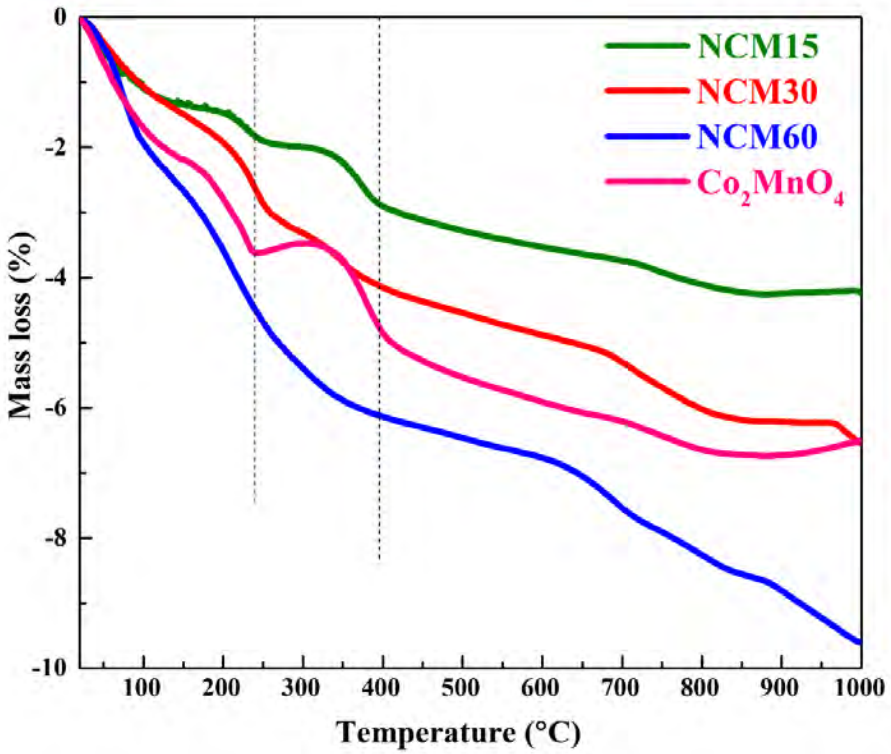

Figure IV. 5: TGA curves of Co_2MnO_4 and NCM compositions.

The first mass loss at low temperature (T < 250 ºC) varying from 2 % to 4 % (depending on the composition), corresponds to the loss of water and carbonate compounds adsorbed on the surface of the particles. This mass loss rate increases with increasing Ni concentration.

The weight variation observed in temperatures between 250 ºC and 400 ºC is attributed to an oxidation phenomenon between Mn^{3+} and Mn^{4+} on octahedral site and between Mn^{2+} and Mn^{3+} on tetrahedral site, that can occur under stoichiometric spinel oxides exhibiting small nanoparticles, as already reported in the literature [14-17]. For instance, Gillot et al. (1994) reported the oxidation temperatures of some oxidizable cations, with $Cu^{+} \rightarrow Cu^{2+}$ occurring at 150 ºC, $Mn^{3+} \rightarrow Mn^{4+}$ at ~ 280 ºC on octahedral sites while $Cu^{+} \rightarrow Cu^{2+}$ occurs at ~ 225 ºC and $Mn^{2+} \rightarrow Mn^{3+}$ at ~ 355 ºC on the tetrahedral sites [16].

At higher temperature (400 ºC < T < 1000 ºC), weight losses correspond to a progressive loss of the excess oxygen in the non-stoichiometric oxides. Rojas et al. (1994) reported the thermogravimetric curves of Co_3O_4 and Co_2MnO_4 powders, with a loss of oxygen and conversion to the stoichiometric spinel Co_2MnO_4 at over 700 ºC [18]. Bordeneuve et al. (2000)

also presented the simultaneous reduction of Co^{3+} to Co^{2+} and Mn^{4+} to Mn^{3+} in mixed spinel oxides of Co – rich phases that can be observed above 1000 ºC, depending on the composition [19].

The X-ray diffraction patterns of NCM sample powders after TGA are presented in Figure IV. 6. Each pattern is indexed with a single spinel oxide phase structure cubic symmetry ($Fd\bar{3}m$ space group). All series of planes are in good agreement with the diffraction data from the database for a cubic spinel (JCPDS: 23-1237). So the structure of the samples remains unchanged after heat treatment, performed in air, up to 1000 ºC. Peaks are sharper due to grain growth with the temperature.

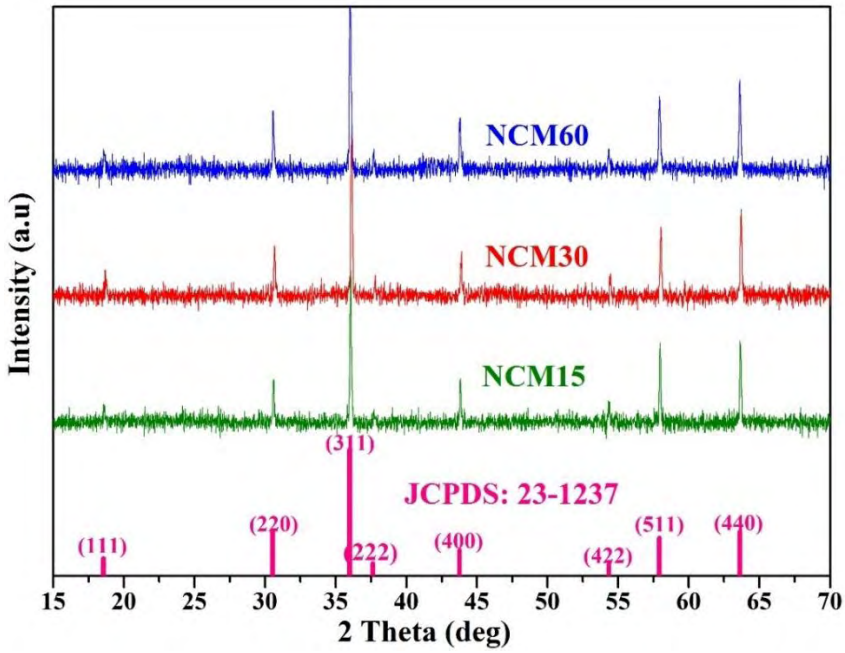

Figure IV. 6: XDR patterns of the NCM sample powders after TGA analysis (T = 1000 ºC in air).

The TGA curves of Co_2MnO_4 and ZCM compositions are presented in Figure IV. 7. Similarly to NCM compositions, the first weight loss below 250 °C is likely due to the removal of physically absorbed (carbonate compounds) and water while the second is assigned to a slight oxidation phenomenon. The third mass loss corresponds to a progressive loss of the excess oxygen in the non-stoichiometric oxide.

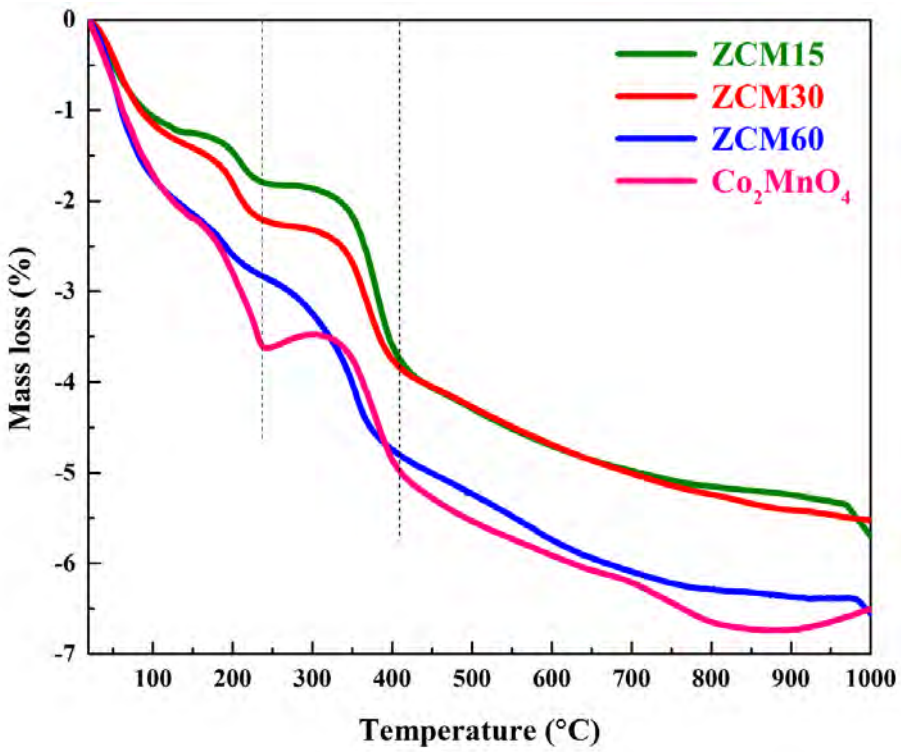

Figure IV. 7: TGA curves of Co_2MnO_4 and ZCM compositions.

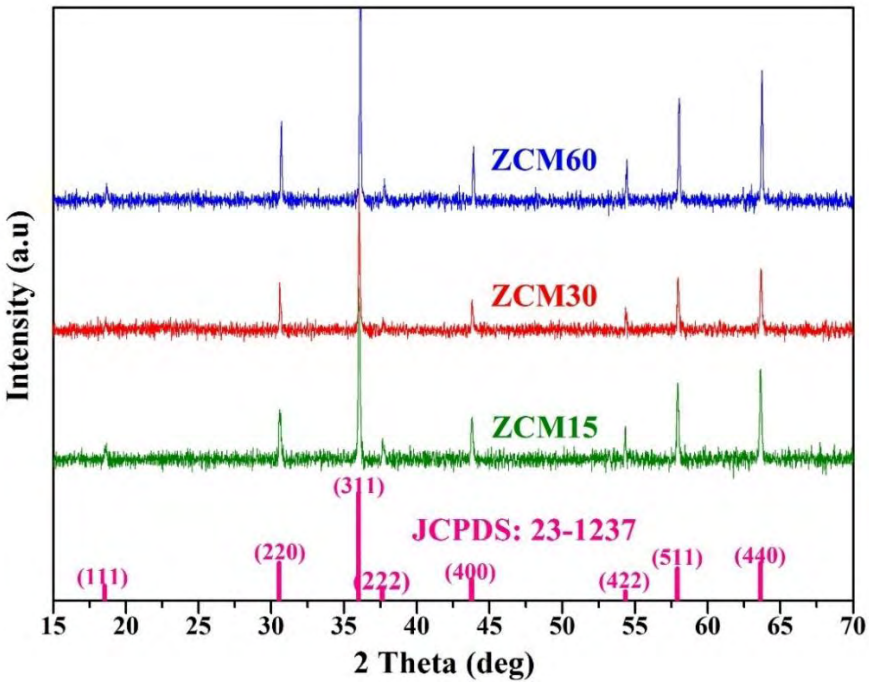

Figure IV. 8: XDR patterns of the ZCM sample powders after TGA analysis (T = 1000 ºC, in air).

XRD patterns of ZCM samples powders after TGA are shown in Figure IV. 8, which are also in good agreement with the diffraction database of the cubic spinel phase JCPDS: 23-1237).

The TGA curve of the CCM15 sample is displayed in Figure IV. 9. The curves of the compositions NCM15, ZCM15 and Co_2MnO_4 are reported as well. The TGA general variation of CCM15 is similar to the others but with a total weight loss limited to 3.5 %.

XRD patterns of CCM15 and Co_2MnO_4 sample powders after TGA are displayed in Figure IV. 10. All series of planes are in good agreement with the diffraction database of the spinel phase (JCPDS: 23-1237).

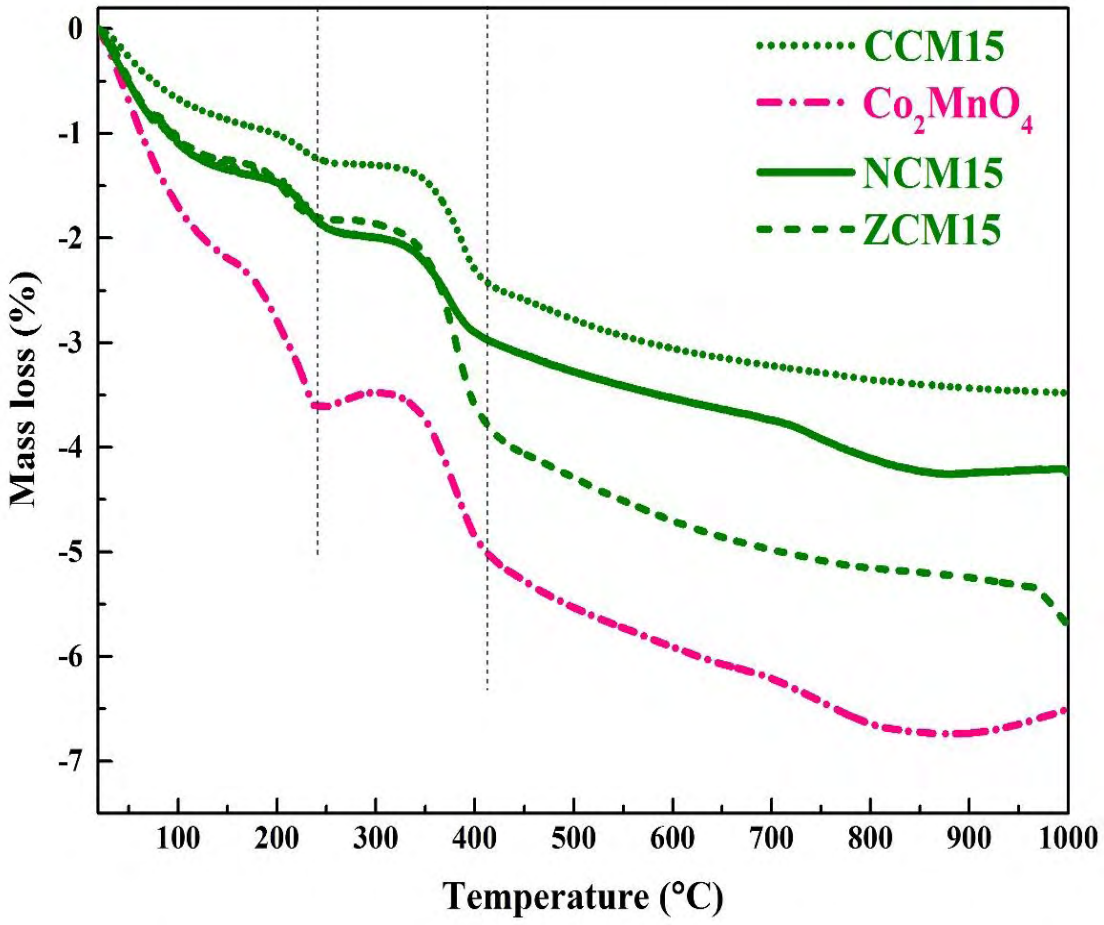

Figure IV. 9: TGA curves of CCM15 comparison with NCM15, ZCM15 and Co_2MnO_4.

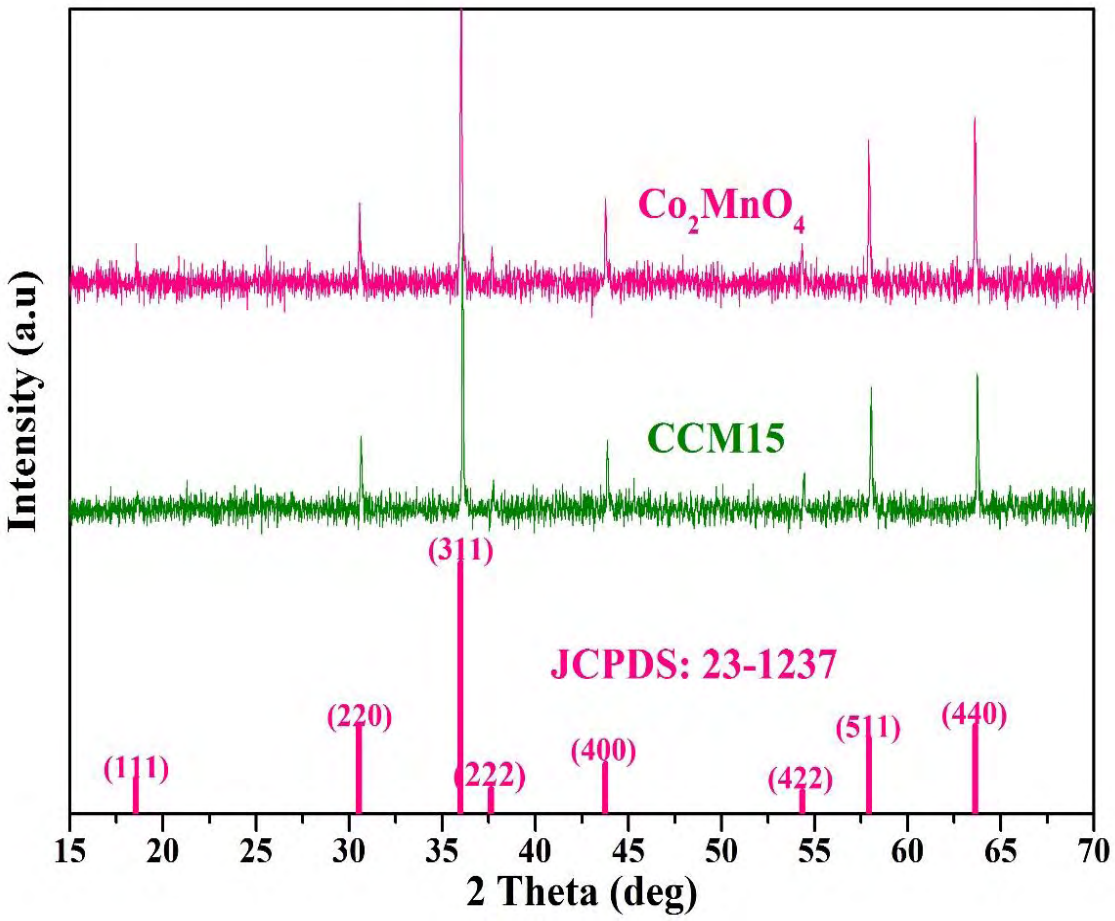

Figure IV. 10: XRD patterns of CCM15 and Co_2MnO_4 sample powders after TGA analysis (T = 1000 ºC, in air).

IV.2.2.4. Study of the sintering conditions

Dilatometry was used to determine the optimal sintering temperature and investigate the doping effect on the sintering characteristics. Figure IV. 11 shows the results of the linear shrinkage ($\Delta L/L_0$) and shrinkage rate ($d(\Delta L/L_0)/dT$) for the NCM samples as a function of temperature during heating in a dilatometer system from room temperature to 1000 ºC for ZCM compositions, 1200 ºC for NCM, CCM15 and Co_2MnO_4 samples at 1.3 ºC/min constant heating rate under air atmosphere. Sample pellets of 6 mm diameter and about 1 mm thickness were compacted with an organics (rhodoviol) at 20 bars by using uniaxial pressure.

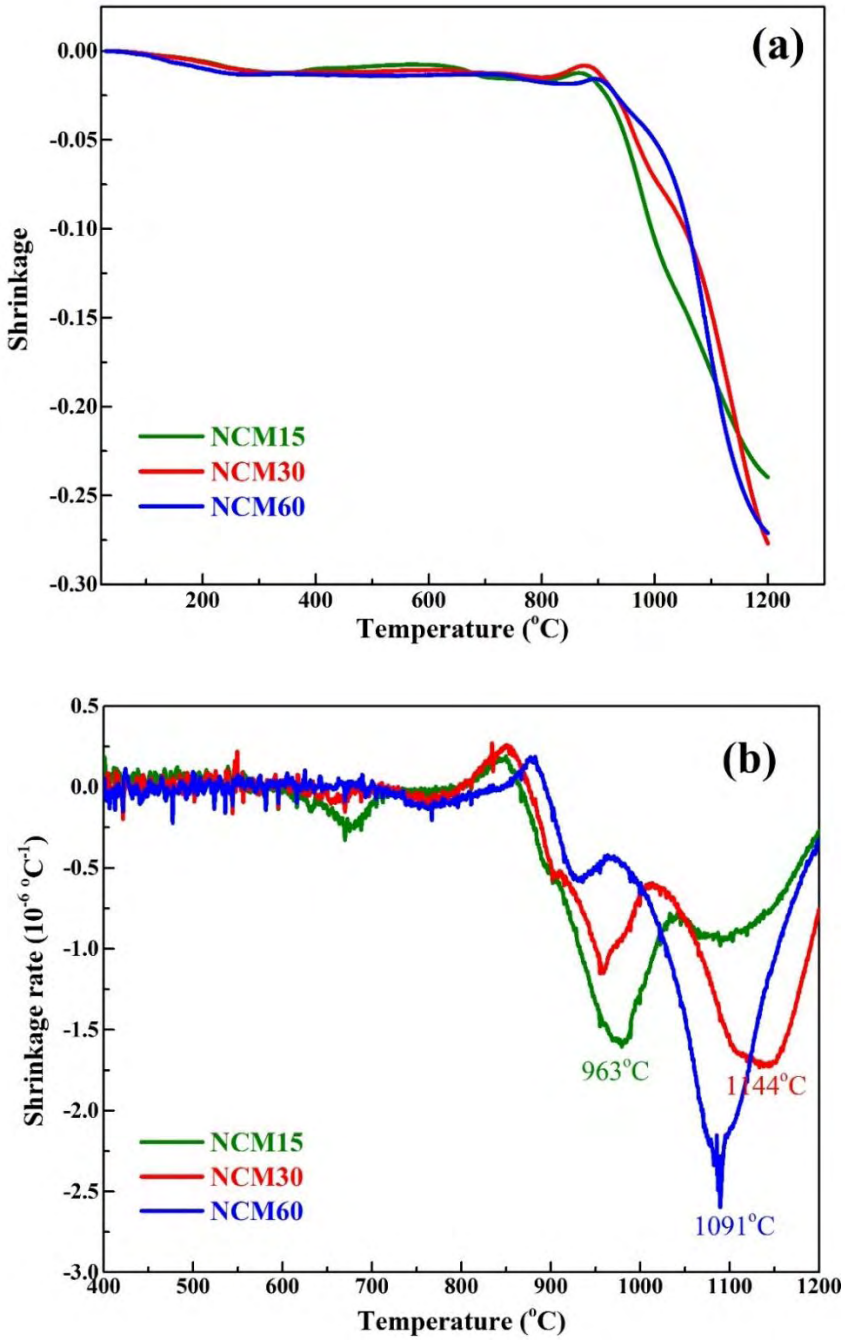

Figure IV. 11: Dilatometry curves (a)-shrinkage vs. temperature and (b)-shrinkage rate vs. temperature for NCM15, NCM30 and NCM60 materials.

For the NCM compositions, the shrinkage starts at approximately 900 ºC. The maximum shrinkage rate occurs at 963 ºC for NCM15, 1144 ºC for NCM30 and 1091 °C for NCM60. Each point of maximum shrinkage suggests the optimum temperature for sintering. The optimal

temperature of sintering is determined at maximum shrinkage rate for each composition. Two different areas can thus be defined as seen in Figure IV. 11b: the first area beginning at 850 ºC – 880 ºC until 910 ºC – 940 ºC that refers to the temperature range before shrinkage and depends on the composition. The next variation temperature range can be defined as shrinkage actually occurring for the sample [20]. Temperatures for the first area and temperature at maximum shrinkage rate for all three NCM compositions are shown in Table IV. 6.

Table IV. 6: Temperatures of the first area and at maximum shrinkage rate of the NCM samples.

Sample	Temperature of the first area (ºC)	Temperature at maximum shrinkage rate (ºC)
NCM15	852 – 913	963
NCM30	859 – 910	1144
NCM60	881 – 940	1091

For the ZCM compositions, the linear shrinkage ($\Delta L/L_0$) and shrinkage rate variations ($d(\Delta L/L_0)/dT$) are shown in Figure IV. 12. The curves are similar to the NCM compositions. The temperature at the maximum shrinkage rate occurs at 913 ºC for ZCM15, 941 ºC for ZCM30 and 975 ºC for ZCM60 (Figure IV. 12b). These latter values can be associated to the optimal sintering temperature of each ZCM composition. The first area and maximum shrinkage rate temperatures for the ZCM compositions are shown in Table IV. 7

Table IV. 7: Temperatures of the first area and at maximum shrinkage rate of the ZCM samples.

Sample	Temperature of the first area (ºC)	Temperature at maximum shrinkage rate (ºC)
ZCM15	875	913
ZCM30	900	941
ZCM60	850	975

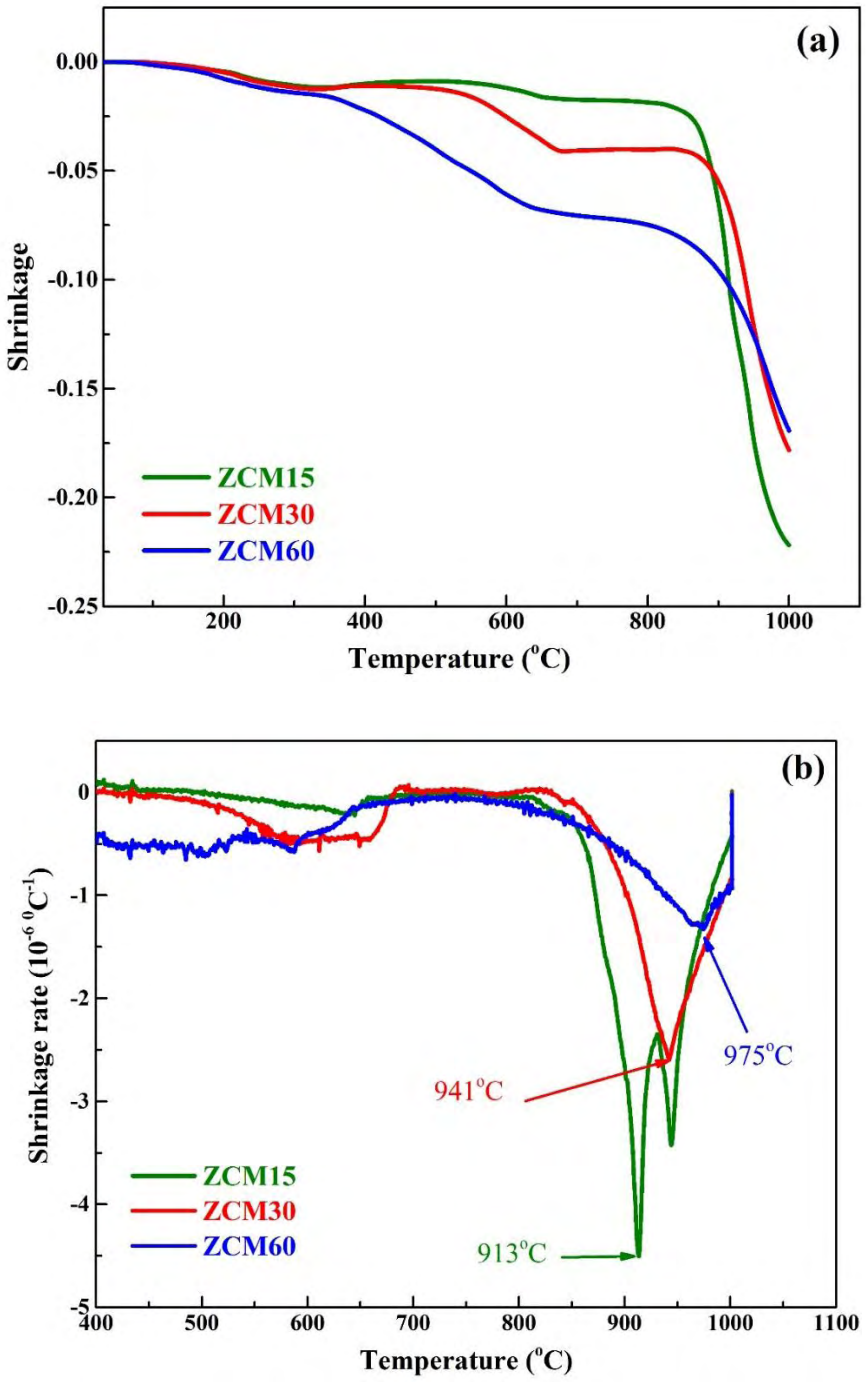

Figure IV. 12: Dilatometry curves (a)-shrinkage vs. temperature and (b)-shrinkage rate vs. temperature for ZCM15, ZCM30 and ZCM60 compositions.

Figure IV. 13 illustrates the linear shrinkage ($\Delta L/L_0$) and shrinkage rate ($d(\Delta L/L_0)/dT$) of CCM15 in comparison with the undoped Co_2MnO_4 sample. Again, shrinkage starts at about

800 ºC for CCM15 and 900 ºC for Co_2MnO_4 samples. From the shrinkage rate thermal variation showed in Figure IV. 13b we can determine a maximum shrinkage rate (or sintering temperature) at 998 ºC for CCM15 and 1143 ºC for Co_2MnO_4 materials.

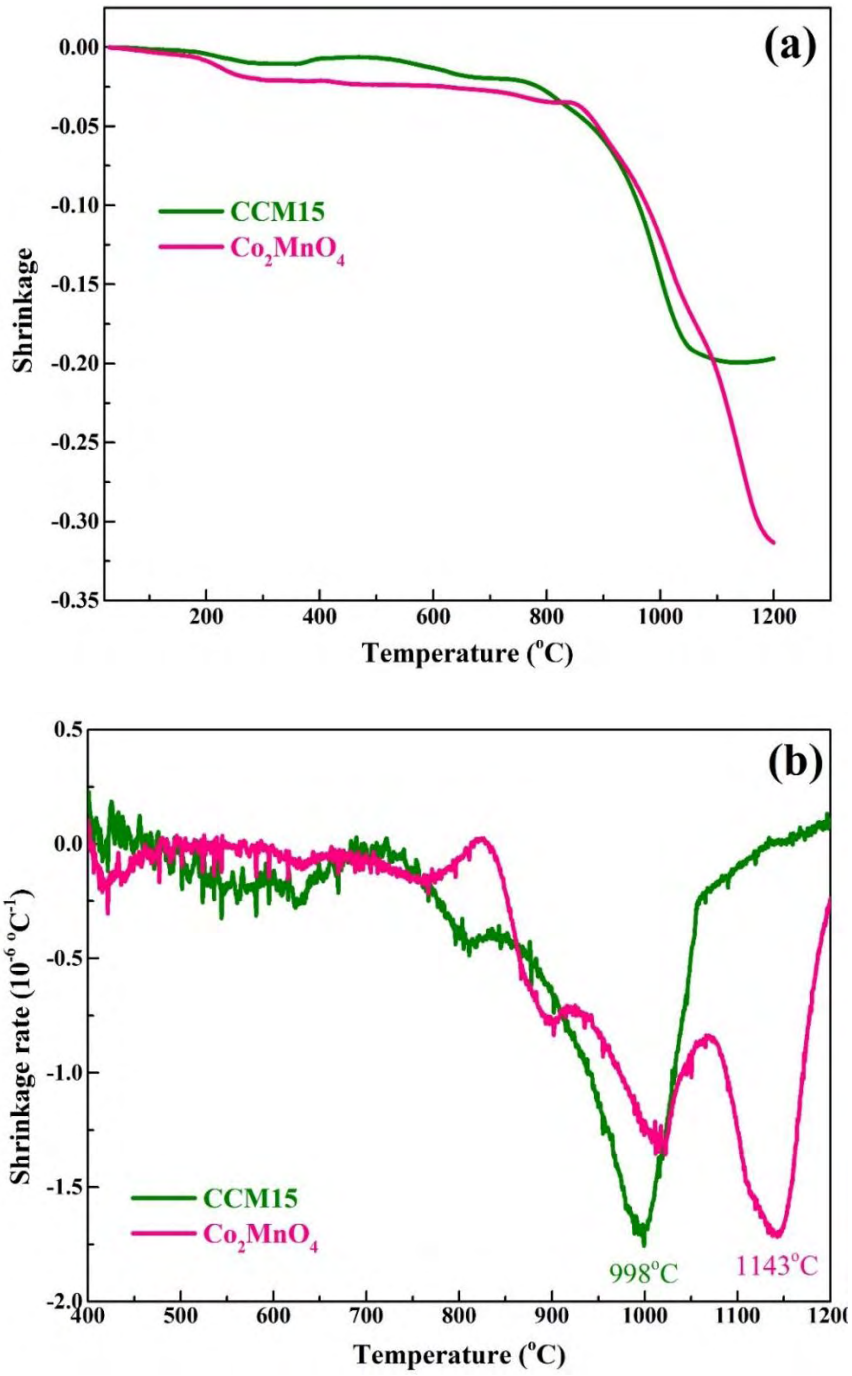

Figure IV. 13: Dilatometric curves (a)-shrinkage vs. temperature and (b)-shrinkage rate vs. temperature for CCM15 and Co_2MnO_4.

Table IV. 8: Temperatures of the first area and at maximum shrinkage rate of the CCM15 and Co_2MnO_4 samples.

Sample	Temperature of the first area (°C)	Temperature at maximum shrinkage rate (°C)
CCM15	900	998
Co_2MnO_4	900	1143

IV.3. Preparation and characterization of thin films

A thin film is a layered material ranging from fractions of a nanometer to several micrometers in thickness prepared by various physical or chemical methods. Thin films facilitate the miniaturization of devices or electronic components as well as tailoring properties of the material as per need. Thin films play a vital role in optoelectronics systems such as solar energy conversation, anti-reflecting coating on solar energy collectors, electrodes etc. [21-23]. Nowadays, thin films made of metal oxides, metal chalcogenides and transition metal dichalcogenides have interesting properties for solar cells application. In this work, we have prepared thin films of spinel oxides $M_xCo_{2-x}MnO_4$ (M = Ni, Zn, Cu and x = 0, 0.15, 0.30, 0.60) by using the dip-coating technique, based on the preliminary stabilization of a colloidal solution. The sol-gel method is indeed useful for three basic techniques used for thin film deposition: dipping, spinning and spraying. The former technique was chosen to immerse the substrate in a liquid (sol) and pull it out with a defined speed to obtain the optimal thin films (see part **IV.3.2.** for details).

In this section, we describe the preparation of colloidal dispersions and thin films by the dip-coating technique. Thin films were analyzed by Grazing Incidence X-ray diffraction (GI-XRD) for crystallinity and phase purity, Field Emission Gun Scanning Electron Microscope (FEG - SEM) for their microstructure, interferometry for surface roughness state.

IV.3.1. Stabilization of colloidal dispersion

The stabilization of colloidal suspensions depends upon many factors as the nature of solvent, the charge separation and particles repulsive properties. The solvent used for the colloidal suspension preparation needs to have a high dipole moment and a dielectric constant sufficient to allow a good repulsion of particles. In addition, a low surface tension, a moderate volatility and an adequate viscosity are also important parameters for the solvent. An azeotrope mixture consisting of 96 % absolute ethanol and 4 % ultrapure water was used as a solvent of colloidal dispersion. The zeta potential (electrophoretic mobility), isoelectric point, rheological behavior, effect of pH on dispersion colloidal were studied and determined on the previous work by Guillaume Salek [24]. Zeta potential measurements were performed by using a Zetasizer 3000 Malvern Instrument at the wavelength of 663 nm in order to determine the best pH areas for preparing colloidal suspensions. Isoelectric points (IEP) values progressively increase with the cobalt content in formula $Co_xMn_{3-x}O_4$ and large domain of constant zeta potential is observed for pH < 7. Zeta potential values of 40 ± 4 mV indicate a good stability of colloidal dispersions. But coloration of solution was observed for pH values lower than 6 due to partial dissolution of particles. Therefore, the preparations were peptized at pH = 6 with HNO_3 and finally stabilized with an azeotrope solution. Figure IV. 14 shows a cup of colloidal solution prepared at room temperature. The granulometric distribution of spinel oxides are mono-disperse with a narrow particle size distribution which was determined by Dynamic Light Scattering (DLS). The colloidal solution concentration was fixed at 60 g/L in order to obtain the thinnest possible homogeneous oxide layer on quartz, metal and alloy substrates [8].

In summary, for this work, the protocol was optimized as follow:

- Dispersion of the powders in dilute nitric acid (HNO_3) at pH = 6.
- Ultrasonication for 15 minutes using a frequency of 35 kHz to break apart the agglomerates of particles in aqueous solution.
- Washing several times with absolute ethanol by using centrifugation.
- Stabilization in azeotrope solution.

Figure IV. 14: A colloidal solution prepared at room temperature.

IV.3.2. Thin films preparation using the dip-coating technique

The dip-coating technique is a simple method with controlled immersion into a reservoir of liquid and withdrawal of any substrate for the purpose of depositing a material as a thin layer. Many factors contribute to determining the final state of the dip-coating of a thin film such as initial substrate surface, submersion time, withdrawal speed, number of dipping cycles, solution composition and temperature in each dipping sequence. The dip-coating technique is generally used to make thin films after preparing colloidal dispersions obtained by the sol-gel method.

In this work, quartz silica (SiO_2), alumina (Al_2O_3), titanium nitride (TiN) and platinum (Pt) were used as substrates. Quartz, which has high transmittance in the UV-VIS-IR regions and can handle very high temperatures (necessary for post-annealing treatments), was used for optical measurements of the spinel oxide thin films. Alumina, titanium nitride and platinum were also used as insulating or conducting supports, respectively, for sintering at high temperatures. These substrates were cut into desired dimensions prior to the dipping process. The surface of quartz was cleaned according to the following procedure:

- Wipe with ethanol and acetone,
- Rinse with de-ionized water,
- Ultrasonication for 30 minutes into de-ionized water solution with 10 % of "Decon 90" and repeat two times,

- Rinse by ultrasound in de-ionized water for 20 minutes and repeat three times,
- Dry with compressed nitrogen gas flow.

The surfaces of Al_2O_3, TiN and Pt were cleaned according to the following procedure:

- Immersion in dilute hydrochloric acid (30 % acid and 70 % water) for 15 minutes to remove alloying elements from the surface,
- Rinse with de-ionized water,
- Rinse by ultrasound in de-ionized water for 20 minutes and repeat three times,
- Dry with compressed nitrogen gas flow.

By choosing an appropriate colloidal concentration (60 g/L) to obtain an homogenous thin film of about 300 nm in thickness, the dip-coating technique was used at ambient temperature with the following features:

- Immersion and withdrawal speed of 200 mm/minute.
- Immersion time of 30 seconds for one-layer deposition.
- Drying in air for 1 minute.

IV.3.3. Characterization of thin films

IV.3.3.1. Structural determination by Grazing Incidence X-ray Diffraction (GI-XRD)

The structure characterization of thin films was performed by Grazing Incidence X-ray Diffraction (GI-XRD). Figure IV. 15 shows the GI-XRD patterns of NCM15 and Co_2MnO_4 thin films deposited on quartz, alumina, titanium nitride and platinum at room temperature. The diffraction patterns were recorded in 2-Theta mode from 15 to 70° overnight at 14 seconds per 0.03° step. Each pattern can be indexed with a single oxide phase structure of cubic symmetry ($Fd\bar{3}m$ space group). All series of planes are in good agreement with the diffraction database JCPDS: 23-1237. Pure spinel oxide thin films were thus prepared after stabilizing colloidal

suspensions of spinel oxide nanoparticles as synthesized by our method and using the dip-coating deposition technique. In addition, diffraction peaks corresponding to the platinum, titanium nitride and alumina substrates are indicated in red circle (JCPDS: 65-2868), brown quadrangle (JCPDS: 65-0565) and green squares (JCPDS: 10-0173) in Figure IV. 15, respectively.

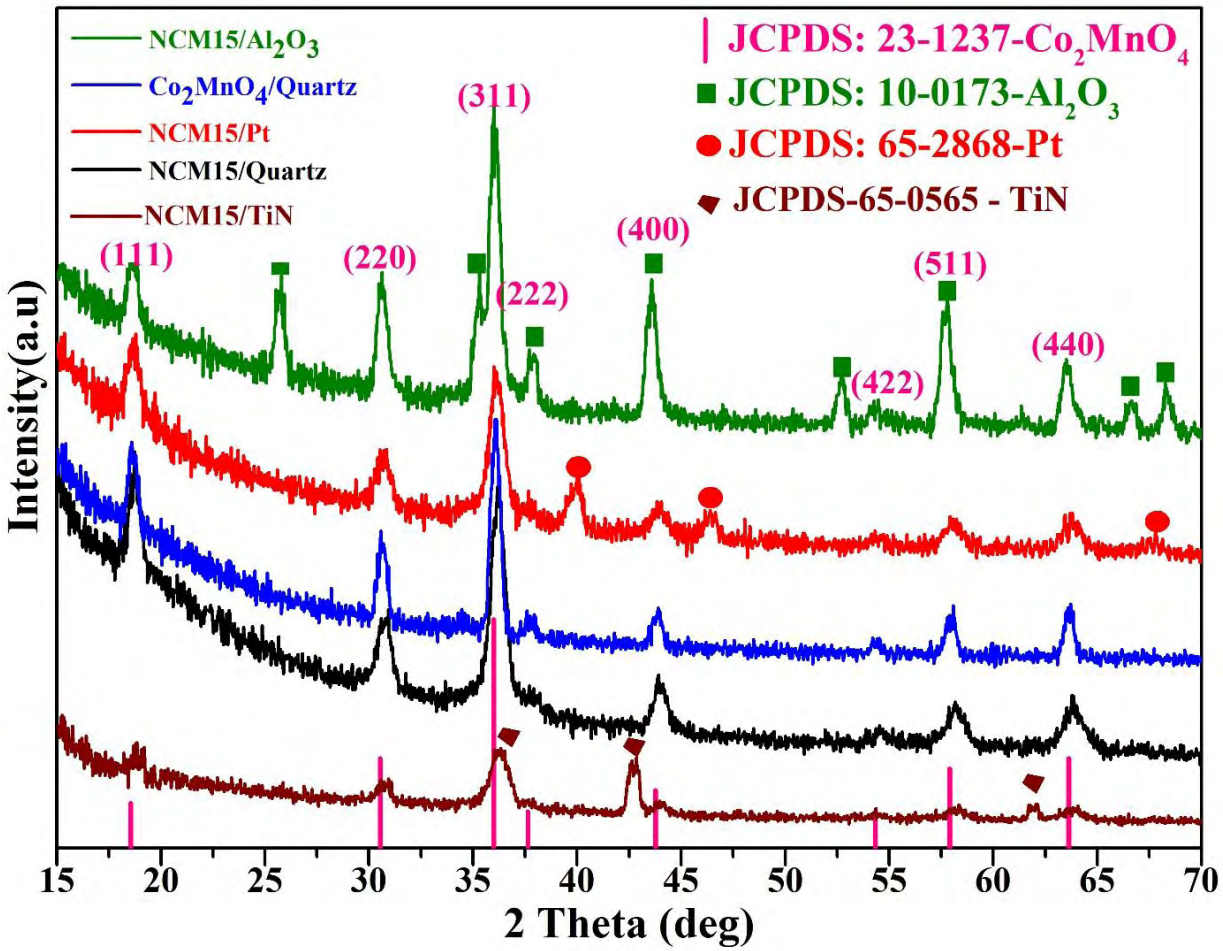

Figure IV. 15: GI-XRD patterns of NCM15 and Co_2MnO_4 thin film deposited on quartz, alumina, titanium nitride and platinum.

IV.3.3.2. Microstructural determination by Field Emission Gun Scanning Electron Microscope (FEG-SEM)

The surface morphology and thickness of thin films deposited on quartz substrate were analyzed using FEG-SEM. The surface morphologies of all thin films deposited on the other substrates are similar. The FEG-SEM images of a NCM15 thin film deposited on quartz substrate are shown in Figure IV. 16.

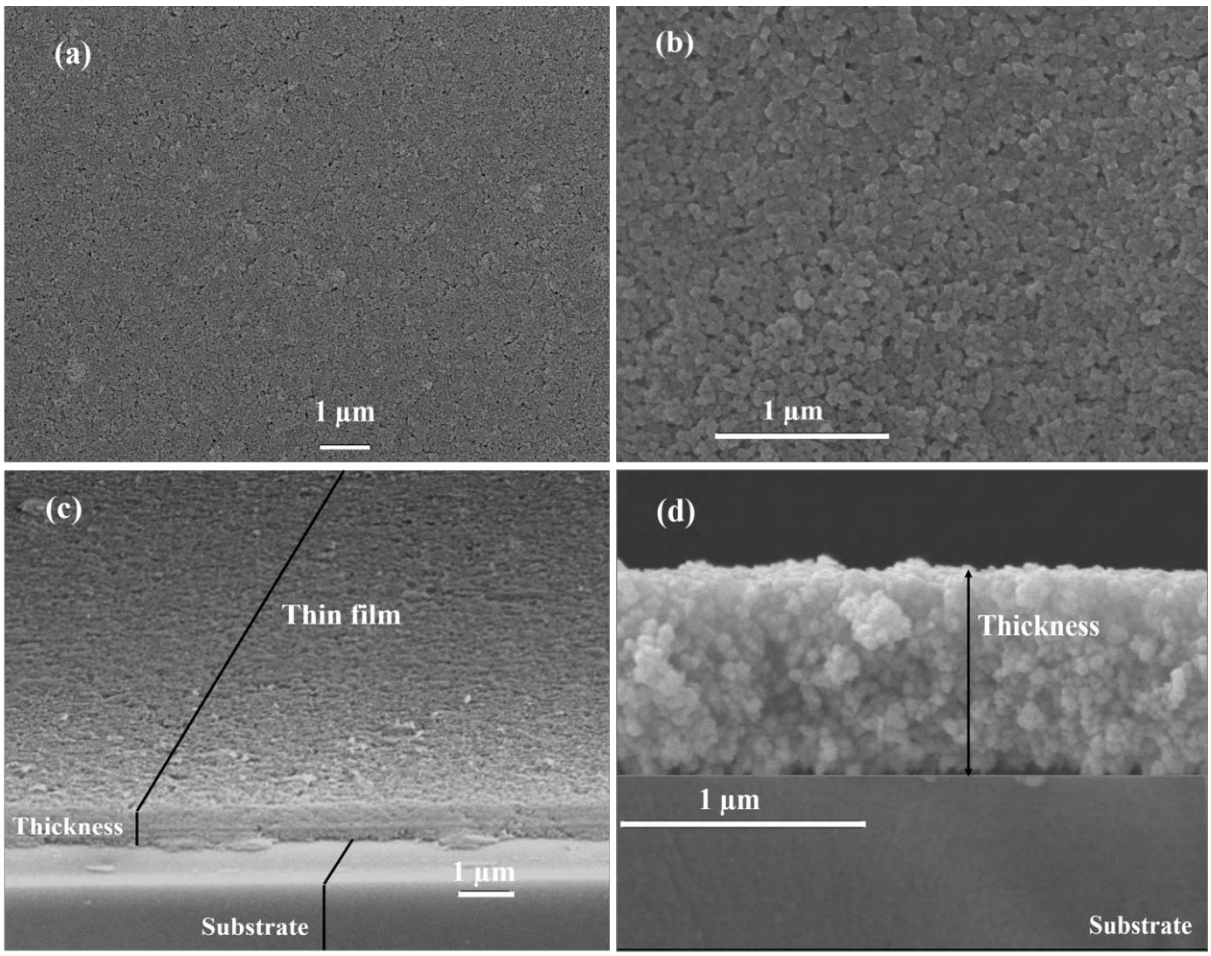

Figure IV. 16: Scanning electron micrographs showing the surface morphology – (a) and (b), and cross-section (c) and (d) of NCM15 thin films deposited on a quartz substrate.

Two top views are presented in Figure IV. 16a and b, to show the surface morphology of thin films, while Figure IV. 16c and d present the thickness of a spinel oxide thin film after three dip-coating sequences. These films are uniform and cover the substrate surface very well.

Oxide thin films are dense, smooth and homogeneous. Cross-sectional FEG-SEM images of the NCM15 thin film deposited on quartz show uniform film thickness of about 750 nm after three dip-coatings (see Figure IV. 16c and d).

IV.3.3.3. Surface roughness of thin films

The surface profile roughness of thin films on the quartz substrate was determined using white light optical interferometry (ZYGO) system. The scan size is fixed by the magnification of the optical system. The magnification of the objective lens used in our measurements was x10 and scan size is 720 µm x 540 µm. Figure IV. 17 shows the 3D surface images of different thin films deposited on quartz substrate after three dip-coating sequences.

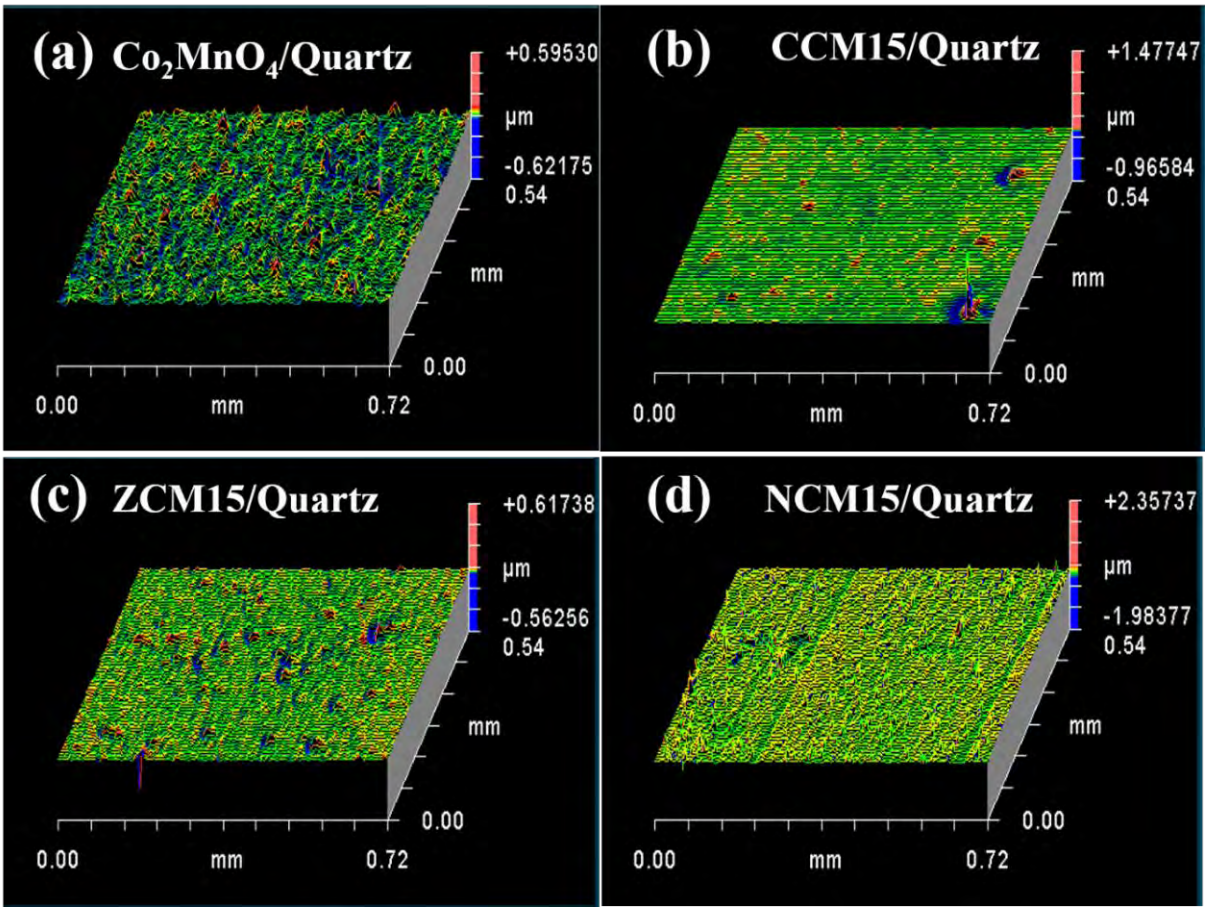

Figure IV. 17: The 3-Dimensional surface images of Co_2MnO_4 - (a), CCM15 - (b), ZCM15 - (c) and NCM15 - (d) thin films prepared by the dip-coating technique.

Thin film surfaces are regular, homogeneous and compact. The surface profile roughness value R_a is given in Table IV. 9 for each compound. The average values lie between 0.003 and 0.03 µm. The R_a value of CCM15 is the smallest one (R_a = 0.003 ± 0.001 µm) while NCM15 exhibits the biggest value (R_a = 0.032 ± 0.005 µm).

Table IV. 9: Surface profile roughness values of spinel oxide thin films deposited on quartz.

Composition	Surface profile roughness R_a (µm)
Co_2MnO_4	0.019 ± 0.003
NCM15	0.032 ± 0.005
ZCM15	0.007 ± 0.004
CCM15	0.003 ± 0.001

IV.4. Characterization of thin films after heat treatment

IV.4.1. Structural determination by Grazing Incidence X-ray Diffraction (GI-XRD)

The structure of the thin films deposited on different substrates were characterized using grazing incidence X-ray diffraction. Most of the results presented in this section will focus on the NCM15 sample deposited on quartz, alumina, titanium nitride and platinum.

IV.4.1.1. GI-XRD of thin films deposited on quartz substrate

Figure IV. 18 shows GI-XRD patterns of NCM15 thin films deposited on quartz substrate obtained at room temperature, after two different heat treatment temperatures, i.e. 900 ºC and 1000 ºC, according to the dilatometry results described before. The thermal treatments of any oxide thin film deposited on quartz at 1000 ºC, drive to the sample reaction with the quartz substrate and the formation of pure Co_2SiO_4, as shown in Figure IV. 18. In order

to avoid the reaction, the thin films were thus annealed at 900 ºC. At this temperature, a pure spinel oxide cubic phase remains. The thickness of the peaks is narrower after the heating process due to the particle growth with the temperature.

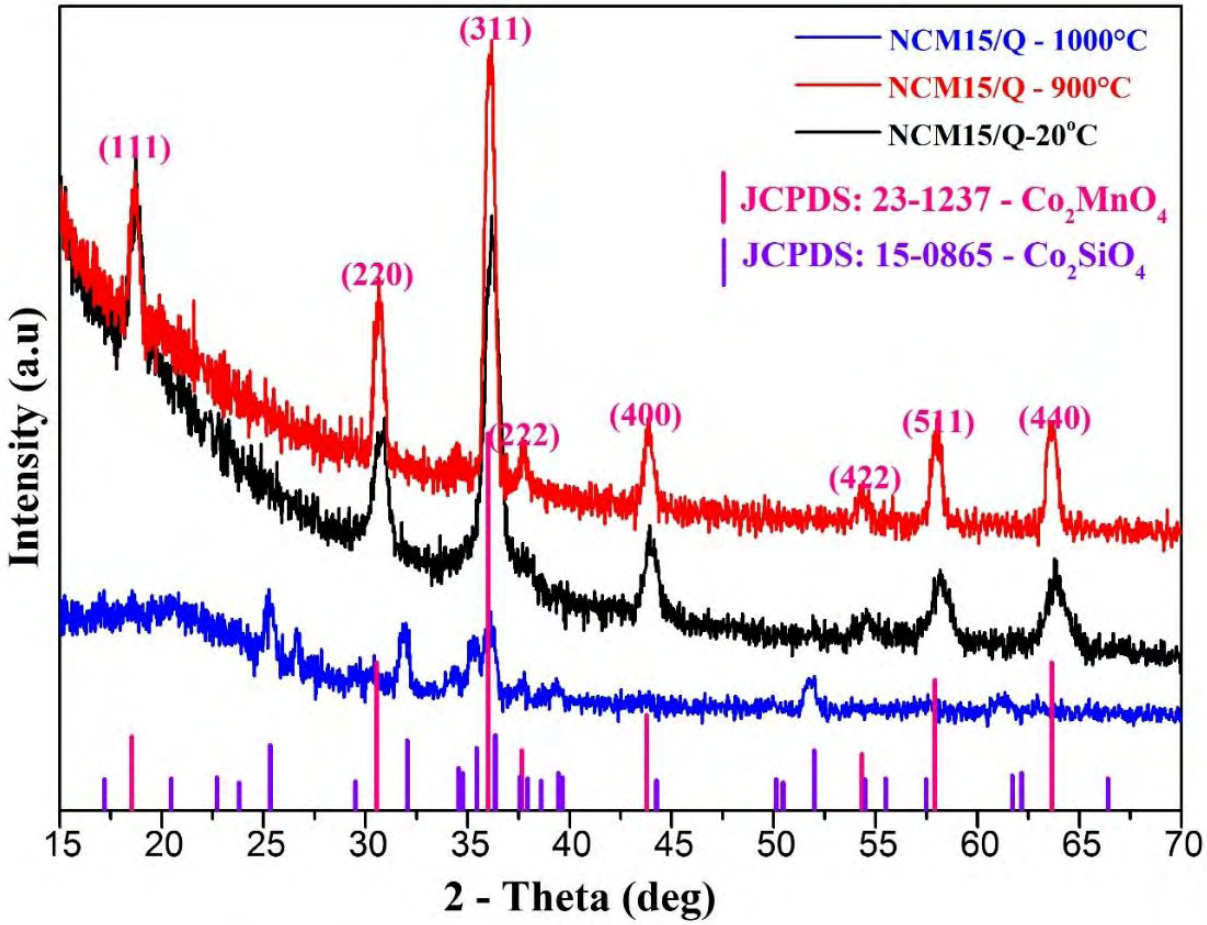

Figure IV. 18: GI-XRD patterns of NCM15 thin films deposited on quartz at room temperature (middle & black), after annealing at 900ºC (top & red) and 1000 ºC (bottom & blue).

GI-XRD of the others thin films deposited on quartz and treated at 900 ºC are shown in Figure IV. 19. All thin films deposited on quartz substrate remain pure after annealing at 900 ºC and the XRD pattern in agreement with the diffraction database of the cubic Co_2MnO_4 spinel oxide (JCPDS: 23-1237).

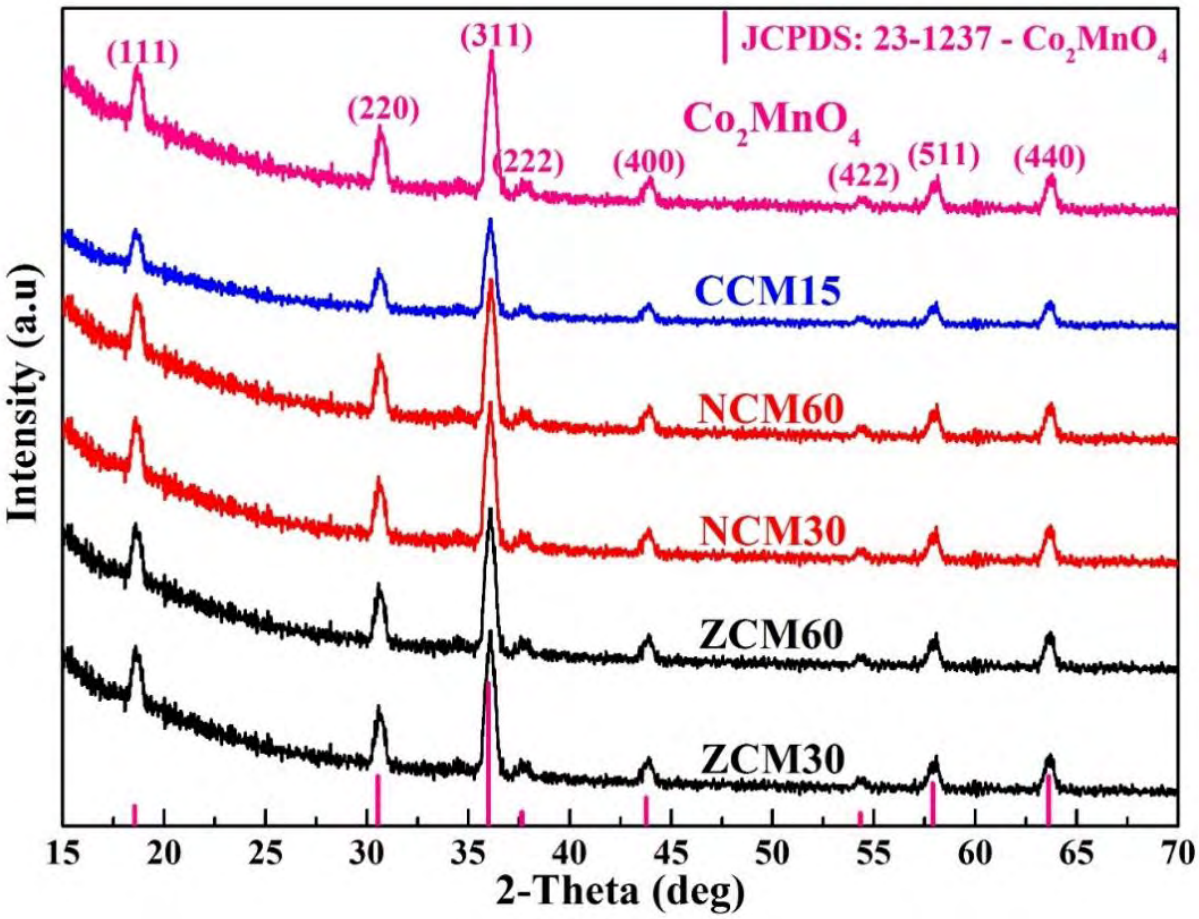

Figure IV. 19: GI-XRD patterns of thin films deposited on quartz and treated at 900 ºC in air.

III.4.1.2. GI-XRD of thin films deposited on alumina

Figure IV. 20 presents the GI-XRD patterns of NCM15 thin film deposited on Al_2O_3 at room temperature, after annealing at 900 ºC and after sintering at 1000 ºC. As for the spinel oxide thin films deposited on quartz substrate, the oxides react with the alumina substrate at 1000 °C to form the $CoAl_2O_4$ phase (JCPDS: 23-1237) while a pure cubic spinel crystal structure is observed after annealing at 900 ºC.

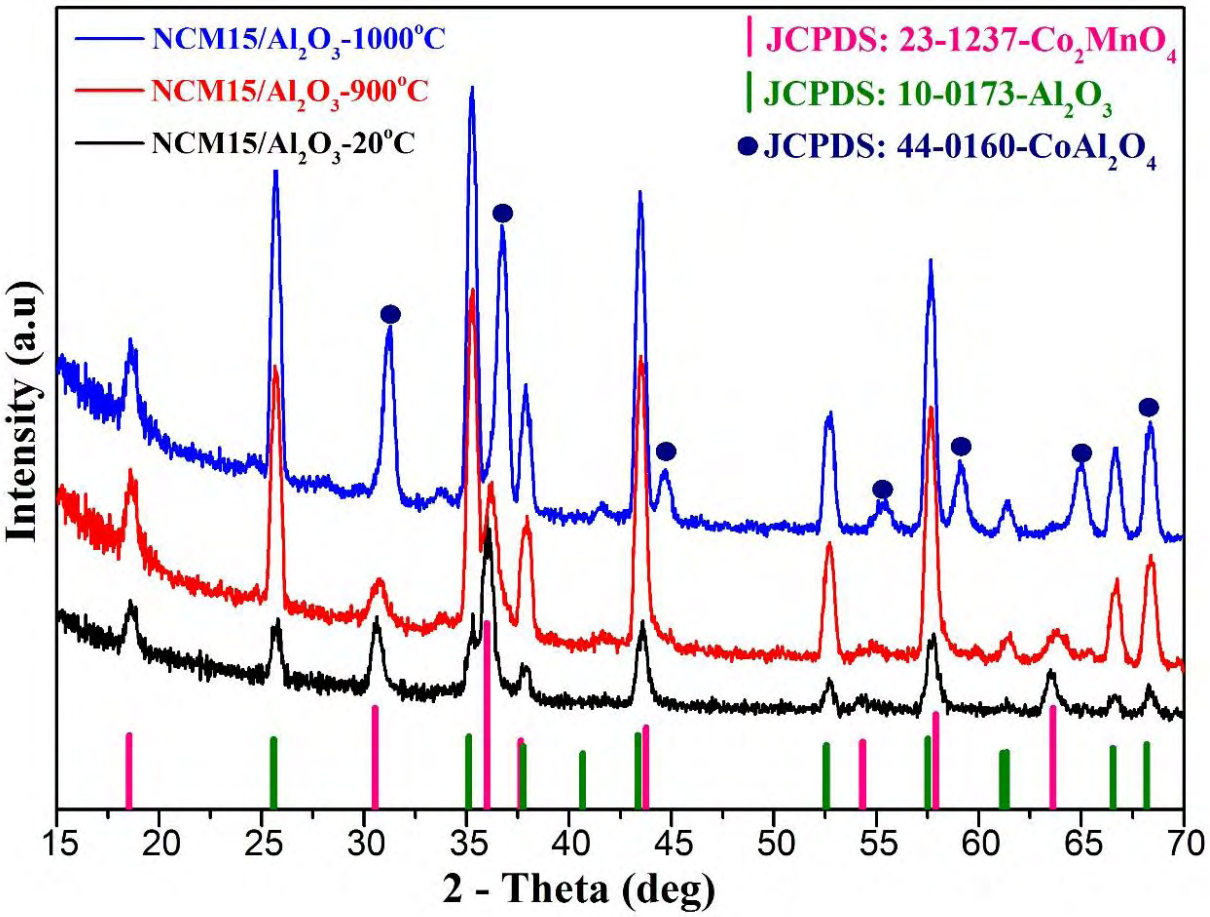

Figure IV. 20: GI-XRD patterns of NCM15 thin films deposited on Al_2O_3 at room temperature (bottom & black), after annealing at 900 ºC (middle & red) and 1000 ºC (top & blue).

III.4.1.3. GI-XRD of thin films deposited on titanium nitride (TiN)

In order to avoid the oxidation of TiN, the thin films deposited on TiN (a high temperature and electrical conductive material) were treated at 900 ºC under nitrogen and argon atmosphere. GI-XRD patterns of NCM15 deposited on TiN at room temperature and annealed at 900 ºC under argon atmosphere and nitrogen are shown in Figure IV. 21. Thin films deposited on titanium nitride are not pure after annealing at 900ºC under argon and nitrogen atmospheres due to the reaction of Ti with oxygen to form the TiO_2 (rutile) phase.

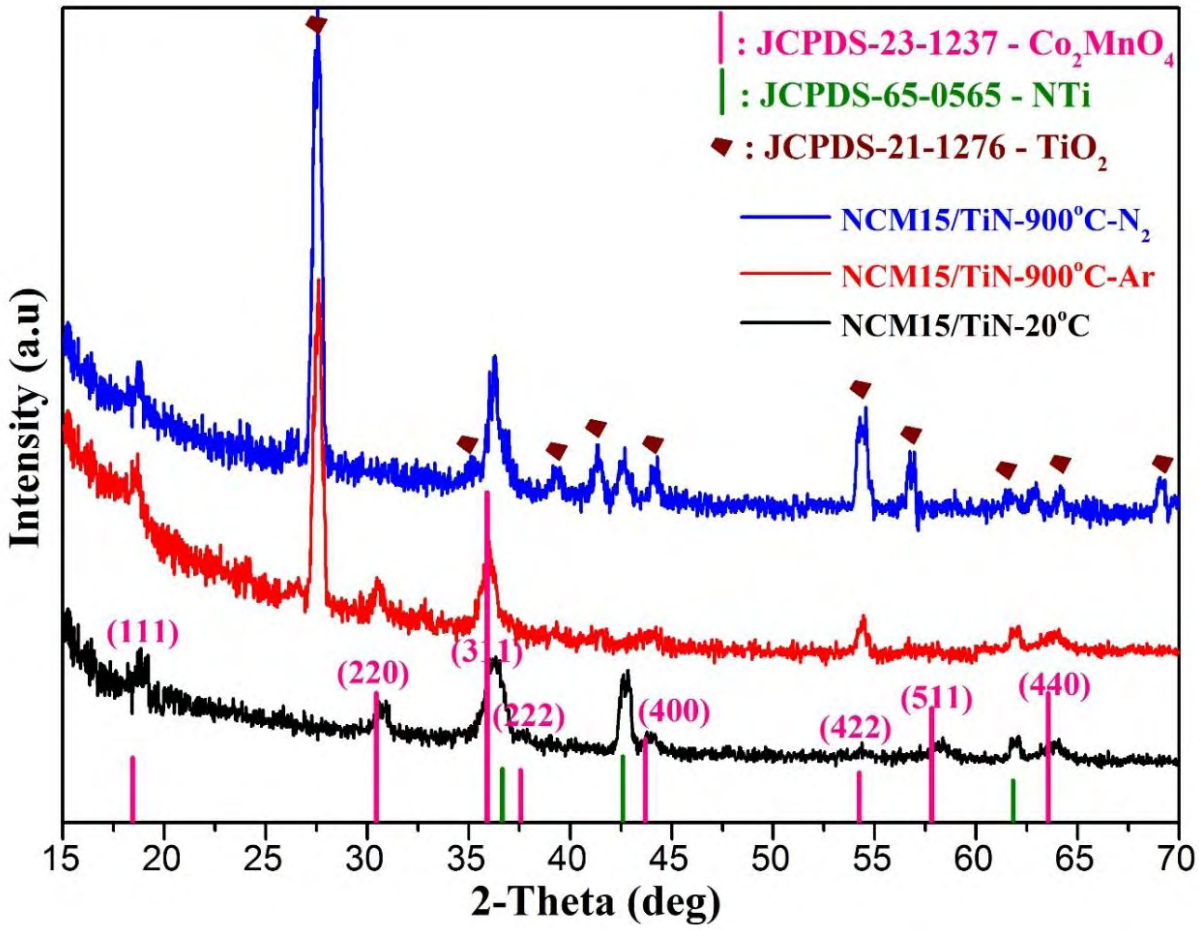

Figure IV. 21: GI-XRD patterns of NCM15 thin films deposited on TiN at room temperature (bottom & black), after annealing at 900 ºC under argon (middle & red) and under nitrogen (top & blue).

III.4.1.4. GI-XRD of thin films deposited on platinum

In order to avoid the reaction of the spinel oxide thin film with the substrate and test the compactness of the layer at the ideal sintering temperature of 1000 °C, also to use a high conductive support for the light absorber oxide layer (i.e. in view of the preparation of a solar cell), we deposited the thin films on platinum. Figure IV. 22 shows GI-XRD patterns of NCM15 thin films deposited on Pt at room temperature and after heat treatment at 900 ºC and sintering at 1000 ºC. GI-XRD shows that spinel oxide thin films are stable and do not react with the platinum substrate up to 1000 ºC.

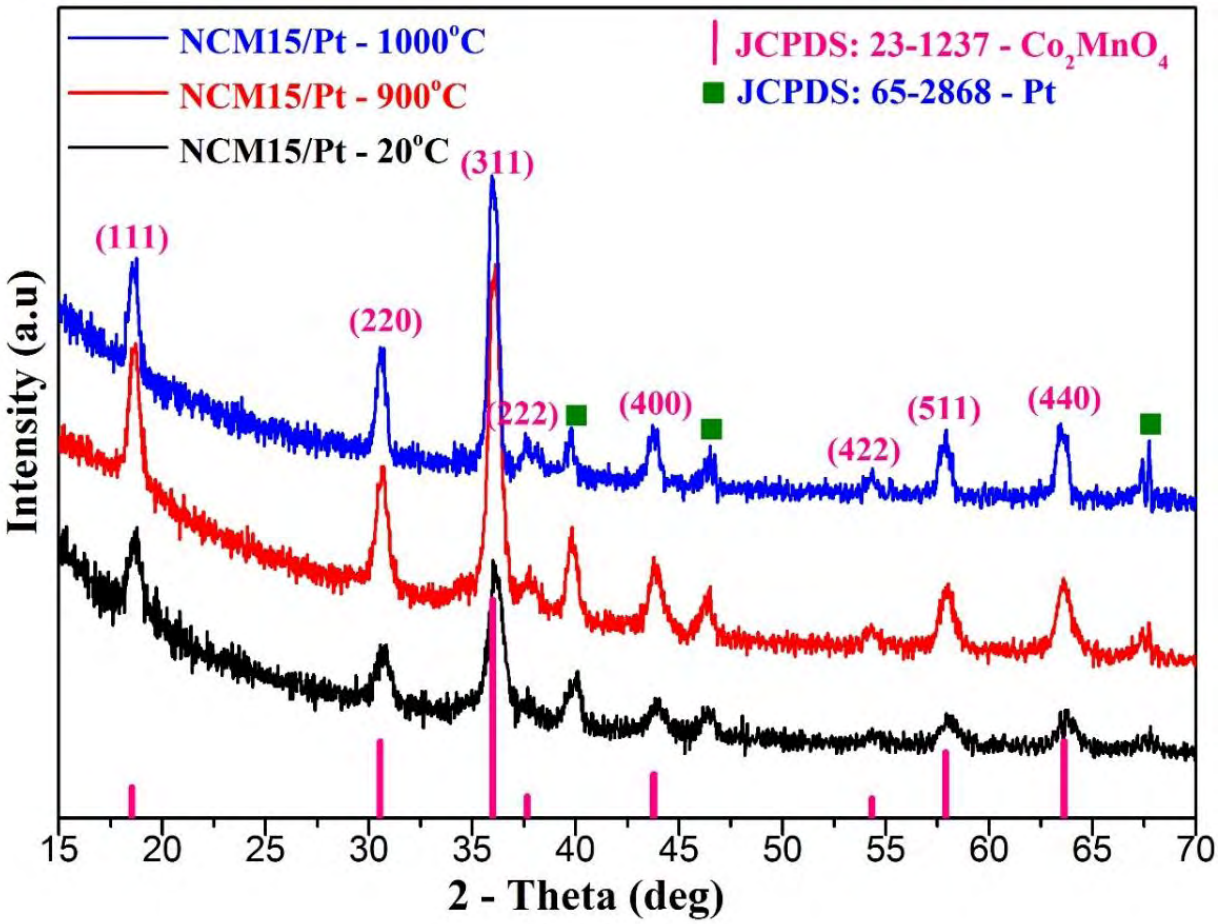

Figure IV. 22: GI-XRD patterns of NCM15 thin films deposited on Pt at room temperature (bottom & black), after annealing at 900 ºC (middle & red) and 1000 ºC (top & blue).

IV.4.2. Microstructure characterization determined by Field Emission Gun Scanning Electron Microscope (FEG-SEM)

Thin films microstructure main features (nanoparticles size and shape, surface morphology and thickness…) were analyzed by FEG-SEM.

Figure IV. 23 shows the FEG-SEM micrographs of the thin films surface deposited on quartz substrate and annealed at 1000 ºC in air. The reaction of the oxides with the quartz substrate lead to the cracking on the samples. The Co_2MnO_4 and CCM15 films present a compact structure while porosity is observed on top of the layer for NCM15 and ZCM15 films.

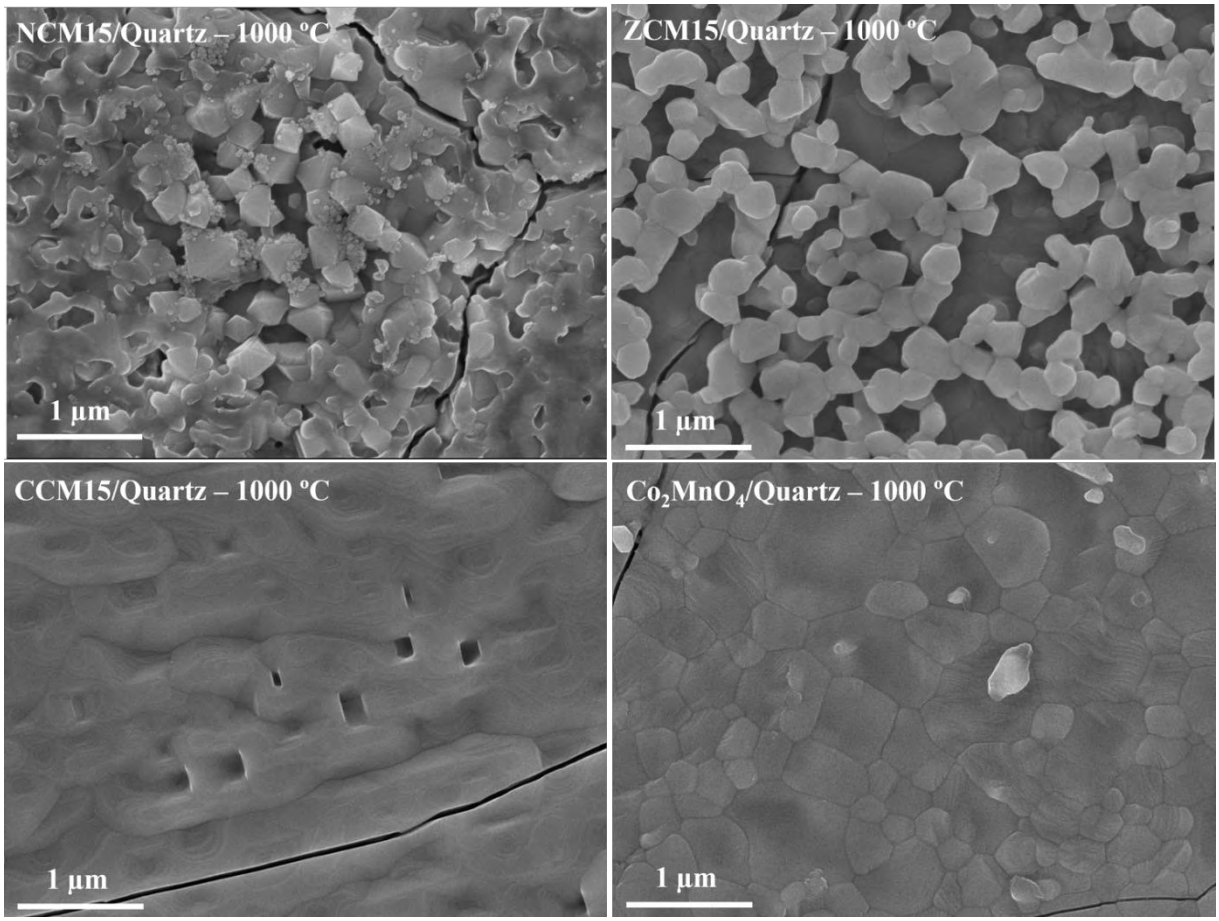

Figure IV. 23: Scanning electron micrographs of thin films deposited on quartz substrate and annealed at 1000 °C in air.

The FEG-SEM pictures of NCM15, ZCM15, CCM15 and Co_2MnO_4 deposited on alumina and annealed at 1000 °C in air are shown in Figure IV. 24. Because of reaction with alumina substrate, surface morphologies are not homogeneous and the structure is not compact, probably because of the reaction of the oxide with the alumina substrate.

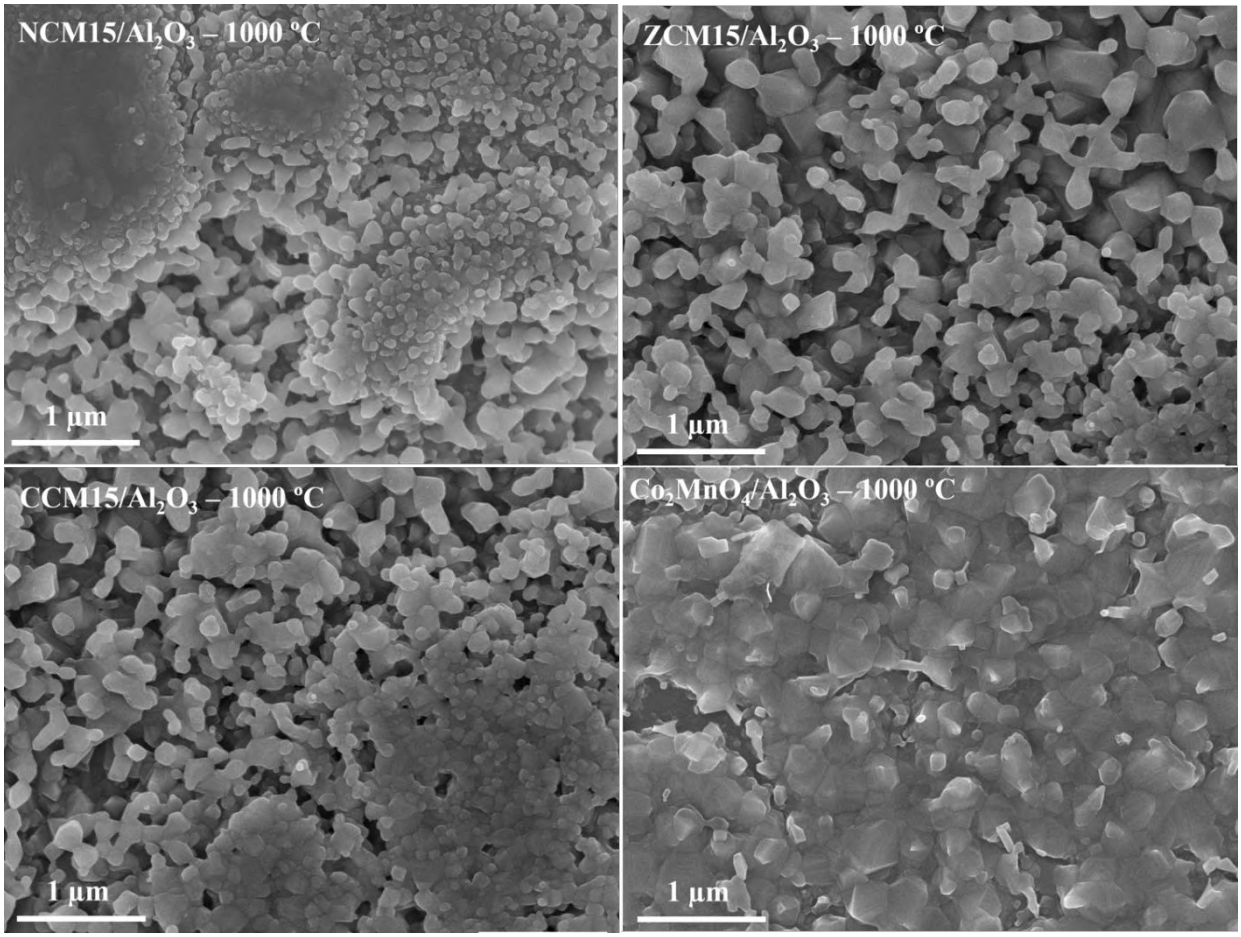

Figure IV. 24: Scanning electron micrographs of thin films deposited on alumina substrate and annealed at 1000ºC in air.

The microstructural characterization of the NCM15 films deposited on quartz, alumina and platinum substrates after heat treatment at 900 ºC obtained by FEG-SEM are presented in Figure IV. 25. Similar surface morphologies are observed for both samples deposited on quartz and alumina substrates. The structure is not compact and a large amount of porosity is observed. The film consists in small particles (~ 100 nm) and larger (~ 300 nm) particles. For NCM15 thin film deposited on platinum and annealed at 900 ºC in air (see bottom & right in Figure IV. 25), few small pores remain on the surface of sample.

The cross-section FEG-SEM images of the NCM15 thin film deposited on quartz and annealed at 900 ºC in air is displayed in the bottom & right in Figure IV. 25. The thickness of about 600 nm (after 3 dip-coatings) is uniform over the substrate. The adherence of the film to

the substrate is improved compared to the room temperature deposited material, without noticeable crack or delamination effect.

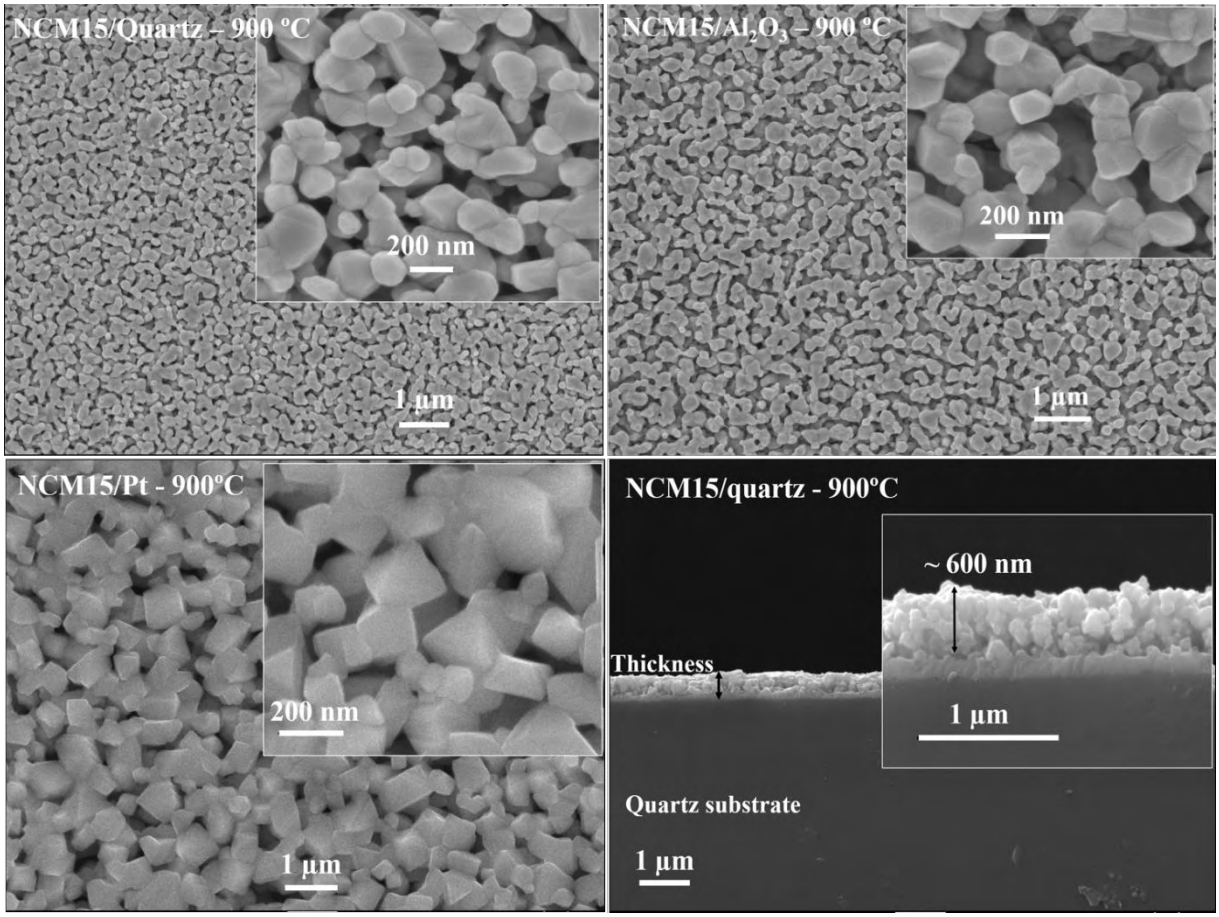

Figure IV. 25: Scanning electron micrographs of the NCM15 sample deposited on quartz (top & left), alumina (top & right), platinum (bottom & left) and cross-section (bottom & right) after annealing at 900 ºC in air.

FEG-SEM image and Energy Dispersive X-ray (EDX) analysis of NCM15 thin films deposited on Pt after heat treatment at 1000 ºC are presented in Figure IV. 26. The surface is more compact. Therefore, the coating reaches a high density at 1000 ºC in air, as predicted by the dilatometry measurements in Figure IV. 11. Energy Dispersive X-ray (EDX) analysis carried out on a NCM15 thin films deposited on Pt after sintering at 1000 ºC indicates the right proportion of elements inserted during the synthesis of the material, showing that these conditions are ideal for the sustainability and compactness of such spinel oxide thin film after sintering.

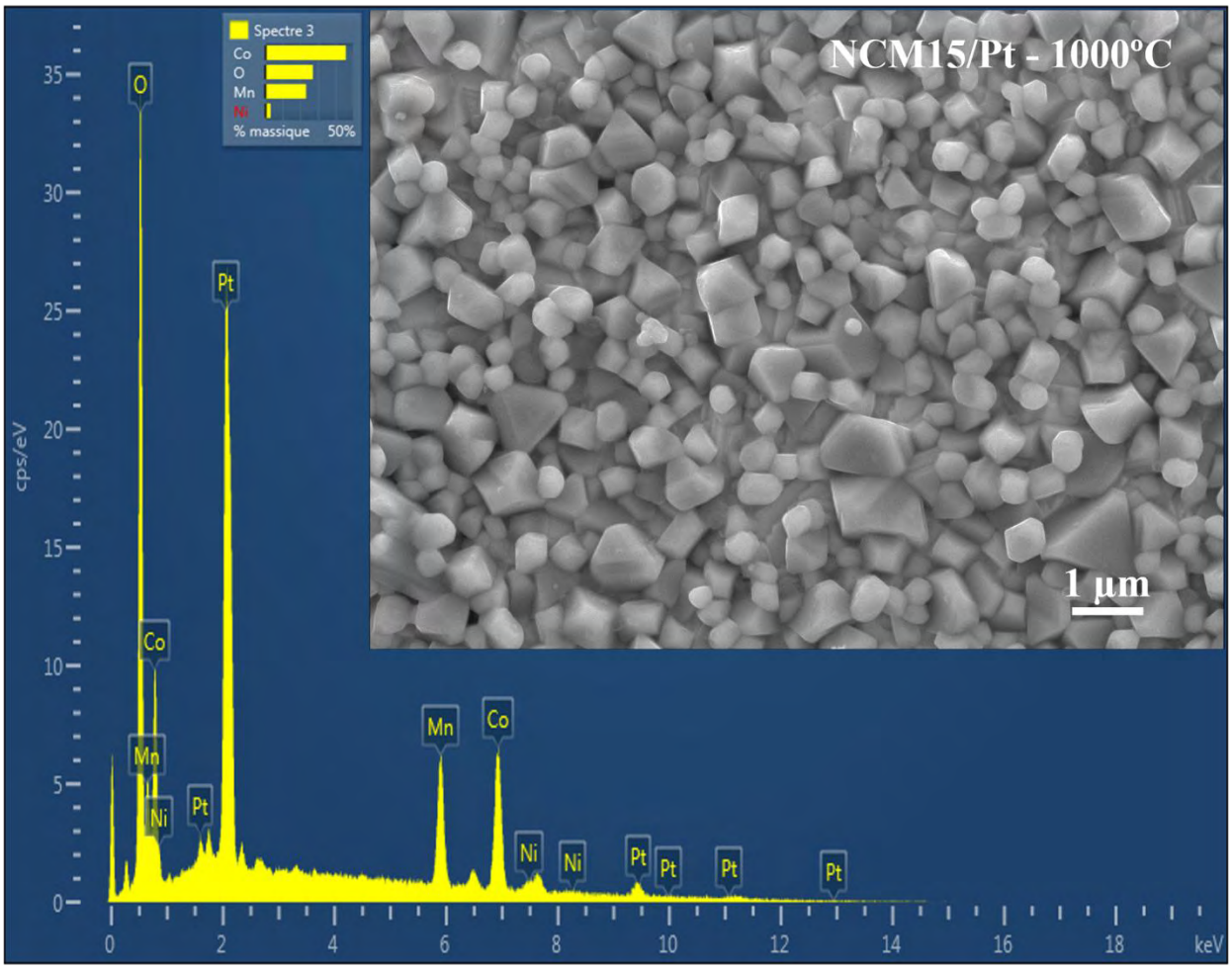

Figure IV. 26: Scanning electron micrograph with EDX analysis of the NCM15 thin film deposited on platinum and treated at 1000 ºC in air.

IV.5. Conclusion

Spinel oxides $M_xCo_{2-x}MnO_4$ (M = Ni, Cu, Zn; x = 0, 0.15, 0.30, 0.60) nanoparticles were synthesized by a simple method based on the inorganic polycondensation. Powder X-ray diffraction analysis shows that all samples crystallize in a cubic spinel structure corresponding to the cubic Co_2MnO_4 phase (database JCPDS: 23-1237), except for $Cu_{0.30}Co_{1.70}MnO_4$ and $Cu_{0.60}Co_{1.40}MnO_4$, which exhibit extra peaks attributed to the presence of Cu-Co-O and CuO phases. The cell parameter increases for the cubic spinel oxide phase of NCM compositions with the addition of nickel, while the lattice constant decreases with increasing Zn content in ZCM compositions due to steric consideration and cation distribution. An average crystallite

size of ~ 15 nm in diameter was determined for NCM compositions, ~ 26 nm for CCM15 composition and ~ 12 nm for ZCM compositions. FEG-SEM observations show that the powder particles are uniform in size and homogeneous in shape. Thermal gravimetric analysis (TGA) demonstrated the thermal stability of samples at high temperature (up to 1000 ºC). The optimal sintering temperature is identical for all compositions and close to about 1000 ºC, as determined by dilatometry analysis, although the shrinkage rate curve tends to indicate an optimal temperature close to 1150 ºC for NCM30 and Co_2MnO_4 compositions.

Homogenous thin films were prepared at room temperature by the dip-coating technique after stabilization of colloidal suspensions using only water and ethanol as solvents. Thin films were deposited on different types of substrates including quartz, alumina, titanium nitride and platinum in order to measure the optical, electrical and thermal stability properties. The structure, the microstructure and the surface roughness of thin films were also carefully analyzed. XRD analysis of the deposited thin films showed a single spinel oxide phase corresponding to Co_2MnO_4. Thin films are homogeneous and well adherent to the substrate. The surface of the films is regular with a low average of roughness (0.003 µm – 0.032 µm).

Thin films were treated at high temperature (900 ºC and 1000 ºC) in order to obtain dense and compact oxide surface. The spinel structure of the films deposited on quartz and alumina is stable at 900 ºC while reactions with both substrates are observed at 1000 ºC, leading to the formation of Co_2SiO_4 and $CoAl_2O_4$, respectively. The spinel oxide thin films deposited on a platinum substrate is kept after annealing at the high temperature (1000 ºC). FEG-SEM images demonstrate that the oxide thin films treated at 900 ºC present some pores while a very dense surface is obtained after heating at 1000 ºC.

IV.6. References

[1] H. Bordeneuve, C. Tenailleau, S. Guillemet-Fritsch, R. Smith, E. Suard, and A. Rousset, "*Structural variations and cation distributions in Mn3−xCoxO4 (0≤ x ≤3) dense ceramics using neutron diffraction data*," **Solid State Sciences,** Vol. **12**, 379-386, **2010**.

[2] R. J. Toh, A. Y. S. Eng, Z. Sofer, D. Sedmidubsky, and M. Pumera, "*Ternary Transition Metal Oxide Nanoparticles with Spinel Structure for the Oxygen Reduction Reaction*," **ChemElectroChem,** Vol. **2**, 982-987, **2015**.

[3] G.-Y. Zhang, B. Guo, and J. Chen, "*MCo2O4 (M = Ni, Cu, Zn) nanotubes: Template synthesis and application in gas sensors*," **Sensors and Actuators B: Chemical,** Vol. **114**, 402-409, **2006**.

[4] C. Ai, M. Yin, C. Wang, and J. Sun, "*Synthesis and characterization of spinel type ZnCo2O4 as a novel anode material for lithium ion batteries*," **Journal of Materials Science,** Vol. **39**, 1077-1079, **2004**.

[5] J. Li, S. Xiong, Y. Liu, Z. Ju, and Y. Qian, "*High Electrochemical Performance of Monodisperse NiCo2O4 Mesoporous Microspheres as an Anode Material for Li-Ion Batteries*," **ACS Applied Materials & Interfaces,** Vol. **5**, 981-988, **2013**.

[6] S. Sun, Z. Wen, J. Jin, Y. Cui, and Y. Lu, "*Synthesis of ordered mesoporous CuCo2O4 with different textures as anode material for lithium ion battery*," **Microporous and Mesoporous Materials,** Vol. **169**, 242-247, **2013**.

[7] G. Zhang and X. W. Lou, "*Controlled Growth of NiCo2O4 Nanorods and Ultrathin Nanosheets on Carbon Nanofibers for High-performance Supercapacitors*," **Scientific Reports,** Vol. **3**, 1470, **2013**.

[8] G. Salek, P. Dufour, S. Guillemet-Fritsch, and C. Tenailleau, "*Sustainable low temperature preparation of Mn3−xCoxO4 (0 ≤ x ≤ 3) spinel oxide colloidal dispersions used for solar absorber thin films*," **Materials Chemistry and Physics,** Vol. **162**, 252-262, **2015**.

[9] W. H. Bragg and W. L. Bragg, "*The Reflection of X-rays by Crystals*," **Proceedings of the Royal Society of London A: Mathematical, Physical and Engineering Sciences,** Vol. **88**, 428-438, **1913**.

[10] R. D. Shannon, "*Revised effective ionic radii and systematic studies of interatomic distances in halides and chalcogenides*," **Acta Crystallographica section a,** Vol. **32**, 751-767, **1976**.

[11] A. Navrotsky and O. J. Kleppa, "*The thermodynamics of cation distributions in simple spinels*," **Journal of Inorganic and Nuclear Chemistry,** Vol. **29**, 2701-2714, **1967**.

[12] P. Sherrer, "*Determination of the size and internal structure of colloidal particles using X rays"*. **Nachr Ges Wiss Goettingen**, p. 394, **1918**.

[13] R. Arulmurugan, B. Jeyadevan, G. Vaidyanathan, and S. Sendhilnathan, "*Effect of zinc substitution on Co–Zn and Mn–Zn ferrite nanoparticles prepared by co-precipitation*," **Journal of Magnetism and Magnetic Materials,** Vol. **288**, 470-477, **2005**.

[14] H. Bordeneuve, "*Etude du système $Mn_{3-x}Co_xO_4$ ($0 \leq x \leq 3$) sous forme de poudres et de céramiques. Structure, microstructure, propriétés magnétiques et électriques. Applications aux thermistances à coefficient de température négatif*," Science et Génie des Matériaux, **Université de Toulouse III - Paul Sabatier**, **2010**.

[15] G. Salek, S. Guillemet-Fritsch, P. Dufour, and C. Tenailleau, "*A Simple Preparation Process of Pure Mn3-xCoxO4 (x = 1, 1.5 and 2) Desert Rose-Like Nanoparticles and Their Optical Properties*," **International Journal of Chemistry,** Vol. **4**, 44-53, **2012**.

[16] B. Gillot, "*DTG Curves of Selective Oxidation of Submicrometer Mixed Valency Spinels: Data Table for the Oxidation Temperature of Transition Metals and Its Relation to the Cation-Oxygen Distance*," **Journal of Solid State Chemistry,** Vol. **113**, 163-167, **1994**.

[17] X. Hao, O. Gourdon, B. J. Liddle, and B. M. Bartlett, "*Improved electrode kinetics in lithium manganospinel nanoparticles synthesized by hydrothermal methods: identifying and eliminating oxygen vacancies*," **Journal of Materials Chemistry,** Vol. **22**, 1578-1591, **2012**.

[18] R. M. Rojas, E. Vila, O. Garcia, and J. L. M. de Vidales, "*Thermal behaviour and reactivity of manganese cobaltites MnCo3 -O4(0.0 ≤ x ≤ 1.0) obtained at low temperature*," **Journal of Materials Chemistry,** Vol. **4**, 1635-1639, **1994**.

[19] H. Bordeneuve, A. Rousset, C. Tenailleau, and S. Guillemet-Fritsch, "*Cation distribution in manganese cobaltite spinels Co3−x Mn x O4 (0 ≤ x ≤ 1) determined by thermal analysis*," **Journal of Thermal Analysis and Calorimetry,** Vol. **101**, 137-142, **2010**.

[20] A. S. A. Chinelatto, E. M. d. J. A. Pallone, A. M. d. Souza, M. K. Manosso, A. L. Chinelatto, and R. Tomasi. "*Mechanisms of Microstructure Control in Conventional Sintering"*, **2012**.

[21] J. Kaneshiro, N. Gaillard, R. Rocheleau, and E. Miller, "*Advances in copper-chalcopyrite thin films for solar energy conversion*," **Solar Energy Materials and Solar Cells,** Vol. **94**, 12-16, **2010**.

[22] M. Grätzel, "*Dye-sensitized solar cells*," **Journal of Photochemistry and Photobiology C: Photochemistry Reviews,** Vol. **4**, 145-153, **2003**.

[23] D. Bouhafs, A. Moussi, A. Chikouche, and J. M. Ruiz, "*Design and simulation of antireflection coating systems for optoelectronic devices: Application to silicon solar cells*," **Solar Energy Materials and Solar Cells,** Vol. **52**, 79-93, **1998**.

[24] S. Guillame, "*Elaboration et caractérisation de films minces absorbants de lumière à partir de dispersions colloïdales de nanoparticules d'oxydes Mn3-xCoxO4 (0≤x≤3) et Cu2O*," Science et Génie des Matériaux, **Université de Toulouse III - Paul Sabatier**, **2013**.

CHAPTER V

PHYSICAL PROPERTIES OF SPINEL OXIDE THIN FILMS $M_xCo_{2-x}MnO_4$ (M = Ni, Cu, Zn; x = 0, 0.15, 0.30, 0.60) AND CHARACTERIZATION OF THIN FILMS PREPARED BY PULSED LASER DEPOSITION

V.1. Introduction

Manganese and cobalt spinel oxides are usually *p*-type semiconductors and present a very strong absorption front in the UV region, which decreases for higher wavelengths but can remain important in the visible region depending on the composition and doping effects. In order to be used as an efficient absorber for solar cells, such material should present a band gap close to 1.5 eV that will correspond to a maximum of absorption of the whole solar spectrum. The charge excitation and transfer within the semiconducting materials are essential for improving the full device performances. Therefore, the absorption areas of the oxide thin films but also their electrical conductivity must be determined in order to prove their efficiency.

This chapter is separated in two different parts:

The first part is dedicated to the optical and electrical properties characterization of the spinel oxides $M_xCo_{2-x}MnO_4$ (M = Ni, Zn, Cu and x = 0, 0.15, 0.30, 0.60) thin films based on the preparation method described in the previous chapter. Thin films were deposited on a quartz substrate for proceeding to the optical (transmittance and reflectance) measurements. Absorption spectra were determined before and after annealing at high temperature, the latter stage being performed to improve the layer compactness and density. Optical band gaps were deduced from the absorption spectra by using Tauc's law. The oxide thin film electrical conductivity was measured by the four-point probe method.

The second part is focused on the thin film structural and physical properties characterizations of Co_2MnO_4 and Cu_2O (the reference *p*-type semiconducting oxide in solar cells) thin films prepared by the pulsed laser deposition (PLD) technique, in collaboration with the NRJ group of Juan Claudio Nino at the University of Florida situated in Gainesville, USA.

V.2. Physical properties of spinel oxide thin films deposited by the dip-coating technique

V.2.1. Optical properties

V.2.1.1. Spinel oxide thin films prepared at room temperature

The spinel oxide thin film optical properties were analyzed after deposition on quartz substrates. Samples optical transmittance and reflectance were determined at room temperature after subtracting the influence of the quartz substrate, by using a Bentham PVE 300 PV characterization system (see details in Chapter II). Transmittance $T(\lambda)$ and reflectance $R(\lambda)$ were measured from the UV (Ultraviolet) region to the NIR (Near-Infrared) region, i.e. 300 – 1100 nm. The average film thickness for all compositions is 600 ± 75 nm after three-dip coating sequences.

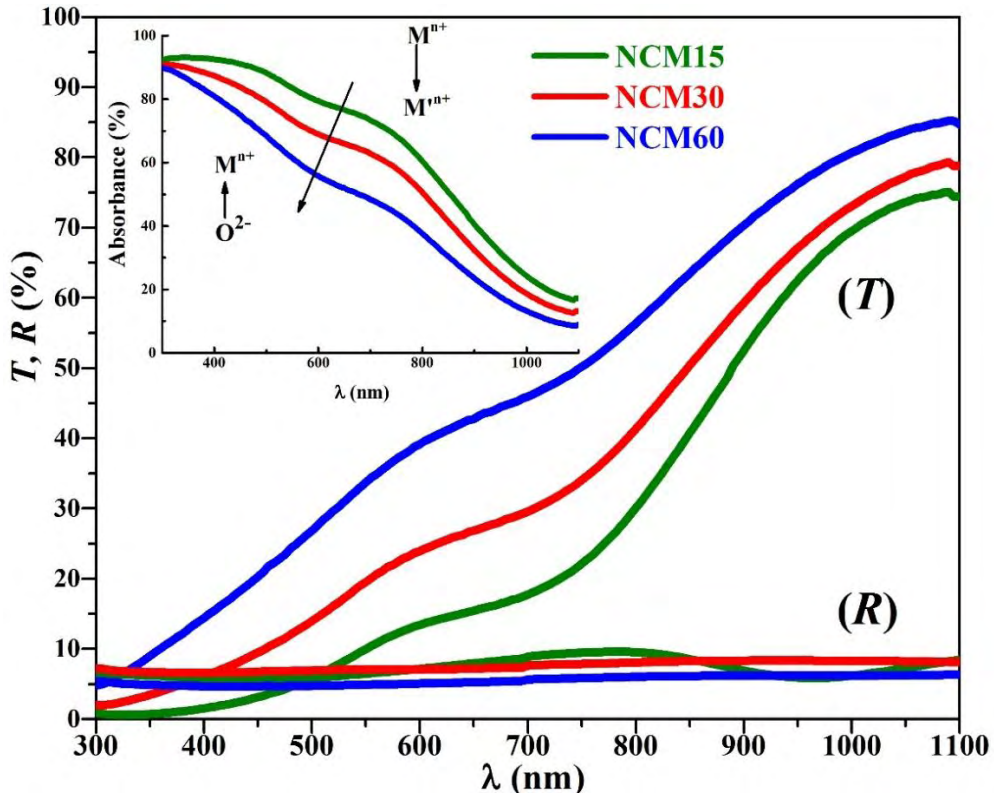

Figure V. 1: Spectral variations of the transmittance, reflectance and deduced absorbance for NCM thin films prepared at room temperature.

Figure V. 1 shows the transmittance and reflectance of our as-prepared NCM compositions. The absorbance is obtained following the simplified relation $A = 1 - T - R$ (see inset in Figure V. 1). The reflectance of NCM compositions is low ($R(\lambda) < 10$ %) over the whole spectral range. Thin films exhibit high transparencies in the infrared spectral region. The absorbance spectrum exhibits two strong absorption bands at around 450 nm and 750 nm in wavelengths for all three compositions, and decreases with increasing Ni concentration. The

first front of absorbance observed in the UV region remains very high whatever the sample (80 % < $A(\lambda)$ < 94 %), usually attributed to the energy transition from O 2*p* to *M* 3*d*-e_g (where *M* is the metal), while the second front of absorbance in the visible region (with a peak ~ 700 nm) corresponds to the energy transition between two metal cations (*M* and *M'*). This latter peak was also attributed to intra-bands transitions. A blueshift is observed with the increasing Ni concentration, which can be explained by the doping of a metal with a higher atomic number than for Co (and Mn), which contribute to more localized orbitals and less overlapping. The interaction with the oxygen anion is also lowered by doping [1-3].

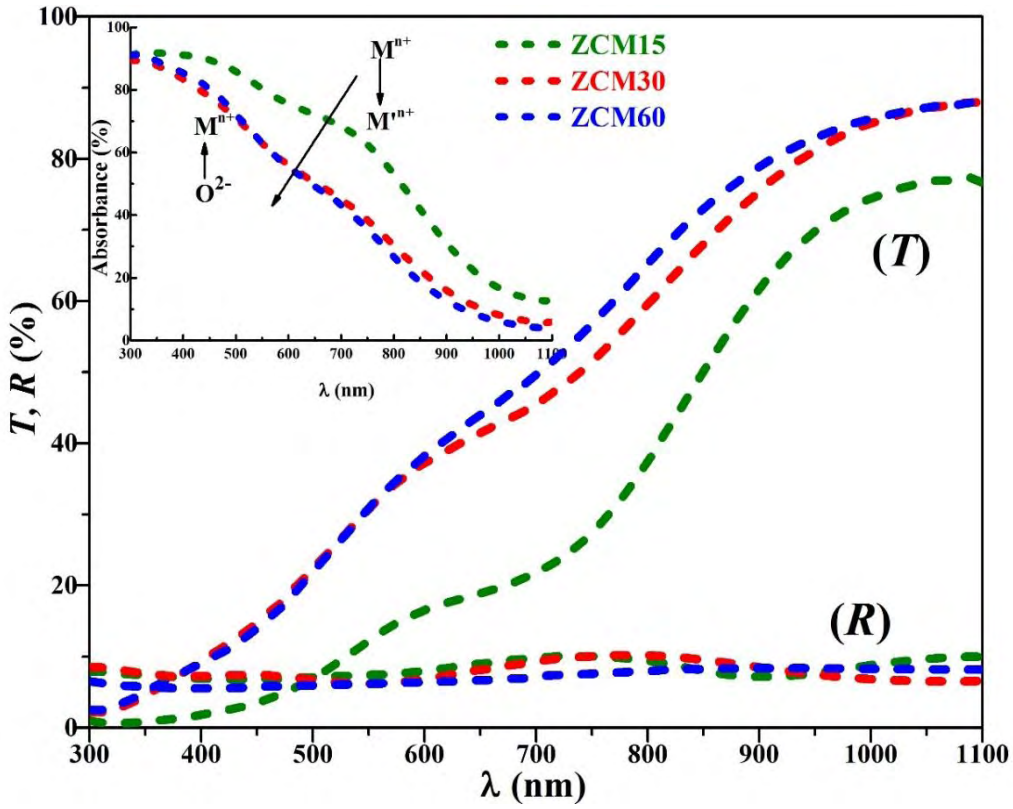

Figure V. 2: Spectral variations of the transmittance, reflectance and deduced absorbance for ZCM thin films prepared at room temperature.

Figure V. 2 presents the optical properties of our ZCM thin films. Alike the NCM thin compounds, the spectral distribution of T(λ) and R(λ) of the ZCM thin films were measured at the normal incidence in the 300-1100 nm wavelength range. The reflectance R(λ) is also lower than 10 % over the whole spectral range. The spectral behavior of A(λ) shows two absorption

band at λ ~ 450 and 750 nm. The absorbance of ZCM15 sample is higher than that of ZCM30 and ZCM60 samples. The larger quantity of zinc introduced in the material will contribute to fill up the energy bands with electrons and decrease the band gap width [4].

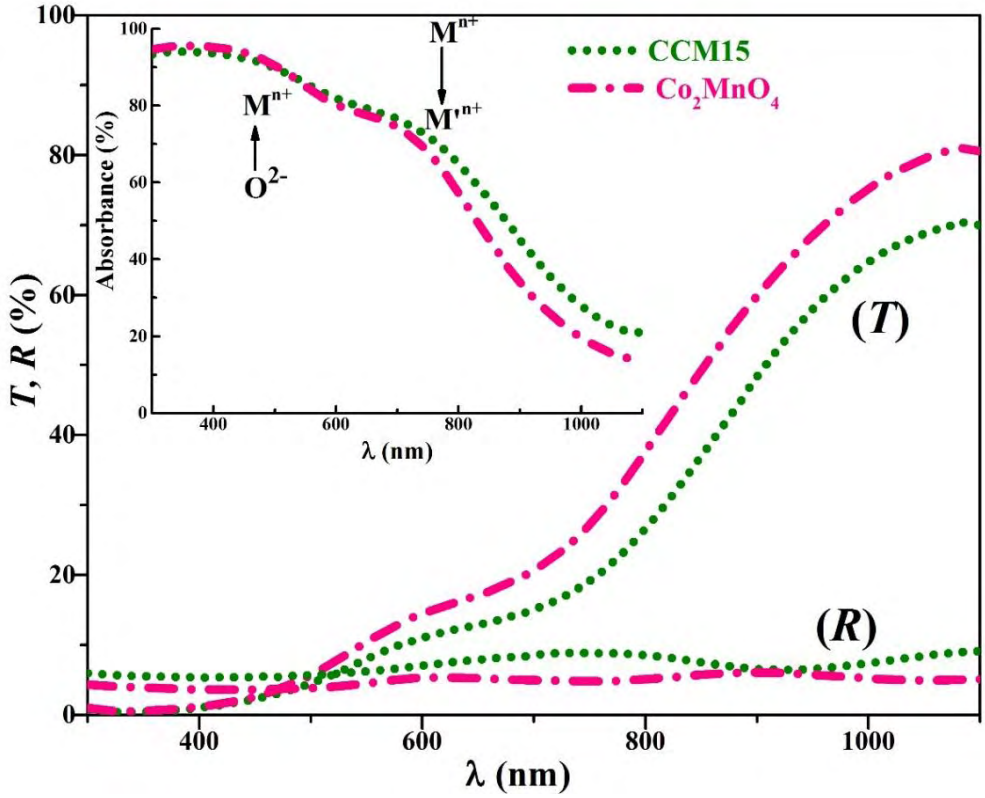

Figure V. 3: Spectral variations of the transmittance, reflectance and deduced absorbance for CCM15 thin films compared to Co_2MnO_4.

Optical properties of the CCM15 sample are compared with the Co_2MnO_4 un-doped sample in Figure V. 3. Both compositional materials show a high absorbance in the UV region, which decreases in the visible region and is lower than 20 % in the infrared area. Just like for the previous samples, two strong absorption bands are observed at around 450 nm and 750 nm in wavelengths that are again usually ascribed to a ligand-metal $O^{2-} \rightarrow M^{n+}$ charge transfer and metal-metal $M^{n+} \rightarrow M'^{n+}$ transition, respectively. Thus, these spinel oxide thin films show high absorbance properties (A(λ) > 65 %) over the UV-VIS region, interesting for photo-absorption applications.

Figure V. 4 shows the spectral variations of the transmittance, reflectance and deduced absorbance of NCM15, ZCM15 and CCM15, in comparison with Co_2MnO_4. The absorbance curves are similar and exhibit two absorption bands in the same regions (with maxima at ~ 450 and 750 nm). The absorbance of the thin films is above 90 % in the UV region, from 90 % down to 65 % in the visible region (400-700 nm) and decreases below 10 % for the infrared region, showing the variety of optical range performances of such materials and their capability to be integrated in optoelectronic devices.

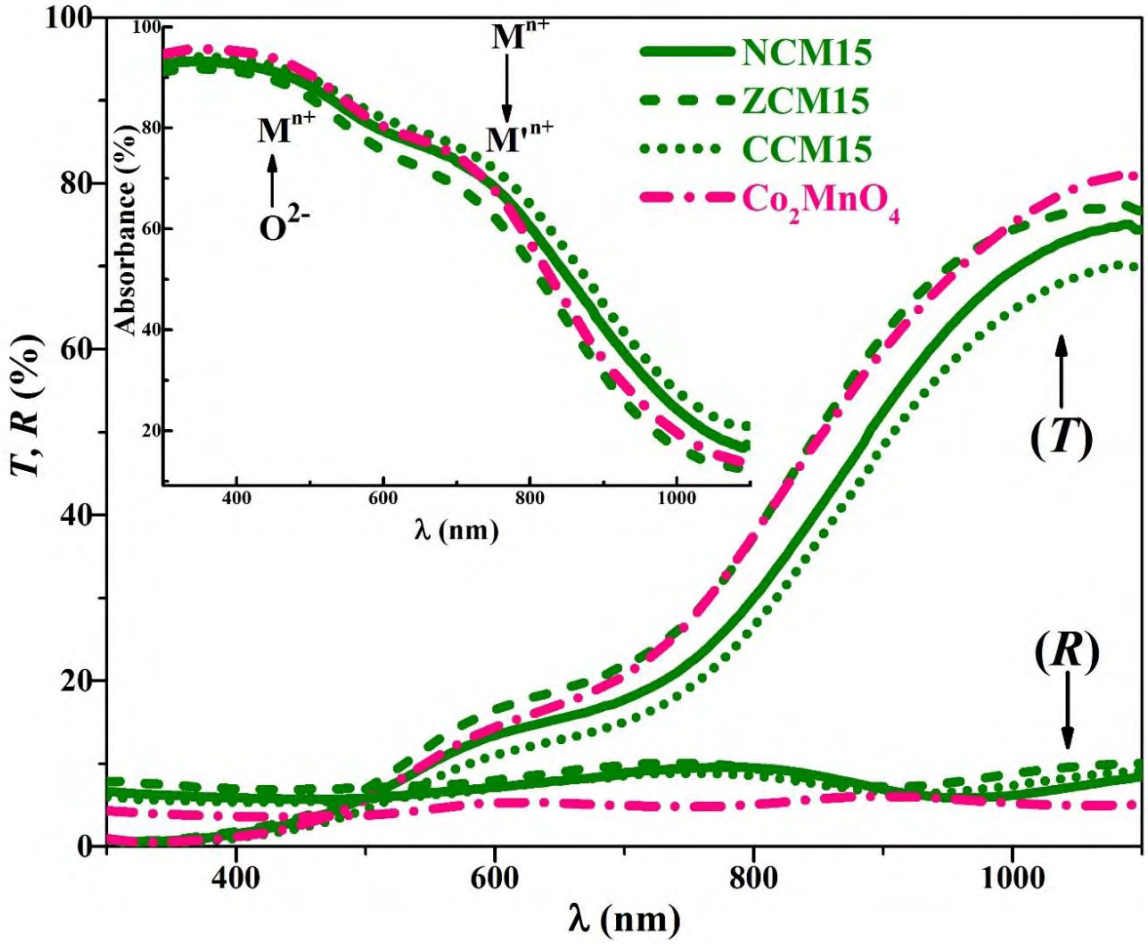

Figure V. 4: Spectral variations of the transmittance, reflectance and deduced absorbance for NCM15, ZCM15 and CCM15 thin films prepared at room temperature, and Co_2MnO_4 thin film used as a reference sample.

V.2.1.2. Spinel oxide thin films heat treated at 900 °C

Homogenous thin films of spinel oxides were obtained at room temperature after dip-coating in colloidal dispersions. But the compactness and mechanical strain of the films are then not good enough for allowing their integration in an optoelectronic device where high conductivity is usually required. Therefore, the spinel oxide thin films underwent a heat treatment at high temperature (900 °C in air for 10 hours, 80 ºC/hour of heating and cooling rates, although one hundred degrees lower than the ideal temperature of 1000 °C required for a full sintering for most compounds as determined by dilatometry measurements, due to reaction problems with the substrate for further heating). The pure spinel oxide phase compactness is then still considerably improved but porous (see chapter IV). The oxide thin film optical properties were measured at room temperature, after subtracting the influence of the quartz substrate.

The spectral variations of the transmittance, reflectance and deduced absorbance for the NCM composition thin films annealed at 900 ºC are shown in Figure V. 5. The absorbance is increased in the Visible (VIS) range after thermal treatment of the spinel oxide thin films in comparison with the curve before heat treatment (see inset in Figure V. 5). The absorbance curve of NCM15 sample is almost constant over the whole UV-VIS range (from 300 nm to 800 nm).

Thin films of ZCM compositions also exhibit a high absorbance in the UV-VIS region with $A(\lambda) > 85$ % for ZCM15 from 300 to 750 nm (see inset in Figure V. 6). The absorbance curves of ZCM30 and ZCM60 are very close and lower than that of ZCM15 sample after 500 nm. Still, $A(\lambda)$ is higher than 65 % at 800 nm, just after the second absorption edge. The absorbance of ZCM thin films was increased in comparison with that before annealing (see the solid lines inset in Figure V. 6).

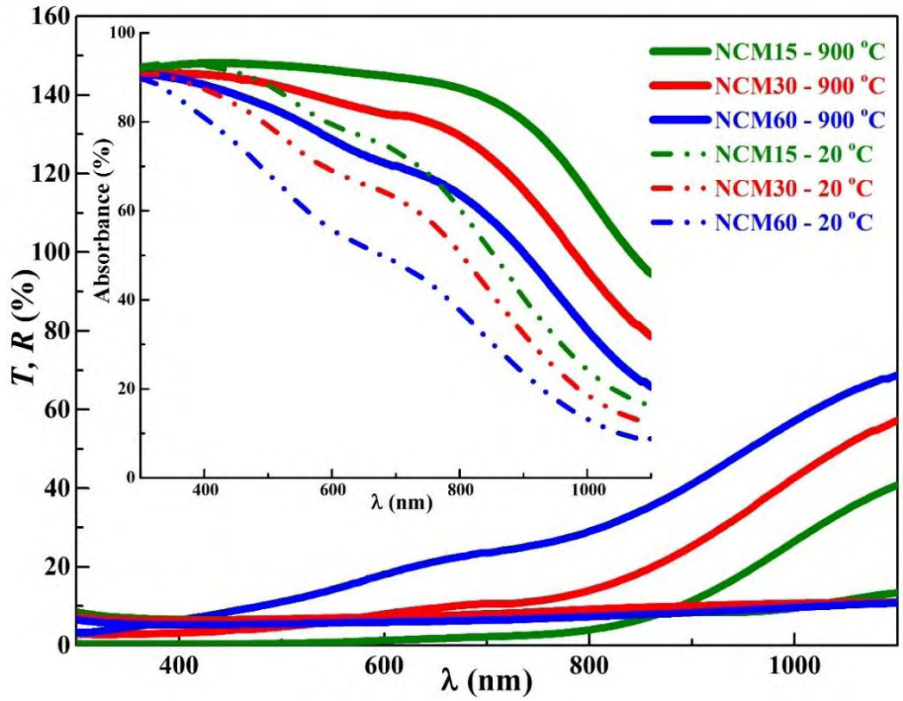

Figure V. 5: Spectral variations of the transmittance, reflectance and deduced absorbance for NCM thin films annealed at 900 ºC.

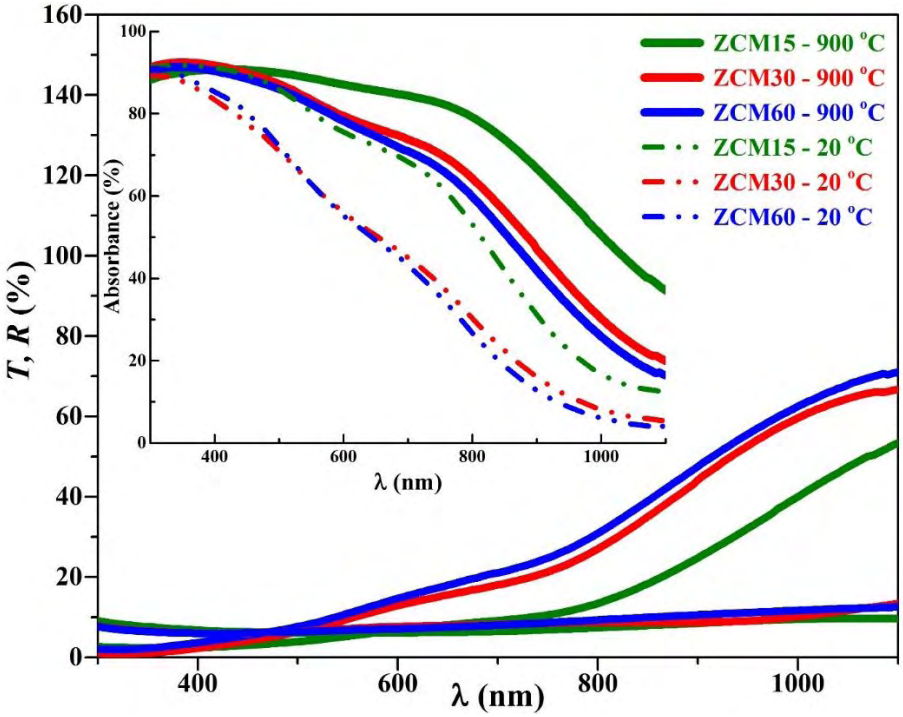

Figure V. 6: Spectral variations of the transmittance, reflectance and deduced absorbance for ZCM thin films annealed at 900 ºC.

Transmittance, reflectance and deduced absorbance of CCM15 and Co_2MnO_4 thin films after heating up at 900 ºC are presented in Figure V. 7. Both films are highly absorbing over the UV-VIS region with $A(\lambda) > 90$ %. This is due to the improved film compactness with the annealing process (see FEG-SEM micrographs in Figure V. 9).

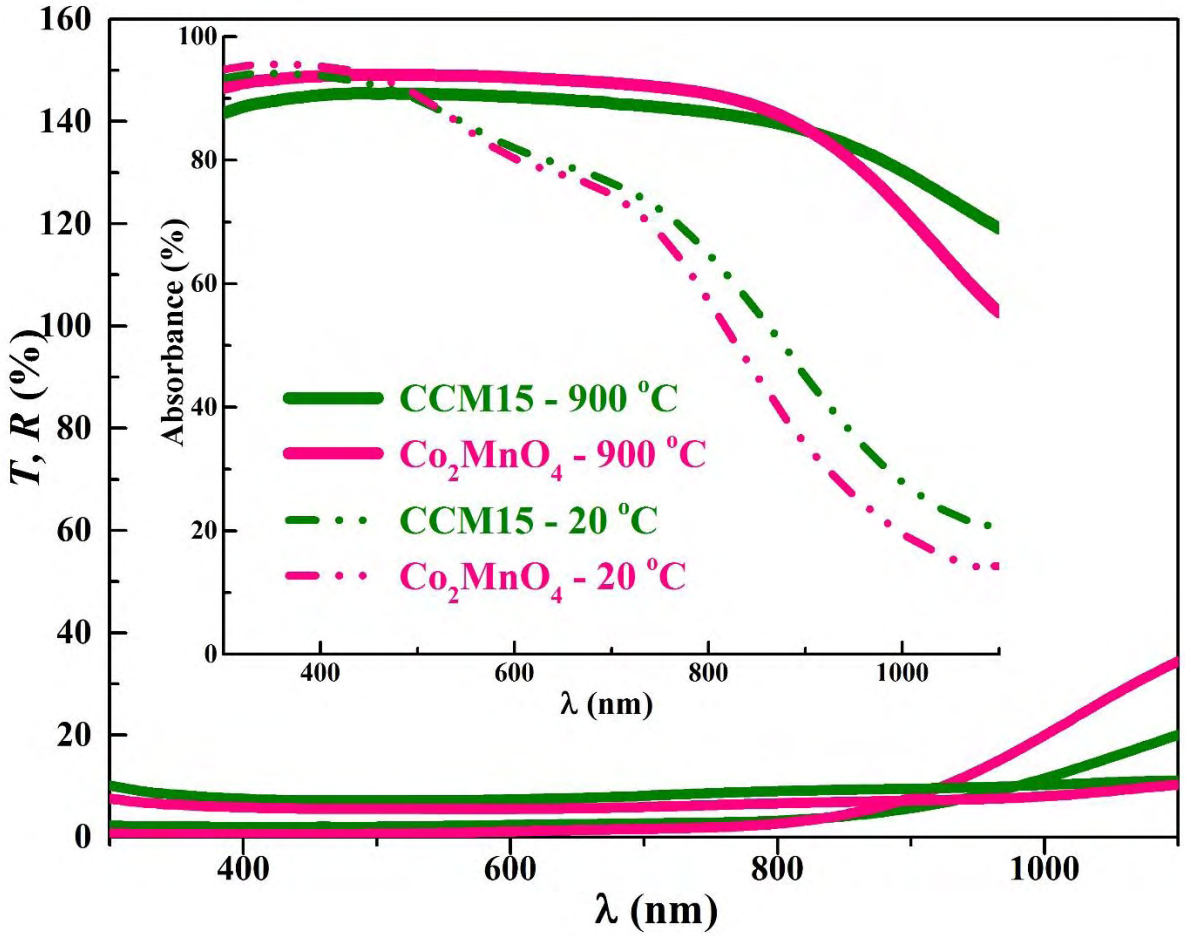

Figure V. 7: Spectral variations of the transmittance, reflectance and deduced absorbance for CCM15 and Co_2MnO_4 thin films annealed at 900 ºC in air.

Thus, the absorbance is increased for all the materials under study after thermal treatment. In order to see the effect of the doping element over the spectral absorption of Co_2MnO_4 after annealing at 900 °C we plotted in Figure V. 8 the optical main features of all three doped samples with 15 at. % of Ni, Zn and Cu, in comparison with Co_2MnO_4. The absorbance of NCM15 is higher than that of CCM15 and ZCM15 in the UV-VIS regions,

probably due to an increasing radius of the doping element. Pure Co_2MnO_4 show the highest absorbance over this spectral range in comparison with Ni, Zn and Cu doped samples.

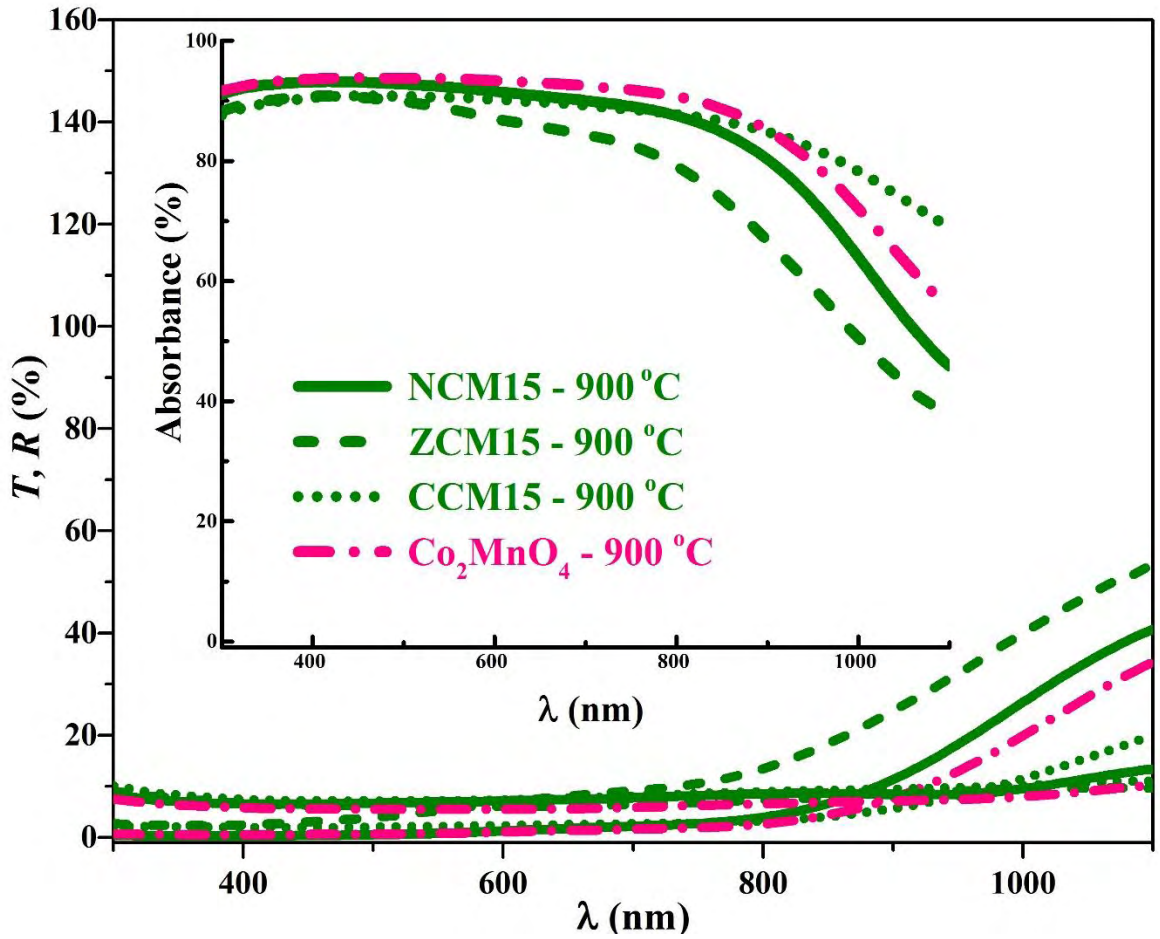

Figure V. 8: Spectral variations of the transmittance, reflectance and deduced absorbance for NCM15, ZCM15 and CCM15 thin films, in comparison with Co_2MnO_4, annealed at 900 °C.

Figure V. 9 shows the FEG-SEM micrographs of the NCM15, ZCM15, CCM15 and Co_2MnO_4 thin films deposited on quartz substrate and annealed at 900 °C in air, to recall the improved film compactness with the annealing process, which explains the large increase in light absorption.

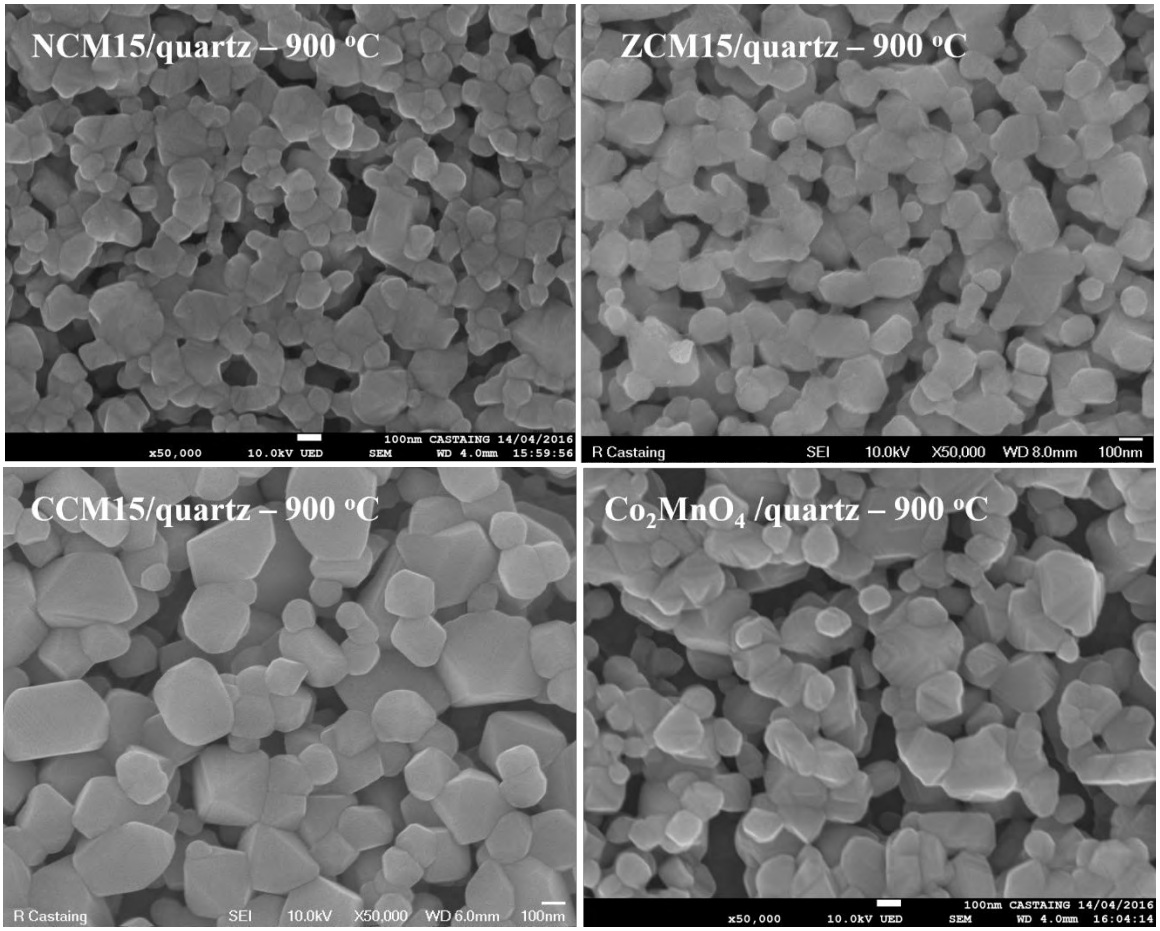

Figure V. 9: Surface SEM micrographs of NCM15, ZCM15, CCM15 and Co_2MnO_4 deposited on quartz substrate and annealed at 900 °C.

V.2.1.3. Band gap determination

The band gap of a material can be estimated by first-principles calculations and density functional theory (DFT) [5] as presented in chapter III, and can also be determined experimentally by ellipsometry measurements or studying its optical transmission and reflection spectra. We have experimentally determined our spinel oxide band gaps by using the optical properties measurements described above and following Tauc's relation (Equation II-7) [6]. Figure V. 10 shows the plots of d [ln ($\alpha h\nu$)] / d ($h\nu$) as a function of photon energy ($h\nu$) for all samples.

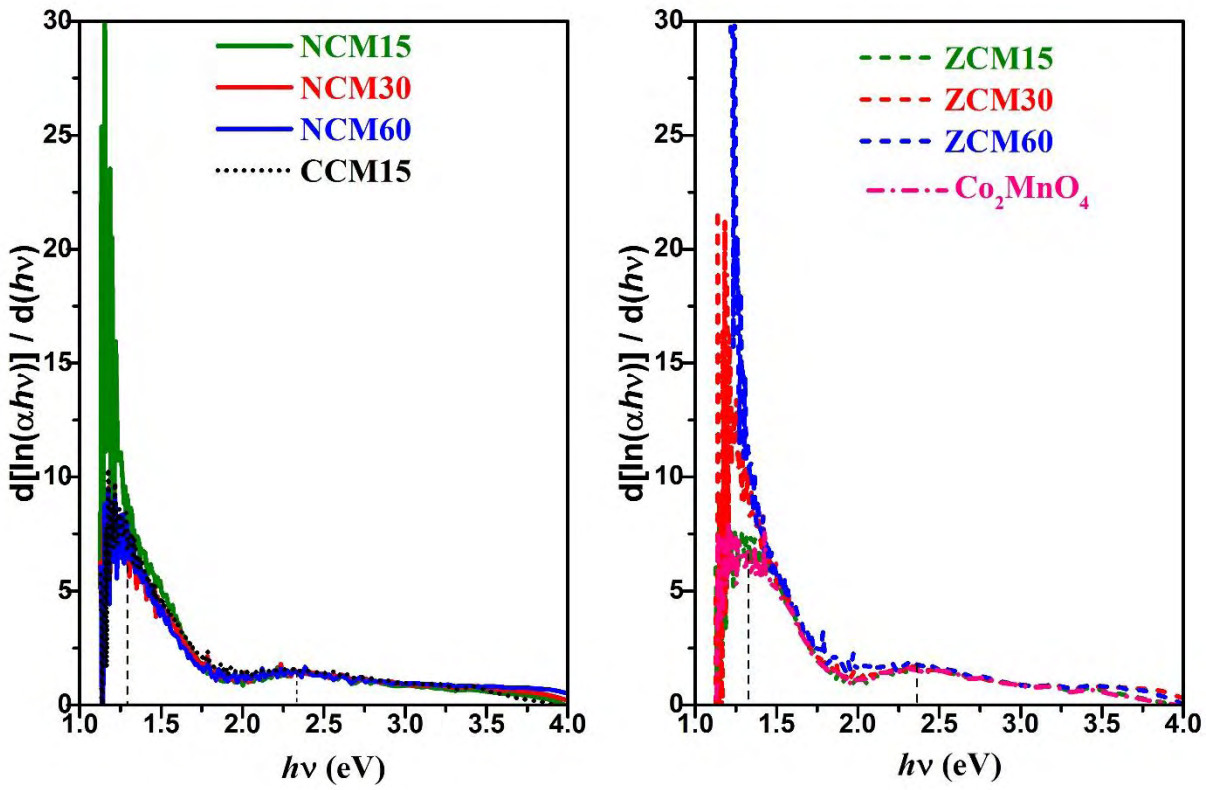

Figure V. 10: Plot of d [ln (αhν)] / d (hν) as a function of photon energy hν for all samples.

Two E_g values are evidenced for each composition, which correspond with the peak maxima observed in Figure V. 10. These E_g values were used to plot ln ($\alpha h\nu$) as a function of $ln\ (h\nu - E_g)$ in order to determine the slope, thus the value of m (see chapter 2 for more details).

Figure V. 11 shows two values of optical band gap and the linear fit always gives the sample slope value of ½, which indicates that direct transitions occur in the spinel oxide thin films under study.

The band gap values were estimated for the thin films obtained at room temperature after dip-coating and once annealed at 900 ºC in air.

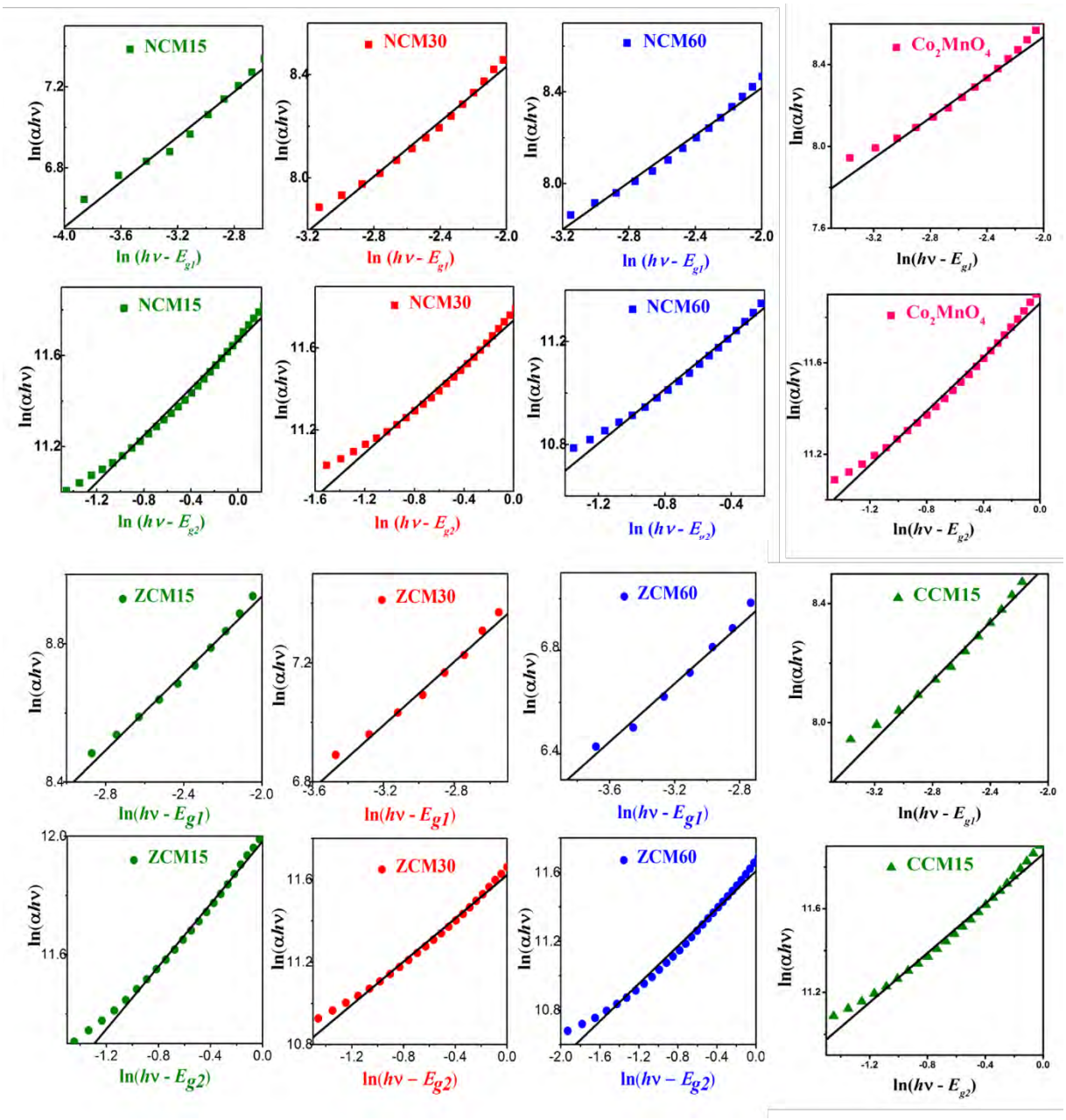

Figure V. 11: Plot of ln (αhν) as a function of ln (hν – E_g) for each spinel oxide.

V.2.4.1. Band gaps of spinel oxide thin films obtained at room temperature

The band gaps for each composition NCM15, NCM30 and NCM60 were estimated by the interception of the straight line from the $(\alpha h\nu)^2$ variation as a function of photon energy ($h\nu$) extrapolated to the $(\alpha h\nu)^2 = 0$ value, as represented in Figure V. 12.

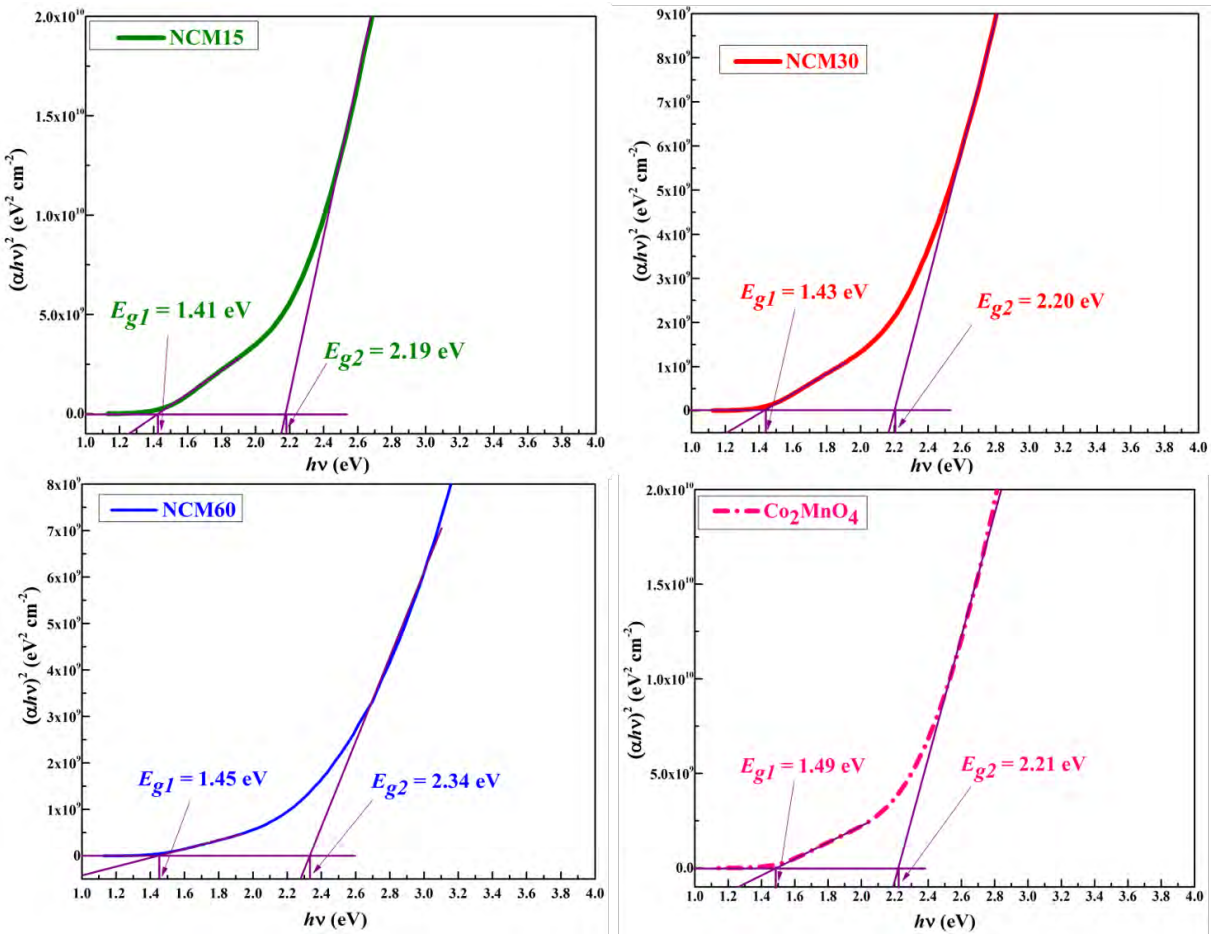

Figure V. 12: $(\alpha h\nu)^2$ vs $(h\nu)$ variations and band gap extrapolations for NCM thin films deposited on quartz, in comparison with Co_2MnO_4 obtained at room temperature.

Each thin film exhibits two band gap values, which correspond to the two strong absorption bands described earlier in the regions close to 450 and 750 nm in wavelengths. The first optical band gap E_{g1}, corresponding to the larger absorption band at about 750 nm, is usually described in the literature by an energy transition between two metal cations, although some discrepancies remain. While the second large optical band gap E_{g2} measured in the region under analysis, corresponding to the smaller absorption band at about 450 nm, can be related to an energy transition from oxygen anion to a metal cation [7-9]. The observed band gaps increase from 1.41 to 1.45 eV and from 2.19 to 2.34 eV with increasing Ni content, but remain very close to those of the reference material Co_2MnO_4.

Figure V. 13 shows the $(\alpha hv)^2$ variation as a function of the photon energy (hv) for ZCM thin films in comparison with Co_2MnO_4.

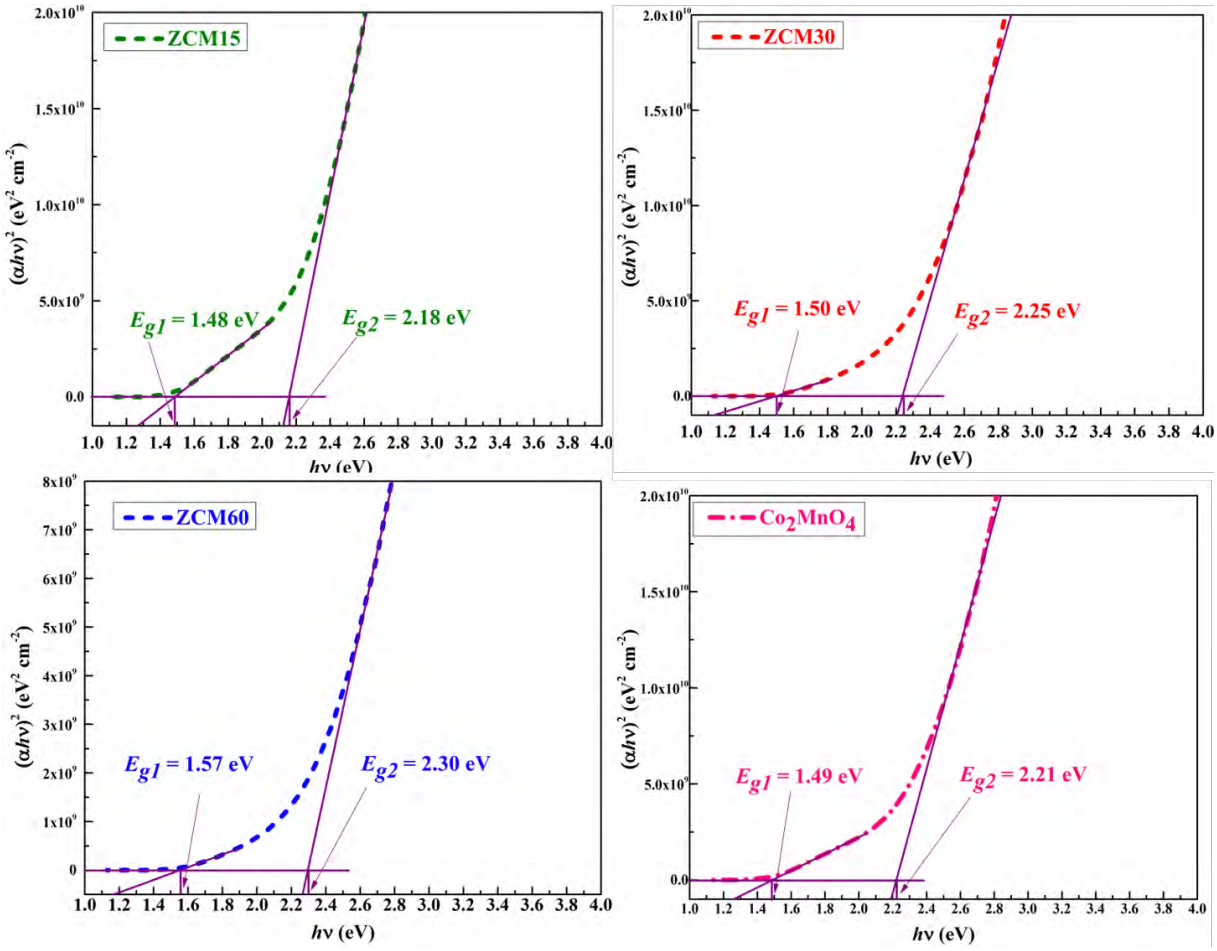

Figure V. 13: $(\alpha hv)^2$ vs (hv) variations and band gap extrapolations for ZCM thin films deposited on quartz, in comparison with Co_2MnO_4 obtained at room temperature.

Each thin film presents two band gaps associated with two strong absorption bands. The first and second optical band gaps increase from 1.48 to 1.57 eV and 2.18 to 2.30 eV, respectively, which can be explained by the reduction of the crystallite size with increasing Zn content. The doping by Zn with a higher atomic number in the cobalt manganese oxide also contribute to more localized orbitals and less overlapping. The interaction with the oxygen anion is also lowered with doping, which can explain the E_{g2} gap increase due to charge transfer from the oxygen 2*p* orbitals to the metal *d* orbitals. With the presence of Zn^{2+} cations in tetrahedral sites and substituted to Co^{2+}, there is no impact on the overall charge neutrality and

in particular on the octahedral site cation distribution but E_{g1} tend to increase with the amount of Zn^{2+} as the tetrahedral orbital are more localized.

Two band gap values of 1.41 and 2.18 eV, slightly smaller than that of Co_2MnO_4, were determined at room temperature for the CCM15 composition (see Figure V. 14). Cu^{2+} is preferentially situated on the octahedral sites. Cu^{2+} cations induce the manganese oxidation on octahedral site. The valence band, which is essentially composed of metal orbitals defining the highest occupied level for the first optical band gap, E_{g1}, is filled in with more electrons as the doping Cu atomic number is increased and this band gap decreases.

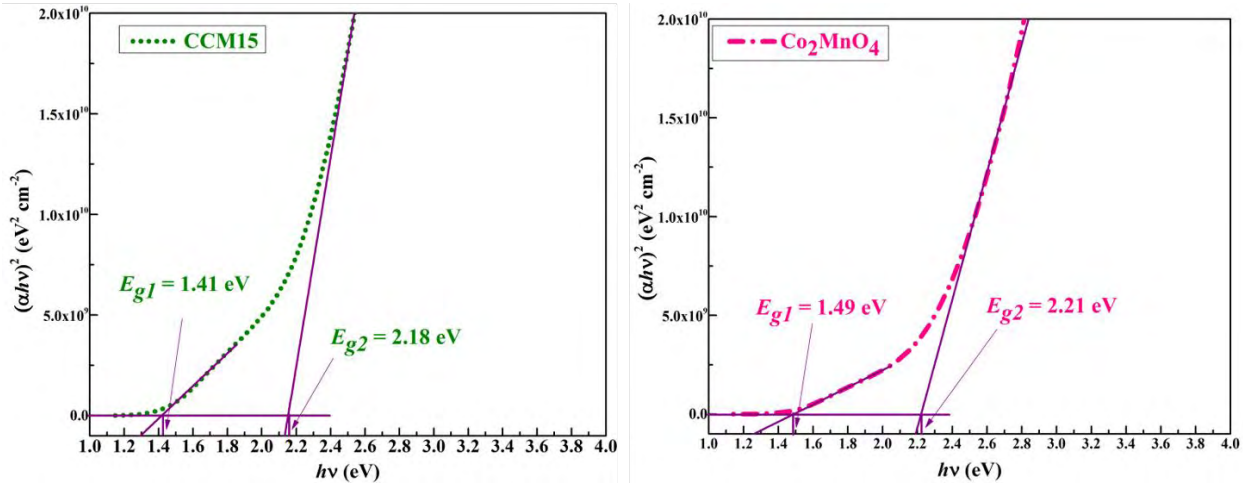

Figure V. 14: $(\alpha h\nu)^2$ vs $(h\nu)$ variations and band gap extrapolations for CCM15 and Co_2MnO_4 thin films deposited on quartz at room temperature.

All the band gap values determined for our spinel oxide thin films deposited on quartz at room temperature are presented in Table V. 1. The band gaps here obtained are in good agreement with those reported in the literature for similar compositions [7, 10-13].

The substitution of 15 at. % Co by a higher atomic number transition metal *M* (*M* = Ni, Cu, Zn) of the same period in $M_xCo_{2-x}MnO_4$ tends to decrease the band gaps. The band gap increase with further doping can again be explained by the presence of more localized orbitals and less overlapping. The interaction with the oxygen anion is also lowered with doping. The presence of M^{2+} (Ni^{2+}, Cu^{2+}) cations on the octahedral sites induces the manganese oxidation on this site and contributes to the material conductivity increase. The increasing

number of electrons filling up the energy levels will contribute to decreasing the oxide band gaps.

Table V. 1: Band gaps of Co_2MnO_4, NCM, ZCM and CCM15 thin films prepared at room temperature.

Compound	E_{g1} (eV)	E_{g2} (eV)
Co_2MnO_4	1.49	2.21
NCM15	1.41	2.19
NCM30	1.43	2.20
NCM60	1.45	2.34
ZCM15	1.48	2.18
ZCM30	1.50	2.25
ZCM60	1.57	2.30
CCM15	1.41	2.18

V.2.4.2. Band gaps of spinel oxide thin films after annealing at 900°C in air

The optical band gap of thin films deposited on quartz substrate after annealing at 900 ºC were also estimated from the optical measurements in the UV-VIS-NIR spectral range following the same procedure than described in the previous section. Figure V. 15, Figure V. 16, Figure V. 17 show $(\alpha h\nu)^2$ plotted as a function of the photon energy ($h\nu$) for each composition of NCM, ZCM and CCM, respectively.

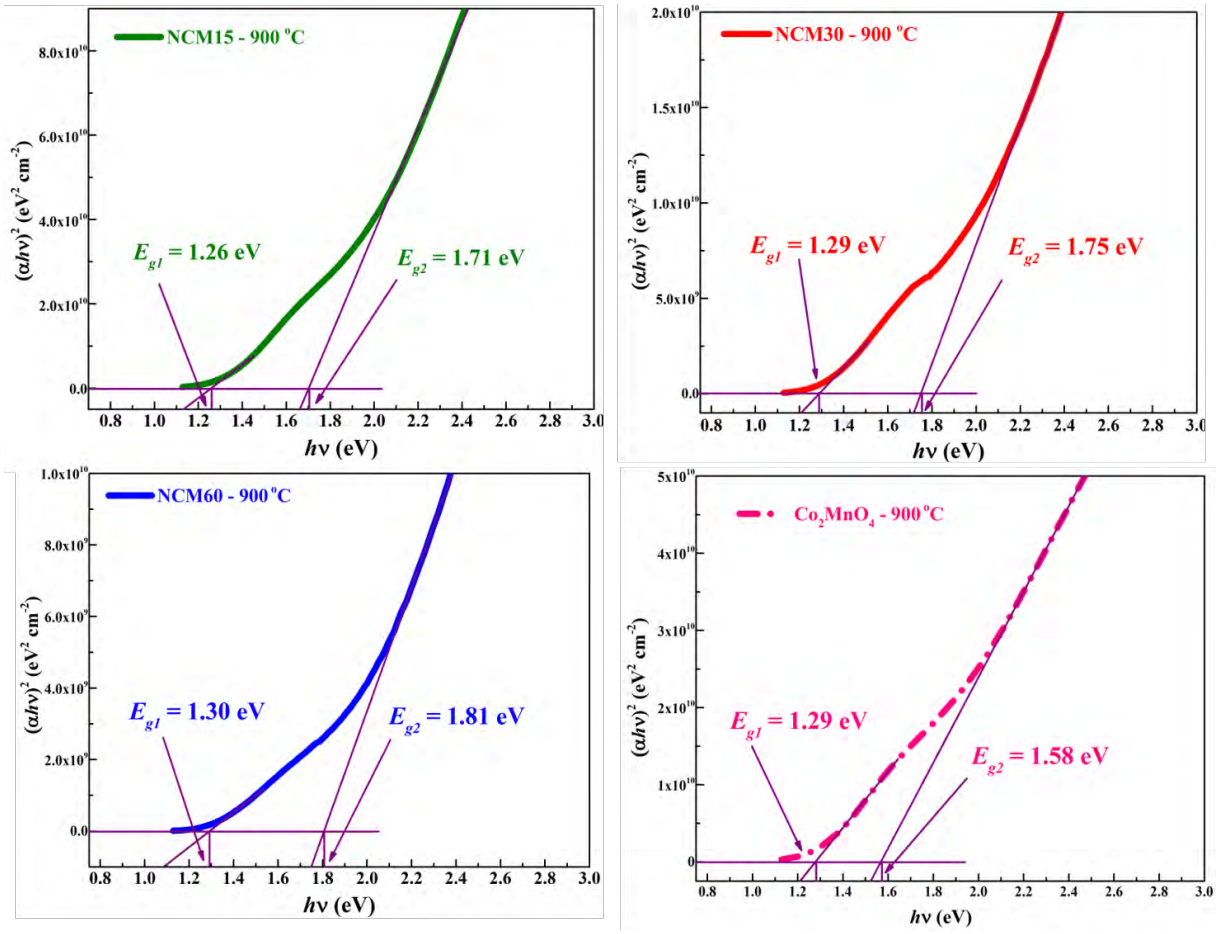

Figure V. 15: $(\alpha h\nu)^2$ vs $(h\nu)$ variations and band gap extrapolations for three different NCM compositions and Co_2MnO_4 thin films deposited on quartz and annealed in air at 900 °C.

The band gaps were again estimated by the extrapolation of the linear part of the curve to the $(\alpha h\nu)^2 = 0$. Two band gap values can still be determined for each composition analyzed in this spectral region. Table V. 2 summarizes the values of the band gaps obtained for all the spinel oxide thin films after heat treatment in comparison with the optical band gaps values as deposited at room temperature. The band gaps are systematically lower than the values obtained before annealing. The falloff in E_g after heat treatment is due to an increase in the average crystal size upon heating and reduction of defect sites [14]. As the grain size increases, the grain boundary density of a film decreases and subsequently the scattering of carriers at grain boundaries is decreased. A continuous increase of the optical constants (α and E_g) associated with the shift in the absorption edge to a higher wavelength after heating may also be attributed to an increase in the particle size of the crystallites along with a reduction in porosity. The

decrease of the optical band gap energy is generally observed in the sintered direct transition-type semiconductor films such as ZnO thin film [15], $SrTiO_3$ thin film [16], CdS thin film [17], Cu_2ZnSnS_4 thin film [18], etc. The oxidation states and cation charge distribution obtained after annealing could also contribute to this band gap decrease.

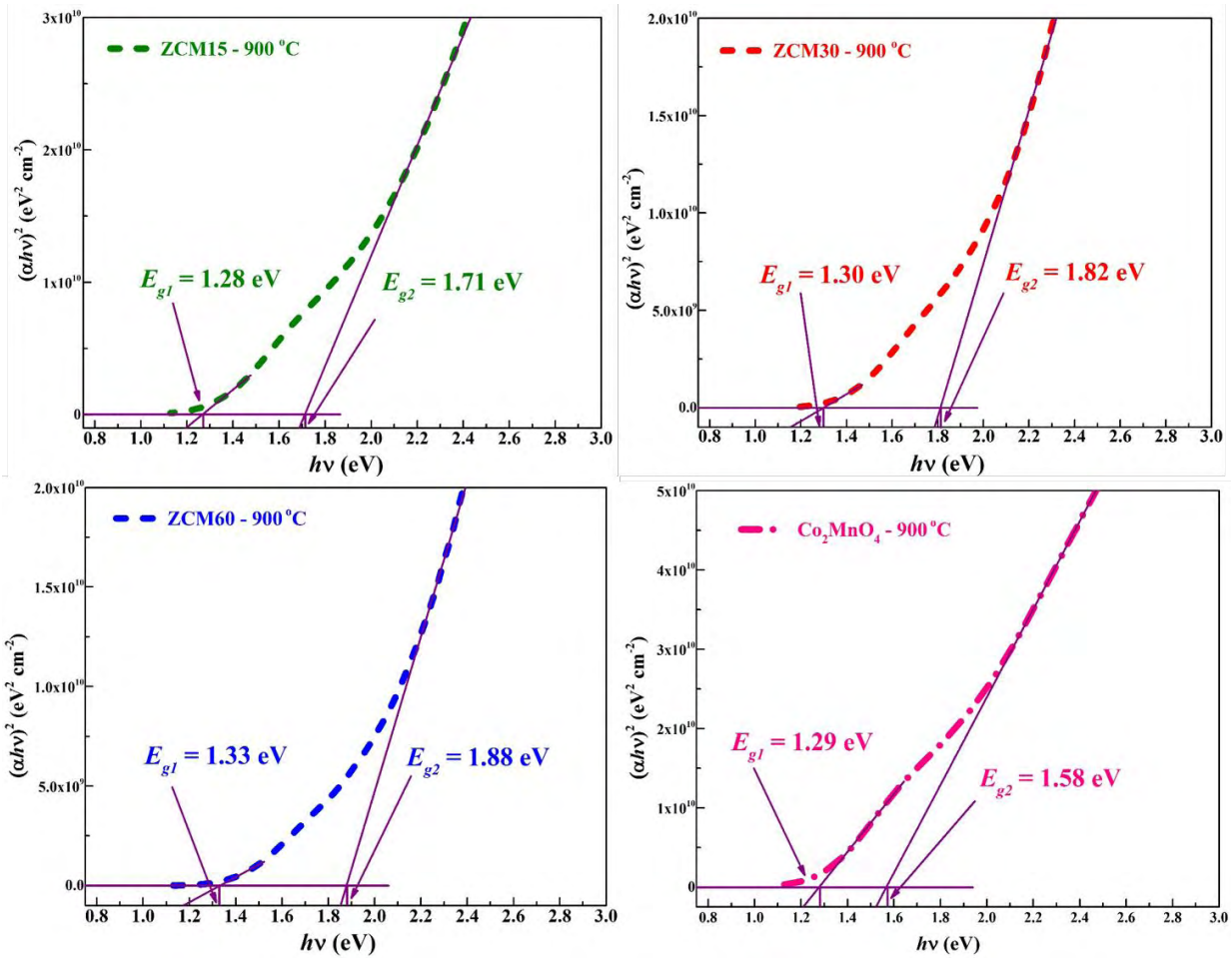

Figure V. 16: $(\alpha h\nu)^2$ vs $(h\nu)$ variations and band gap extrapolations for ZCM thin films deposited on quartz, in comparison with Co_2MnO_4 annealed at 900 °C.

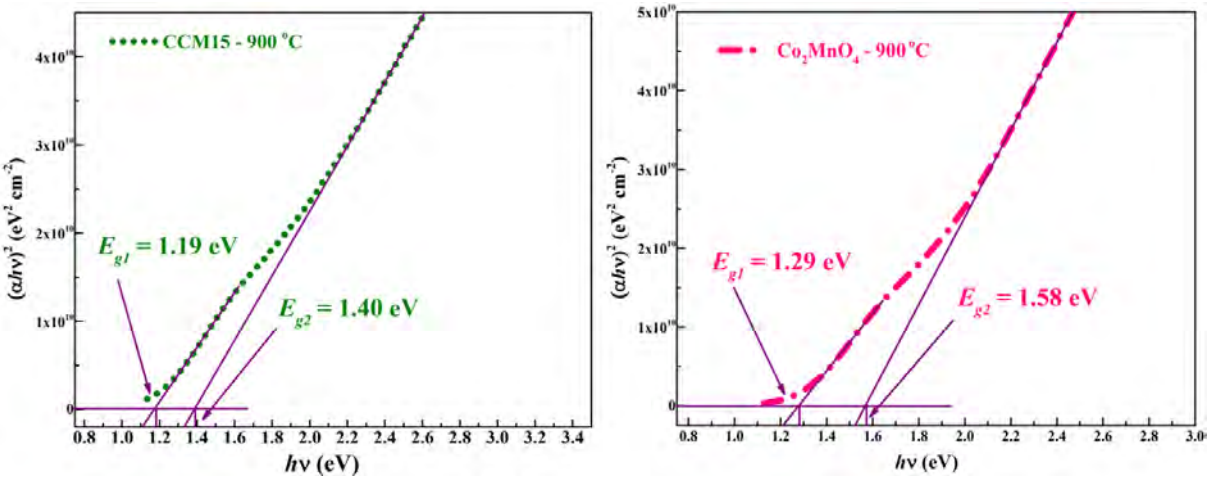

Figure V. 17: $(\alpha h\nu)^2$ vs $(h\nu)$ variations and band gap extrapolations for CCM15 and Co_2MnO_4 thin films deposited on quartz and annealed at 900 °C.

Table V. 2: The optical band gaps of Co_2MnO_4, NCM, ZCM and CCM15 thin films after annealing at 900 °C in comparison with the values as deposited at room temperature.

Compound	E_{g1} (eV)		E_{g2} (eV)	
	At 20 °C	After 900 °C	At 20 °C	After 900 °C
Co_2MnO_4	1.49	1.29	2.21	1.58
NCM15	1.41	1.26	2.19	1.71
NCM30	1.43	1.29	2.20	1.75
NCM60	1.45	1.30	2.34	1.81
ZCM15	1.48	1.28	2.18	1.71
ZCM30	1.50	1.30	2.25	1.82
ZCM60	1.57	1.33	2.30	1.88
CCM15	1.41	1.19	2.18	1.40

E_{g1} decreases in average by 0.20 ± 0.06 eV and E_{g2} by 0.48 ± 0.06 eV after annealing the spinel oxide thin films at 900 °C in air. A much stronger decrease of 0.63 eV for E_{g2} of the reference material Co_2MnO_4 is even measured after annealing while the highest jump of all samples is obtained for the copper-based material CCM15, with a decrease of E_{g2} equals to

0.78 eV! This material then exhibits the lowest band gaps with E_{g1} = 1.19 eV and E_{g2} = 1.40 eV, closer to the indirect band gap of silicon, with E_g(Si) = 1.1 eV.

V.2.2. Electrical properties of the spinel oxide thin films

V.2.2.1. Current-voltage (I-V) characteristics

I-V characteristics of NCM15, ZCM15, CCM15 and Co_2MnO_4 thin films annealed at 900 ºC and recorded at different temperatures in the bias range of -0.5 V to 0.5 V are shown in Figure V. 18.

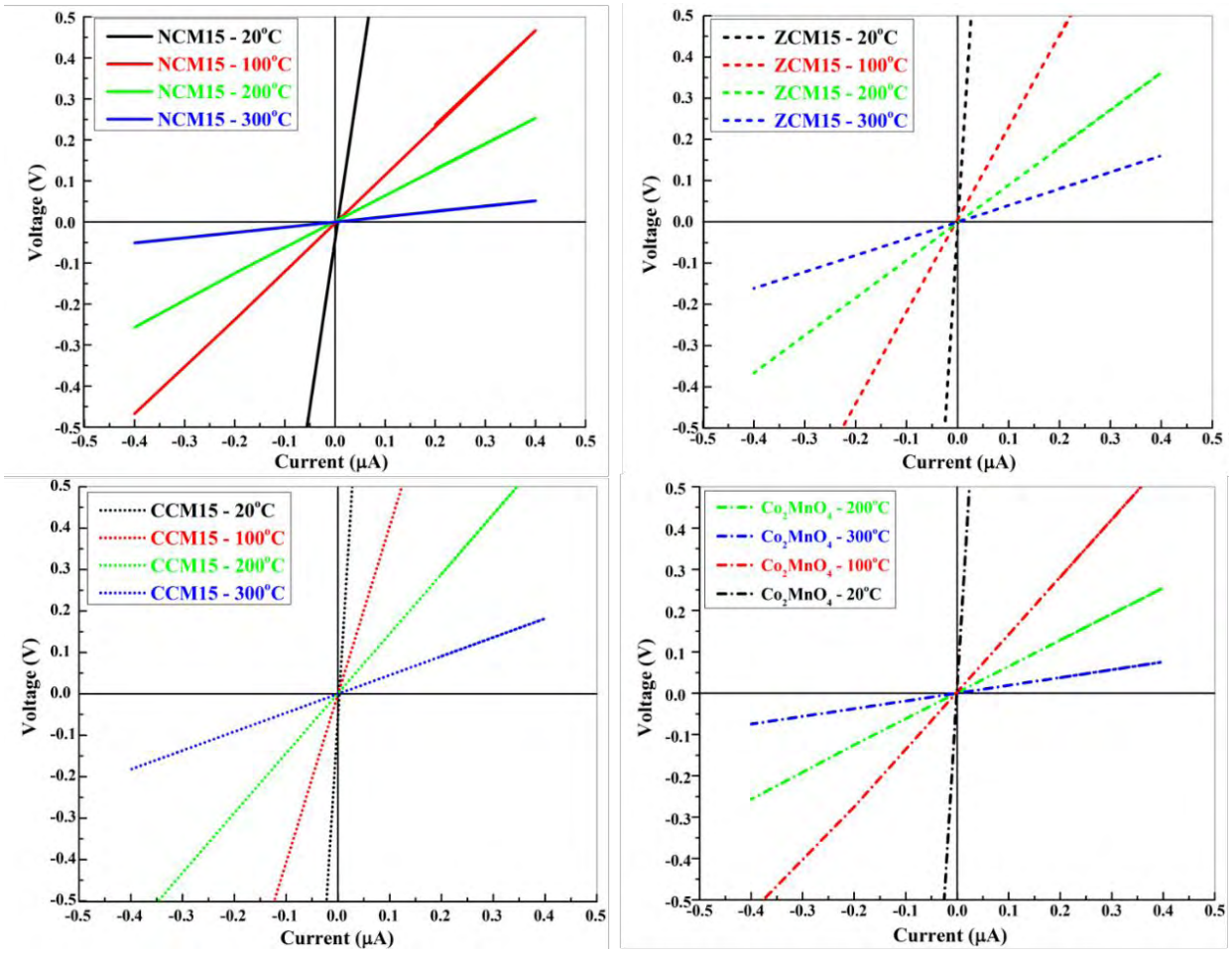

Figure V. 18: Current-voltage characteristics of spinel oxide thin films annealed at 900 ºC in air and measured at different temperatures.

The linear I-V characteristics passes through the origin and is related to an ohmic behavior. The slope strongly decreases with increasing the measurement temperature that corresponds to an increase in conductivity with the temperature. The current is swept across the electrodes and the bias passing through the samples is recorded. I-V curves are straight and non-hysteretic for all the samples. Grain size enlargement enhances the movement of electron. The same behaviors of the I-V characteristics are observed for the other compositions (NCM30, NCM60, ZCM30 and ZCM60).

V.2.2.2. Electrical conductivity of the spinel oxide thin films annealed in air at 900 °C

The electrical conductivity was determined in the temperature range of 20 – 300 ºC for the spinel oxide thin films annealed in air at 900 ºC. The temperature dependence of electrical conductivity is shown in Arrhenius equation [19]:

$$\sigma = \frac{\sigma_0}{T}\, e^{-\frac{E_a}{k\,T}} \qquad \text{(V.1)}$$

Where:

σ : Electrical conductivity ($S.cm^{-1}$)

σ_0 : Pre-exponential factor ($S.cm^{-1}.K$)

E_a : Activation energy (eV)

k : Boltzmann constant ($eV.K^{-1}$), $k = 8.6173.10^{-5}$ ($eV.K^{-1}$)

T : Absolute temperature (K)

Figure V. 19, Figure V. 20 and Figure V. 21 show the electrical conductivity plots as function of the temperature determined for NCM, ZCM, CCM15 in comparison with the Co_2MnO_4 composition in air, respectively. The inset presents ln (σ.T) as function of 1000/T curves. The electrical conductivity increase with temperature, as show in Table V. 3, indicates the semiconducting character of the oxide thin films and the mobility of charge carriers is

thermally activated based on a hopping conduction mechanism [10, 20, 21]. The charge carrier concentration and mobility are increased, as well as the crystalline state with the higher temperature, which can also justify this behavior [22-25]. The electrical conductivity of Co_2MnO_4 is increased by doping. The highest conductivity value obtained at low temperature correspond to a 15 at. % substitution of Co by Ni (see Table V. 3). It is known that the electrical conduction in Co_2MnO_4 based spinels proceeds by a hopping mechanism in exchange pairs of Mn^{3+}/Mn^{4+} and Co^{2+}/Co^{III} on octahedral sites [26]. The incorporation of Ni, Cu or Zn into Co_2MnO_4 not only leads to the formation of cations with different valence states (Cu^{2+}, Ni^{2+} on octahedral sites, Zn^{2+} on tetrahedral site), but also induces the transitions of Mn^{2+} and Mn^{3+} to Mn^{3+} and Mn^{4+} due to the constraint of charge neutrality. Thus, the presence of cations with different valence states on octahedral sites would facilitate electrical conduction [23, 27].

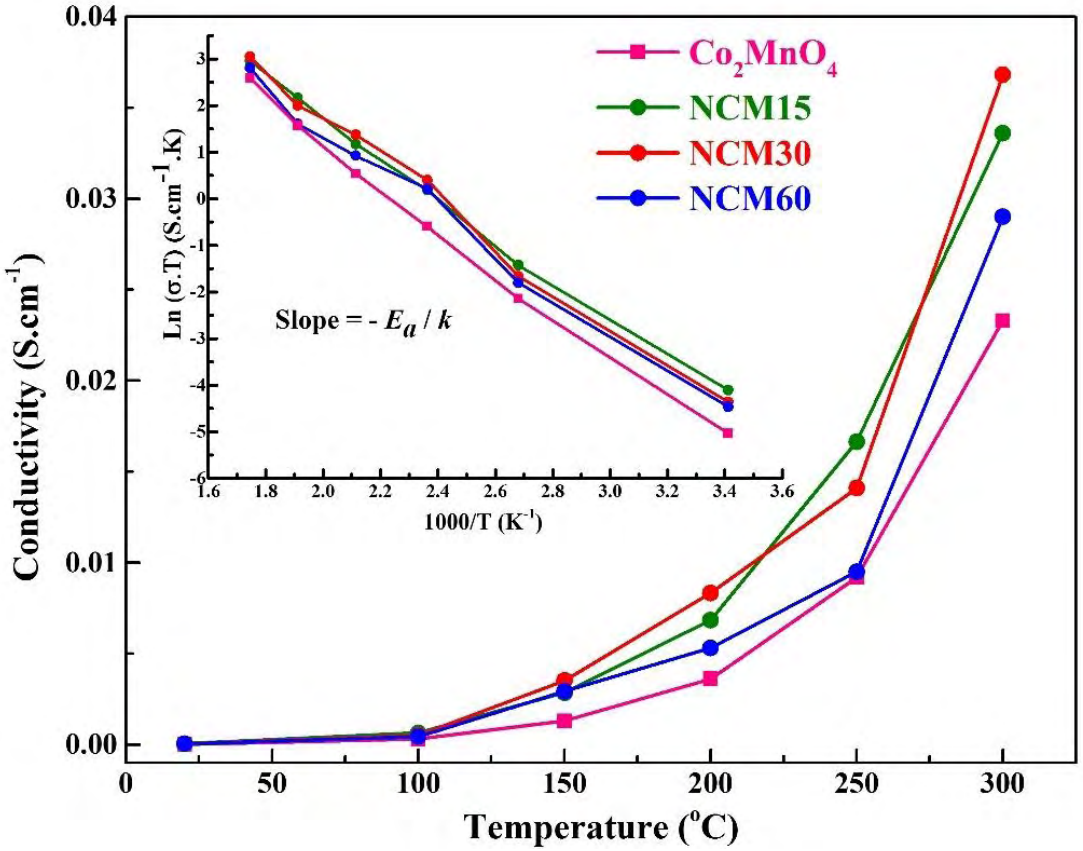

Figure V. 19: Plots of electrical conductivity (σ) vs. temperature determined from NCM compositions and Co_2MnO_4 in air. The ln (σ.T) vs. (1000/T) curves are presented in the inset.

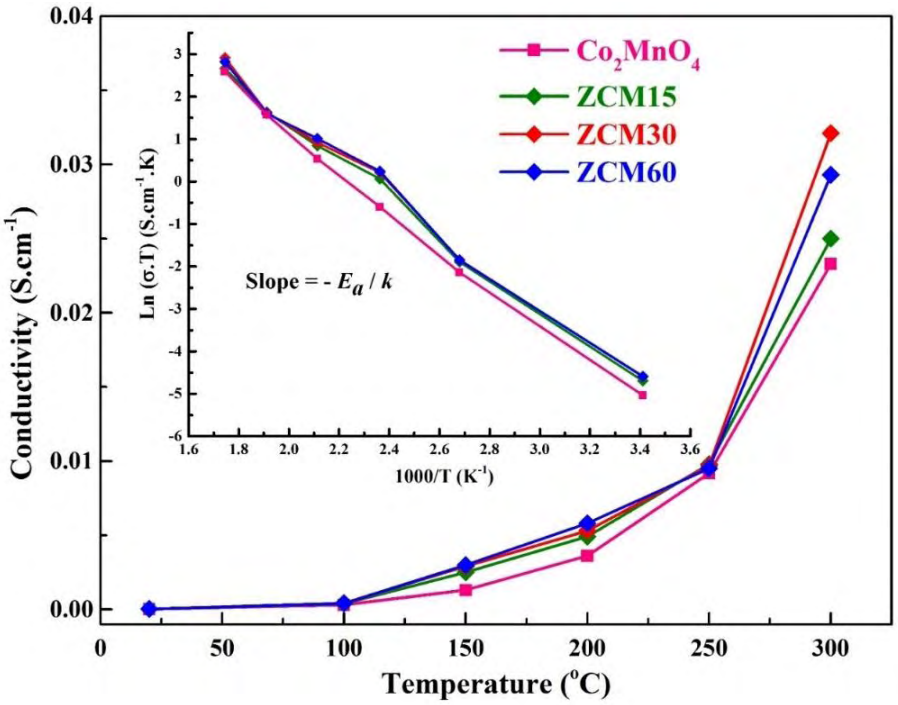

Figure V. 20: Plots of electrical conductivity (σ) vs. temperature determined from ZCM compositions and Co_2MnO_4 in air. Inset shows ln(σT) vs. (1000/T) curves.

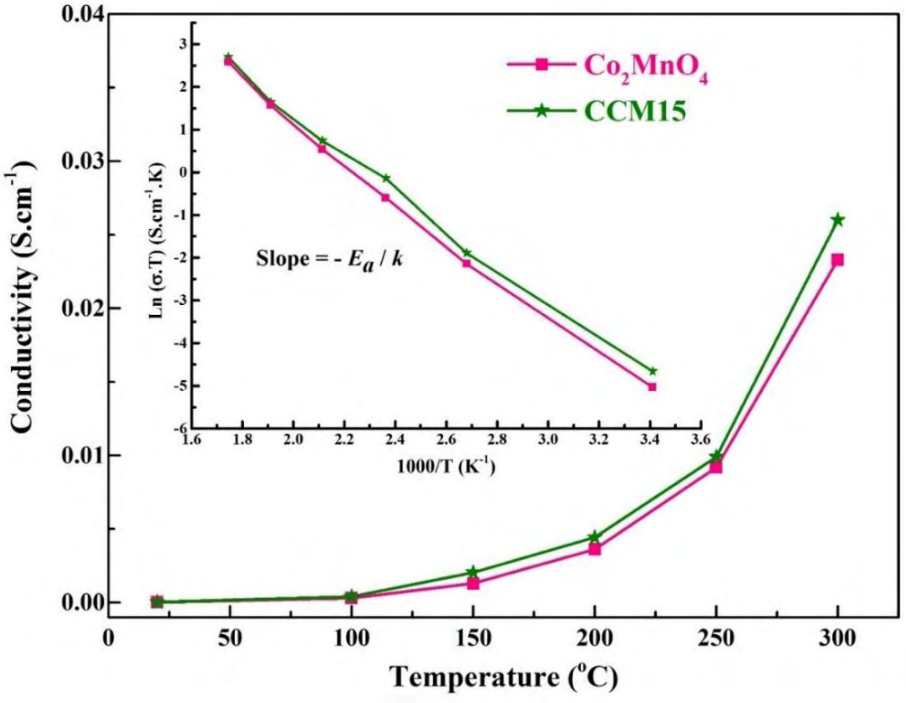

Figure V. 21: Plots of electrical conductivity (σ) vs. temperature determined from CCM15 and Co_2MnO_4 in air. The ln(σT) vs. (1000/T) curves are presented in the inset.

Table V. 3: Electrical conductivity of the spinel oxide thin films previously annealed at 900 °C in air and measured at different temperatures.

	σ (20 ºC) ($S.cm^{-1}$)	σ (100 ºC) ($S.cm^{-1}$)	σ (150 ºC) ($S.cm^{-1}$)	σ (200 ºC) ($S.cm^{-1}$)	σ (250 ºC) ($S.cm^{-1}$)	σ (300 ºC) ($S.cm^{-1}$)
Co_2MnO_4	2.22×10^{-5}	3.14×10^{-4}	1.30×10^{-3}	3.62×10^{-3}	9.19×10^{-3}	2.33×10^{-2}
NCM15	5.62×10^{-5}	6.44×10^{-4}	2.85×10^{-3}	6.84×10^{-3}	1.67×10^{-2}	3.36×10^{-2}
NCM30	4.35×10^{-5}	5.09×10^{-4}	3.52×10^{-3}	8.33×10^{-3}	1.41×10^{-2}	3.68×10^{-2}
NCM60	3.94×10^{-5}	4.42×10^{-4}	2.93×10^{-3}	5.31×10^{-3}	9.50×10^{-3}	2.90×10^{-2}
ZCM15	3.12×10^{-5}	4.04×10^{-4}	2.51×10^{-3}	4.92×10^{-3}	9.80×10^{-3}	2.50×10^{-2}
ZCM30	3.45×10^{-5}	4.23×10^{-4}	2.92×10^{-3}	5.31×10^{-3}	9.69×10^{-3}	3.21×10^{-2}
ZCM60	3.46×10^{-5}	4.21×10^{-4}	3.00×10^{-3}	5.81×10^{-3}	9.50×10^{-3}	2.93×10^{-2}
CCM15	3.23×10^{-5}	4.05×10^{-4}	2.05×10^{-3}	4.43×10^{-3}	9.90×10^{-3}	2.60×10^{-2}

The activation energy (E_a) for the thermally activated hopping process was obtained from equation (V.1), which can be rewritten as:

$$ln(\sigma.T) = -\left(\frac{E_a}{k}\right)\frac{1}{T} + C \qquad \text{(V.2)}$$

So, the activation energy can be obtained from the slope of $ln\ (\sigma.T)$ versus $1/T$. The E_a values were calculated and listed in Table V. 4. The activation energy values are very close for all compositions (E_a = 0.37(2) eV) and in agreement with the values reported elsewhere for similar sample compositions of spinel oxide thin films [24, 28].

Table V. 4: The activation energy (E_a) and electrical conductivity at 300 °C of all compositions annealed at 900 ºC.

	σ (S.cm^{-1}) at 300 ºC	E_a (eV)
Co_2MnO_4	2.33 x10^{-2}	0.39
NCM15	3.36 x10^{-2}	0.36
NCM30	3.68 x10^{-2}	0.36
NCM60	2.90 x10^{-2}	0.38
ZCM15	2.50 x10^{-2}	0.37
ZCM30	3.21 x10^{-2}	0.36
ZCM60	2.93 x10^{-2}	0.38
CCM15	2.60 x10^{-2}	0.38

In summary, the main optical and electrical properties of spinel oxides thin films were characterized. The optical properties measurements performed at room temperature show high absorbance in the UV region (A ~ 80 to 94 %), which decrease in the VIS-NIR regions. Two optical band gap values were determined for each composition. The absorbance of each thin film was strongly improved after annealing at 900 ºC in air with a high absorbance in the UV-VIS spectral range. The conductivity of thin films annealed, was measured at different temperature. The values obtained are promising but still need to be improved before these spinel oxide thin films can be integrated in solar cells for efficiency tests.

Thin films homogeneity and compactness (and conductivity) can also be improved by Physical Vapor Deposition (PVD) or Pulsed Laser Deposition (PLD).

V.3. Preparation and study of spinel oxide and cuprite thin films deposited by the PLD technique

V.3.1. Thin films preparation

The Pulsed Laser Deposition (PLD) method was used to prepare Cu_2O (the reference material used as a *p*-type light absorber in all oxide solar cells) and Co_2MnO_4 thin films on different substrates such as glass, quartz, ITO, stainless steel and copper. 30 mm in diameter and 5 mm thick pellets of Cu_2O and Co_2MnO_4 were prepared separately at the CIRIMAT laboratory (see Figure V. 22) following our inorganic polycondensation method used to obtain pure powders and the Spark Plasma Sintering technique (see chapter II for more details). The dense pellets (densification > 95 %) were then used as targets for a high-power pulsed laser beam that is focused inside a vacuum chamber to strike the target and project the material toward the chosen substrate for the thin film preparation. PLD was carried out at the Department of Materials Science and Engineering from the University of Florida in the United States of America (USA) by George Baure from the Energy Group lead by Juan Claudio Nino.

Variable thicknesses of oxide thin films (with dimensions 6 x 6 mm) were deposited on the different types of substrate, depending on the PLD conditions used during the film preparation. For instance, a thin film of Co_2MnO_4 having a thickness of 61 ± 11 nm (measured by profilometry) can be deposited on quartz at 500 ºC using a 10 mTorr oxygen pressure and 5 Hz frequency for 45 minutes, while 113 ± 33 nm thick Cu_2O film can be prepared by PLD on quartz at 750 ºC after 60 minutes under 1 mTorr oxygen pressure and using 5 Hz frequency.

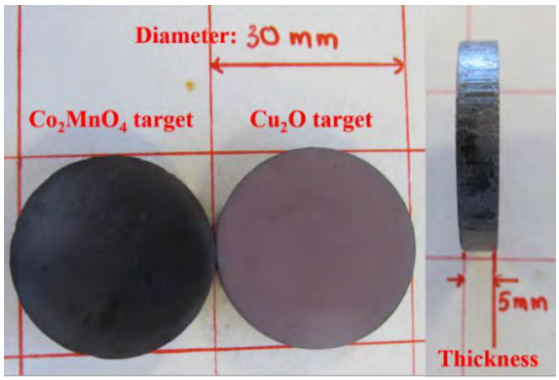

Figure V. 22: Co_2MnO_4 and Cu_2O pellets obtained after Spark Plasma Sintering.

V.3.2. Characterization of the oxide thin films deposited by the PLD method

V.3.2.1. Structural determination by GI-XRD

The structural characterization of Co_2MnO_4 oxide thin films deposited by the PLD technique was performed by Grazing Incidence X-Ray Diffraction (GI-XRD) at room temperature, as shown in Figure V. 23a. The diffraction patterns were recorded in 2-theta mode from 15 to 70º overnight at 14 seconds per 0.03º step. Co_2MnO_4 thin films exhibits a single oxide phase structure of cubic symmetry. The series of planes are in good agreement with the diffraction database JCPDS: 23-1237, and is similar to the XRD pattern obtained for Co_2MnO_4 deposited by the dip-coating technique.

GI-XRD pattern of Cu_2O thin film is shown in Figure V. 23b. A pure crystalline phase corresponding to Cu_2O of cuprite structure is determined by XRD analysis, in accordance with the diffraction database JCPDS: 01-071-3654. Note that a hump is observed in the base of the XRD patterns around 20° in 2-Theta due to the amorphous quartz substrate.

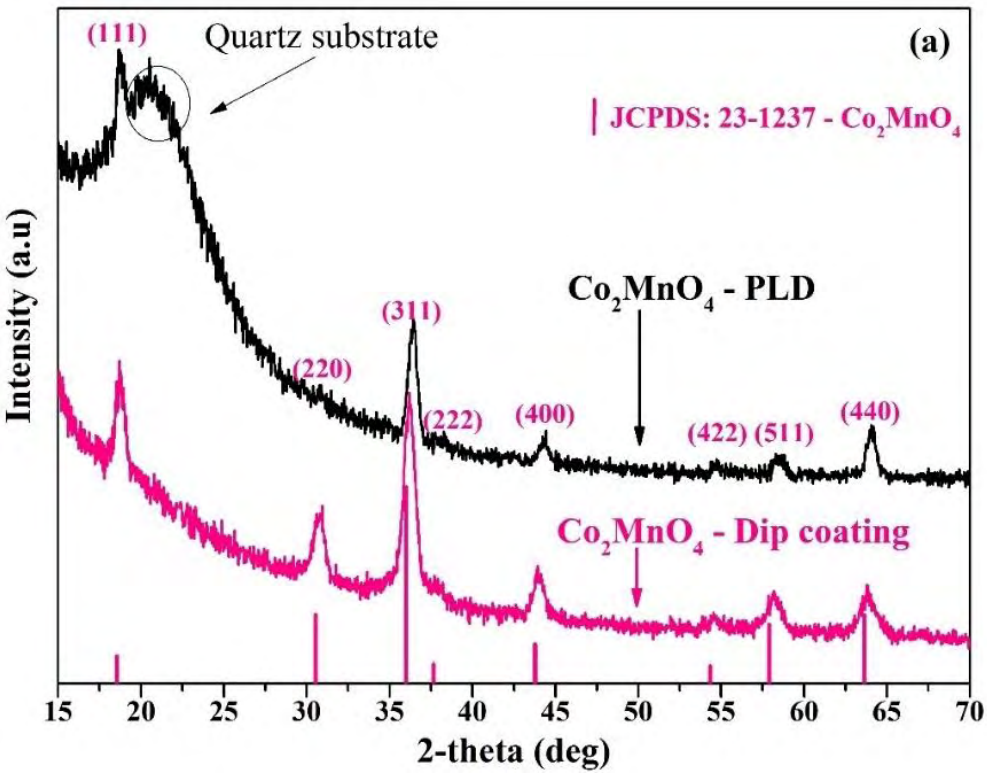

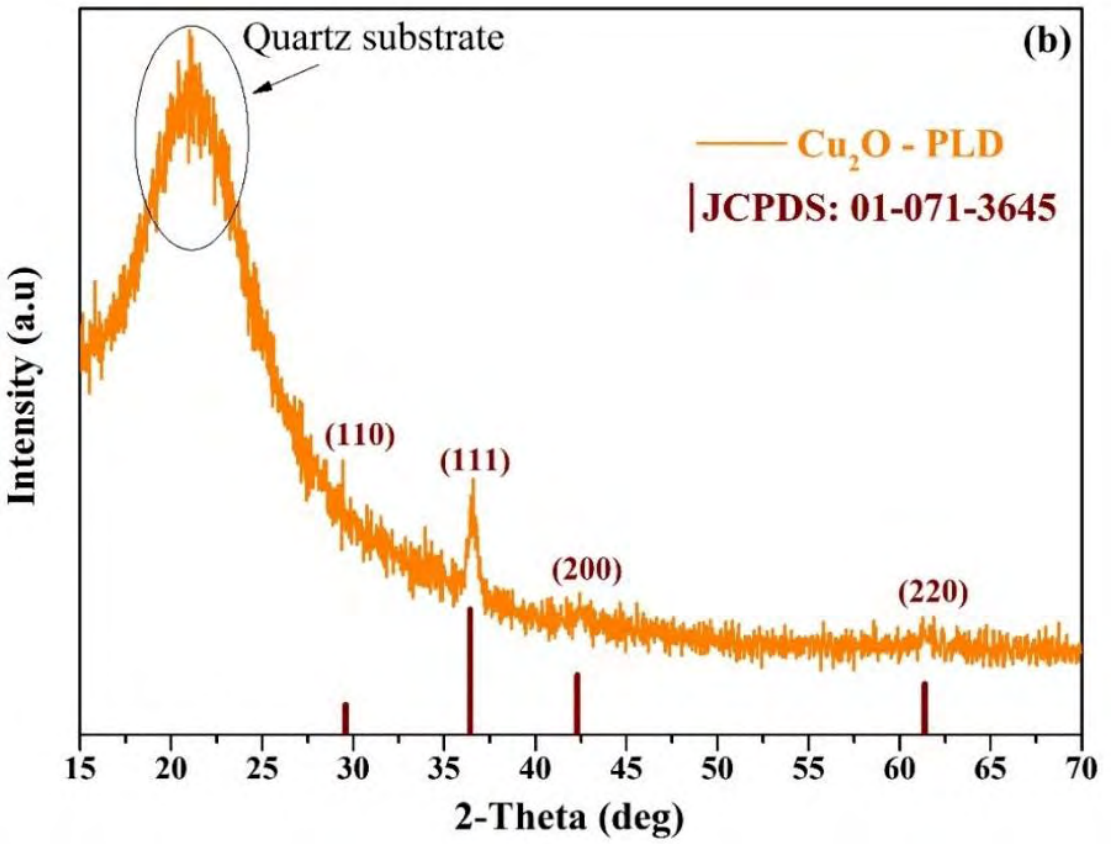

Figure V. 23: GI-XRD of Co_2MnO_4 (a) and Cu_2O (b) thin films deposited on quartz substrate by the PLD technique.

V.3.2.2. Microstructural determination by FEG-SEM

The surface morphology of Co_2MnO_4 and Cu_2O thin films deposited by PLD was studied by FEG-SEM. Figure V. 24 shows FEG-SEM images of Co_2MnO_4 and Cu_2O thin films deposited on quartz and Cu substrates.

Thin films are highly dense and smooth on the quartz surface, but the important roughness of the copper substrate hamper the ability to obtain a nice homogenous coating in that case. This substrate should be polished further in order to improve the thin film quality. Some droplet crystals appear on top of the surface of Cu_2O due to the operating frequency during PLD that needs to be decreased to obtain more homogeneous thin layers.

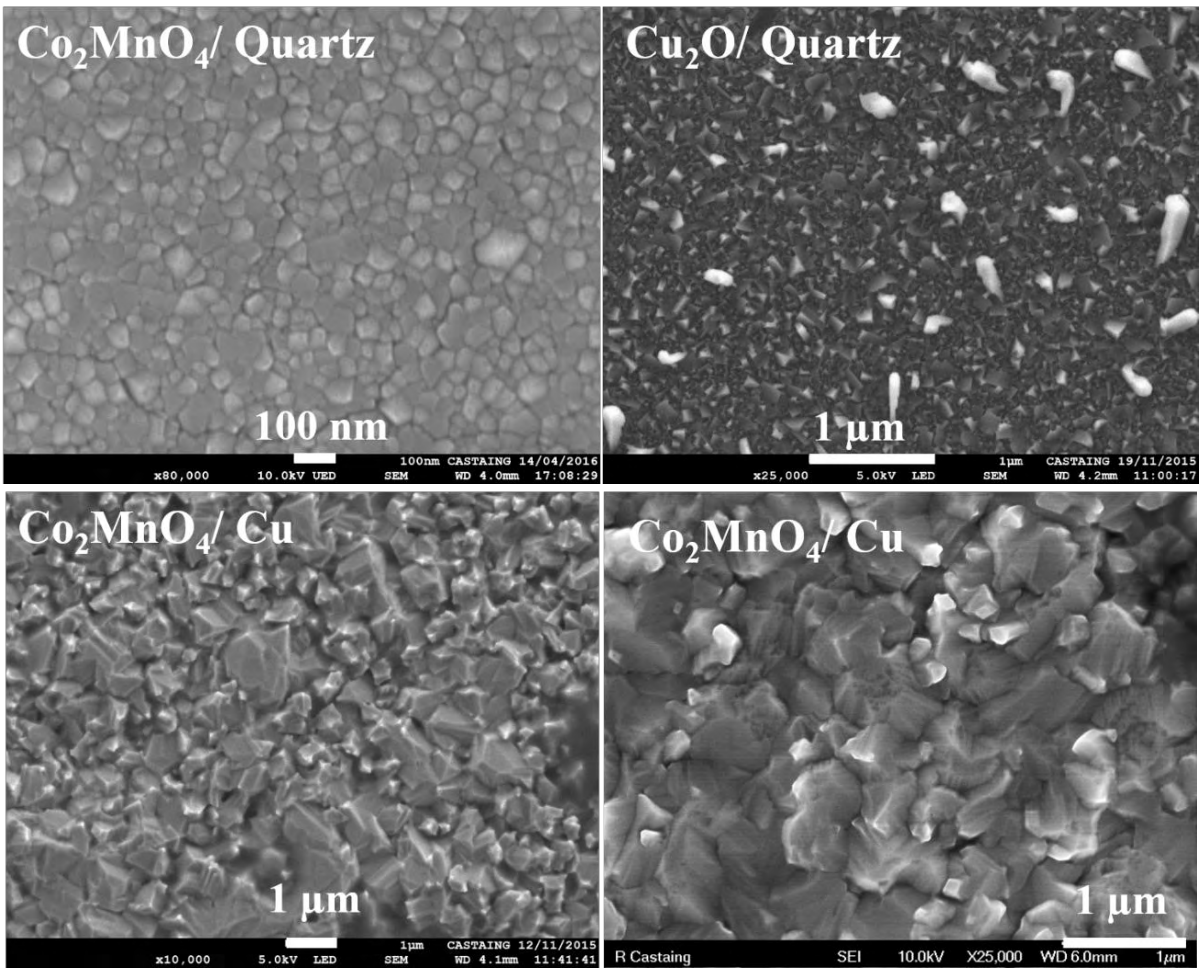

Figure V. 24: Scanning electron micrographs of Co_2MnO_4 deposited on quartz and copper substrates by the PLD technique.

V.3.2.3. Optical and electrical characterizations

Figure V. 25 shows the absorbance variations of Cu_2O and Co_2MnO_4 thin films deposited by PLD, deduced from transmittance and reflectance measurements following the simplified relation $A(\lambda) = 1 - T(\lambda) - R(\lambda)$. Two absorption edges are observed for the thin film of Co_2MnO_4 (~ 60 nm in thickness) with peak maxima measured at ~ 300 nm ($A(\lambda)$ = 77 %) and 700 nm ($A(\lambda)$ = 46 %), in the UV-VIS regions, respectively. The absorbance still decreases for higher wavelengths but remains above 25 % in the near infrared region. The absorbance of the Cu_2O thin film is the highest in the UV region but is only 52 % due to the small film thickness (~ 110 nm). The absorbance gradually decreases down to 10 % with the wavelength

until λ = 500 nm, then a small slope is observed for higher wavelengths, becoming almost invisible for the infrared region.

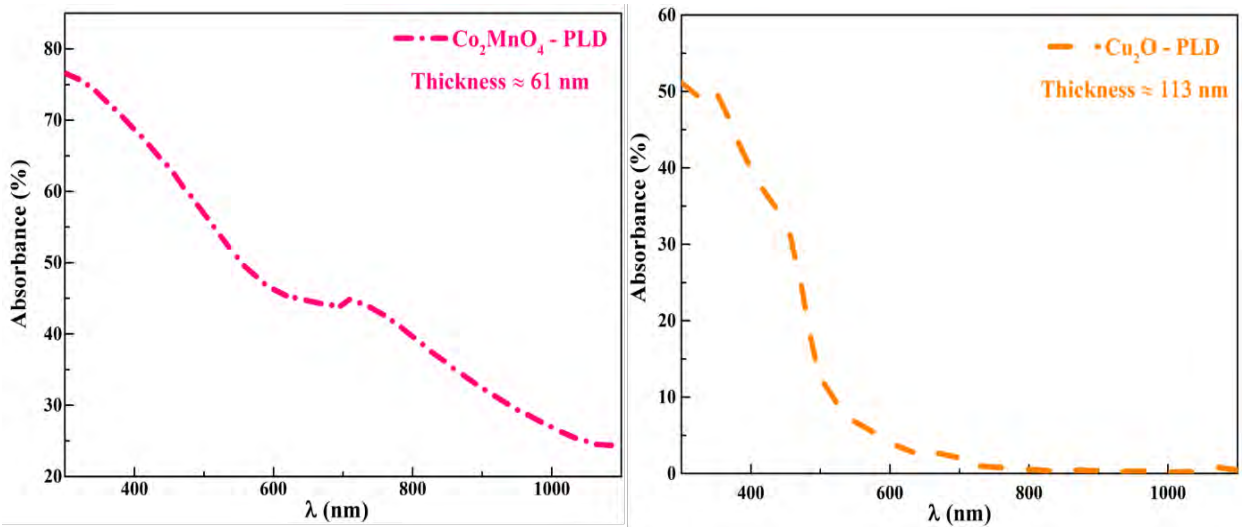

Figure V. 25: Absorbance spectra for Co_2MnO_4 (left) and Cu_2O (right) deposited by PLD techniques.

The variation of the direct current electrical conductivity of Co_2MnO_4 and Cu_2O thin films prepared by the PLD method are shown in Figure V. 26.

The electrical conductivity of Co_2MnO_4 thin film increases from 3.89 x 10^{-5} $S.cm^{-1}$ measured at room temperature to 3.60 x 10^{-2} $S.cm^{-1}$ at 300 ºC, while it increases from 5.71 x 10^{-5} $S.cm^{-1}$ to 3.90 x 10^{-2} $S.cm^{-1}$ for Cu_2O thin film. The conductivity values measured on Co_2MnO_4 thin films prepared by PLD (~ 60 nm in thickness) and prepared by dip-coating (~ 500 nm) and annealed at 900 °C in air before conductivity measurements are in the same range, although the conductivity is improved due to a better layer compactness with the PLD technique.

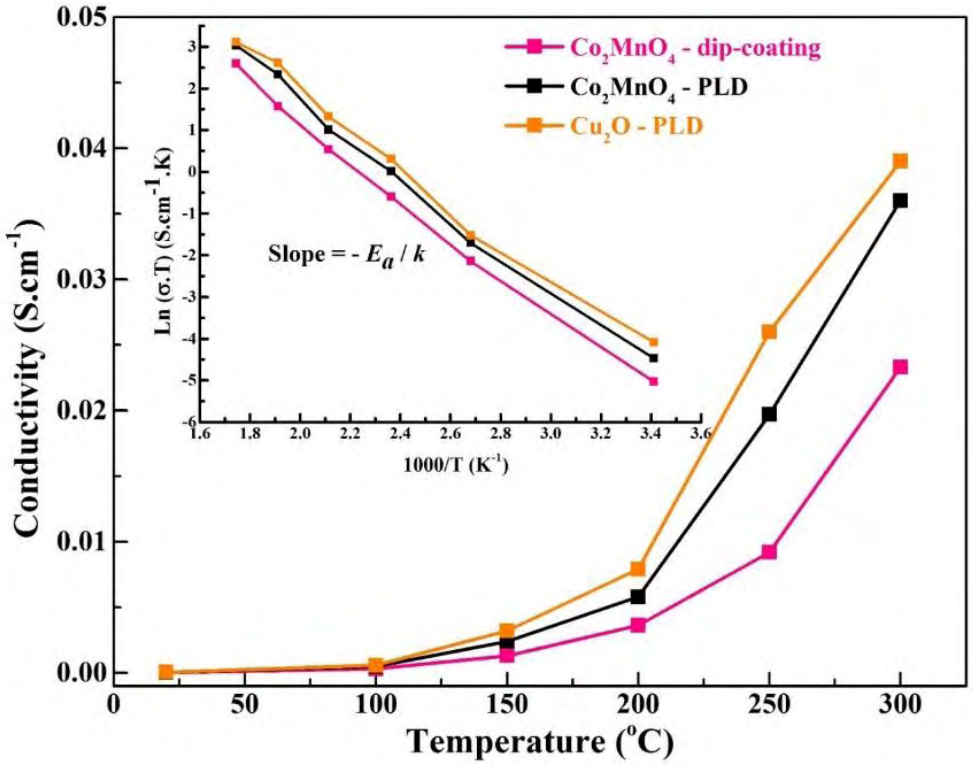

Figure V. 26: Plots of electrical conductivity (σ) vs. temperature determined from Co_2MnO_4 and Cu_2O thin films prepared by the PLD technique. The ln(σT) vs. (1000/T) curves are presented in the inset.

V.4. Conclusion

Optical and electrical properties of spinel oxides $M_xCo_{2-x}MnO_4$ (M = Ni, Cu, Zn; x = 0, 0.15, 0.30, 0.60) thin films were analyzed. The absorbance spectrum exhibits two strong absorption bands at around 450 and 750 nm in wavelengths for each composition. Thin films prepared at room temperature (RT) exhibit high absorbance (A > 90 %) in the UV range. The absorbance decreases with increasing wavelength but remains higher than 70 % across the visible region. It strongly decreases down to ~ 20 % at 1000 nm and thereafter. The absorption properties are strongly increased by an annealing step at high temperature (T > 900 °C) in air. Indeed, the absorbance remains then higher than 90 % over the whole UV and VIS ranges. The optical band gap values were determined after Tauc's law. Each composition exhibits two band gaps, which are associated with the two absorption edges determined in the UV-VIS regions. The first optical band gap E_{g1} ~ 1.5 eV at RT, corresponding to a wide absorption band at

~ 750 nm, is usually related to an energy transition between two metal cations. The second band gap E_{g2} ~ 2.2 eV at RT, associated with the UV absorption front, is usually associated with oxygen to metal transitions, although our first-principles calculations would rather relate it to a metal-metal transition between a cation in tetrahedral site toward a cation in an octahedral site. E_{g1} and E_{g2} are ~ 0.2 and 0.5 eV lower after annealing, respectively. This strong gap decrease is essentially due to the increased compactness and density of thin films after heating.

Electrical properties of thin films were studied at different substrate temperatures. The linear I-V characteristics passes through the origin and the curve slop decreases with increasing temperature, which is due to an increase of the electrical conductivity upon heating. The electrical conductivity increases from ~ 10^{-5} to ~ 10^{-2} $S.cm^{-1}$ with the increasing temperature from 20 ºC to 300 ºC, which indicates that thin films are semiconducting in nature, with increasing crystal size of thin film particles, concentration and mobility of charge carriers. The activation energy is close of 0.38 eV.

Finally, we also prepared crystalline thin films of Co_2MnO_4 and Cu_2O by the PLD technique. Our synthesis method was repeated a dozen of times in order to obtain enough sample powder (~ 23 g) for one sample pellet that could be used for PLD after SPS treatment. Thin films (less than 120 nm in thickness) appear smooth and homogenous when prepared on appropriate substrates, although size grains differences or droplets could probably be avoided in more adequate conditions. The absorbance of Co_2MnO_4 thin films prepared by PLD and after dip-coating are similar. Cu_2O presents a band gap of 2.4 eV. The electrical conductivity is in the same order of magnitude for both PLD and after dip-coating and annealing at 900 °C, although higher after PLD. Further studies are required in order to improve the film homogeneity and density, at room temperature and upon heating in specific atmospheres, and evaluate their capabilities in integrated systems.

V.5. References

[1] J. Wu, Z. Huang, W. Zhou, C. Ouyang, Y. Hou, Y. Gao, *et al.*, "*Investigation of cation distribution, electrical, magnetic properties and their correlation in Mn2-xCo2xNi1-xO4 films*," **Journal of Applied Physics,** Vol. **115**, 1137031-1137038, **2014**.

[2] R. D. Shannon, "*Revised effective ionic radii and systematic studies of interatomic distances in halides and chalcogenides*," **Acta Crystallographica section a,** Vol. **32**, 751-767, **1976**.

[3] A. V. Salker and S. M. Gurav, "*Electronic and catalytic studies on Co1−xCuxMn2O4 for CO oxidation*," **Journal of Materials Science,** Vol. **35**, 4713-4719, **2000**.

[4] R. Arulmurugan, B. Jeyadevan, G. Vaidyanathan, and S. Sendhilnathan, "*Effect of zinc substitution on Co–Zn and Mn–Zn ferrite nanoparticles prepared by co-precipitation*," **Journal of Magnetism and Magnetic Materials,** Vol. **288**, 470-477, **2005**.

[5] N. J. Podraza, W. Qiu, B. B. Hinojosa, H. Xu, M. A. Motyka, S. R. Phillpot, *et al.*, "*Band gap and structure of single crystal BiI3: Resolving discrepancies in literature*," **Journal of Applied Physics,** Vol. **114**, 0331101-0331109, **2013**.

[6] J. Tauc, "*Amorphous and liquid semiconductors"*, **London and New York**, p. 175, **1974**.

[7] G. Salek, P. Dufour, S. Guillemet-Fritsch, and C. Tenailleau, "*Sustainable low temperature preparation of Mn3−xCoxO4 ($0 \leq x \leq 3$) spinel oxide colloidal dispersions used for solar absorber thin films*," **Materials Chemistry and Physics,** Vol. **162**, 252-262, **2015**.

[8] S. Thota, A. Kumar, and J. Kumar, "*Optical, electrical and magnetic properties of Co3O4 nanocrystallites obtained by thermal decomposition of sol–gel derived oxalates*," **Materials Science and Engineering B,** Vol. **164**, 30-37, **2009**.

[9] P. Y. Keng, B. Y. Kim, I.-B. Shim, R. Sahoo, P. E. Veneman, N. R. Armstrong, *et al.*, "*Colloidal Polymerization of Polymer-Coated Ferromagnetic Nanoparticles into Cobalt Oxide Nanowires*," **ACS Nano,** Vol. **3**, 3143-3157, **2009**.

[10] Y. Q. Gao, Z. M. Huang, Y. Hou, J. Wu, and J. H. Chu, "*Optical and electrical properties of Mn1.56Co0.96Ni0.48O4 thin films*," in ***Eighth International Conference on Thin Film Physics and Applications***, 90680J90681-90680J90685, **2013**.

[11] S. Kim, J. A. Cianfrone, P. Sadik, K.-W. Kim, M. Ivill, and D. P. Norton, "*Room temperature deposited oxide p-n junction using p-type zinc-cobalt-oxide*," **Journal of Applied Physics,** Vol. **107**, 1035381-1035385, **2010**.

[12] F. Zasada, J. Gryboś, P. Indyka, W. Piskorz, J. Kaczmarczyk, and Z. Sojka, "*Surface Structure and Morphology of M[CoM']O4 (M = Mg, Zn, Fe, Co and M′ = Ni, Al, Mn, Co) Spinel Nanocrystals—DFT+U and TEM Screening Investigations*," **The Journal of Physical Chemistry C,** Vol. **118**, 19085-19097, **2014**.

[13] W. Zhou, L. Zhang, C. Ouyang, J. Wu, Z. Huang, and X.-f. Xu, "*Micro structural, electrical and optical properties of highly (220) oriented spinel Mn–Co–Ni–O film grown by radio frequency magnetron sputtering*," **Applied Surface Science,** Vol. **311**, 443-447, **2014**.

[14] R. Manogowri, R. Mary Mathelane, S. Valanarasu, I. Kulandaisamy, A. Benazir Fathima, and A. Kathalingam, "*Effect of annealing temperature on the structural, morphological, optical and electrical properties of Co3O4 thin film by nebulizer spray pyrolysis technique*," **Journal of Materials Science: Materials in Electronics,** Vol. **27**, 3860-3866, **2016**.

[15] R. Hong, J. Huang, H. He, Z. Fan, and J. Shao, "*Influence of different post-treatments on the structure and optical properties of zinc oxide thin films*," **Applied Surface Science,** Vol. **242**, 346-352, **2005**.

[16] D. Bao, X. Yao, N. Wakiya, K. Shinozaki, and N. Mizutani, "*Band-gap energies of sol-gel-derived SrTiO3 thin films*," **Applied Physics Letters,** Vol. **79**, 3767-3769, **2001**.

[17] S. A.-J. Jassim, A. A. R. A. Zumaila, and G. A. A. Al Waly, "*Influence of substrate temperature on the structural, optical and electrical properties of CdS thin films deposited by thermal evaporation*," **Results in Physics,** Vol. **3**, 173-178, **2013**.

[18] P. K. Sarswat and M. L. Free, "*A study of energy band gap versus temperature for Cu2ZnSnS4 thin films*," **Physica B: Condensed Matter,** Vol. **407**, 108-111, **2012**.

[19] K. A. Connors, "*Chemical Kinetics: The study of Reaction rates in solide"*, **VCH Publishers**, p. 496, **1998**.

[20] R. Dannenberg, S. Baliga, R. J. Gambino, A. H. King, and A. P. Doctor, "*Resistivity, thermopower and the correlation to infrared active vibrations of Mn1.56Co0.96Ni0.48O4 spinel films sputtered in an oxygen partial pressure series*," **Journal of Applied Physics,** Vol. **86**, 514-523, **1999**.

[21] R. Schmidt, A. Basu, and A. W. Brinkman, "*Small polaron hopping in spinel manganates*," **Physical Review B,** Vol. **72**, 115101, **2005**.

[22] N. Ponpandian, P. Balaya, and A. Narayanasamy, "*Electrical conductivity and dielectric behaviour of nanocrystalline NiFe 2 O 4 spinel*," **Journal of Physics: Condensed Matter,** Vol. **14**, 3221, **2002**.

[23] B.-K. Park, J.-W. Lee, S.-B. Lee, T.-H. Lim, S.-J. Park, C.-O. Park, *et al.*, "*Cu-and Ni-doped Mn1.5Co1.5O4 spinel coatings on metallic interconnects for solid oxide fuel cells*," **International Journal of Hydrogen Energy,** Vol. **38**, 12043-12050, **2013**.

[24] N. Hosseini, F. Karimzadeh, M. H. Abbasi, and G. M. Choi, "*Microstructural characterization and electrical conductivity of CuxMn3−xO4 (0.9≤x≤1.3) spinels produced by optimized glycine–nitrate combustion and mechanical milling processes*," **Ceramics International,** Vol. **40**, 12219-12226, **2014**.

[25] H. Behzad and F. E. Ghodsi, "*Effect of Zn content on the structural, optical, electrical and supercapacitive properties of sol–gel derived ZnCo2O4 nanostructured thin films*," **Journal of Materials Science: Materials in Electronics,** Vol. **27**, 6096-6107, **2016**.

[26] H. Bordeneuve, S. Guillemet-Fritsch, A. Rousset, S. Schuurman, and V. Poulain, "*Structure and electrical properties of single-phase cobalt manganese oxide spinels Mn3−xCoxO4 sintered classically and by spark plasma sintering (SPS)*," **Journal of Solid State Chemistry,** Vol. **182**, 396-401, **2009**.

[27] A. Petric and H. Ling, "*Electrical Conductivity and Thermal Expansion of Spinels at Elevated Temperatures*," **Journal of the American Ceramic Society,** Vol. **90**, 1515-1520, **2007**.

[28] S. A. Kanade and V. Puri, "*Composition dependent resistivity of thick film Ni(1−x)CoxMn2O4 (0≤ x ≤1) NTC thermistors*," **Materials Letters,** Vol. **60**, 1428-1431, **2006**.

GENERAL CONCLUSION AND FUTURE WORK

Solar energy conversion to electricity is a good alternative to fossil fuels which are non-renewable resources and contaminants for the environment. Among the few light-absorber and semiconducting materials used for making photovoltaics, silicon is still the most commonly commercialized not only thanks to its conversion efficiency but also to its non-toxicity as an element and large natural abundance, despite an indirect gap. The next generation of photovoltaics could be entirely based on nanostructured or superimposed thin layers of transparent and absorber conducting metal oxides. While the former *n*-type of semiconducting oxides is well reported (ZnO, ITO, TiO_2 for TCOs) the latter is often limited to *p*-type Cu_2O. However, the quantum yield for Cu_2O is yet to be improved with 6 % conversion efficiency measured in the best case compared to the theoretical value (~ 20 %). Recent developments of all-oxide photovoltaics are a very interesting alternative to produce low cost and large scale solar cells.

Spinel oxides are among the best candidates to replace Cu_2O as a *p*-type semiconductor for photo-absorption applications, including photovoltaics. This was recently proven to be effective with the efficiency tests performed on new types of all-oxide solar cells containing the materials also under study in our team [1-3]. Spinel oxides offer interesting absorbance in the UV and VIS regions. Theoretical studies predict a very small band gap (E_g ~ 0.5 eV) which would be associated with cation-cation transition in octahedral sites with a spin up direction, as shown by our first-principles calculations. The atomic structures calculated were well fitted with the values reported in the literature for Co_3O_4 and Mn_3O_4, as well the magnetic properties. The density of states and electronic structures of the intermediate $Mn_xCo_{2-x}O_4$ ($0 < x < 3$) compounds are much more difficult to determine due to the variety of elements, crystallographic sites, oxidation states and spin charges. Considering an electron correlation between cations improves the determination but the origin and nature of band gaps in such complex metal oxides remain uncertain and there are still some discrepancies about the type of transitions involved.

Our recent preparation method was optimized for metal spinel oxide materials MM'_2O_4 (*M, M'* = Co, Mn, Cu, Zn and Ni) [4, 5]. This simple synthetic method, free of complex organic agents or surfactants, drives to the formation of crystalline oxide nanoparticles and was developed under ambient atmosphere, and up to 120 °C with a reflux stage for Co-rich phases.

Spherical nanoparticles (30 < diam. < 50 nm) of stoichiometric and single cubic spinel phases $M_xCo_{2-x}MnO_4$ (M = Ni, Zn or Cu; $0 < x < 0.6$) were synthesized and characterized. Crystallite sizes are ~ 15 nm and these materials are stable up to at least 1000 °C in air, which also corresponds to the sintering temperature, as determined by dilatometry measurements.

Colloidal dispersions can then be stabilized using only water and ethanol in order to obtain homogenous spinel oxide thin films on glass, quartz or metal substrates by the dip-coating technique. The oxide structural and microstructural characteristics were studied, in relationships with optical and electronic properties, and thermal treatments were performed in order to densify the layers with the objective of integrating those sun light absorber *p*-type semi-conductors in solar cells. The homogenous thin films present two absorption fronts at ~ 450 and 750 nm, which are associated with two direct band gaps of E_{g1} ~ 1.5 eV and E_{g2} ~ 2.2 eV, respectively, at room temperature. These two gaps decreased by at least 0.2 eV after annealing the thin films at 900 °C for one day in air. Compact layers are observed after annealing, and the electrical conductivity is ~ 10^{-5} S.cm^{-1} after annealing at 1000 °C in air on platinum, in the same magnitude of order than a similar composition of $MnCo_2O_4$ (and Cu_2O, the reference *p*-type oxide material) prepared by PLD.

This thesis was carried out entirely at the CIRIMAT laboratory and the PhD salary was funded by the Vietnamese government and the University of Sciences and Technology in Hanoi (USTH) program for about 88 %. The results are likely to have a larger impact in the fields of optical-electronics and solar energy harvesting by metal-oxide semiconductors.

Indeed, spinel oxide materials are also interesting for other applications that are being developed in our OVM team at the CIRIMAT such as catalysis, photo-catalysis and photo-electrochemistry. For instance, we have recently been able to reach a record catalytic activity for the oxidation of propane with our synthetic material Co_3O_4 that will allow interesting improvements in this area [6]. Self-organized platelets separated by a tenth of nanometers nanoparticles of the same composition drive to a porosity close to 75 %. CoOOH precursors and Co_3O_4 thus prepared exhibit a high catalytic activity. Carbon monoxide is fully converted at 80 °C while complete conversion of propane occurs at 220 °C, the latter being the lowest temperature ever recorded at this time. The catalytic activity of $Mn_xCo_{2-x}O_4$ can also be adjusted

by modification of the sample composition over a wide range, and doping by other elements. It is however less efficient with manganese-rich compounds. The attractive catalytic activity associated with high specific surface area, stability in alkaline solutions and low cost make such materials excellent substitutes to noble metals, much more expensive. A starting collaborative work with the team of D.P. Tran from the University of Sciences and Technology in Hanoi, will allow us to test the electro-catalytic and photocatalytic activities of our spinel oxide thin films in order to improve, for instance, the oxidation (or reduction) of water…

References

[1] B. Kupfer, K. Majhi, D. A. Keller, Y. Bouhadana, S. Rühle, H. N. Barad, *et al.*, "*Thin Film Co3O4/TiO2 Heterojunction Solar Cells*," **Advanced Energy Materials,** Vol. **5**, 14010071-14010075, **2015**.

[2] Z. Yan, D. A. Keller, K. J. Rietwyk, H.-N. Barad, K. Majhi, A. Ginsburg, *et al.*, "*Effect of Spinel Inversion on (CoxFe1−x)3O4 All-Oxide Solar Cell Performance*," **Energy Technology,** 1-8, **2016**.

[3] S. Rühle, A. Y. Anderson, H.-N. Barad, B. Kupfer, Y. Bouhadana, E. Rosh-Hodesh, *et al.*, "*All-Oxide Photovoltaics*," **The Journal of Physical Chemistry Letters,** Vol. **3**, 3755-3764, **2012**.

[4] G. Salek, C. Tenailleau, P. Dufour, and S. Guillemet-Fritsch, "*Room temperature inorganic polycondensation of oxide (Cu2O and ZnO) nanoparticles and thin films preparation by the dip-coating technique*," **Thin Solid Films,** Vol. **589**, 872-876, **2015**.

[5] T. L. Le, S. Guillemet-Fritsch, P. Dufour, and C. Tenailleau, "*Microstructural and optical properties of spinel oxide MxCo2 − xMnO4 (M = Ni, Zn or Cu; 0 < x < 1) thin films prepared by inorganic polycondensation and dip-coating methods*," **Thin Solid Films,** Vol. **612**, 14-21, **2016**.

[6] G. Salek, P. Alphonse, P. Dufour, S. Guillemet-Fritsch, and C. Tenailleau, "*Low-temperature carbon monoxide and propane total oxidation by nanocrystalline cobalt oxides*," **Applied Catalysis B: Environmental,** Vol. **147**, 1-7, **2014**.

Résumé de thèse

Introduction Générale

Le développement de la société et l'augmentation de la consommation d'énergie montrent que nous aurons besoin de plus d'énergies à l'avenir. Dans le contexte de la crise de l'énergie, le changement climatique, l'approvisionnement à long terme et de la sécurité, l'énergie solaire est une source intéressante. L'énergie solaire est inépuisable et peut fourni suffisamment d'énergie pour notre société. Cependant, la production d'électricité et de carburants à partir de l'énergie solaire reste une technologie coûteuse, principalement à cause des matériaux utilisés pour la construction des cellules qui permettent leur transformation.

Les oxydes semi-conducteurs à base de métaux de transition sont peu chers et abondants. Les matériaux nanométriques ont été largement étudiés ces dernières années en raison des propriétés diverses très intéressantes qu'ils présentent telles que les propriétés catalytiques, thermiques, magnétiques, électriques, optiques… Au cours des dernières années, diverses méthodes ont été développées pour la préparation d'oxydes spinelles nanostructurés comme les dépôts physiques et chimiques en phase vapeur, la chimie douce etc. En particulier, les oxydes de métaux de transition à structure type spinelle sont des matériaux particulièrement intéressants pour des applications en tant que capteur, piles à combustible, catalyseurs, cellules solaires, transformateurs, etc.

Au CIRIMAT, nous avons développé une nouvelle thématique visa à valoriser les matériaux oxydes inorganiques, en particulier les oxydes spinelles, pour évaluer leurs potentialités à être intégrés dans les cellules solaires. Actuellement, les principaux matériaux semi-conducteurs inorganiques étudiés pour cette application sont le Si, le $CuInSe_2$, CdTe et GaAs. Cependant, certains éléments limitants s'opposent au développement de ces matériaux tels que le gap indirect (pour Si), la rareté et/ou la toxicité des éléments et le coût élevé de revient. Ainsi, en plus d'études visa à améliorer l'efficacité des cellules solaires, il est nécessaire de trouver de nouveaux composés ayant des propriétés semi-conductrices appropriées afin d'ouvrir de nouveaux horizons. Les cellules solaires à base d'oxydes de métaux ont un fort potentiel pour lutter contre toutes les difficultés rencontrées dans les cellules solaires habituelles. L'approche photovoltaïque « tout oxyde » est très intéressante en raison de la stabilité chimique, la toxicité négligeable et l'abondance de nombreux oxydes métalliques qui permettent potentiellement la fabrication de cellules solaires dans des conditions usuelles. Les oxydes métalliques sont largement utilisés comme composants dans l'électronique en tant

qu'électrodes conductrices transparentes et couches de transport d'électrons, tandis que très peu d'oxydes métalliques ont été utilisés comme absorbeurs solaires, essentiellement à base de Cu_2O de type *p*.

L'objectif de ce travail est de synthétiser, par une voie de chimie-douce, des nanoparticules d'oxydes type spinelle semi-conducteurs absorbeurs de lumière, en vue de les mettre sous forme de couches minces et les intégrer dans un système de conversion énergétique. Différentes substitutions permettront de moduler les caractéristiques physiques telles que le gap énergétique, l'absorption de la lumière et le transport de charge pour différent applications, y compris pour le photovoltaïque.

Par conséquent, l'objectif principal de cette thèse est de développer et d'étudier de nouveaux matériaux photo-absorbeurs à base d'oxydes spinelle semi-conducteurs en vue de leur intégration dans des cellules photovoltaïque. Notre travail se focalise sur le système $M_xCo_{2-x}MnO_4$ (M = Ni, Cu, Zn ; x = 0, 0,15, 0,30, 0,60) en se basant sur le fait que le composé Co_2MnO_4 est un bon semi-conducteur type *p*, absorbeurs de lumière.

Chapitre I

Le premier chapitre présente une revue bibliographique qui reporte le contexte de la crise énergétique, les sources d'énergies renouvelables, les générations de cellules photovoltaïques, les cellules photovoltaïques « tout oxyde » et les oxydes spinelles de valence mixte absorbeurs solaires.

1. La crise énergétique et les solutions en énergie renouvelable

Les ressources naturelles sont limitées alors que la demande énergétique mondiale augmente. La crise énergétique dans les années 1970 était due à un manque d'approvisionnement en pétrole des pays comme l'Allemagne, la France, les Etats-Unis, au Canada et d'autres pays développés. Ainsi, il est fondamental de trouver d'autres sources d'énergie renouvelables qui constituaient une alternative en source d'énergie. Les sources d'énergie renouvelable sont l'énergie éolienne, l'énergie hydraulique, l'énergie géothermique, la biomasse et l'énergie solaire. Les cellules solaires, qui peuvent fournir suffisamment d'énergie pour le monde devraient maintenant être une priorité. Cette thèse est consacrée à l'énergie solaire qui produit l'énergie électrique en utilisant l'effet photovoltaïque.

2. Trois générations de cellules photovoltaïques

La première génération comprend des cellules composées de silicium (ou germanium) dopés avec du bore (type *p*) et du phosphore (type *n*) dans une jonction *pn* (Figure 1).

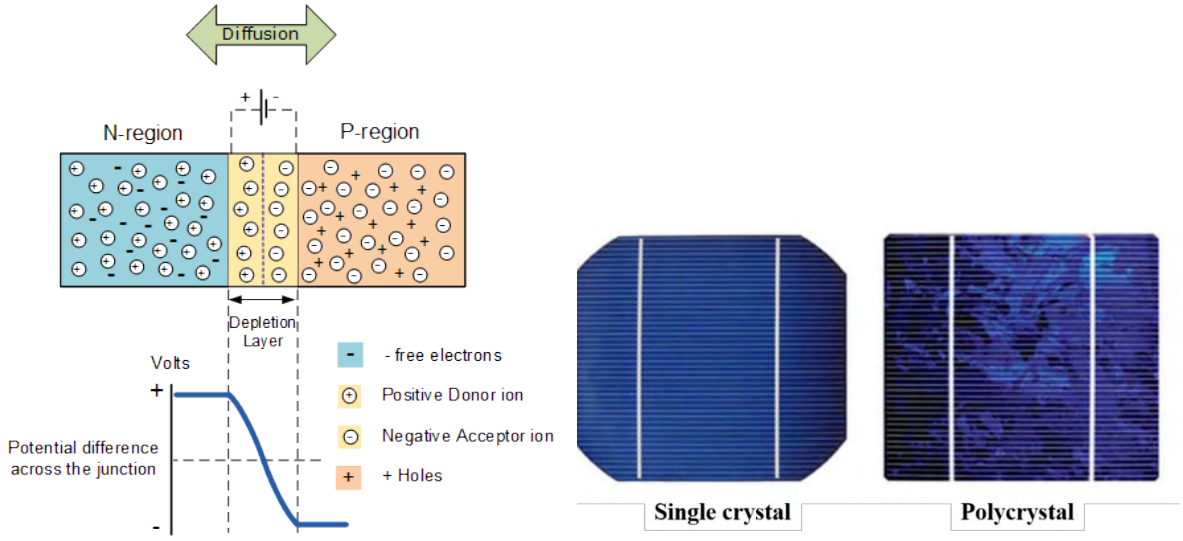

Figure 1: La jonction pn et deux types de la première génération de cellules solaires.

Il existe trois types de cellules solaires pour cette première génération. Ils se distinguent par le taux de cristallisation du silicium, qui peut se présenter sous la forme d'un monocristal ou être composée de grains cristallins, que l'on nomme alors poly-cristal (Figure 1). Cette technologie présente une efficacité très élevée mais le silicium très pur et coûteux. Le silicium peut aussi être amorphe mais son rendement de conversion reste faible.

La deuxième génération de cellules photovoltaïques est constituée de couches minces de CdTe/CdS, de séléniure de cuivre et indium (CIS), de séléniure d'indium gallium et cuivre (CIGS), de sulfure de zinc cuivre et étain (CZTS) et l'arséniure de gallium (GaAs). Les cellules à base de CdTe ou GaAs sont souvent exploitées pour des applications spatiales. Elles sont difficilement transposables à grande échelle en raison de leurs coûts de fabrication et de la toxicité des éléments chimiques les constituant. Le CIS, de structure type chalcopyrite présente en revanche une alternative intéressante. La conversion d'énergie lumineuse en énergie électrique présente un rendement supérieur à 20 % pour les cellules solaires de CdTe [1], et 19,5 % pour CIGS [2].

La troisième génération de cellules photovoltaïques est de type Grätzel ou « Dye Sensitized Solar Cells » (DSSC), à base de Quantum Dots (QDSSC) ou « Extremely Thin Absorbers » (ETA). Ces cellules sont constituées d'électrodes à base d'électrodes d'oxydes métalliques déposées sur substrat de TCO et recouvert est d'une fine couche d'absorbant. Le rendement maximum des DSSC est de 15 % qui a été annoncé en 2013 par l'équipe de M. Grätzel à l'Ecole Polytechnique de Lausanne [3].

3. Les hétérojonctions « tout oxyde » pour le photovoltaïque

Cu_2O est le matériau type absorbant de lumière avec un gap d'environ 2 eV permettant de prédire un rendement de conversion théorique de 20 % et une utilisation très intéressante pour des cellules solaires semi-transparentes. Un rendement maximum de 6,25 % a été démontré expérimentalement dans des cellules « toute oxyde » par la juxtaposition de MgF_2 / AZO / $(Ga_{0,95}Al_{0,025})_2O_3$/$Cu_2O$: Na [4].

Les matériaux de structure pérovskite pour le photovoltaïque ont été largement étudiés et développés ces dernières années. Le rendement de conversion a augmenté rapidement ces en 7 ans (de 3,8 % à 20,2 % de 2009 à 2015). Ce dernier a été atteint pour le formamidinium iodure de plomb ($NH_2CHNH_2PbI_3$) [5].

Récemment, de nombreuses études ont portées sur des oxydes ferroélectriques de structure perovskite, qui présentent de fortes potentialités dans l'application de cellules photovoltaïques. Ces cellules sont des exemples de jonctions *pn* et les électrons et trous photo-générés sont séparés spontanément par un champ électrique au sein du matériau ferroélectrique. BFO ($BiFeO_3$), PZT ($Pb(Zr,Ti)O_3$), PLZT ($(Pb,La)(Zr,Ti)O_3$) sont des matériaux ferroélectriques pour le photovoltaïque. Des hétérostructures de ITO/BFO/SRO présentent une efficacité externe quantique (EQE) de 10 % [6]. Un rendement de 1,25 % est rapporté dans les structures de type Ag/*n*-a-Si/PZT/ITO/verre [7].

Récemment, un intérêt s'est porté sur des oxydes type spinelle de formule AB_2O_4 qui sont des semi-conducteurs de type *p* et absorbants de lumière. Ils sont constitués d'éléments abondants et stables chimiquement et présentent toutes les caractéristiques essentielles pour l'application photovoltaïque. Un exemple d'hétérojonction d'oxyde spinelle pour la cellule photovoltaïque inorganique est TiO_2/Co_3O_4 où Co_3O_4 est un semi-conducteur type *p*, qui a deux transitions directes notables dans la gamme du visible avec des bandes interdites d'énergie de

1,45 eV et 2,26 eV [8]. La cellule solaires « tout oxyde » avec une géométrie en multicouches à base de verre/FTO/TiO_2/$(Co_xFe_{1-x})_3O_4$/Au avec J_{SC} de 53 µA cm^{-2} et V_{OC} de 534 mV a été présentée en 2016 [9].

4. Les oxydes mixtes type spinelle comme absorbeurs solaires

La structure spinelle est complexe et intéressante du fait de la présence de deux sites cristallographiques différents, tétraédriques (*A*) et octaédriques (*B*), dans lesquels se distribuent les cations métalliques de natures et de degrés d'oxydation différents. La structure idéale peut être décrite par un arrangement cubique à faces centrées d'ions O^{2-} (groupe d'espace *Fd-3m*). La maille élémentaire contient 32 anions, autant de sites octaédriques et deux fois plus de sites tétraédriques. Ces derniers sont occupés au huitième tandis que la moitié des sites octaédriques sont occupés. La présence de deux sites cristallographiques confère donc des possibilités variables d'arrangement cationique, généralement décrits par le degré d'inversion λ. La répartition des cations *A* et *B* sur les différents sites, peut s'écrire : $(A_{1-2x}B_{2x})[A_{2x}B_{2-2x}]O_4$. Conventionnellement, on note () pour les sites tétraédriques, [] pour les sites octaédriques. Quand $x = 0$, le spinelle est dit « normal » ou « direct » $(A^{2+})[B_2^{3+}]O_4$. Pour $x = 0,5$, le spinelle est « inverse » $(B^{3+})[A^{2+}B^{3+}]O_4$. Et dans le dernier cas, $0 < x < 0,5$, le spinelle est dit « désordonné ».

La conductivité électrique des oxydes de structure spinelle est décrite par le phénomène de sauts de polarons. La loi de Verwey permet de justifier le saut de polarons en imposant que le transfert de charges ne soit possible qu'entre deux cations d'un même élément dont le degré d'oxydation diffère d'une unité, et situés sur un même site cristallographique [10].

Les propriétés optoélectroniques des oxydes type spinelle sont directement reliées à leurs structures de bandes. La bande de valence (BV) est constituée d'orbitales d'oxygène pleines alors que la bande de conduction (BC) est constituée principalement d'orbitales du cation *d* vides. Les propriétés d'absorption de lumière des oxydes de métaux de transition sont principalement liées à des transferts de charges de diverses natures dans le matériau : transfert de charges inter-atomiques qui peuvent se faire entre anions et cations (transitions *p-d*) ou entre cations (transitions *d-d*) donnant naissance à de larges fronts d'absorption. Le deuxième type de transfert de charges est le transfert de charges intra-atomiques (transition *d-d* sur un même cation) qui n'est valable que dans certains cas (effet du champ des ligands).

Nous avons choisi le composé Co_2MnO_4 comme système pivot. Le dopage avec les métaux de transition va permettre de moduler les propriétés physiques et chimiques. Il présente par ailleurs la plus haute de conductivité électrique dans la solution solide Mn_3O_4-Co_3O_4 [11]. Co_2MnO_4 est un système spinelle cubique complètement inversé. En outre, les propriétés optiques de Co_2MnO_4 ont montré deux valeurs de gap (1,48 et 2,13 eV) appropriées pour les absorbeurs solaires [12-14].

Les oxydes mixtes type spinelle à base de Ni-Co-Mn-O sont intéressants pour nombreuses applications telles que les thermistances de haute performance, bolomètres et à détecteurs infrarouge non refroidis [15-17]. Dannenberg et al. (1999) ont montré que les oxydes type spinelle de Mn-Co-Ni sont de type *p*, avec une conductivité électrique par hopping de polarons et une fenêtre de transparence de 6 à 14 µm en longueurs d'ondes [18]. Zhou et al. (2014) ont étudié ce type de composé dans l'UV-VIS-NIR et les constantes d'optique de $Mn_{1,4}Co_{0,6}O_4$ par ellipsométrie spectroscopique [19]. Quelques études ont été réalisées sur des spinelles oxydes de Cu-Co-Mn-O and Zn-Co-Mn-O. Xu et al. (2011) ont synthétisé la poudre de $Cu_xMn_{1,5-0,5x}Co_{1,5-0,5x}O_4$ (x = 0,1, 0,3 et 0,5) par la méthode acide citrique-nitrate et les couches minces ont été déposées sur acier inoxydable ferritique par trempage-retrait. La couche de $Cu_{0,3}Mn_{1,35}Co_{1,35}O_4$ a été compactée après frittage et la valeur de 16 $m\Omega.cm^2$ mesurée pour l'ASR (area specific resistance) [20].

Chapitre II

Dans ce chapitre, nous décrivons les techniques de synthèses et de caractérisations des poudres et des couches minces. Les poudres ont été synthétisées par la méthode de polycondensation inorganique à basse température et les couches minces ont été obtenues par la méthode trempage-retrait (dip-coating) mais aussi par PLD (Pulsed Laser Deposition). Les céramiques massives ont été obtenues après frittage SPS (Spark Plasma Sintering).

Les principales techniques d'analyses utilisées au cours de ce travail sont la fluorescence de rayons X (FRX), la diffraction de rayons X (DRX), le microscope électronique à balayage à effet de champ (MEB-FEG), l'analyse thermogravimétrique (ATG), l'analyse thermique mécanique (ATM), des mesures de topographie et de rugosité. Les propriétés optiques et électriques ont également été déterminées.

Les analyses chimiques des éléments ont été effectuées à partir des poudres par fluorescence de rayons X. Les diagrammes de DRX sur poudres à température ambiante ont été obtenues grâce à un diffractomètre Bruker D4 Endeavour. L'analyse structurale des poudres en température a été réalisée à l'aide d'un diffractomètre Bruker D8. Un diffractomètre SIEMENS D5000 a permis d'obtenir les diagrammes de DRX sur couches minces à température ambiante. L'analyse microstructurales a été réalisée grâce à un système JEOL JEM 6700F. L'analyse thermogravimétrique a été effectuée à l'aide d'un système SETARAM – TAG 16. La détermination dea température de frittage optimale a été réalisée par le système de dilatométrie SETSYS Evolution TMA. La porosité et la surface spécifique ont été déterminées en utilisant un système ZYGO. Les mesures de spectrophotométrie, non destructives, correspondent aux mesures de transmission et de réflexion sur couches minces en utilisant un Bentham PVE 300 PV. Un système de mesures 4 pointes a été utilisé pour analyser les propriétés électriques des couches minces, le Keithley 237.

Chapitre III

La structure de bandes électroniques, les paramètres de maille et les caractéristiques magnétiques de $Mn_xCo_{3-x}O_4$ ($0 \leq x \leq 3$) ont été déterminés pour la première fois sur l'ensemble de la solution solide grâce à des calculs DFT (Density Function Theory). Ces simulations sont comparées aux données expérimentales.

Nos résultats sont conformes aux données de la littérature pour les compositions Co_3O_4 et Mn_3O_4. Les propriétés antiferromagnétiques de Co_3O_4 sont reproduites, même si une incertitude subsiste sur la valeur du gap plus faible (≈ 0,8 eV) par rapport à la valeur calculée en utilisant la méthode mBJ (Tran-Blaha modified Becke-Johnson) (≈ 2,91 eV). Le cas de Mn_3O_4 est plus complexe car il présente un ordre ferrimagnétique particulier à basse température. Cette caractéristique peut être décrite par des calculs de magnétisme colinéaires par les états magnétiques différents présentant une énergie similaire. Nous avons trouvé que la solution plus stable correspond à un ordre antiferromagnétique complet, avec une valeur du gap de 1,92 eV.

L'interprétation des résultats dépend des méthodes et des paramètres utilisés et est plus délicate pour les composés intermédiaires ($0 < x < 3$), en raison de la complexité de la distribution cationique et des états d'oxydation possibles pour les phases cubique et

quadratique. Cependant, nos calculs montrent une évolution de la phase cubique vers quadratique avec l'augmentation de *x*. Les calculs prévoient que la transition de phase apparaisse pour $x > 2,0$ valeur supérieure à la valeur observée expérimentalement ($x > 1,25$). Nos modélisations ne sont pas toujours conformes avec les données et l'effet détail par Jahn-Teller. Plusieurs contributions d'inter-corrélation peuvent être proposées pour expliquer cette différence, comme un volume calculé plus faible et une fausse description des effets de corrélation d'électrons ou d'un ordre magnétique non-colinéaire plus complexe.

Les calculs de structure montrent que tous les matériaux de compositions intermédiaires sont ferrimagnétiques, avec des cations dans les sites *A* ayant des moments magnétiques de spin antiparallèles à ceux des sites *B*, en accord avec les études expérimentales. Cependant, cet ordre ferrimagnétique est certainement non-colinéaire, et devient complexe à décrire lorsque la teneur en cations Mn augmente dans les sites *B*. D'autre part, la présence éventuelle de défauts structuraux peut expliquer la valeur d'aimantation inférieure déterminée expérimentalement et la diminution mesurée pour $x > 1,25$. Les cations Co_B^{III} se trouvent toujours dans un état de bas spin pour $0 \leq x < 2$ avec la méthode mBJ, alors que la méthode GGA+*U* prédit une transition vers un état de haut spin pour $x > 0,5$. La méthode de Monte-Carlo pourrait peut-être permettre de tenir compte de l'ordre magnétique complexe et de la température et d'accéder ainsi à en détermination de la structure.

Les structures de bandes électroniques de ces oxydes type spinelle à base de cobalt et manganèse ont été également déterminées. La valeur de bande interdite des oxydes binaires Mn_3O_4 et Co_3O_4 est fortement diminuée par le dopage, ce qui peut être expliqué par la plus faible valeur de bande interdite, des bandes e_g (d_{z^2} pour les bandes occupées et $d_{x^2-y^2}$ pour les bandes inoccupées). Cette valeur de bande interdite est rasement mentionnée dans la littérature, principalement en raison de la plage restreinte de mesures. La valeur de bande interdite est de ~ 0,5 eV pour la phase cubique, et est plus élevée, environ 1,5 eV, pour la phase quadratique. Cette transition pourrait être liée aux transitions de cations-cations avec une direction de haut-spin dans les sites octaédriques.

Chapitre IV

La préparation et les caractérisation (micro-) structurales des poudres et des couches minces d'oxydes type spinelle de $M_xCo_{2-x}MnO_4$ (M = Ni, Cu, Zn ; x = 0, 0,15, 0,30, 0,60) sont présentées dans ce chapitre. La méthode de polycondensation inorganique a été utilisée pour synthétiser les échantillons de poudres à basse température (120 °C). Les sels métalliques ont été précipités dans la solution aqueuse, avec comme agent précipitant, une base (LiOH). La concentration de la solution saline est fixée à 0,3 mol/L. Le pH est maintenu constant par l'utilisation d'une quantité bien supérieure à la quantité nécessaire pour faire précipiter tous les sels (4,19 g LiOH dans 1400 mL eau). Un temps de mûrissement arbitraire de 90 min a été choisi pour l'ensemble de l'étude. Une étape de reflux de deux heures a été utilisée pour évaluer la stabilité de l'oxyhydroxyde mixte (Co,Mn)OOH et pour obtenir des oxydes parfaitement cristallisés. Le spinelle cubique unique est observé par diffraction des rayons X pour toutes les compositions synthétisées. Pour les compositions riches en cuivre, on observe par contre la présence de la phase CuO et d'un oxyde contenant du cuivre et du cobalt. Les nanoparticules sont de forme sphérique avec une taille variant entre 20 et 50 nm (Figure 2).

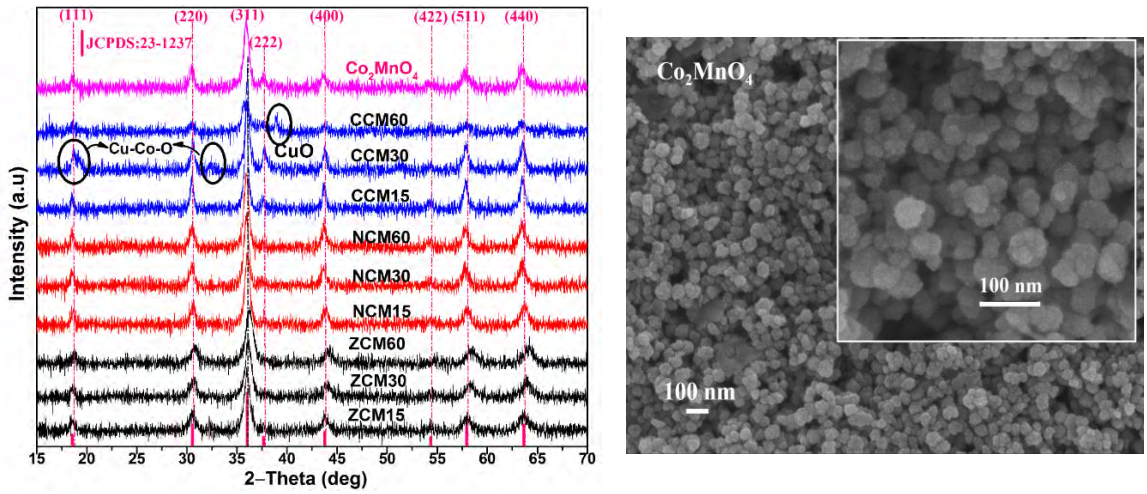

Figure 2: Diffractogrammes de rayon X des différents échantillons préparés et clichés de MEB de poudres de Co_2MnO_4.

Le paramètre de maille de chaque composition a été déterminée. Pour les compositions contenant du Ni, la valeur du paramètre de maille augmente régulièrement avec la teneur du Ni car le rayon ionique de Ni^{2+} est plus grand que celui de Mn^{2+} et de Co^{2+}. L'inverse est observé

pour les poudres contenant du Zn à cause du rayon ionique plus petit du zinc [21, 22]. La taille moyenne des cristallites a été calculée en utilisant la formule de Debye Scherrer.

La stabilité thermique des échantillons a été étudiée par analyses thermogravimétriques sous air jusqu'à 1000°C. Elle nous permet d'anticiper l'apparition d'éventuelles transformations structurales pouvant intervenir lors du frittage des couches minces d'oxydes.

La température du frittage de chaque composition a été déterminée. Elle est voisine de 1000 °C sous air. Les oxydes sont stables jusqu'à 900 °C quel que soit le substrat.

Dans la deuxième partie de ce chapitre, nous présentons la méthode de dépôt des couches minces sur des substrats différents et les caractérisations des couches minces avant et après traitement thermique. La méthode de mise en forme que nous avons utilisée pour la fabrication de couches minces est le trempage-retrait, ou dip-coating, à température ambiante. Pour l'obtention d'une dispersion de nanoparticules d'oxydes relativement stable, nous avons choisi un mélange azéotrope constitué de 96 % d'éthanol et d'eau distillée. Ce mélange présente l'avantage de conserver une composition constante au cours du temps et représente un bon compromis entre les différentes propriétés requises. Les conditions de trempage-retrait sont fixées. La vitesse de trempage et de retrait est égale à 200 mm/min et le substrat reste immergé 30 s dans la solution avant d'être retiré. Cette durée permet de rétablir l'équilibre dans la solution après les turbulences causées par l'immersion du substrat. Les substrats de quartz, alumine, nitrure de titane et platine ont été utilisés pour le dépôts des couches minces, afin d'étudier leurs propriétés optiques et électriques dans le prochain chapitre.

Les couches minces sont homogènes et relativement compactes avec une épaisseur moyenne de 750 nm après trois dépôts consécutifs. La rugosité moyenne la plus faible est observée pour le composé CCM15 ($Cu_{0,15}Co_{1,84}Mn_{1,01}O_4$) ($R_a$ = 0,003 ± 0,001 µm).

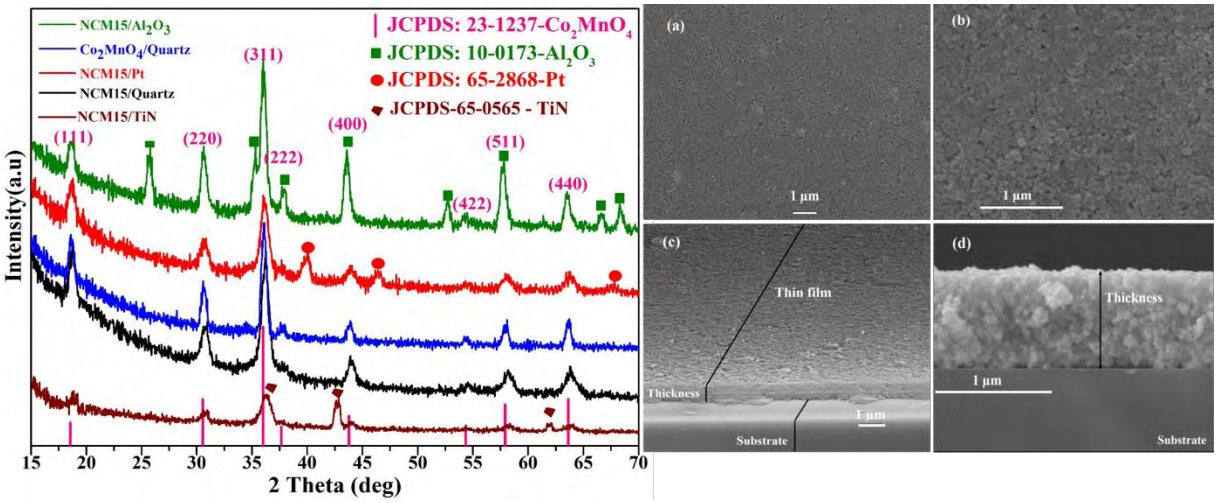

Figure 3: Diffractogrammes de rayons X en incidence rasante (à gauche) et cliché MEB des couches minces de NCM15 (à droite).

Les couches minces ont été traitées à une température comprise entre 900 °C et 1000 °C en vue de leur densification. Tout d'abord, les couches minces ont été traitées à 1000 °C sous air pendant 5 heures. Mais après traitement, les couches minces déposées sur les substrats de quartz, alumine et nitrure de titane, avaient réagi avec les substrats. Nous avons diminué la température de traitement des couches minces déposées sur quartz jusqu'à 900 °C. La structure initiale n'a alors pas évoluée. Ces couches ont été caractérisées pour déterminer leurs propriétés otiques et électriques. Les couches minces déposées sur platine sont stables jusqu'à 1000 °C (Figure 4).

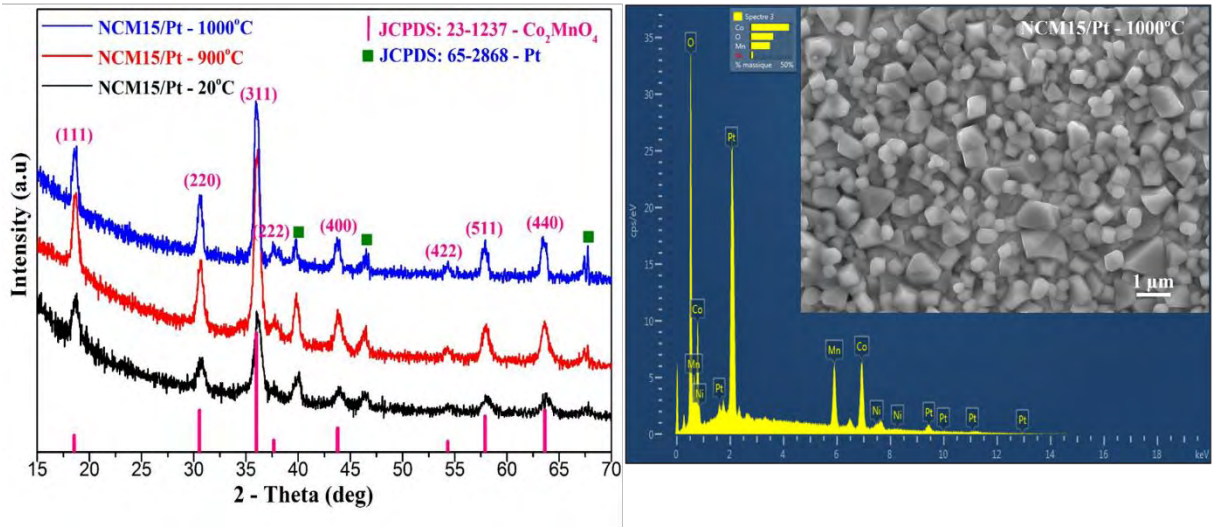

Figure 4: Diffractogrammes de rayons X en incidente rasante et cliché MEB de la couche mince de NCM15 déposé sur platine après traitement thermique.

Les observation MEB-FEG ont permis de préciser la microstructure des couches minces d'oxydes déposées sur les différents substrats. Les couches minces après traitements thermiques sont homogènes. Les couches minces traitées à 900 °C ne sont pas densifiées. On observe des pores en surface (Figure 5). En revanche, la couche mince déposée sur platine et traitée à 1000 °C est beaucoup plus dense (voir Figure 4).

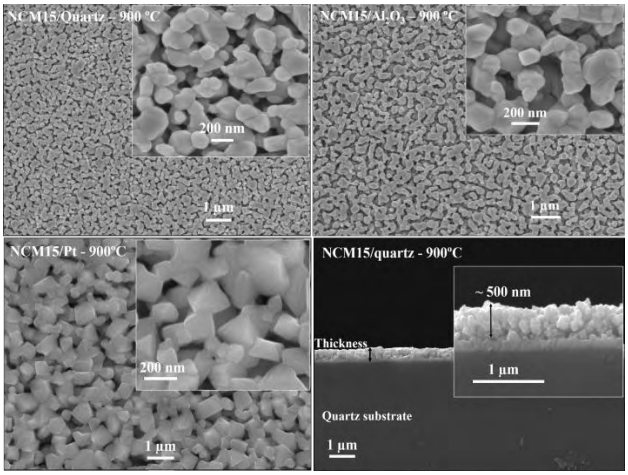

Figure 5: Clichés de MEB-FEG en surface et coupe transversale des couches minces de NCM15 déposées sur quartz, alumine et platine après traitement thermique à 900 °C sous air.

Chapitre V

Ce chapitre présente les propriétés optiques et électriques des couches minces avec le traitement thermique. Les propriétés d'absorbance de lumière des couches minces ainsi préparées, mesurées sur une gamme de longueurs d'ondes du domaine spectral UV-VIS, montrent deux bandes d'absorbance, correspondantes à deux valeurs de gap pour chaque composition. L'absorbance des couches minces augmente dans la gamme du visible après traitement thermique à 900 °C pour les couches minces déposées sur substrat de quartz et leurs gaps diminuent (Tableau 1). Les couches minces sont plus compactées. La résistivité des couches minces diminue de 10^5 à 10^2 Ω.cm avec l'augmentation de la température de 20 à 300 °C (Tableau 2). Une étude parallèle, basée sur la préparation de films minces absorbants de lumière de Co_2MnO_4 et Cu_2O par la technique de PLD (Pulsed Laser Deposition) est également présentée.

Les propriétés optiques des oxydes spinelles $M_xCo_{2-x}MnO_4$ (M = Ni, Cu, Zn, x = 0, 0,15, 0,30, 0,60) ont été déterminées dans une gramme de 300 à 1100 nm. Le spectre d'absorbance

présente deux fortes bandes d'absorption à 450 et 750 nm. Les couches minces sont fortement absorbantes dans l'ultraviolet. Cette absorbance diminue dans la zone visible et infrarouge. La première bande d'absorption située dans la gamme de l'UV (450 nm) est attribuée à un transfert de charge inter-atomiques (anion-cation). La présence de la bande d'absorption vers 750 nm est expliquée par le transfert de charge inter-atomiques (cation-cation) entre les orbitales *d* des cations en sites octaédriques et tétraédriques [23]. Les propriétés d'absorbance des couches minces augmentent après traitement thermique dans l'air (Figure 6). Les gap optiques des oxydes $M_xCo_{2-x}MnO_4$ (M = Ni, Cu, Zn, x = 0, 0,15, 0,30, 0,60) obtenus à partir de la relation de Tauc présentent la meilleure interpolation de la courbe $(\alpha hv)^m$ en fonction de hv, pour m = 2, mettant en évidence la présence de deux gap directs dans chaque composition (Figure 7). Le traitement thermique à 900 °C sous air des couches minces déposées sur quartz a permis d'améliorer les propriétés optiques (Figure 6). Les valeurs des gaps optiques de chaque composition avant et après traitement thermique sont présentées le Tableau 1. Les valeurs des gaps optiques de chaque composition ont diminué après traitement thermique.

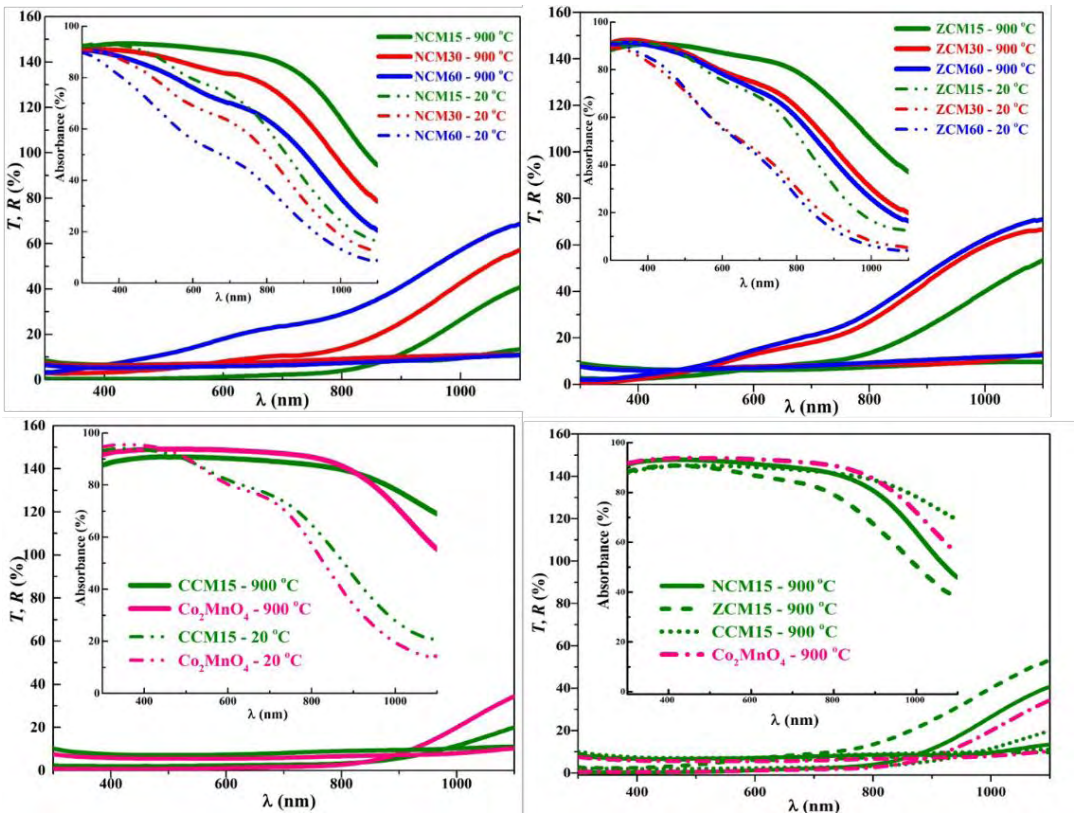

Figure 6: Les propriétés optiques des couches minces déposées sur quartz avant et après traitement thermique dans l'air.

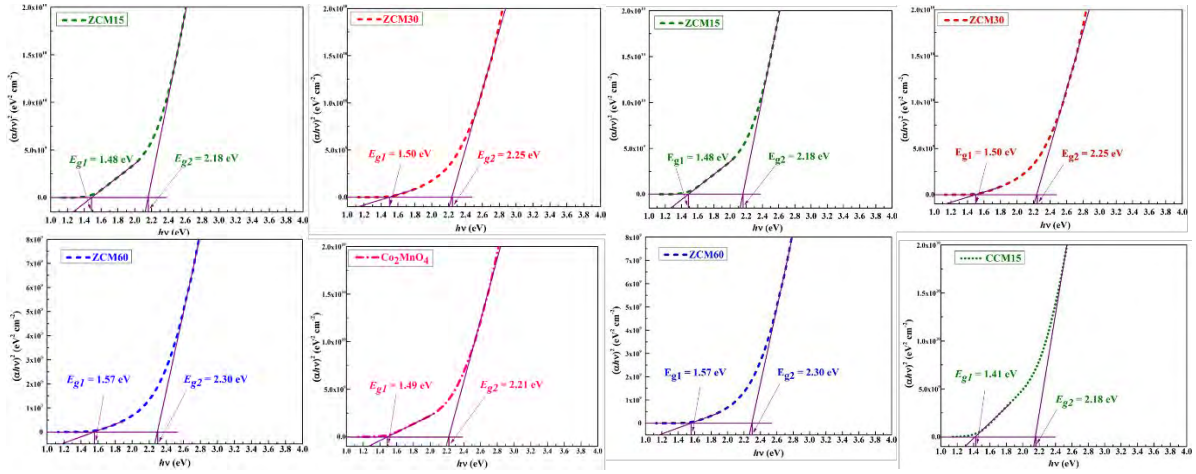

Figure 7: Détermination des gaps des couches minces avant traitement thermique par l'intersection de l'extrapolation linéaire de la courbe de $(\alpha h\nu)^2$ avec l'axe des abscisses (hν).

Tableau 1: Valeurs des gap optiques en fonction de la composition avant et après traitement thermique à 900 °C sous air

Composition	E_{g1} (eV)		E_{g2} (eV)	
	20 ºC	Après 900 ºC	20 ºC	Après 900 ºC
Co_2MnO_4	1.49	1.29	2.21	1.58
NCM15	1.41	1.26	2.19	1.71
NCM30	1.43	1.29	2.20	1.75
NCM60	1.45	1.30	2.34	1.81
ZCM15	1.48	1.28	2.18	1.71
ZCM30	1.50	1.30	2.25	1.82
ZCM60	1.57	1.33	2.30	1.88
CCM15	1.41	1.19	2.18	1.40

La conductivité des couches minces d'oxydes, déterminée par la mesures des 4 pointes de la température ambiante à 300 °C pour les couches minces, est présentée dans le Tableau 2. La conductivité augmente en fonction de la température pour toutes les compositions. L'énergie d'activation a été déterminée en utilisant la formule d'Arrhenius [24]. La valeur de l'énergie d'activation est environ de 0, 37 eV, ce qui corresponds à la valeur de littérature [25, 26].

Tableau 2: Conductivité électrique des couches minces en fonction de la température.

	σ (20 ºC) (S.cm^{-1})	σ (100 ºC) (S.cm^{-1})	σ (150 ºC) (S.cm^{-1})	σ (200 ºC) (S.cm^{-1})	σ (250 ºC) (S.cm^{-1})	σ (300 ºC) (S.cm^{-1})
Co_2MnO_4	2.22 x10^{-5}	3.14 x10^{-4}	1.30 x10^{-3}	3.62 x10^{-3}	9.19 x10^{-3}	2.33 x10^{-2}
NCM15	5.62 x10^{-5}	6.44 x10^{-4}	2.85 x10^{-3}	6.84 x10^{-3}	1.67 x10^{-2}	3.36 x10^{-2}
NCM30	4.35 x10^{-5}	5.09 x10^{-4}	3.52 x10^{-3}	8.33 x10^{-3}	1.41 x10^{-2}	3.68 x10^{-2}
NCM60	3.94 x10^{-5}	4.42 x10^{-4}	2.93 x10^{-3}	5.31 x10^{-3}	9.50 x10^{-3}	2.90 x10^{-2}
ZCM15	3.12 x10^{-5}	4.04 x10^{-4}	2.51 x10^{-3}	4.92 x10^{-3}	9.80 x10^{-3}	2.50 x10^{-2}
ZCM30	3.45 x10^{-5}	4.23 x10^{-4}	2.92 x10^{-3}	5.31 x10^{-3}	9.69 x10^{-3}	3.21 x10^{-2}
ZCM60	3.46 x10^{-5}	4.21 x10^{-4}	3.00 x10^{-3}	5.81 x10^{-3}	9.50 x10^{-3}	2.93 x10^{-2}
CCM15	3.23 x10^{-5}	4.05 x10^{-4}	2.05 x10^{-3}	4.43 x10^{-3}	9.90 x10^{-3}	2.60 x10^{-2}

Les couches minces préparées par la méthode de PLD (Pulsed Laser Deposition) sont également présentées dans ce chapitre. Ces couches minces ont été préparées à l'Université de Gainseville (Floride) dans l'équipe du Professeur Juan Claudio Nino. Préalablement, des pastilles de Co_2MnO_4 et Cu_2O (diamètre de 30 mm et d'épaisseur de 5 mm), ont été préparées au laboratoire CIRIMAT par la méthode SPS (Spark plasma sintering). Les couches minces ont

été déposées sur quartz et cuivre. L'épaisseur des couches préparées par PLD est plus mince que celles des couches obtenues par dip-coating. Les couches minces de PLD sont parfaitement cristallisées et compactes (Figure 8). La conductivité électrique augmente en fonction de la température. Pour Co_2MnO_4, on observe une augmentation de 3,89. 10^{-5} $S.cm^{-1}$ (20 °C) à 3,60. 10^{-2} $S.cm^{-1}$ (300 °C). Pour Cu_2O, la conductivité augmente de 5,71. 10^{-5} $S.cm^{-1}$ (20 °C) à 3,90. 10^{-2} $S.cm^{-1}$ (300 °C).

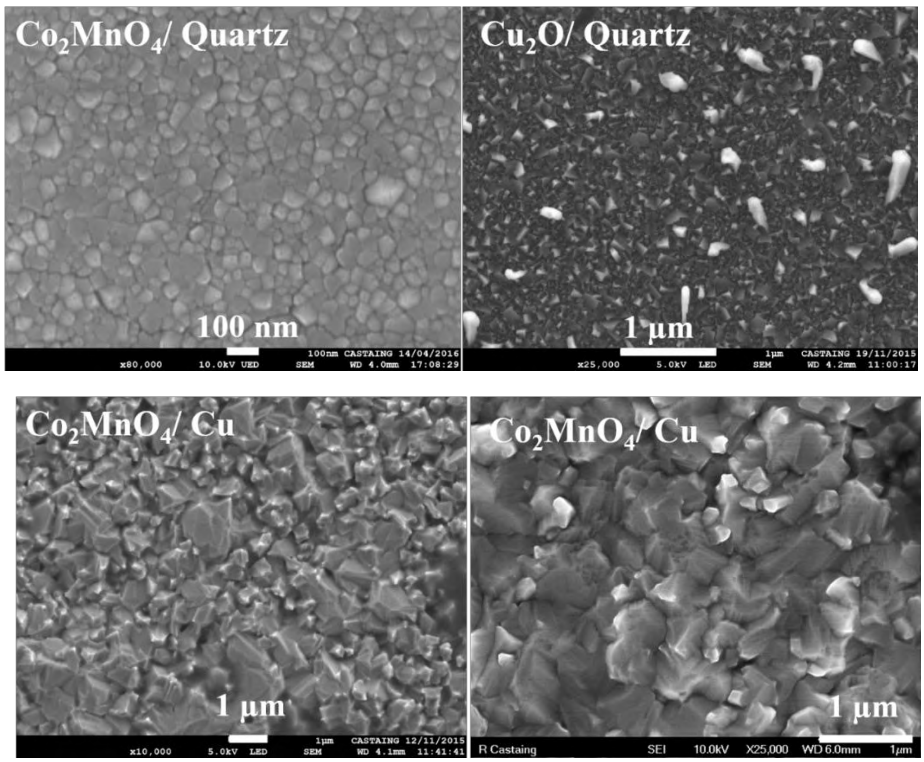

Figure 8: Clichés MEB des couches minces déposées par la méthode de PLD.

Conclusion générale et perspectives

La conversion de l'énergie solaire en électricité est une alternative intéressante aux combustibles fossiles. Parmi quelques matériaux absorbeurs solaires et semi-conducteurs utilisés pour la fabrication de cellules photovoltaïques, le silicium, élément abondant et malgré un gap indirect, est toujours le plus couramment commercialisé non seulement à cause de son efficacité de conversion, mais aussi de sa non-toxicité. La prochaine génération de systèmes photovoltaïques pourra être constituée de couches minces d'oxydes à base métaux conducteurs transparents et absorbants. Les oxydes semi-conducteurs de type *n* sont souvent utilisés, tels que ZnO, ITO, TiO_2 comme TCOs. L'oxyde semi-conducteur de type *p* est généralement limité

à Cu_2O. Cependant, le rendement de conversion est de 6 % seulement (valeur basse par rapport à la valeur théorique de 20 %). Donc le développement d'une cellule photovoltaïque « tout oxyde » est très intéressant pour produire à faible coût et de grandes cellules solaires à grande échelle.

Les oxydes à structure type spinelle sont parmi les meilleurs candidats pour remplacer Cu_2O comme semi-conducteur de type *p* pour les applications de photo-absorption, y compris pour le photovoltaïque. Cela a été montré dans des tests d'efficacité effectués sur de nouvelle cellules solaires « tout oxyde » comprenant les matériaux à l'étude dans notre équipe [9, 27, 28]. Les oxydes spinelles présentent une absorption intéressante dans la région UV-VIS. Les études théoriques prévoient une faible valeur de band gap optique (E_g ~ 0,5 eV) qui correspondent à la transition cation-cation dans les sites octaédriques avec une direction spin-up. Les structures atomiques calculées pour Co_3O_4 et Mn_3O_4 sont en accord avec les valeurs reportées dans la littérature. Il en est de même pour les propriétés magnétiques. La densité des états et les structures électroniques du système $Mn_xCo_{2-x}O_4$ ($0 < x < 3$) sont plus difficiles à déterminer en raison de la variété des éléments, des sites cristallographiques, de l'état d'oxydation et des charges de spin.

La méthode de polycondensation inorganique a été optimisée pour la préparation de nanoparticules d'oxydes spinelles MM'_2O_4 (*M, M'* = Co, Mn, Cu, Zn et Ni) [29, 30]. C'est une méthode simple, à bas coût, réalisée à basse température et sous atmosphère ambiante. Elle nécessite une phase de reflux en plus pour les phases riches en Co. Des nanoparticules sphériques (de 30 à 50 nm de diamètre) des oxydes spinelles en phase cubique unique $M_xCo_{2-x}MnO_4$ (M = Ni, Cu, Zn, $0 \leq x \leq 0,6$) ont été synthétisées et caractérisées. Les tailles des cristallites sont d'environ 15 nm et ces matériaux sont stables à haute température dans l'air.

Les dispersions colloïdales peuvent être stabilisées en utilisant uniquement de l'eau et de l'éthanol afin d'obtenir les couches minces d'oxyde spinelle homogène sur quartz ou des substrats métalliques par la technique de trempage-retrait (ou dip-coating). Les caractéristiques structurales et microstructurales des oxydes ont été étudiées. Des traitements thermiques ont été réalisés afin de densifier les couches avec l'objectif d'intégrer ces semi-conducteurs de type *p* absorbeurs solaire, dans les cellules solaires. Les couches minces homogènes présentent deux fronts d'absorption à ~ 450 nm et 750 nm, qui correspondent aux valeurs du gap optique de E_{g1} ~ 1,5 eV et E_{g2} ~ 2,2 eV à température ambiante. Les valeurs du gap diminuent ~ 0,2 eV

après traitement thermique des couches minces à 900 °C pendant 20 h sous air. Les couches déposées sur platine et traitées à 1000 °C sous air sont compactes et présentent une conductivité électrique de 10^{-5} S.cm^{-1}.

Cette thèse a été menée exclusivement au laboratoire CIRIMAT et le salaire du doctorant financé à 88 % par le gouvernement Vietnamien et programme de l'Université des Sciences et Technologies de Hanoï (USTH) et à 12 % par l'Université Paul Sabatier.

Les résultats sont susceptibles d'avoir un impact plus important dans les domaines de l'opto-électronique et l'énergie solaire à base d'oxydes métalliques semi-conducteurs. Les matériaux d'oxydes type spinelles sont également intéressants pour d'autres applications qui ont été développées dans l'équipe OVM au CIRIMAT. On peut citer la catalyse, la photo-catalyse et la photo-électrochimie. Nous avons mesuré une activité catalytique pour l'oxydation du propane avec Co_3O_4 qui est intéressante dans ce domaine [31]. Des plaquettes auto-organisées séparées par des nanoparticules (~ 10 nm) de la même composition présentant une porosité d'environ 75 % ont été préparées. Des précurseurs CoOOH et des oxydes Co_3O_4 présentent une activité catalytique élevée. Le monoxyde de carbone est totalement converti à 80 °C tandis que la conversion totale du propane se produit à 220 °C (plus faible température, reportée dans la littérature). L'activité catalytique de $Mn_xCo_{2-x}O_4$ peut être ajustée par une modification de composition de l'échantillon et le dopage par d'autres éléments. Il est cependant moins efficace avec des composés riches en manganèse. L'activité catalytiques attractive est liée à la surface spécifique élevée, la stabilité dans les solutions alcalines et la faible coûte de synthèse de ces matériaux. Une étude menée en collaboration avec l'équipe de Dr. D. P Tran de l'Université des Sciences et Technologies de Hanoi (USTH) va nous permettre de tester les activités électro-catalytiques et photo-catalytiques des couches minces d'oxydes spinelles afin d'améliorer, l'oxydation et la réduction de l'eau…

References

[1] M. Gloeckler, I. Sankin, and Z. Zhao, "*CdTe Solar Cells at the Threshold to 20 % Efficiency*," **IEEE Journal of Photovoltaics,** Vol. **3**, 1389-1393, **2013**.

[2] M. A. Contreras, K. Ramanathan, J. AbuShama, F. Hasoon, D. L. Young, B. Egaas, *et al.*, "*Short communication: Accelerated publication: Diode characteristics in state-of-the-art ZnO/CdS/Cu(In1−xGax)Se2 solar cells*," **Progress in Photovoltaics: Research and Applications,** Vol. **13**, 209-216, **2005**.

[3] J. Burschka, N. Pellet, S.-J. Moon, R. Humphry-Baker, P. Gao, M. K. Nazeeruddin, *et al.*, "*Sequential deposition as a route to high-performance perovskite-sensitized solar cells*," **Nature,** Vol. **499**, 316-319, **2013**.

[4] M. Tadatsugu, N. Yuki, and M. Toshihiro, "*Cu 2 O-based solar cells using oxide semiconductors*," **Journal of Semiconductors,** Vol. **37**, 014002, **2016**.

[5] W. S. Yang, J. H. Noh, N. J. Jeon, Y. C. Kim, S. Ryu, J. Seo, *et al.*, "*High-performance photovoltaic perovskite layers fabricated through intramolecular exchange*," **Science,** Vol. **348**, 1234-1237, **2015**.

[6] M. A. Jalaja and S. Dutta, "*Ferroelectrics and multiferroics for next generation photovoltaics*," **Advanced Materials Letters,** Vol. **6**, 568-584, **2015**.

[7] F. Zheng, Y. Xin, W. Huang, J. Zhang, X. Wang, M. Shen, *et al.*, "*Above 1% efficiency of a ferroelectric solar cell based on the Pb(Zr,Ti)O3 film*," **Journal of Materials Chemistry A,** Vol. **2**, 1363-1368, **2014**.

[8] P. Y. Keng, B. Y. Kim, I.-B. Shim, R. Sahoo, P. E. Veneman, N. R. Armstrong, *et al.*, "*Colloidal Polymerization of Polymer-Coated Ferromagnetic Nanoparticles into Cobalt Oxide Nanowires*," **ACS Nano,** Vol. **3**, 3143-3157, **2009**.

[9] Z. Yan, D. A. Keller, K. J. Rietwyk, H.-N. Barad, K. Majhi, A. Ginsburg, *et al.*, "*Effect of Spinel Inversion on (CoxFe1−x)3O4 All-Oxide Solar Cell Performance*," **Energy Technology,** 1-8, **2016**.

[10] E.J.V Verwey, P.W Haaijman, F.C Fomeijn, and G. W. v. Oosterhout, "*Controlled-valency semiconductors*," **Philips research reports** Vol. **5**, 173-187, **1950**.

[11] H. Bordeneuve, A. Rousset, C. Tenailleau, and S. Guillemet-Fritsch, "*Cation distribution in manganese cobaltite spinels Co3−x Mn x O4 (0 ≤ x ≤ 1) determined by thermal analysis*," **Journal of Thermal Analysis and Calorimetry,** Vol. **101**, 137-142, **2010**.

[12] S. M. A. Shibli, P. S. Arun, and A. V. Raj, "*Exploration of octahedrally shaped MnCo2O4 catalyst particles for visible light driven photocatalytic water splitting reaction*," **RSC Advances,** Vol. **5**, 19393-19399, **2015**.

[13] F. Zasada, J. Gryboś, P. Indyka, W. Piskorz, J. Kaczmarczyk, and Z. Sojka, "*Surface Structure and Morphology of M[CoM']O4 (M = Mg, Zn, Fe, Co and M' = Ni, Al, Mn, Co) Spinel Nanocrystals—DFT+U and TEM Screening Investigations*," **The Journal of Physical Chemistry C,** Vol. **118**, 19085-19097, **2014**.

[14] G. Salek, P. Dufour, S. Guillemet-Fritsch, and C. Tenailleau, "*Sustainable low temperature preparation of Mn3−xCoxO4 (0 ≤ x ≤ 3) spinel oxide colloidal dispersions used for solar absorber thin films*," **Materials Chemistry and Physics,** Vol. **162**, 252-262, **2015**.

[15] Y. Hou, Z. Huang, Y. Gao, Y. Ge, J. Wu, and J. Chu, "*Characterization of Mn1.56Co0.96Ni0.48O4 films for infrared detection*," **Applied Physics Letters,** Vol. **92**, 202115, **2008**.

[16] T. Nakajima and T. Tsuchiya, "*Flexible thermistors: pulsed laser-induced liquid-phase sintering of spinel Mn-Co-Ni oxide films on polyethylene terephthalate sheets*," **Journal of Materials Chemistry C,** Vol. **3**, 3809-3816, **2015**.

[17] Z. Huang, W. Zhou, C. Ouyang, J. Wu, F. Zhang, J. Huang, *et al.*, "*High performance of Mn-Co-Ni-O spinel nanofilms sputtered from acetate precursors*," **Scientific Reports,** Vol. **5**, 10899, **2015**.

[18] R. Dannenberg, S. Baliga, R. J. Gambino, A. H. King, and A. P. Doctor, "*Infrared optical properties of Mn1.56Co0.96Ni0.48O4 spinel films sputter deposited in an oxygen partial pressure series*," **Journal of Applied Physics,** Vol. **86**, 2590-2601, **1999**.

[19] W. Zhou, J. Wu, C. Ouyang, Y. Q. Gao, X. F. Xu, and Z. M. Huang, "*Optical properties of Mn-Co-Ni-O thin films prepared by radio frequency sputtering deposition*," **Journal of Applied Physics,** Vol. **115**, 0935121-0935127, **2014**.

[20] Y. Xu, Z. Wen, S. Wang, and T. Wen, "*Cu doped Mn–Co spinel protective coating on ferritic stainless steels for SOFC interconnect applications*," **Solid State Ionics,** Vol. **192**, 561-564, **2011**.

[21] A. Navrotsky and O. J. Kleppa, "*The thermodynamics of cation distributions in simple spinels*," **Journal of Inorganic and Nuclear Chemistry,** Vol. **29**, 2701-2714, **1967**.

[22] R. D. Shannon, "*Revised effective ionic radii and systematic studies of interatomic distances in halides and chalcogenides*," **Acta Crystallographica section a,** Vol. **32**, 751-767, **1976**.

[23] S. Thota, A. Kumar, and J. Kumar, "*Optical, electrical and magnetic properties of Co3O4 nanocrystallites obtained by thermal decomposition of sol–gel derived oxalates*," **Materials Science and Engineering B,** Vol. **164**, 30-37, **2009**.

[24] K. A. Connors, "*Chemical Kinetics: The study of Reaction rates in solide"*, **VCH Publishers**, p. 496, **1998**.

[25] N. Hosseini, F. Karimzadeh, M. H. Abbasi, and G. M. Choi, "*Microstructural characterization and electrical conductivity of CuxMn3−xO4 (0.9≤x≤1.3) spinels produced by optimized glycine–nitrate combustion and mechanical milling processes*," **Ceramics International,** Vol. **40**, 12219-12226, **2014**.

[26] Y. Q. Gao, Z. M. Huang, Y. Hou, J. Wu, Y. J. Ge, and J. H. Chu, "*Optical properties of Mn1.56Co0.96Ni0.48O4 films studied by spectroscopic ellipsometry*," **Applied Physics Letters,** Vol. **94**, 0111061-0111063, **2009**.

[27] B. Kupfer, K. Majhi, D. A. Keller, Y. Bouhadana, S. Rühle, H. N. Barad, *et al.*, "*Thin Film Co3O4/TiO2 Heterojunction Solar Cells*," **Advanced Energy Materials,** Vol. **5**, 14010071-14010075, **2015**.

[28] S. Rühle, A. Y. Anderson, H.-N. Barad, B. Kupfer, Y. Bouhadana, E. Rosh-Hodesh, *et al.*, "*All-Oxide Photovoltaics*," **The Journal of Physical Chemistry Letters,** Vol. **3**, 3755-3764, **2012**.

[29] G. Salek, C. Tenailleau, P. Dufour, and S. Guillemet-Fritsch, "*Room temperature inorganic polycondensation of oxide (Cu2O and ZnO) nanoparticles and thin films preparation by the dip-coating technique*," **Thin Solid Films,** Vol. **589**, 872-876, **2015**.

[30] T. L. Le, S. Guillemet-Fritsch, P. Dufour, and C. Tenailleau, "*Microstructural and optical properties of spinel oxide MxCo2 − xMnO4 (M = Ni, Zn or Cu; 0 < x < 1) thin films prepared by inorganic polycondensation and dip-coating methods*," **Thin Solid Films,** Vol. **612**, 14-21, **2016**.

[31] G. Salek, P. Alphonse, P. Dufour, S. Guillemet-Fritsch, and C. Tenailleau, "*Low-temperature carbon monoxide and propane total oxidation by nanocrystalline cobalt oxides*," **Applied Catalysis B: Environmental,** Vol. **147**, 1-7, **2014**.

Abstract

The present thesis deals with the synthesis and structural characterization of transition metals doped cobalt and manganese based spinel oxides $M_xCo_{2-x}MnO_4$ (with M = Ni, Cu, Zn and x = 0, 0.15, 0.30, 0.60), in relationships with their conduction and optical properties. These materials are good p-type semiconductors and light absorbers in the UV and visible regions, therefore interesting for photo-catalysis and photovoltaics.

The first chapter is a brief overview of the energy context and nature of global warming, renewable energy resources and a literature review of materials used for solar cells including the newly studied system type based on all-oxide photovoltaics.

Chapter two presents all the experimental methods and characterization techniques used for this research work. The inorganic polycondensation method optimized in our laboratory and used for synthesizing spinel oxide powders at low temperature (T < 120 °C) without complex organic agents is described. Then, the preparation of colloidal dispersions stabilized at room temperature using an azeotrope solution based on absolute ethanol and water only is described, in order to obtain homogenous oxide thin films by the dip-coating technique.

The third chapter presents detailed results on the atomic and electronic structures of the materials under study performed by using a full density functional theory investigation thanks to a collaboration with the CEMES. First principles electronic structure calculations were performed for the first time to our knowledge over the whole spinel oxide solid solution range $Mn_xCo_{3-x}O_4$ ($0 \leq x \leq 3$), and compared with our experimental data. A small band gap of ~ 0.8 eV is calculated, due to metal-metal transitions in B sites. The experimental band gaps observed at 1.5 and 2.2 eV, which increase with the amount of manganese, would correspond to *B*-*A* and O-*B* transitions, respectively. The magnetic properties of these materials are also discussed.

Chapter four shows the experimental details of the preparation and characterization of the spinel oxide powders, colloidal dispersions and thin films. All samples (Ni, Cu or Zn-doped Co_2MnO_4) are well crystallized with a single cubic spinel oxide phase. Nanoparticles are spherical and their diameters vary from 20 to 50 nm, doping with Zn, Ni to Cu, mainly due to steric effects. Homogenous oxide thin films were deposited on quartz, alumina, titanium nitride and platinum in order to measure their optical and electrical properties, and to increase the film compactness (thus electrical conductivity and light absorbance) after thermal treatment. Thin films are well preserved up to 900 °C in air and can handle higher temperatures (up to 1000 ºC) on platinum without reaction with the substrate.

Chapter five deals with the optical and electrical properties of thin films before and after sintering. The optical properties were measured over a wide range of wavelengths (UV-VIS). The optical properties of spinel oxide thin films show two strong absorption band gaps for each composition at the UV front and close to 700 nm in wavelength. These band gaps are direct and mostly lower than 2 eV for the first band. Both band gaps increase with further doping and decrease after annealing. Thin film resistivity is about 10^5 Ω.cm at room temperature and decreases with increasing temperature (a few tens of Ω.cm at 300 ºC). In parallel to the soft chemistry method and dip-coating technique used to prepare our spinel oxide thin layers, Pulsed Laser Deposition technique was used to prepare pure Co_2MnO_4 and Cu_2O dense thin films. Their structural and optical main features are discussed.

Keywords: *p*-type semiconductors, light absorbers, spinel oxide $M_xCo_{2-x}MnO_4$ (M = Ni, Cu, Zn, x = 0, 0.15, 0.30, 0.60), conduction, optical properties, photo-catalysis, photovoltaic.

Résumé :

Ce travail de thèse a porté sur l'élaboration de nanoparticules et de couches minces d'oxydes spinelles mixtes de $M_xCo_{2-x}MnO_4$ (M = Ni, Cu, Zn ; x = 0, 0,15, 0,30, 0,60) semi-conducteurs, absorbants de lumière avec d'intéressantes applications potentielles pour la photo-catalyse et le photovoltaïque.

Le premier chapitre présente tout d'abord une vue globale du contexte énergétique à l'échelle mondiale et des ressources d'énergie renouvelables, alternatives aux énergies fossiles les plus répandues. Une revue détaillée est ensuite faite des différents matériaux et systèmes employés dans la fabrication de cellules solaires, en portant une attention plus particulière à un nouveau type de cellules photovoltaïques en couches minces, dites « Tout-oxyde », basées notamment sur l'utilisation d'oxydes de type spinelle utilisés comme absorbeurs solaires.

Le deuxième chapitre présente les techniques expérimentales de synthèse et de caractérisation utilisées lors de ce travail de thèse. Le procédé de polycondensation inorganique, optimisé au laboratoire, utilisé pour synthétiser les poudres d'oxydes à basse température (T < 120 °C) sans agent organique complexe est décrit. Ensuite, les méthodes de préparation de dispersions colloïdales à l'ambiante dans l'éthanol et de films minces homogènes d'oxydes par trempage-retrait sont explicitées.

Le troisième chapitre présente les résultats détaillés des structures atomiques et électroniques des matériaux de base à l'étude, issus de calculs par la méthode *Density Functional Theory* (DFT), réalisés en collaboration avec le laboratoire CEMES de Toulouse. Les résultats des calculs de densités électroniques et détermination de structures de bandes, réalisés pour la première fois à notre connaissance, sur l'ensemble de la solution solide $Mn_xCo_{3-x}O_4$ ($0 \leq x \leq 3$), sont comparés à nos données expérimentales, obtenues notamment sur les largeurs de bande interdite (*gap*) à partir de mesures optiques faites sur couches minces. Un *gap* de 0,8 eV est calculé, qui serait dû à des transitions inter-métalliques en sites *B*. Deux gaps à 1,5 et 2,2 eV, obtenus expérimentalement dans l'UV-VIS, qui augmentent avec la quantité de manganèse, correspondraient à des transitions respectives *B*-*A* et O-*B*, respectivement. Les propriétés magnétiques de ces matériaux sont également discutées.

Le quatrième chapitre présente l'élaboration et la caractérisation (micro-)structurale des poudres et des couches minces d'oxydes de type spinelle. Toutes les compositions (Co_2MnO_4 dopé au Ni, Cu ou Zn) cristallisent dans une phase cubique. Les nanoparticules sont sphériques avec la taille variant entre 20 et 50 nm. Les couches minces homogènes ont été déposées sur quartz, alumine, nitrure de titane et platine afin de mesurer leurs propriétés électriques et optiques. Une température de frittage environ de 1000 °C sous air a été déterminée par dilatométrie et les couches sont stables jusqu'à 900 °C quel que soit le substrat. En revanche, seules les couches déposées sur platine permettent d'atteindre la température de frittage sous air (et d'accroitre la compacité donc la conductivité des couches) sans réaction avec le substrat.

Le chapitre cinq présente les variations des propriétés optiques et électriques des couches minces avec le frittage. Les propriétés d'absorbance de lumière des couches minces ainsi préparées, mesurées sur une gamme de longueurs d'ondes du domaine spectral UV-visible, montrent deux bandes d'absorbance, correspondantes à deux valeurs de *gap* pour chaque composition. La propriété d'absorbance des couches minces augmente dans la gamme du visible après frittage et les *gaps* diminuent. Les couches minces sont plus compactées. La résistivité des couches minces diminue de 10^5 à 10^2 Ω.cm avec l'augmentation de la température de 20 à 300 ºC. Une étude parallèle, basée sur la préparation de films minces absorbants de lumière de Co_2MnO_4 et Cu_2O par la technique de *Pulsed Laser Deposition* (PLD) est également présentée.

Mots clés : semi-conducteurs type *p*, absorbant de lumière, $M_xCo_{2-x}MnO_4$ (M = Ni, Cu, Zn ; x = 0, 0,15, 0,30, 0,60), conduction, propriétés optique, photo-catalyse, photovoltaïque.